

Experimental Dynamic Substructuring

Analysis and Design Strategies for Vehicle Development



Maarten van der Seijs

Experimental Dynamic Substructuring

Analysis and Design Strategies for Vehicle Development

PROEFSCHRIFT

ter verkrijging van de graad van doctor
aan de Technische Universiteit Delft,
op gezag van de Rector Magnificus prof. ir. K. C. A. M. Luyben,
voorzitter van het College voor Promoties,
in het openbaar te verdedigen op donderdag 16 juni 2016 om 12:30 uur
door

Maarten Vincent VAN DER SEIJS

werktuigkundig ingenieur
geboren te Heiloo, Nederland.

Dit proefschrift is goedgekeurd door de

promotor: Prof. dr. ir. D. J. Rixen
copromotor: Dr. ir. D. de Klerk

Samenstelling promotiecommissie:

Rector Magnificus	voorzitter
Prof. dr. ir. D. J. Rixen	Technische Universiteit Delft / TU München, promotor
Dr. ir. D. de Klerk	Technische Universiteit Delft, copromotor

Onafhankelijke leden:

Prof. dr. P. Avitabile	University of Massachusetts Lowell
Prof. dr. A. T. Moorhouse	University of Salford
Prof. dr. ir. N. B. Roozen	Katholieke Universiteit Leuven
Prof. dr. ir. J. W. Verheij	Voormalig hoogleraar Technische Universiteit Eindhoven
Prof. dr. ir. E. G. M. Holweg	Technische Universiteit Delft
Prof. dr. ir. J. L. Herder	Technische Universiteit Delft, reservelid



Rolls-Royce
Motor Cars Limited

Copyright © 2016 by Maarten van der Seijs

– All rights reserved – No part of the material protected by this copyright notice may be reproduced or utilised in any other form or by any other means, electronic or mechanical, including photocopying, recording or by any information storage and retrieval system, without the prior permission of the author.

ISBN 978-94-6186-671-4

An electronic version of this dissertation is available at
<http://repository.tudelft.nl/>.

Printed by: Gildeprint, Enschede

Cover art by: Thijs ten Brummelhuis

Author email: mvdseijs@gmail.com

Abstract

Experimental Dynamic Substructuring

– *Analysis and Design Strategies for Vehicle Development* –

Sound and vibration have a defining influence on our perception of product quality. They are especially well-known aspects in the automotive industry; a branch which sees, besides safety and driving comfort, ever-increasing expectations of the acoustic experience. After all, a smooth and silent driving experience appeals to a feeling of *premiumness*, a connotation no longer reserved to the top segment in the industry. While traditional combustion engines are gradually getting replaced by hybrid or full-electric drive-lines, other electromechanical (so-called *mechatronic*) systems make their entrance. As a consequence, the sound experience shifts from low-frequent engine roar to high-frequent humming and whining — a yet unfamiliar experience that calls for redefinition of the soundscape. To support such change, it is necessary that sound and vibration aspects can be considered in an early phase of development by means of simulations. This poses a true challenge: although state-of-art numerical modelling techniques can simulate the low-frequent dynamics fairly well, they often fail to provide reliable answers for the higher acoustic frequency range.

This thesis presents techniques that aim to implement measurements of structural dynamics and active vibration sources into development processes. By characterising the passive and active dynamics of yet available components by means of measurements and combining those with numerical models, a hybrid simulation emerges that may provide answers to high-frequent problems in an early phase of development. This hybrid simulation is facilitated by use of *Experimental Dynamic Substructuring*: a methodology that determines structural dynamic aspects of complete products based on individually measured components.

Part one of this thesis presents a variety of methods for simulation and substructuring that form the basic toolbox for generation, analysis, coupling and decoupling of dynamic models. Pivotal is the *experimental* approach, which means that dynamic models are obtained from measurements rather than numerical modelling efforts. To transform such measurements into a model that is compatible for coupling with other (numerical) models, the *virtual point transformation* is proposed. This method considers measured responses and applied forces around (user-chosen) points as locally rigid displacements and forces. Doing so, every connection point of a component can be described by three translations and three rotations with respect to a global reference frame, perfectly suited for substructuring. At the same time, the quality of the measurement and transformed frequency response functions can be quantified objectively using the proposed consistency functions. Altogether, the virtual point method bridges the gap between experimental and numerical modelling activities and enables us to exploit substructuring effectively for complex high-frequency systems.

Part two presents a comprehensive study of Transfer Path Analysis (TPA); a collection of methods that contemplate a vibration problem as a source, transmission and receiver. A general framework for TPA is presented by re-interpreting eleven methods from the perspective of substructuring. It is shown that these methods can be categorised into three

families, that in turn differ in the nature of characterisation of the source. The component-based TPA is regarded the most promising family, which allows to characterise a source *independent* of the environment in which it has been measured. The vibrations of the active source can be replaced by equivalent force spectra that, multiplied with the (simulated) FRFs of the assembled vehicle, predict what this source would sound like in the vehicle. Several practical methods are discussed to determine such equivalent forces: from forces measured against a blocked boundary, using free velocities, based on measurements on a compliant test bench or using the so-called *in-situ* and *pseudo-forces* methods. For further generalisation, a notation is presented that governs the abovementioned principles and facilitates the application and comparison of component-based TPA methods. In particular, it is shown that *controllability* and *observability* — concepts adopted from control theory — are strongly related to TPA; proper understanding of these principles yields interesting opportunities for analysis and simulation.

The developed methods have been applied to analyse the vibrations of the electric power-assisted steering (EPS) system, which is reported on in part three. It is demonstrated that the virtual point transformation is able to determine accurate FRFs in a frequency range up to 6000 Hertz. Substructuring is applied to simulate the FRFs of a vehicle by applying the principle of *substitute coupling*, which employs a substitute beam during measurement in the vehicle to represent the dynamic effects of the steering system to couple. For the purpose of characterisation of the steering system's excitations, several testing environments are discussed: a stiff test bench, more compliant test benches and the vehicle itself. Each configuration is accompanied by a specific method for source characterisation, for which it is demonstrated that the equivalent forces are indeed an environment-independent description of the active excitations of the steering system. It is shown that these forces can be used for the prediction of sound and vibrations in the vehicle. The presented applications offer, with understanding of substructuring and TPA theory, insights in the practical aspects of the methodology. This opens interesting opportunities for early-phase development of sound and vibration.

Samenvatting

Experimentele Dynamische Substructurering – Strategieën voor Analyse en Ontwerp in Voertuigontwikkeling –

Trillingen en geluid hebben een bepalende invloed op onze perceptie van productkwaliteit. Het zijn met name bekende aspecten in de automobielinindustrie; een markt waarin, naast veiligheid en rijcomfort, ook steeds hogere eisen worden gesteld aan de akoestische ervaring. Immers, een geruisloze rijervaring appelleert aan een gevoel van *premiumness*, iets dat niet meer alleen is weggelegd voor het topsegment van de industrie. Terwijl de traditionele verbrandingsmotor gaandeweg plaats maakt voor hybride of volledig elektrische aandrijflijnen, doen andere elektrisch-mechanische (zogeheten *mechatronische*) systemen hun intrede. Hiermee verschuift de geluidservaring van laagfrequent motorgebrom naar hoogfrequent zoemen en fluiten — een nu nog onbekende ervaring die vraagt om herdefinitie van het klankprofiel. Om zulke veranderingen te ondersteunen is het noodzakelijk dat trillingen en geluid in een vroege fase van ontwikkeling kunnen worden beschouwd door middel van simulaties. Hierin schuilt een grote uitdaging: hoewel de hedendaagse numerieke modellerings-technieken goed in staat zijn om het laagfrequente dynamische gedrag te simuleren, bieden zij voor het hogere akoestische frequentiebereik nog geen betrouwbaar antwoord.

Dit proefschrift presenteert technieken die erop gericht zijn om metingen aan structuurdynamica en actieve trillingsbronnen te implementeren in ontwerpprocessen. Door de passieve en actieve eigenschappen van reeds beschikbare onderdelen door middel van metingen te karakteriseren en deze te combineren met numerieke modellen, ontstaat een hybride simulatie die in een vroege fase van ontwikkeling antwoorden kan bieden voor hoogfrequente dynamische problemen. Deze hybride simulatie is mogelijk door gebruik te maken van *Experimentele Dynamische Substructurering*: een methodiek die in staat stelt om structuurdynamische eigenschappen van een totaalproduct te bepalen op basis van individueel gemeten componenten.

Deel één van dit proefschrift presenteert een verscheidenheid aan methoden voor simulatie en substructurering die als basisgereedschap dient om dynamische modellen te verkrijgen, analyseren, koppelen en ontkoppelen. Centraal hierin staat de *experimentele* benadering, hetgeen in dit geval betekent dat dynamische modellen worden verkregen door middel van metingen in plaats van numerieke berekeningen. Om zulke metingen om te vormen naar een model dat geschikt is voor koppeling met andere (numerieke) modellen, wordt de *virtuele punttransformatie* voorgesteld. Deze methode beschouwt metingen en toegepaste krachten rondom (vrij te kiezen) punten als lokaal starre bewegingen en excitaties. Hierdoor kan elk koppelpunt van een component worden beschreven door drie translaties en drie rotaties in een globaal coördinatenstelsel, ideaal geschikt voor substructurering. Tegelijkertijd kunnen de kwaliteit van de meting en de getransformeerde overdrachtsfuncties objectief worden gekwantificeerd aan de hand van voorgestelde consistentie-functies. De virtuele puntmethode slaat daarmee een brug tussen de experimentele en numerieke modelleeractiviteiten en stelt ons in staat om substructurering effectief in te zetten voor complexe hoogfrequente systemen.

In deel twee wordt een uitvoerige studie gepresenteerd van Transfer Path Analysis (TPA); een verzameling van methodes die een trillingsprobleem analyseren als bron, overdracht en antwoord. Een algemeen raamwerk voor TPA wordt gepresenteerd door elf methodes te herinterpreteren vanuit het perspectief van substructurering. Aangetoond wordt dat deze methodes in drie families onder te brengen zijn, die zich op hun beurt onderscheiden in de wijze waarop de bron wordt gekarakteriseerd. Als meest veelbelovende familie wordt de component-gebaseerde TPA aangemerkt, die een bronkarakterisering afleidt *onafhankelijk* van de structuur waarin deze is gemeten. De trillingsbron kan als zodanig worden vervangen door equivalente krachtspectra die, wanneer vermenigvuldigd met de (gesimuleerde) overdrachtsfuncties van een geassembleerd voertuig, voorspellen hoe deze bron zou klinken in het voertuig. Verschillende praktische methodes worden besproken om zulke equivalente krachten af te leiden: van gemeten krachten tegen star, vrije trillingen, op basis van metingen op een flexibele testbank en volgens de zogeheten *in-situ* en *pseudo-krachten* methodes. Als verdere generalisatie wordt een notatie gepresenteerd die voorgenoemde principes onderbrengt en de toepassing en vergelijking van component-gebaseerde TPA methodes vergemakkelijkt. In het bijzonder wordt bewezen dat *controleerbaarheid* en *observeerbaarheid* — principes ontleend aan de systeem en regeltheorie — duidelijk verband houden met TPA en dat goed begrip hiervan waardevolle mogelijkheden biedt voor analyse en simulatie.

De ontwikkelde methodes zijn in het kader van dit project toegepast op de trillingen van het elektromechanische stuursysteem, waarvan in deel drie verslag wordt gedaan. Het wordt aangetoond dat de virtuele puntransformatie in staat is om accurate overdrachtsfuncties te bepalen in een frequentiegebied tot aan 6000 Hertz. Substructurering wordt gebruikt om de overdrachtsfuncties van een voertuig te simuleren op basis van het *substitute coupling* principe, waarbij gebruik wordt gemaakt van een vervangingsbalk tijdens meting in het voertuig om de effecten van een eventueel stuursysteem te representeren. Ter karakterisering van de excitaties van het stuursysteem worden verschillende testomgevingen besproken: een starre testbank, meer flexibele testbanken en het voertuig zelf. Elke configuratie gaat gepaard aan een specifieke methode voor bronkarakterisering, waarvan wordt aangetoond dat de equivalente krachten inderdaad een omgevingsonafhankelijke beschrijving zijn van de actieve excitaties van het stuursysteem. Getoond wordt dat deze krachten kunnen worden gebruikt voor het voorspellen van trillingen en geluid in het voertuig. De gepresenteerde toepassingen bieden, met inachtneming van de theorie van substructurering en TPA, inzicht in de praktische aspecten en beperkingen van de methodiek. Dit biedt interessante mogelijkheden voor vroege-fase ontwikkeling van trilling en geluid.

Acknowledgements

In the spring of 2010, I got the opportunity to spend some time at the *NATO Undersea Research Centre* in the beautiful bay around La Spezia, Italy, as part of my studies at TU Delft. The pleasant environment of multicultural PhD and post-doc scientist, combining hard-core research with the good things in life, probably sparked the idea of trying academics for myself. This idea materialised in September 2011 when I got the opportunity to start a research project in the group of Engineering Dynamics and write a proposal for collaboration with the BMW Group.

A PhD candidacy is a rather undefined journey which, I believe, you have to invent and shape for yourself. Nonetheless, many people have been involved to make it such an enjoyable and colourful endeavour, to whom I like to extend my appreciation here.

First I would like to thank my promotor Daniel Rixen and co-promotor Dennis de Klerk for their all-round involvement in my 4½-year PhD project. You have been a great source of inspiration and quite a complementary team in discussing the theory and practice of dynamics. Yet, what I have valued most is your shared interest in the person behind the PhD candidate: stimulating to maintain a good work-life balance, always be on the lookout for opportunities and make the most out of the years that have been granted. On this level you are united and I look back on the many nice off-the-job events that we have undertaken in Delft, Munich, Hattem and elsewhere.

I would also like to thank the department of Precision and Microsystems Engineering (PME) at TU Delft. Even during challenging times of personnel changes, the department remains a strong family, which is certainly also due to the great secretary and support staff. Special thanks goes out to Gaby Offermans, who has always been constructive and open-minded in finding ways to support our project, especially during my frequent times in Munich.

This project would not have been possible without the support of the BMW Group. I would like to thank the colleagues of the Mechatronics department for our pleasant times and collaboration: Jan Biermann, Stefan Schubert, Michael Spickenreuther and many others, but most of all Matthias Fenzl for being such a committed project leader. Another big thanks goes out to Bastian Däxl, also on behalf of the students from TU Delft, for his kind support and ever-pragmatic mind-set.

I would also like to thank the Msc. students that I had the pleasure working with: Tim, Daniël, Emiel, Eric, Tessa and Mathieu. I have never believed in the need for a professional distance and I appreciate how this resulted in you becoming part of the team.

Finally, I am grateful for the support and care of my family and friends, including the many colleagues at TU Delft. You have made the past years an unforgettable and rich experience and I am proud to have you around me!

Maarten van der Seijs
Den Haag, May 2016

Contents

Abstract	iii
Samenvatting	v
Acknowledgements	vii
Contents	ix
Nomenclature	xi
1 General Introduction	1
1.1 Research context	1
1.2 Trends & challenges in vehicle development	2
1.3 Developments in component modelling	4
1.4 Predictive noise & vibration engineering	8
1.5 Application to vehicle mechatronics	9
1.6 Thesis contributions	10
Part I Practical Guide to Dynamic Substructuring	
2 Introduction to dynamic simulation	13
2.1 Introduction	13
2.2 Physical domain	14
2.3 Modal domain	15
2.4 Frequency domain	17
2.5 Time domain	19
2.6 State-space domain	20
2.7 Conversion between domains	22
2.8 Summary	24
3 Substructure coupling and decoupling	27
3.1 Introduction	27
3.2 Interface conditions	28
3.3 Substructure coupling	32
3.4 Substructure decoupling	38
3.5 Summary	43
4 Obtaining dynamic models by experiment	45
4.1 Introduction	45
4.2 Virtual point transformation	49
4.3 Interface displacement modes	55
4.4 Measurement quality indicators	58
4.5 Instrumentation in practice	61
4.6 Example	63
4.7 Summary	67

Part II | Transfer Path Analysis & Source Characterisation

5	Introduction to TPA	71
5.1	Introduction	71
5.2	History of TPA techniques	73
6	General framework for TPA	77
6.1	The transfer path problem	77
6.2	Classical TPA	80
6.3	Component-based TPA	84
6.4	Transmissibility-based TPA	95
6.5	Summary	104
7	Practical considerations & advanced strategies	107
7.1	Source dependency on mounting conditions	107
7.2	Multiple simultaneous sources	108
7.3	Air-borne transmission paths	110
7.4	Interface description & rotational DoFs	111
7.5	Observability & controllability of the transfer problem	115
7.6	Evaluation of paths contributions	117

Part III | Application to Steering Gear Vibrations

8	Validation of frequency-based substructuring techniques	121
8.1	Introduction	121
8.2	General subsystem description	123
8.3	Vehicle FRFs from experimental modelling	126
8.4	FRF uncertainty & benchmark study	133
8.5	Application of Dynamic Substructuring	138
9	Steering noise prediction from test bench measurements	143
9.1	Introduction	143
9.2	Development of component-based TPA approaches	145
9.3	In-situ TPA from vehicle and test bench measurements	152
9.4	Summary	162

Part IV | Conclusions and Recommendations

10	Conclusions and recommendations	167
10.1	Conclusions	167
10.2	Recommendations	170
	List of personal publications	173
	Curriculum vitae	175
	References	177

Nomenclature

Few scientific dissertations written as a book occur without any compromise in notation. Initial discouragement notwithstanding, a shortage of unique symbols and embellishments could also be seen as an indication that one has approached the matter from sufficient different angles. With that in mind, the following list is an attempt to enumerate the symbols and conventions that are used recurrently throughout this thesis.

Roman symbols

B	signed Boolean matrix	p	acoustic pressures
C	viscous damping matrix	q	generalised / virtual point motion; volume velocities
e	unit direction vector	R	modal reduction / IDM matrix
E	rotation matrix	t	time (in seconds)
f	applied forces	T	virtual point transformation matrix; transmissibility matrix
F	IDM filter matrix; array of force vectors	u	dynamic displacements / rotations
g	interface forces / moments	U	array of response vectors
H	acoustic transfer function matrix	W	virtual point weighting matrix
K	stiffness matrix	Y	admittance FRF matrix
L	Boolean localisation matrix	Z	impedance matrix
m	generalised / virtual point loads	0/I	null / identity matrix
M	mass matrix		

Greek symbols

δ	interface incompatibilities	ν	force residual
ζ	modal damping ratio	ρ	consistency criterion
η	modal amplitude	φ	mode shape
θ	angle (in degrees)	χ	reciprocity criterion
λ	Lagrange multipliers	ω	frequency (in Hertz)
μ	displacement residual		

Embellishments

\star^A	pertaining to active system A	\star^{free}	free interface
\star^B	pertaining to passive system B	\star^{mt}	mount stiffness
\star^C	pertaining to substitute beam C	\star_1	internal / source excitation DoF
\star^R	pertaining to test rig R	\star_2	interface DoF
\star^{AB}	pertaining to target assembly AB	\star_3	internal / receiver DoF
\star^{AR}	pertaining to test assembly AR	\star_4	indicator DoF
\star^{eq}	equivalent force	\star_{ps}	pseudo-force DoF
\star^{bl}	blocked force		

Notation conventions

The following typographical conventions are used throughout this thesis:

- ▶ Scalars are denoted by lower-case symbols, e.g. n, k, ρ ;
- ▶ Vectors and sets are denoted by bold-face lower-case symbols, e.g. $\mathbf{u}, \mathbf{f}, \boldsymbol{\mu}$;
- ▶ Matrices and vector arrays are denoted by bold-face capitals, e.g. $\mathbf{I}, \mathbf{Y}, \boldsymbol{\Phi}$;
- ▶ Column-wise and block-diagonal concatenations are denoted as follows:

$$\text{col}(\mathbf{u}^A, \mathbf{u}^B) = \begin{bmatrix} \mathbf{u}^A \\ \mathbf{u}^B \end{bmatrix}; \quad \text{diag}(\mathbf{Y}^A, \mathbf{Y}^B) = \begin{bmatrix} \mathbf{Y}^A & \mathbf{0} \\ \mathbf{0} & \mathbf{Y}^B \end{bmatrix}$$

- ▶ Function derivatives to time are denoted by dotted notations, e.g. velocity \dot{u} and acceleration \ddot{u} . Complex conjugate values read u^* ; the transpose and complex-conjugate (Hermitian) transpose of a matrix are indicated by \mathbf{Y}^T and \mathbf{Y}^H , respectively.
- ▶ Some equations appear *scribbled*; this is typically used to highlight the governing equation of a theory or method, often to be compared on the same level with other scribbled notions.

▶ This paragraph is intended as an in-depth, loosely related or otherwise superfluous discussion with respect to the main message of the text. It was chosen to use this *glossy*-style formatting to clearly distinguish between text and context. Sometimes, the blue boxes provide a more practical view on matter based on personal experience. ◀

Abbreviations

BMW	Bayerische Motoren Werke	IRF	impulse response function
DoF	degree of freedom	LM-FBS	Lagrange multiplier FBS
DS	dynamic substructuring	MAC	modal assurance criterion
EMA	experimental modal analysis	NVH	noise, vibration and harshness
EPS	electric power steering	SVD	singular value decomposition
FBS	frequency-based substructuring	TPA	transfer path analysis
FE	finite element	VP	virtual point
FRF	frequency response function		

General Introduction

1.1 Research context

1.1.1 *The music of sound*

Few sensations are as fascinatingly diverse and revealing as audible sound. Although quite simply defined as oscillating air pressure, the information contained in even a short bit of sound can be immense. We perceive and analyse sound by our human hearing system, which has evolved to a remarkably advanced sensing instrument. Almost effortlessly, we listen to speech, hear a car approaching a road crossing or enjoy a symphony played by an orchestra. Even more, the trained ear could detect certain emotions from a slight resonance in the voice, identify the engine type of the approaching car or determine the exact harmony played by the orchestra's string section.

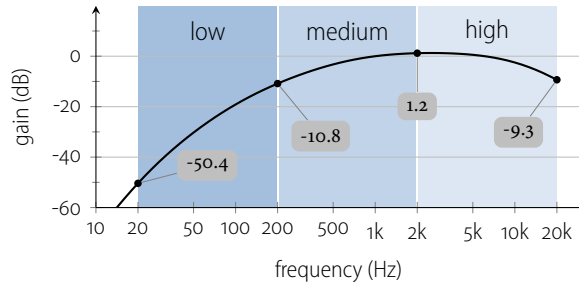
When hearing the sound generated by a mechanical system, we deduce a lot of information about the very processes going on. The fact that this happens largely unconsciously might explain why we attach so much emotion to particular aspects of sound. Sounds that exhibit a regular harmonic content and smooth envelopes of amplitude and pitch may be experienced as pleasant or even musical. On the contrary, when exposed to squeaking or rattling noise — for instance coming from the engine compartment of a car — one would directly stop to assess the structural integrity of the components under the bonnet.

Fundamentals of sound and vibration have been studied in the late 19th century by great scientists as John William Strutt (better known as Lord Rayleigh) [160] and Hermann von Helmholtz [81]. In fact, theory on pitch and harmonic intervals had already been known since the age of Pythagoras around 600 B.C. This was all long before any real engineering application was in mind. Indeed, the ages of industrialisation are not particularly remembered for their quietly operating machines or compelling acoustic experiences, apart perhaps from the finesse found in some musical instruments of that time, as a result of profound dedication and craftsmanship.

1.1.2 *Sound and vibration in automotive engineering*

From this perspective it can be understood why vehicle manufacturers of today are so much concerned with sound and vibration engineering. Besides mechanical performance (think of speed, acceleration and handling) and interior comfort, the customer has developed precise expectations of the acoustic performance. In the automotive industry, this relates to the domain of noise, vibration and harshness (NVH) engineering. The definition, that holds a slightly pessimistic connotation, might suggest that NVH only concentrates on reducing the undesired sounds. On the contrary, NVH engineering has nowadays become the area of sound design, stretching from the tiniest nuances in engine roar to the muffled *boom* of a shutting door. Altogether they contribute to the customer perception of *premiumness* or *sportiness* of a vehicle, hence the value on the market [30, 149, 181].

The audible frequency spectrum divided in the low, medium and high frequency range, normally defined as respectively 20–200, 200–2k and 2k–20k Hertz. The black curve indicates the A-weighting, resembling the sensitivity of the human ear.



All sounds in a car can be attributed to one or more sources of vibration. One way to look at the complex chain of reactions from a vibration source to received sound is using the *source–transmission–receiver* model. A source is normally considered as an entire active component, as the internal processes that make it vibrationally active are often difficult to describe. Regarding the transmission, distinction is made in *structure-borne* and *airborne* sound. Structure-borne sound concerns the vibrations that are transmitted through solid structures connected to the source, in turn actuating passive parts closer to the receiver that radiate sound¹. Airborne sound relates to the acoustic waves directly emitted by the source structure, possibly modified by acoustic shielding material. Altogether they contribute to the total sound or level at a point of interest, denoted by the receiver.

1.2 Trends & challenges in vehicle development

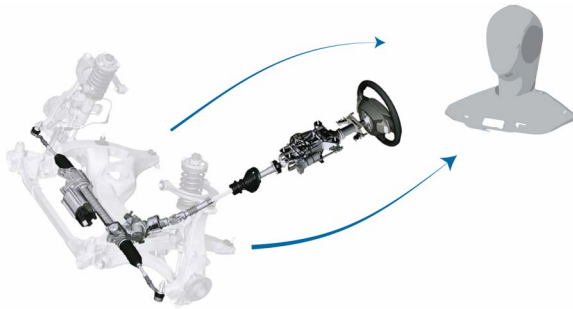
Considering the vast amount of active systems in today's vehicles, the interior sound would become a sheer cacophony without proper NVH engineering. Therefore, NVH efforts focus on either minimising the overall vibrations or shaping its characteristics to sound more pleasant to the ear. This requires integrated analysis and simulation methodologies. Some of the current trends and challenges herein are introduced next.

1.2.1 Electric & mechatronic components

Driven by the global need for sustainable transportation solutions, traditional combustion engines are gradually getting replaced by hybrid or electric drive-lines. Aside from getting quieter in general, electric motors generate a radically different, more high-frequent sound than combustion engines. For instance: the sound of a typical four-stroke four-cylinder engine has a fundamental frequency between 50–200 Hertz (the number of combustions per second), accompanied by a strong pattern of harmonic orders due to the impulsive nature of the combustion. An electric motor on the other hand generates more fluent sine waves at higher frequencies and at odd harmonic ratios related to e.g. the number of poles.

Besides engine noise, sound of secondary mechanic or mechatronic components, otherwise masked by the low-frequent rumbling of the combustion engine, may now be audible as well. An example of such a mechatronic component is the electric power steering (EPS) system. In the particular case of a parallel parking manoeuvre, the EPS motor delivers a great amount of power at relatively high steering speed, while the main engine is almost idling. The EPS transmission, typically consisting of a toothed belt and a planetary gear-

¹A classical example of structure-borne sound transmission is the tin-can telephone, that transports sound as mechanical vibrations through a string.



Vibrations of the steering system (source) propagate through the bodywork (transmission) to the vehicle's interior and the driver's ear (receiver). Due to the stiff connection of the steering system to the chassis, the structure-borne part of the experienced sound is dominant.

ing system, generating distinct orders in a frequency range of several kHz. As EPS noise is predominantly of structure-borne nature, a simple remedy would be to mount the steering system resiliently with absorbing dampers. However, added flexibility reduces the stiffness in the lateral (sideways) direction, compromising the handling and thereby the sportiness of the car. As a consequence, controlling the noise of such components asks for an approach on a total vehicle (German: "Gesamtfahrzeug") level.

1.2.2 Specifying component targets

Virtually all noise and vibration levels in a car are bound to targets, typically specified as maximum levels in certain frequency bands. These targets are carefully defined in an early development phase, based on pre-development and extensive benchmarking of competitive products in the same market segment. At first, targets are specified on a total vehicle level, for instance as a sound pressure level (SPL) at the driver's ear. These *global targets* then have to be translated into *component targets* for each relevant structure in the chain from source to receiver.

Definition and communication of component targets is by no means a trivial task. Active components are often connected at several points to the chassis, which means that their vibrations may choose various paths to propagate into the vehicle. The component's vibrating mechanisms are often not influenced by the mounting conditions, but the dynamic interaction between component and vehicle affects the paths of vibration transmission considerably. As a consequence, a global NVH target does not easily translate to a unique combination of vibration targets for the component's interfaces.

1.2.3 Predictive NVH technology

In a product branch as saturated and volatile as the automotive industry, it is essential to maintain a short time-to-market (TTM). This implies that NVH engineering should be incorporated right from the start of development. Yet, working with acoustic targets in an early phase is a tremendous challenge. At the start of design, one might fairly well predict the looks and total horsepower of the vehicle in the making. Using finite element modelling (FEM), multi-body simulations and modal analysis, low-frequent behaviour responsible for handling and driving comfort can also be engineered. However, to simulate the medium- and high-frequency sound experienced in the interior of the vehicle, one should understand the complex interplay between countless vibration sources, structural components and radiating parts.

Ideally, one desires to listen to the sound in the vehicle's interior before a prototype has actually been built. With the availability of such predictive technology, important NVH-related design problems could be identified and resolved up front, or, as vividly put in the words of the notorious Dutch football-philosopher Johan Crujff [24]:

“Voordat ik een fout maak, maak ik die fout niet” — [Before I make a mistake, I don't make that mistake].

The current state of technology and the main challenges in realising such a design strategy are introduced in the next two sections. First the field of component modelling is discussed, identifying dynamic substructuring as a means to bridge the efforts in the numerical and experimental domain. The section thereafter describes the problem of source characterisation and predictive analysis of transfer paths. The last section introduces the application and validation of theory on an automotive NVH problem.

1.3 Developments in component modelling

The virtues of computerised engineering technology have had profound impact on many scientific disciplines, ranging from architectural design and weather forecasting to all fields of structural engineering. Many design dilemmas, previously requiring some engineering judgement from experts in the field, now find an objective answer in the form of a numerical solution, provided by the impeccable accuracy of the modern computer.

In the automotive industry, computerised engineering starts right after a new design leaves the stage of hand-drawn sketches and mock-up modelling. Three-dimensional models are generated for each component with a profound level of detail. Several levels of computer-aided engineering (CAE) are nowadays available from within the computer-aided design (CAD) environment, such as finite element analysis (FEA) for static and dynamic calculations and multi-body dynamics (MBD) to simulate the low-frequency interaction between suspension systems.

But besides pushing the frontiers of design possibilities, the shift towards computerised engineering also changed the common understanding of the word *modelling*. A century ago, only a handful of analytical equations would be at our disposal to model the mechanical behaviour of a structure. As these equations require some degree of continuity, a lot of simplifications were needed to model something in primitive systems like masses, springs and beams — in fact, many designs ended up looking like their elementary analytical counterparts. A typical example is the cantilever beam as depicted in Fig. 1.1, for which closed form solutions are available to calculate the deflection caused by a point load (think of the Dutch “vergeet-me-nietjes”, the rules of thumb for structural mechanics). Hence, the task of analytical modelling implies a process of abstraction steps to get from the actual structure to an analytical description, comprising just a few degrees of freedom.

1.3.1 Numerical modelling

The introduction of the finite element (FE) method around 1960 [32, 34, 84, 242] marks one of the most notable advances in engineering. The basic idea of FE modelling is to decompose or *discretise* complex-shaped structures into much smaller domains, for which the displacement field can be approximated by low-order continuous shape functions. Within

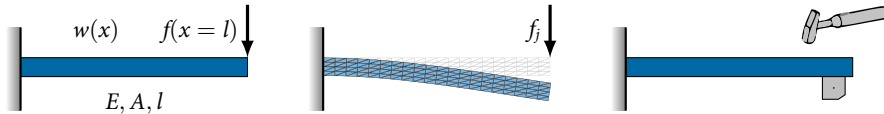


Figure 1.1: Three ways of modelling a cantilever beam: the analytical (left), numerical (middle) and experimental (right) approach.

these finite elements, essentially the same analytical equations apply, allowing to write potential and kinetic energies for the finite elements in a closed-form. Linearised properties such as mass, stiffness and damping can then be derived and gathered in large system matrices, that form a starting point for all kinds of engineering purposes.

Numerical modelling has become such common practice that the verb “modelling” itself nowadays means something like “building an FE model and performing some standard static and dynamic analysis”. Over the past fifty years, numerical modelling technology has become more advanced and versatile and can now also be employed for multi-physical simulation and topology optimisation. Still, an occasional experimental test could be desired to validate the numerical model and perhaps tune some material properties such that the FE model better reflects the actual structure (model updating).

For automotive engineering, the numerical approach is very adequate to model solid structures with homogeneous material properties, such as metal chassis and bodywork parts. However, for modelling of compound mechanic or mechatronic components, numerical modelling is not without limitations. Internal mechanisms such as gearing systems and bearings are often left out of a numerical model because of their complex geometry and kinematics. Yet they contribute to the global dynamics in a very complicated way, possibly also depending on the pre-loading or configuration. Another difficulty are components from compound materials. The interaction between parts, often connected by welds, bolts or adhesives, introduces damping effects that transcend the linear mechanics theory on which classic FE techniques are built. Proper modelling of damping is essential if the model is used for dynamic analysis, especially in the mid- and high-frequency range.

Hence, when pushing the frequency of interest up to the kHz range, there appears to be an almost mythical (or at least unsubstantiated) boundary from where numerical models do not seem trustworthy any longer. Some inaccuracies can indeed be attributed to a high modal density of the structure or unmodelled damping effects. Other uncertainties are often easily dispatched by calling the structure non-linear. Altogether it limits the applicability of numerical modelling to static and low-frequency analysis, or at least requires careful interpretation of the modelling results.

1.3.2 Experimental modelling: beyond model validation

Whereas the FE method marks a milestone in numerical modelling, the introduction of digital spectrum analysers in the 1970s has been instrumental to the development of experimental technology². Developments in digital data acquisition and the discovery of the

²For ones not initiated in this particular engineering field, the adjective “experimental” may have the connotation of something not yet in the final phase (e.g. an experimental medical treatment) or an avantgardistic form of art (e.g. experimental jazz). In dynamics it means “founded on empirical observations”, so based on measurements rather than numerics or mathematics. See [54, 55] for a historical lesson and a definition of preferred wording.

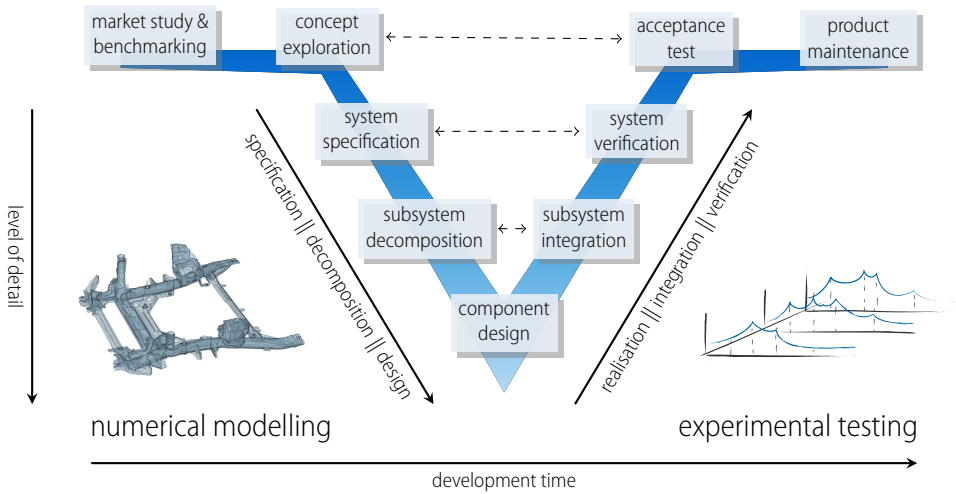


Figure 1.2: The V-model life-cycle of product development.

fast Fourier transform (FFT) by Cooley and Tukey in 1965 [33] enabled to do a modal test and obtain frequency response functions (FRFs) almost right away. These FRFs can be interpreted directly or used as a starting point for further analysis, such as experimental modal analysis (EMA) [53, 197]. The aim of EMA is to transform an experimental model into a *modal model* consisting of vibration modes, frequencies and damping values. These can then be used to validate a numerical model. Nowadays, EMA is implemented in many development processes, for both large and very small scale systems.

In fact, the science of experimental testing itself has been evolving to yet another discipline to describe dynamic behaviour, denoted in this thesis by *experimental modelling*. The FRFs obtained from admittance testing can be employed directly to build an experimental model of the component. This model is potentially as powerful as any numerical model, inasmuch as it can be used for purposes like dynamic substructuring, transient simulation and transfer path analysis. Also, there are in principle no restrictions on the accuracy of the experimentally obtained model. In fact, if the experimental measurements are carefully performed, accurate results could be obtained in a multi-kHz range where a numerical model would already fail to produce credible results. Yet, to assure such a level of accuracy in practice, measurements needs to be conducted carefully and with profound understanding of the component's dynamics. The experimental techniques to do so take a central part in this thesis.

1.3.3 The need for a hybrid modelling strategy

In industrial practice, numerical and experimental engineering activities very often live side-by-side, as being preached by two different churches. The numerical approach is mainly present in early phases of specification, decomposition and design, whereas experimental techniques are typically used to integrate and validate once the components are realised. These two movements can be recognised in the well-known "V-model" development life-cycle, which is characteristic for (but not limited to) automotive development.

Many different guises of the V-model appear in literature [8, 180]; a slightly altered version is depicted in Fig. 1.2.

With this V-model in mind, let us consider the downwards development direction of specification and decomposition. In this phase, high-level functions are being subdivided into subsystems that are delegated to either in-house manufacturing departments or external suppliers. In the automotive industry, one could imagine that core parts such as the engine and chassis are developed by the manufacturer themselves, whereas the audio system, tires and mechatronic systems are outsourced to specialist external suppliers. All these parts are subjected to extensive lists of requirements or component-targets, in order to guarantee proper functionality once integrated in the end-product.

As discussed in Sec. 1.2, this target-setting is particularly challenging in the field of NVH engineering. In order to assess the dynamics of subsystems with respect to their performance in the full product, methods are required to integrate their dynamical contributions in a physically correct way. As active mechatronic components tend to be too complex to model numerically, a fully numerical approach is often not feasible. A hybrid numerical/experimental approach could resolve this problem, if component prototypes are available for measurement in an early-phase. Altogether this requires a methodology that allows to implement experimentally measured models into a numerical modelling environment or, rather, assemble subsystems regardless of their modelling nature. The approach to do so in structural dynamics is discussed next.

1.3.4 Dynamic substructuring

Dynamic Substructuring (DS) is a powerful engineering concept to model and analyse dynamic systems in terms of its components or *substructures* [104]. It is often related to the mathematical concept of domain decomposition by Schwarz [183] or, for the more nostalgic-minded, the ancient principle of “divide and conquer”³. The first methods of DS emerged in the 1960s as a solution to solving large FEM models, unmanageable with the computational resources at that time. Smaller substructures could be solved for individually and synthesised by satisfying coordinate compatibility and force equilibrium at the substructures’ interfaces [35, 85].

Nowadays DS stands for a much broader collection of methods in various domains, but the principal concept of solving an interface problem remains common. Besides a potential gain in computational efficiency, advantages of DS are manifold (see also [101, 215]):

- ▶ Substructures can be modelled and analysed in the domain that is most appropriate. In particular, experimentally obtained (measured) substructures can be combined with numerical models, enabling hybrid modelling approaches.
- ▶ Models of different development groups can be shared and combined. Details of the component model can be kept proprietary, because the substructuring interaction only requires dynamic information of the interfacing points.
- ▶ Large systems can be optimised on a substructure-level with respect to their performance in the full product. Global sensitivities can be traced back to critical substructures.

³After the Latin “divide et impera”, a strategy exercised by ancient rulers such as Julius Caesar and Philip II of Macedon.

This thesis mainly focuses on frequency-based substructuring (FBS) [95, 105], with particular attention for the experimental practice. A general introduction to DS is provided in Chap. 3.

1.4 Predictive noise & vibration engineering

The preceding section has discussed aspects of modelling, aimed at quantifying the passive dynamics of a structure. With “passive dynamics”, we designate those intrinsic dynamic properties that express the structural sensitivity to applied forces, such as frequency response functions, but also vibration modes, frequencies and damping. Hence, with respect to the source–transmission–receiver model introduced in Sec. 1.1.2, one would now have characterised the aspect of transmission.

In the analysis of sound and vibration, at least as important is the identification of the source, as without a source one misses an important dimension in the prediction of received sound. This section introduces the field of transfer path analysis, with particular interest in characterising the source as an independent mechanism, in order to realise predictive strategies for NVH engineering.

1.4.1 Transfer path analysis

Transfer Path Analysis (TPA) denotes a wide family of diagnostic tools for analysing noise and vibration problems. A TPA concerns the study of a product’s actively vibrating components and the transmission of these vibrations to the connected passive structures. TPA is particularly useful when the actual vibrating mechanisms are too complex to model or measure directly, as it allows to represent a source by forces and vibrations displayed at the interfaces with the passive side. In this way the *source excitations* can be separated from the structural/acoustic *transfer characteristics*, allowing to troubleshoot the dominant paths of vibration transmission. The engineer can then anticipate by making changes to either the source itself or the receiving structures that are connected to it.

Classically, TPA has been used for troubleshooting of NVH problems in existing designs. Such strategies are referred to as *classical TPA*; some notable examples include matrix-inverse and mount-stiffness methods [119], Operational TPA [102, 142] and OPAX [91]. However, the potential to predict the effects of design changes is limited: the excitation characterisation is built upon measurements in the total assembly rather than the active component itself, such that any change at the passive side would require a new measurement. This strategy does not offer the flexibility that is desired to predict NVH performance in an early development phase.

1.4.2 Environment-independent source characterisation

A second class of TPA methods, denoted in this thesis by *component-based TPA*, attempts to characterise the excitations as a property of the active component only. The dynamics of the passive side are added in a later stage, such that physically correct transfer paths and NVH predictions can be obtained by means of simulation. This concept is very attractive indeed: it enables development strategies such as product optimisation through experimental/numerical Dynamic Substructuring [104] and auralisation by means of virtual acoustic prototyping [133].

The main challenge in component-based TPA is the characterisation of the source activity. This is currently a popular research topic and has led to several practical approaches [26, 50, 94, 103, 134, 185, 187]. Essentially, all approaches consist in substituting the source excitation by a set of equivalent forces, that render the same responses at the passive side as the original source. These forces can thus be considered as externally applied forces to the combined system at rest: the transfer paths can be calculated by multiplication with the FRFs of the assembled system. In addition, the equivalent forces can be shown to be a property of the source structure only. Sec. 6.3 reviews a variety of source characterisation principles within the family of component-based TPA and proposes a generalisation of the concepts.

In all cases, one has to cope with uncertainties due to measurement errors, matrix conditioning, bandwidth limitations of sensors etcetera, such that obtaining a reliable prediction in a large frequency band is a true challenge. In Part II of this thesis, the theory and application of TPA is investigated in its numerous facets. In particular, the theory is approached from the perspective of dynamic substructuring, in order to compare the methods on a conceptual level.

1.5 Application to vehicle mechatronics

Part III of this thesis reports on several automotive case studies, all conducted in collaboration with the BMW Group. Within a four-year project, the fields of experimental dynamic substructuring and transfer path analysis have been researched, with a special interest in the practical applicability of the processes. The applications focus on the structure-borne transmission of the electric power steering (EPS) system vibrations into the vehicle's interior. Within this research direction, three main goals have been identified:

1. Simulation of the transmission characteristics of the vehicle based on a substructuring assembly of experimentally modelled subsystems;
2. Characterisation of the EPS system as an independent source of excitation by means of measurement on a test bench;
3. Development of a methodology for definition of component targets with respect to the global vehicle targets.

The first research goal aligns with the theory of Part I of this thesis. Several measurement campaigns have been conducted for the determination of vehicle FRFs, namely from the connection points of the EPS system with the subframe to the sound pressure measured at the driver's ears. A special interest was in the validation of the methodology in a high-frequency range, i.e. up to 6kHz. For that purpose, a benchmark study with three different, yet identically equipped vehicles has been conducted. For validation of dynamic substructuring, the relevant subsystems have been modelled experimentally and assembled using various coupling and decoupling approaches. All applications of experimental modelling and substructuring are reported in Chap. 8.

The second and third research goal concern source characterisation and transfer path analysis, which is the topic of Part II. Throughout the course of the research project, several variants of component-based TPA have been researched. This has resulted in a continuous iteration on test bench designs, in order to suit the TPA method and component of interest.

Blocked-force test bench measurements as well as in-situ vehicle measurements have been performed to characterise the EPS system under operation.

A novelty is the in-situ measurement of the EPS system on a test bench, combined with FRFs of the vehicle. This approach anticipates to the second and third goal as mentioned above: it enables a physically correct assessment of EPS noise in the vehicle, using a independent characterisation of the source from measurements in a test assembly. In a second step, the vehicle FRFs are assembled from component measurements, which reflects the first research goal. This answers to the original aim of predictive NVH technology as stated in Sec. 1.2. All applications with respect to the active EPS system are reported in Chap. 9.

1.6 Thesis contributions

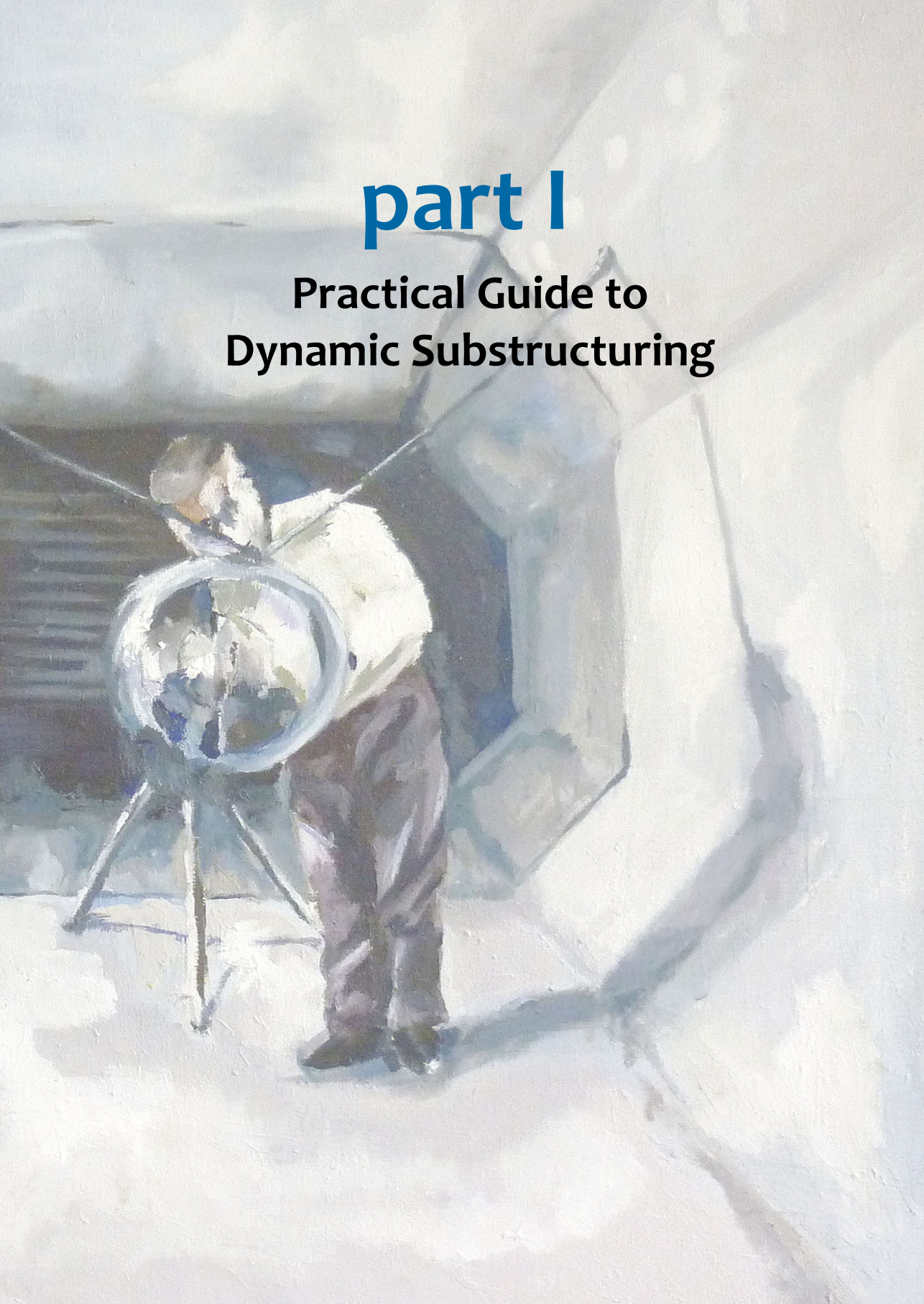
This thesis reports on the most important theoretical and experimental findings as a result of a four-year research project. As with most research, progress has been made iteratively and by no means in a straight path headed towards the final goal. Intermediate results, not per definition reflected in this thesis, have been reported in [12, 26, 184, 186–190], whereas [185] is included in this thesis in almost original form.

The following developments are reported in this thesis that may extend the current state of technology:

- ▶ A concise, yet practical methodology has been proposed for experimental modelling of a structure, with proper consideration of rotational dynamics. The virtual point transformation allows to transform FRFs from a typical admittance measurement into a set of collocated nodal FRFs, fully compatible with FE models. The quality of the experimental steps can be monitored objectively and errors can be traced back to their responsible sensor channel or impact position. See Chap. 4.
- ▶ A large collection of TPA methods has been presented and classified into a general framework. Existing methods have been re-interpreted and categorised in three families. All methods are derived using a consistent notation, exposing many conceptual similarities. See Chap. 5–7.
- ▶ The component-based TPA methods have been generalised using a notation familiar to Lagrange multiplier frequency-based substructuring (LM-FBS). The proposed notation allows to swiftly investigate the influence of different instrumentation and alternative choices for equivalent forces, implementing the concepts of in-situ source characterisation and the pseudo-forces methodology. See Sec. 6.3.7.
- ▶ The applicability of experimental modelling, substructuring and TPA theory has been demonstrated on a complex real-life system, exposing the potential and some of the limitations of current state-of-the-art. See Chap. 8–9.

part I

Practical Guide to Dynamic Substructuring



2

Introduction to dynamic simulation

chapter contents:

2.2 Physical domain	14
2.3 Modal domain	15
2.3.1 Natural vibration modes	15
2.3.2 Modal reduction by truncation	16
2.4 Frequency domain	17
2.4.1 Impedance & admittance notation	17
2.4.2 Relation to experimental testing	18
2.5 Time domain	19
2.5.1 Duhamel integral for impulse-based simulation	19
2.6 State-space domain	20
2.6.1 The dynamic equation in first-order form	20
2.6.2 State-space in the frequency domain	21
2.7 Conversion between domains	22
2.7.1 Mode synthesis	22
2.7.2 Modal parameter estimation	24
2.8 Summary	24

2.1 Introduction

An essential part of product engineering is the prediction or simulation of a product's behaviour, based upon some model that is deemed appropriate for a specific purpose. Product performance can be expressed in a variety of dimensions, but quite often the statics and dynamics are among the critical aspects that need to be assessed. Especially in product branches where there is a high interest in comfort or acoustic performance, the dynamic behaviour plays a significant, if not crucial role.

Structural dynamic simulation in a general sense can have an ambiguous meaning, as it does not prescribe a particular domain in which the system's dynamics are to be modelled. In fact, several domains can be chosen depending on the component at hand, the targeted analysis, the availability of computational or experimental resources and perhaps personal preference. Fig. 2.1 shows a schematic overview of five domains that are commonly encountered in structural dynamic simulation, namely the physical, modal, frequency, time and state-space domain. Although this overview might be incomplete, these five domains are all well suited to simulate multiple input / multiple output behaviour, which qualifies them for use in dynamic substructuring applications [104].

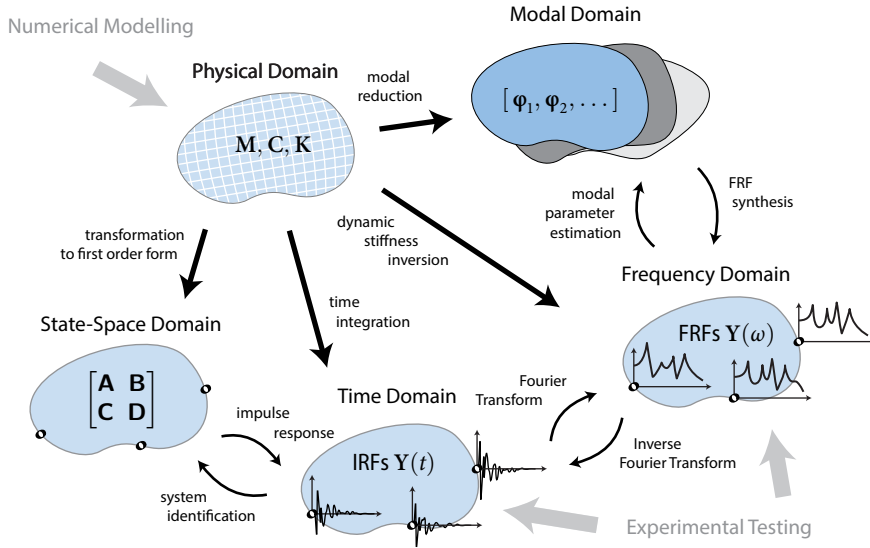


Figure 2.1: Five domains for structural dynamic simulation, approached from either a numerical modelling or experimental testing perspective. Some typical (but not all) conversions between the domains are indicated by arrows.

Dynamic substructuring (DS) is the approach of decomposing a complex dynamic system into smaller parts; the so-called *substructures*. The substructuring approach offers several advantages compared to an integral modelling approach, some of which have been discussed in the previous chapter, see Sec. 1.3.3. Rather than a method on its own, DS is best understood as a systematic framework for modelling and synthesis of components. In light of this, the domains of the overview of Fig. 2.1 are regarded as different, yet potentially equivalent means to model a substructure’s dynamic behaviour¹. All domains implement a common systematic to describe the interface (or boundary) conditions, which allows to “hybridise” a substructuring simulation.

This chapter introduces the basic formulations to model a linear dynamic system in each of the five domains. Two different approaches are emphasized: the numerical modelling approach and the experimental testing approach. Some means to transform from one domain to another are discussed in Sec. 2.7. A summary of the five domains is presented in Sec. 2.8.

2.2 Physical domain

The physical domain is designated “physical” because it is described by properties that carry a straightforward physical interpretation. Considering a discrete dynamic system, one can write an equilibrium between the externally applied forces and the internal forces due to inertia, viscous damping and elasticity. The resulting equilibrium is probably the most elementary formula in structural dynamics, namely the second order differential equation

¹With dynamic behaviour we denote those properties that describe the *passive* dynamics of a structure, i.e. the reaction forces as a result of an imposed displacement or, inversely, the structure’s response to an applied load.

for a discrete linear(ised) dynamic system:

$$\mathbf{M}\ddot{\mathbf{u}}(t) + \mathbf{C}\dot{\mathbf{u}}(t) + \mathbf{K}\mathbf{u}(t) = \mathbf{f}(t) \quad \mathbf{u} \in \mathbb{R}^n \quad (2.1)$$

Here \mathbf{M} , \mathbf{C} and \mathbf{K} represent the linearised system matrices for respectively mass, damping and stiffness, \mathbf{u} the set of displacements for all n degrees of freedom (DoFs) and \mathbf{f} the set of externally applied loads, vectorially associated with \mathbf{u} . In case of a 3D problem, 3 DoFs are used to describe the linear motion of a node in (x, y, z) -direction; a 6D problem adds rotations and associated moments about the respective axes.

System matrices like $(\mathbf{M}, \mathbf{C}, \mathbf{K})$ are typically obtained from finite element (FE) modelling and are together referred to as the *numerical model* of a structure. Although FE modelling used to be a craft on its own (see for instance [32, 34] and a brief discussion in Sec. 1.3.1), FE models or *meshes* are nowadays easily generated from within the computer design applications. However, with curved surfaces, small features or compound geometries, meshes quickly get too detailed, resulting in a DoF-count in the order of hundreds of thousands. Such level of detail might be desired for a static stress analysis, but renders the direct formulation of Eq. (2.1) impractical for most dynamic simulations.

Rather than defining a new mesh with a lower degree of detail, one can apply *modal reduction* to obtain a reduced-order representation of the full model. This is discussed next.

2.3 Modal domain

A dynamic analysis typically concentrates on the structural behaviour in the lower frequency range, for which the structure deforms rather globally. In other words, rapid phenomena such as travelling waves through elements, which the solution space of an FE model also accommodates for, are generally not of interest. By discarding the solution space associated with these rapid and local phenomena, one retains a smaller solution space, suited to describe the global behaviour of the structure more efficiently. This is the general idea of *modal reduction*. Note that different reduced-order representations exist; see for instance [20] for an overview of techniques.

2.3.1 Natural vibration modes

For linear and proportionally-damped structures², the global behaviour is portrayed by the lowest natural vibration modes. Natural vibration modes or *eigenmodes* are vibration shapes at a fixed frequency for which the inertia forces are — in the absence of damping — in harmony with the elastic forces. These eigenmodes and their corresponding *eigenfrequencies* can be computed iteratively by an eigensolver, that seeks for a solution in the form:

$$(\mathbf{K} - \omega_r^2 \mathbf{M}) \boldsymbol{\varphi}_r = \mathbf{0} \quad r = 1, \dots, n \quad (2.2)$$

A numerical model comprises as many *eigen-solutions* as there are DoFs in the system. The eigenmodes $\boldsymbol{\varphi}$ are typically stored in the columns of a mode shape matrix $\boldsymbol{\Phi}$, in order of

²See for instance [3, 70] for more information on modelling of damping in structural vibrations.

increasing eigenfrequency ω_r , orthogonal and mass-normalised, such that:

$$\left\{ \begin{array}{l} \Phi = [\varphi_1, \varphi_2, \dots, \varphi_n] \end{array} \right. \quad (2.3a)$$

$$\left\{ \begin{array}{l} \Phi^T M \Phi = I \end{array} \right. \quad (2.3b)$$

$$\left\{ \begin{array}{l} \Phi^T K \Phi = \text{diag}(\omega_1^2, \dots, \omega_n^2) \end{array} \right. \quad (2.3c)$$

A special solution to (2.2) are the rigid body modes for which $\omega_r = 0$. These modes essentially span the null-space of the stiffness matrix.

2.3.2 Modal reduction by truncation

The modes with lowest eigenfrequency are in general the most accurate in an FE model and relevant to typical dynamic analyses (Sec. 2.5 discusses situations when this is not the case). By limiting the full displacement field $\mathbf{u}(t)$ to the subspace spanned by the first³ $m \ll n$ natural vibration modes, namely a reduction matrix $\mathbf{R} = [\varphi_1, \dots, \varphi_m]$, one can drastically reduce the effective dimension of the original problem. This reduction is called a *modal truncation* and yields an approximation of the vector of displacements:

$$\mathbf{u}(t) \approx \mathbf{R}\boldsymbol{\eta}(t) \quad \boldsymbol{\eta} \in \mathbb{R}^m \quad (2.4)$$

The physical displacements are now replaced by a smaller set of time-dependent *modal coordinates* $\boldsymbol{\eta}(t)$, representing the amplitudes of the mode shapes in the columns of \mathbf{R} . Substituting Eq. (2.4) into the differential equation of Eq. (2.1), the equilibrium reads:

$$\mathbf{M}\mathbf{R}\ddot{\boldsymbol{\eta}}(t) + \mathbf{C}\mathbf{R}\dot{\boldsymbol{\eta}}(t) + \mathbf{K}\mathbf{R}\boldsymbol{\eta}(t) = \mathbf{f}(t) + \mathbf{r}(t) \quad (2.5)$$

As the reduction of Eq. (2.4) is an approximation, the internal force terms on the left-hand side might not be able to fully equalise the applied forces. In other words: the system does not respond to the high-frequency content in \mathbf{f} . Hence the remaining part is governed by the residual force vector \mathbf{r} . To get rid of this residual and find a solution in the reduced space, Eq. (2.5) is pre-multiplied with \mathbf{R}^T , ensuring that $\mathbf{R}^T\mathbf{r} = \mathbf{0}$. One now obtains the modally-reduced problem of dimension m :

$$\mathbf{M}_m\ddot{\boldsymbol{\eta}}(t) + \mathbf{C}_m\dot{\boldsymbol{\eta}}(t) + \mathbf{K}_m\boldsymbol{\eta}(t) = \mathbf{f}_m(t) \quad \text{with} \quad \left\{ \begin{array}{l} \mathbf{M}_m = \mathbf{R}^T\mathbf{M}\mathbf{R} \\ \mathbf{C}_m = \mathbf{R}^T\mathbf{C}\mathbf{R} \\ \mathbf{K}_m = \mathbf{R}^T\mathbf{K}\mathbf{R} \\ \mathbf{f}_m = \mathbf{R}^T\mathbf{f} \end{array} \right. \quad (2.6)$$

The matrices with subscript m are the reduced-order system matrices of the component. A solution to Eq. (2.6) can be expanded to the physical DoFs using Eq. (2.4).

Projection on the space of natural vibration modes is particularly efficient, because the resulting modal matrices are diagonal if the damping matrix is proportional. Hence Eq. (2.6) becomes a system of m single-DoF equations which is very efficient to solve. Reduction using the free vibration modes is however not the only way. For the purpose of substructuring, it is often desired to make a distinction between internal DoFs and boundary DoFs, which leads to very different reduction spaces such as the reduction techniques of Craig-Bampton [35] or Rubin [172]. These pertain to the field of *component mode synthesis* (CMS), see for instance [36, 221] for an overview of techniques.

³In fact one would select the modes based on spatial and spectral convergence with the time history of the applied load $\mathbf{f}(t)$.

response quantity	impedance notation	Z	admittance notation	Y
displacement	<i>dynamic stiffness</i>	f/u	<i>receptance</i>	u/f
velocity	<i>(mechanical) impedance</i>	f/\dot{u}	<i>mobility</i>	\dot{u}/f
acceleration	<i>apparent mass</i>	f/\ddot{u}	<i>accelerance</i>	\ddot{u}/f

Table 2.1: Typical denotations encountered in literature for impedance and admittance FRFs.

2.4 Frequency domain

One of the primary interests in dynamic analysis is the *harmonic response analysis*, namely the structure's response to an harmonic load. This correlates with the intrinsic resonance frequencies and damping ratios, which are a result of the distribution of mass, damping and stiffness over the structure. A convenient domain to assess a structure's harmonic behaviour is the frequency domain. The frequency domain assumes a synchronous response to an harmonic load, such that the time-dependency of the coordinates and loads can be replaced by a frequency-dependency. Note however that this poses certain requirements on the structure, that must be linear (or linearised), time-invariant (constant system matrices) and steady-state (transient effects have been damped out).

Omitting further derivation, one can apply a Fourier transform on the coordinates and force vector and write the dynamic equilibrium of Eq. (2.1) as a function of the excitation frequency ω . Using now the fact that $\dot{\mathbf{u}}(\omega) = j\omega\mathbf{u}(\omega)$ and $\ddot{\mathbf{u}}(\omega) = -\omega^2\mathbf{u}(\omega)$, the terms on the left-hand side can be collected into a single frequency-dependent matrix $\mathbf{Z}(\omega)$:

$$\begin{aligned} \mathbf{M}\ddot{\mathbf{u}}(\omega) + \mathbf{C}\dot{\mathbf{u}}(\omega) + \mathbf{K}\mathbf{u}(\omega) &= \mathbf{f}(\omega) \\ [-\omega^2\mathbf{M} + j\omega\mathbf{C} + \mathbf{K}]\mathbf{u}(\omega) &= \mathbf{f}(\omega) \\ \mathbf{Z}(\omega)\mathbf{u}(\omega) &= \mathbf{f}(\omega) \end{aligned} \quad (2.7)$$

Matrix $\mathbf{Z}(\omega)$ is called the *dynamic stiffness* matrix. It consists of complex-valued frequency-dependent functions, describing the force needed to generate a unit harmonic displacement on one particular DoF, while all other DoF are constrained. As this relation is not very intuitive, one often considers the inverse of Eq. (2.7), which yields the admittance notation:

$$\mathbf{u}(\omega) = \mathbf{Y}(\omega)\mathbf{f}(\omega) \quad \text{with} \quad \mathbf{Y}(\omega) \triangleq (\mathbf{Z}(\omega))^{-1} \quad (2.8)$$

The elements in the *receptance* matrix $\mathbf{Y}(\omega)$ are called frequency response functions (FRFs) and describe the displacement response as a result of a unit harmonic force⁴.

2.4.1 Impedance & admittance notation

Receptance, or in general *admittance* (see Table 2.1 for an overview of common terminology), allows for much clearer interpretation of a structure's dynamic behaviour than *impedance*. For instance: a column of $\mathbf{Y}(\omega)$ governs the global response of all DoFs as a result of an excitation at one particular DoF. Hence every element in $\mathbf{Y}(\omega)$ reveals something of

⁴A large part of the community uses \mathbf{H} to denote an FRF matrix; a symbol commonly used for transfer functions in a general sense. We adopt the notation \mathbf{Y} to denote admittance, which has historical roots in papers by e.g. Rubin [173, 174] and Jetmundsen [95] and is alphabetically nicely adjacent to impedance \mathbf{Z} .

the global structural behaviour, whereas dynamic stiffness, by the definition of Eq. (2.7), only comprises element behaviour. As a consequence, $\mathbf{Z}(\omega)$ can be sparse whereas $\mathbf{Y}(\omega)$ is generally a full matrix. In general, the elements of the two variants are defined as follows:

$$\text{impedance: } Z_{ij}(\omega) \triangleq \frac{f_i(\omega)}{u_j(\omega)} \quad u_{k \neq j} = 0 \quad (2.9a)$$

$$\text{admittance: } Y_{ij}(\omega) \triangleq \frac{u_i(\omega)}{f_j(\omega)} \quad f_{k \neq j} = 0 \quad (2.9b)$$

Subscripts i and j denote the element in the full set of n DoFs, meaning that $\mathbf{Z}(\omega)$ and $\mathbf{Y}(\omega)$ are matrices of complex-valued frequency-dependent functions in $\mathbb{C}^{n \times n}$.

2.4.2 Impedance & admittance in relation to experimental testing

As it happens, the admittance form is normally obtained by experimental testing. An admittance test consists of measuring a limited number of output responses for multiple corresponding input forces. The practice of admittance testing is discussed in Sec. 1.3.2 and Chap. 4, but one fundamental aspect is noteworthy in the context of this chapter.

Let us denote by \mathbf{Z} the dynamic stiffness matrix of a simple finite element model, as illustrated by Fig. 2.2a. The matrix is defined for all n DoFs and has a sparse structure due to the finite element formulation⁵. In order to determine the dynamics at the corner nodes from an admittance test, the DoFs \mathbf{u} are partitioned as $n - n_2$ unmeasured internal DoFs \mathbf{u}_1 and n_2 measured boundary DoFs \mathbf{u}_2 . Hence the experimental test only yields an admittance matrix \mathbf{Y}_{22} , which is illustrated by the deformed shape of Fig. 2.2b. The following partitioned systems of equations are equivalent (the frequency dependency is omitted for brevity):

$$\begin{bmatrix} \mathbf{Y}_{11} & \mathbf{Y}_{12} \\ \mathbf{Y}_{21} & \mathbf{Y}_{22} \end{bmatrix} \begin{bmatrix} \mathbf{0} \\ \mathbf{f}_2 \end{bmatrix} = \begin{bmatrix} \mathbf{u}_1 \\ \mathbf{u}_2 \end{bmatrix} \quad \Rightarrow \quad \mathbf{u}_2 = \mathbf{Y}_{22} \mathbf{f}_2 \quad (2.10a)$$

$$\begin{bmatrix} \mathbf{Z}_{11} & \mathbf{Z}_{12} \\ \mathbf{Z}_{21} & \mathbf{Z}_{22} \end{bmatrix} \begin{bmatrix} \mathbf{u}_1 \\ \mathbf{u}_2 \end{bmatrix} = \begin{bmatrix} \mathbf{0} \\ \mathbf{f}_2 \end{bmatrix} \quad \Rightarrow \quad \mathbf{u}_2 = \left(\mathbf{Z}_{22} - \mathbf{Z}_{21} (\mathbf{Z}_{11})^{-1} \mathbf{Z}_{12} \right)^{-1} \mathbf{f}_2 \quad (2.10b)$$

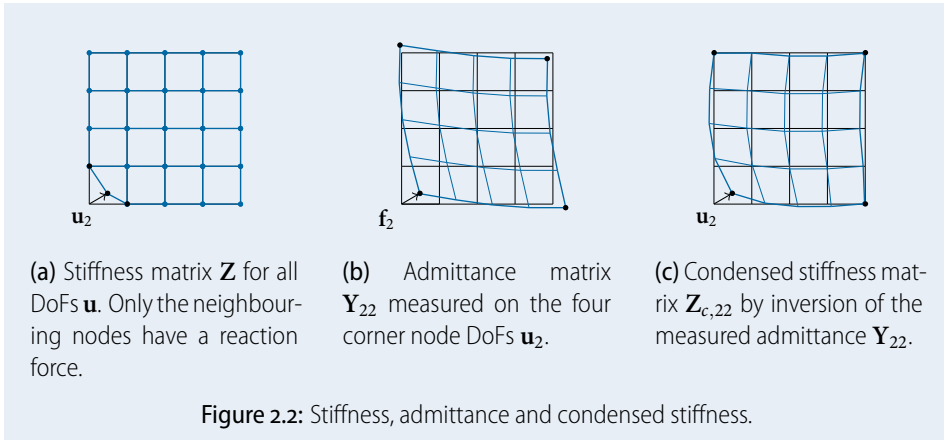
The dynamic stiffness matrix obtained by inversion of the measured admittance \mathbf{Y}_{22} reads:

$$(\mathbf{Y}_{22})^{-1} = \mathbf{Z}_{c,22} \quad \text{with} \quad \mathbf{Z}_{c,22} \triangleq \mathbf{Z}_{22} - \mathbf{Z}_{21} (\mathbf{Z}_{11})^{-1} \mathbf{Z}_{12} \quad (2.10c)$$

Matrix $\mathbf{Z}_{c,22} \neq \mathbf{Z}_{22}$ is the condensed dynamic stiffness matrix of dimension $n_2 \times n_2$ for the DoFs \mathbf{u}_2 , all DoFs \mathbf{u}_1 being unrestrained. The matrix is no longer sparse, because the effects of the freely vibrating \mathbf{u}_1 are incorporated in \mathbf{u}_2 ; see Fig. 2.2c. This is also called a static condensation or *Schur complement* by mathematicians, which can be used for impedance assembly using the measured \mathbf{u}_2 as coupling DoFs. In the static case, $\mathbf{Z}_{c,22}$ is called a *Guyan reduction*, which is considered the most primitive reduction method in CMS.

Hence, it can be concluded that an admittance FRF is always an observation of the structure's dynamics *independent* of the other FRFs in the measurement. In other words, adding

⁵Looking at Eq. (2.9a), Z_{ij} is only non-zero if a displacement on i creates a force in j , all other DoFs being fixed. So if the DoF of one node is perturbed, no forces will be created further then the surrounding nodes, which explains the sparse nature of the impedance matrix.



additional FRFs to the matrix will not affect the other functions. An impedance function on the other hand is always subject to the other impedances in a matrix, as a direct cause of the configuration of the structure under measurement. Indeed, the DoF-space of \mathbf{Z} prescribes the mounting points of the structure. This difference has profound consequences for the substructuring methods discussed later on and also indicates why admittance is often the preferred, if not only choice in the experimental practice.

2.5 Time domain

Although the frequency domain is suitable to analyse a wide range of problems, some problems are better posed in the time domain, such as:

- ▶ Structures with high / non-viscous damping or high modal density;
- ▶ Excitations of impact-like nature or high-frequent spatial distribution;
- ▶ Systems with (local) non-linear behaviour;
- ▶ Real-time substructuring applications.

A time-domain solution can easily be computed for a numerical model using a discrete time-integration technique such as a Newmark time-stepping scheme. However this operates on the full set of N DoFs, which is computationally not efficient if the interest is only in a few inputs and outputs. On the other hand, a solution in the modal domain would require a great number of modes to accommodate for the high-frequency content of the load vector, which is not efficient either. For such cases, simulation based on impulse response functions (IRFs) can be appropriate. Simulation and coupling based on IRFs is a relatively new field of research, referred to as impulse-based substructuring (IBS) [166, 168, 170, 189, 190, 211, 212, 214]. The basic principle of impulse-based simulation is summarised here.

2.5.1 Duhamel integral for impulse-based simulation

Let us recall the frequency-based admittance notation of Eq. (2.8) that provides a solution for harmonic load cases $\mathbf{f}(\omega)$. This solution is already reduced, in the sense that the admittance FRFs contain all the structural dynamics condensed in the DoFs of interest. A quick

way to obtain a solution in the time domain would be to compute a frequency-domain solution $\mathbf{u}(\omega)$ first and apply an inverse Fourier transform to get $\mathbf{u}(t)$. Alternatively, the solution itself can be sought in the time domain directly, namely using the inverse Fourier transform of the dynamic equation Eq. (2.8). This yields the classic Duhamel convolution integral for a system that is initially at rest:

$$\mathbf{u}(t) = \mathbf{Y}(t) * \mathbf{f}(t) = \int_{\tau=0}^t \mathbf{Y}(\tau)\mathbf{f}(t - \tau)d\tau \quad (2.11)$$

$\mathbf{Y}(t)$ is a matrix of impulse response functions (IRFs) with similar input/output properties as its frequency-domain counterpart. Each IRF describes the displacement response to an applied impulse of unit momentum (1 Ns) and infinitely short time. As shown in the schematic overview of Fig. 2.1, IRFs can be obtained either numerically or experimentally. With respect to numerical modelling, an IRF governs the transient solution to Eq. (2.1) for the following load case:

$$\begin{cases} Y_{ij}(t) \triangleq u_i(t) \\ \dot{Y}_{ij}(t) \triangleq \dot{u}_i(t) \\ \ddot{Y}_{ij}(t) \triangleq \ddot{u}_i(t) \end{cases} \quad \text{s.t.} \quad \mathbf{M}\ddot{\mathbf{u}}(t) + \mathbf{C}\dot{\mathbf{u}}(t) + \mathbf{K}\mathbf{u}(t) = \mathbf{1}_j \delta(t) \quad (2.12)$$

The time-derivative dots on Y are used to distinguish IRFs for respectively displacement, velocity and acceleration responses. The notation $\mathbf{1}_j$ denotes a vector with a one on element j and zeros on all the other elements; $\delta(t)$ is the Dirac function with unit impulse. A solution to Eq. (2.12) can be computed by discrete time integration or from a superposition of natural vibration modes, as discussed in Sec. 2.7.1.

With respect to experimental modelling, a good approximation of an IRF is obtained from an impact hammer measurement. To approximate the true IRE, several approaches are discussed in [114, 190, 212, 213].

2.6 State-space domain

Perhaps a lesser-known domain for structural dynamic simulation is the state-space domain. State space notation is commonly encountered in control theory and signal processing. Within this vast research field, advanced system identification methods are available that can be very well utilised for structural dynamic identification. Yet, the procedures to do so are not as established as methods in the modal domain or frequency domain. Based on some ideas by Su and Juang [201], several procedures have been developed by Sjövall and Abrahamsson [191, 193, 194]. This section merely provides a brief insight in the application of state-space to structural dynamics; see for instance [71] for a thorough overview.

2.6.1 The dynamic equation in first-order form

State space theory is based on a system of first-order differential equations, constituted by the well-known **ABCD**-quadruple. To bring the second-order form of Eq. (2.1) to first-order form, a state vector $\mathbf{x}(t)$ is introduced that contains both displacements and velocities. The vector of applied forces $\mathbf{f}(t)$ is replaced by an input vector $\mathbf{v}(t)$. The basic state-space formulation reads (note that state-space variables are distinguished from physical variables

by the use of a sans-serif typeface):

$$\begin{cases} \dot{\mathbf{x}}(t) = \mathbf{A}\mathbf{x}(t) + \mathbf{B}\mathbf{v}(t) \\ \mathbf{y}(t) = \mathbf{C}\mathbf{x}(t) + \mathbf{D}\mathbf{v}(t) \end{cases} \quad \text{with} \quad \mathbf{x}(t) \triangleq \begin{bmatrix} \mathbf{u}(t) \\ \dot{\mathbf{u}}(t) \end{bmatrix}; \quad \mathbf{v}(t) \triangleq \mathbf{f}(t) \quad (2.13)$$

Matrix \mathbf{A} needs to fulfil two tasks: constitute the second-order differential equation and express the internal elastic and damping forces. Matrix \mathbf{B} and \mathbf{C} link the controllable inputs (i.e. applied forces) and observable outputs (i.e. displacements and velocities) to the state vector \mathbf{x} and input vector \mathbf{v} . Matrix \mathbf{D} serves for feed-forward of forces to velocities and displacements, which is zero for a second-order dynamic system. After some manipulation of Eq. (2.1), the following state-space matrices can be established for the state-space system of Eq. (2.13):

$$\mathbf{A} \triangleq \begin{bmatrix} \mathbf{0} & \mathbf{I} \\ -\mathbf{M}^{-1}\mathbf{K} & -\mathbf{M}^{-1}\mathbf{C} \end{bmatrix}; \quad \mathbf{B} \triangleq \begin{bmatrix} \mathbf{0} \\ \mathbf{M}^{-1}\mathbf{P}_f \end{bmatrix}; \quad \mathbf{C} \triangleq \begin{bmatrix} \mathbf{P}_d & \mathbf{0} \\ \mathbf{0} & \mathbf{P}_v \end{bmatrix}; \quad \mathbf{D} \triangleq \begin{bmatrix} \mathbf{0} \\ \mathbf{0} \end{bmatrix} \quad (2.14)$$

Eq. (2.14) is a classic first-order representation of a second-order dynamic system of equations. Matrices \mathbf{P}_d , \mathbf{P}_v and \mathbf{P}_f are (usually) Boolean matrices that allow to select a subset of input forces and output displacement / velocity coordinates. If they are chosen as $n \times n$ identity matrices, all forces \mathbf{f} are considered in the input vector \mathbf{v} and the output \mathbf{y} comprises all displacements and velocities \mathbf{u} and $\dot{\mathbf{u}}$:

$$\mathbf{u}(t) \triangleq [\mathbf{P}_d \quad \mathbf{0}] \mathbf{y}(t); \quad \dot{\mathbf{u}}(t) \triangleq [\mathbf{0} \quad \mathbf{P}_v] \mathbf{y}(t); \quad \mathbf{f}(t) \triangleq \mathbf{P}_f \mathbf{v}(t) \quad (2.15)$$

The state-space representation of Eq. (2.14) does not reduce the dimension size of the problem yet: in fact the size of the state matrix \mathbf{A} itself is of size $2n \times 2n$. To actually reduce the problem dimension, one can apply modal reduction on $(\mathbf{A}, \mathbf{B}, \mathbf{C})$ such that a state realisation of minimal or reduced order is obtained; see for instance [2, 71].

2.6.2 State-space in the frequency domain

The frequency domain solution to Eq. (2.13) takes the following classic form:

$$\mathbf{y}(\omega) = \left[\mathbf{C} (j\omega\mathbf{I} - \mathbf{A})^{-1} \mathbf{B} \right] \mathbf{v}(\omega) = \mathbf{H}(\omega) \mathbf{v}(\omega) \quad (2.16)$$

Matrix $\mathbf{H}(\omega)$ contains the transfer functions for the linear time-invariant (LTI) system. If the problem is set up using the definitions of Eq. (2.14)–(2.15), it appears that the transfer functions represent the frequency response functions for the chosen input forces and output coordinates:

$$\begin{cases} \mathbf{u}(\omega) = \mathbf{Y}(\omega) \mathbf{f}(\omega) = [\mathbf{P}_d \quad \mathbf{0}] \mathbf{H}(\omega) \mathbf{P}_f \mathbf{f}(\omega) & (2.17a) \\ \dot{\mathbf{u}}(\omega) = \dot{\mathbf{Y}}(\omega) \mathbf{f}(\omega) = [\mathbf{0} \quad \mathbf{P}_v] \mathbf{H}(\omega) \mathbf{P}_f \mathbf{f}(\omega) & (2.17b) \\ \ddot{\mathbf{u}}(\omega) = \ddot{\mathbf{Y}}(\omega) \mathbf{f}(\omega) = j\omega [\mathbf{0} \quad \mathbf{P}_v] \mathbf{H}(\omega) \mathbf{P}_f \mathbf{f}(\omega) & (2.17c) \end{cases}$$

The very fact that FRFs, as e.g. obtained from admittance testing, can be made compatible with state-space notation, suggests the applicability of system identification methods. An admittance test can be regarded as an input/output measurement, hence the measured data can be fed into a system identification algorithm such as a subspace identification method.

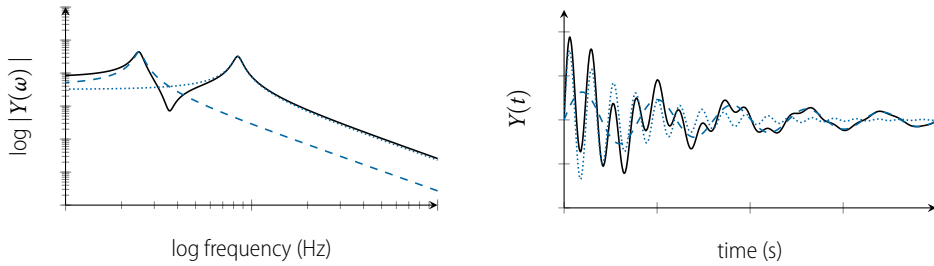


Figure 2.3: FRF (left) and IRF (right) by mode synthesis of two vibration modes.

This results in a state matrix \mathbf{A} for a predetermined number of poles, together with a \mathbf{B} and \mathbf{C} matrix to link the identified states to the input forces and output responses, respectively. The poles of \mathbf{A} appear in complex pairs and represent the identified eigenfrequencies and damping values.

For the purpose of dynamic substructuring, several procedures are outlined in [113, 192–194] to massage the identified state model in such a way that it can be coupled to other structures.

2.7 Conversion between domains

So far it has been discussed how a dynamic model in five domains (see Fig. 2.1) can be derived from either numerical modelling or experimental testing. It often occurs that models or information from different domains need to be blended. This may either be because the models are provided as such, or because another domain suits the targeted analysis better. This section discusses several standard techniques to convert between domains, in order to allow for hybrid analysis and design strategies.

2.7.1 Mode synthesis

Eq. (2.8) provides a direct way to calculate FRFs by inversion of the dynamic stiffness matrix from a numerical model. Note that this can be an expensive operation if the dimension size n is large and the frequency dependency ω is evaluated at many frequency points $(\omega_1, \dots, \omega_K)$. Hence to solve Eq. (2.8), an $n \times n$ system should be inverted K times, which rapidly exhausts the available computational resources.

An alternative way to compute FRFs is by means of *mode synthesis*, which uses the natural vibration modes or normal modes of the structure (see Sec. 2.3) to build up the FRFs. This is only possible for systems with uncoupled modes, i.e. linear systems with a proportional damping matrix. Assuming mass-normalised modes, the uncoupled modal parameters read:

$$\begin{cases} \Phi^T \mathbf{M} \Phi = \mathbf{I} & \text{modal mass} & (2.18a) \\ \Phi^T \mathbf{C} \Phi = 2 \text{diag}(\zeta_1 \omega_1, \dots, \zeta_n \omega_n) & \text{modal damping ratios } \zeta_r & (2.18b) \\ \Phi^T \mathbf{K} \Phi = \text{diag}(\omega_1^2, \dots, \omega_n^2) & \text{modal frequencies } \omega_r & (2.18c) \end{cases}$$

Hence the modal system matrices are all diagonal and therefore fully uncoupled, which allows to construct FRFs from a smaller selection of modes $m < n$, i.e. apply modal trunca-

Modal parameter	Definition	Unit
Modal mass	$\mu = \boldsymbol{\varphi}^T \mathbf{M} \boldsymbol{\varphi}$	kg
Modal damping	$\beta = \boldsymbol{\varphi}^T \mathbf{C} \boldsymbol{\varphi}$	Ns/m
Modal stiffness	$\gamma = \boldsymbol{\varphi}^T \mathbf{K} \boldsymbol{\varphi}$	N/m
Natural frequency	$\omega = \sqrt{\gamma/\mu}$	rad/s
Damping ratio	$\zeta = \beta / (2\mu\omega)$	-
Damping time constant	$\sigma = \zeta\omega$	1/s
Damped frequency	$\omega_d = \sqrt{(1 - \zeta^2)} \omega$	rad/s
Complex poles	$\lambda, \lambda^* = -\sigma \pm j\omega_d$	1/s
Complex angle	$\theta = \tan^{-1}(\zeta)$	rad

Table 2.2: List of modal parameters for a single vibration mode. The graphic on the right depicts the relationship between several modal parameters for a complex pair of poles λ, λ^* .

tion. This proves useful if the interest is only in the frequency range of the rigid body modes and lowest vibration modes, as discussed in Sec. 2.3. It is good practice to include eigenfrequencies up to twice the highest frequency of interest in the summation, i.e. $\omega_m > 2\omega_K$.

Admittance FRFs can be synthesised using a superposition of single-DoF modal solutions. An example is shown in Fig. 2.3. The m_{RB} rigid body modes (if present) need to be treated differently as they have an eigenfrequency $\omega_r = 0$ and no damping ratio related to frequency. The superposition for receptance, i.e. displacement over force, reads as follows⁶:

$$\mathbf{Y}(\omega) \approx \underbrace{-\frac{1}{\omega^2} \sum_1^{m_{\text{RB}}} \boldsymbol{\varphi}_r \boldsymbol{\varphi}_r^T}_{\text{rigid body modes}} + \underbrace{\sum_{m_{\text{RB}}+1}^m \frac{\boldsymbol{\varphi}_r \boldsymbol{\varphi}_r^T}{-\omega^2 + 2j\omega \zeta_r \omega_r + \omega_r^2}}_{\text{vibration modes}} \quad (2.19)$$

Eq. (2.19) can be evaluated for all K frequency points. The nominator only comprises the spatial or modal part of the response, which remains constant over frequency. The denominator controls the spectral part, adding a resonance frequency for each mode r , namely for $\omega = \omega_r$. As there is no inversion in the spatial terms, one can choose to assemble only for the DoFs that are relevant to the analysis. This offers an additional computational advantage over the direct inversion of Eq. (2.8), which needs the inversion to act on the full ($n \times n$) space.

To construct time-domain IRFs, a similar mode synthesis technique can be used⁷; see Fig. 2.3 on the right. Instead of computing the full set of IRFs by time integration of Eq. (2.12), the modes of interest can be superimposed using the same mass-normalised vibration modes of Eq. (2.18) and the modal parameters additionally listed in Table 2.2:

$$\mathbf{Y}(t) \approx \underbrace{t \sum_1^{m_{\text{RB}}} \boldsymbol{\varphi}_r \boldsymbol{\varphi}_r^T}_{\text{rigid body modes}} + \underbrace{\sum_{m_{\text{RB}}+1}^m \boldsymbol{\varphi}_r \boldsymbol{\varphi}_r^T \frac{e^{\lambda_r t} - e^{\lambda_r^* t}}{2j\omega_d}}_{\text{vibration modes}} \quad (2.20)$$

⁶FRFs for velocities or accelerations are obtained by multiplication of $\mathbf{Y}(\omega)$ with $j\omega$ and $-\omega^2$, respectively.

⁷This conversion method is not displayed in the overview of Fig. 2.1 but can be seen as the link between the modal domain and the time domain.

The parameters λ_r form the complex poles corresponding to the vibration modes. Again, a spatial and temporal part can be distinguished; the temporal part adds decaying waves with damped frequency ω_{dr} and time constant σ_r . Various means to synthesize IRFs are discussed in [212].

2.7.2 Modal parameter estimation

As explained in Sec. 2.4, admittance FRFs can be naturally obtained from experimental testing. These FRFs can either be used as raw material, for instance for frequency based substructuring, or used for the purpose of experimental modal analysis (EMA). The goal of EMA is to identify the vibration modes from measured response data, resulting in a series of mode shapes with associated frequency and damping parameters. This procedure is called *modal parameter estimation* and can be understood as the inverse action of mode synthesis.

EMA has been a popular research field since the 1970s and remains active up until today [53, 197]. Several methods have been proposed for modal identification of linear systems, that can roughly be put in the following categories:

- ▶ *Frequency-domain vs. time-domain based.* A frequency-domain method tries to fit FRFs by introducing a finite number of vibration modes at resonance frequencies that are normally already identified. Time-domain solutions may operate fully automatically and have more similarity to finite impulse response (FIR) techniques.
- ▶ *Single-DoF fit vs. multi-DoF algorithm.* Single-DoF models fit the response functions by consecutively introducing a single mode, i.e. without considering the interaction between modes. For systems with close resonance peaks or high damping, it is often preferred to use a multi-DoF model, that tries to identify a larger set of modes at once.
- ▶ *Normal mode vs. complex mode model.* A normal mode model assumes proportional damping and synchronous response at all DoFs. This implies that the modes are real-valued and are assumed to be superimposed in the sense of Eq. (2.19). A complex-mode model fits response functions using complex pairs of modes, allowing for more sophisticated damping properties.

A full review of EMA is beyond the scope of this chapter; see for instance [11, 53] for an overview of methods.

2.8 Summary

This chapter has demonstrated five domains for modelling and simulation of a structure's dynamics. Starting from the dynamic equations in the physical domain, four alternative domains have been derived. The respective equations of motion all relate displacements to applied force — either directly or through some modal transformation — but vary in the representation or *manifold* (in the meaning of topological space) to describe the structure's internal dynamics.

The physical-domain modelling approach yields a second order differential equation based on an equilibrium between internal forces of the structure and applied forces. To simu-

Domain	Section	Dynamic equation	Reduction
Physical domain	Sec. 2.2	$\mathbf{f}(t) = \mathbf{M}\ddot{\mathbf{u}}(t) + \mathbf{C}\dot{\mathbf{u}}(t) + \mathbf{K}\mathbf{u}(t)$	-
Modal domain	Sec. 2.3	$\mathbf{f}_m(t) = \mathbf{M}_m\ddot{\boldsymbol{\eta}}(t) + \mathbf{C}_m\dot{\boldsymbol{\eta}}(t) + \mathbf{K}_m\boldsymbol{\eta}(t)$	modal
Frequency domain	Sec. 2.4	$\mathbf{f}(\omega) = \mathbf{Z}(\omega) \mathbf{u}(\omega)$ $\mathbf{u}(\omega) = \mathbf{Y}(\omega) \mathbf{f}(\omega)$	(condensation) FRFs
Time domain	Sec. 2.5	$\mathbf{u}(t) = \mathbf{Y}(t) * \mathbf{f}(t)$	IRFs
State-space domain	Sec. 2.6	$\begin{cases} \dot{\mathbf{x}}(t) = \mathbf{A}\mathbf{x}(t) + \mathbf{B}\mathbf{v}(t) \\ \mathbf{y}(t) = \mathbf{C}\mathbf{x}(t) + \mathbf{D}\mathbf{v}(t) \end{cases}$	(min. realisation)

Table 2.3: Five domains for structural dynamic modelling and simulation, corresponding to the overview of Fig. 2.1.

late the structure's response to a load case in the time-domain, one could apply a time-integration algorithm to either the full or the reduced-order system matrices. The latter are obtained by a modal reduction, which leads to a representation in the modal domain as presented in Sec. 2.3.

The frequency domain allows to gather the physical-domain system matrices into a single dynamic stiffness matrix, depending on frequency. By inversion of this matrix, a matrix of admittance FRFs is obtained, governing the global dynamic responses to concentrated applied loads. The admittance FRFs are more familiar and intuitive, as they are naturally obtained by experimental testing. To that extend, the frequency domain forms a bridge between the numerical modelling and experimental testing approach.

By inverse Fourier transform of the admittance matrix, we obtain impulse response functions (IRFs). These functions, convolved with the history of applied forces, also yield a response solution in the time domain. However, in contrast to the original physical domain, only the input/output DoFs in the system need to be considered for a simulation, as the effects of the internal dynamics are already condensed in the IRFs.

The state-space domain, finally, expresses the structural dynamics as a system of first-order differential equations. It employs the well-known ABCD-quadruple, which can be obtained by transforming the physical-domain system matrices (the numerical approach) or by system identification using measurement data (the experimental approach).

Table 2.3 lists the five domains and their primary dynamic equation. Compared to the physical domain, all four derived domains implement some principle of model reduction. It should be noted that for a given structure, some reduction methods may be more effective than others. For instance: a structure with few modes and low damping can be very effectively reduced in the modal domain, but may lead to agonizingly slow simulation in the time domain due to the long decay time of the natural vibrations.

It is therefore a blessing to have different modelling domains at our disposal and be able to benefit from the particular specialities of each of them, provided that we can combine them in a dynamically correct way. Means to assemble the structure models will be the topic of the next chapter.

3

Substructure coupling and decoupling

chapter contents:

3.1 Introduction	27
3.2 Interface conditions	28
3.2.1 Coordinate compatibility	28
3.2.2 Force equilibrium	29
3.3 Substructure coupling	32
3.3.1 Primal assembly	33
3.3.2 Dual assembly	35
3.3.3 Lagrange-multiplier FBS	36
3.4 Substructure decoupling	38
3.4.1 Primal disassembly	38
3.4.2 Dual disassembly	39
3.4.3 Decoupling with alternative interface definitions	41
3.5 Summary	43

3.1 Introduction

Dynamic substructuring stands for the collection of methods for synthesising large dynamic systems using models of its substructures. The substructuring approach assumes that the dynamic interaction between substructures is confined to a limited set of interface DoFs. This means that the substructure models can be considered as super-elements; only the dynamics that are displayed at the interfaces are of relevance to the substructured assembly. Modelling domains that employ condensed dynamic information, such as the admittance FRFs in the frequency domain, are therefore particularly suited for substructuring.

Substructuring is by no means a new concept. Frequency-based assembly has already been considered since the 1960s, see for instance [38, 95, 161, 174, 202, 209]. For a long time, it has been conceived as a difficult and elaborate method, involving long sequences of subsystem matrices. A systematic approach was thus needed to streamline the assembly procedure, especially for coupling of more than two substructures. A promising systematic notation for dynamic substructuring was introduced by De Klerk et al. [105] in 2006, in turn based on the frequency-based substructuring paper of Jetmundsen et al. [95] in 1988. An essential strength of this methodology is the definition of two types of Boolean matrices, that handle all the “bookkeeping” involved in the assembly procedures. The theory and notation in this chapter is primarily based on the substructuring framework as presented in [104] and

additional concepts from [220]. Some slight variations are made to the notation as found in these papers to improve consistency throughout this thesis.

Before continuing with the discussion of interface conditions, let us make two remarks:

1. A DoF does not necessarily represent a one-directional displacement or rotation. Other possibilities include a deformation mode along a line or surface (as discussed in Chap. 4) or a linear combination of coordinates in case of non-conforming meshes (see for instance [221]). Notwithstanding the choice, it is crucial that the DoFs at the interfaces represent the same motion for both connecting structures. This is sometimes referred to as *collocated* [221] or *vectorially associated* DoFs [1]. In what follows, one-directional displacements are considered to illustrate the theory.
2. Of course, the relation between displacements and forces in a subsystem is governed by some set of dynamic equations, for instance obtained by modelling in one of the five domains discussed in Chap. 2. In the first section however, the dynamics of the substructures are intentionally disregarded, in order to concentrate on the interface conditions themselves and to demonstrate the general applicability of the presented procedures.

3.2 Interface conditions

Let us consider the two substructures depicted in Fig. 3.1, comprising four nodes in total. Two subsets of DoFs are denoted \mathbf{u}_2 and concern the nodes of the interface; \mathbf{u}_1 and \mathbf{u}_3 are DoFs of the nodes internal to substructure A and B, respectively. An overview of the DoFs in this chapter is presented in Table 3.1. The following sets of coordinates, applied forces and interface forces can be defined:

$$\mathbf{u} \triangleq \begin{bmatrix} \mathbf{u}_1^A \\ \mathbf{u}_2^A \\ \mathbf{u}_2^B \\ \mathbf{u}_3^B \end{bmatrix}; \quad \mathbf{f} \triangleq \begin{bmatrix} \mathbf{f}_1^A \\ \mathbf{f}_2^A \\ \mathbf{f}_2^B \\ \mathbf{f}_3^B \end{bmatrix}; \quad \mathbf{g} \triangleq \begin{bmatrix} \mathbf{0} \\ \mathbf{g}_2^A \\ \mathbf{g}_2^B \\ \mathbf{0} \end{bmatrix}; \quad \mathbf{u}, \mathbf{f}, \mathbf{g} \in \mathbb{R}^n \quad (3.1)$$

The interface forces \mathbf{g} are yet unknown, hence the substructures are uncoupled. A physically correct assembly can be realised by satisfying two conditions for each pair of interface DoFs \mathbf{u}_2 .

3.2.1 Coordinate compatibility

The first and trivial condition is the *coordinate compatibility* at the matching pairs of DoFs. Every collocated coordinate must have the same value and sign at both sides. Let us express this in three different, yet functionally equivalent ways:

$$\mathbf{u}_2^A = \mathbf{u}_2^B \quad \Leftrightarrow \quad \mathbf{u}_2^B - \mathbf{u}_2^A = \mathbf{0} \quad \Leftrightarrow \quad \begin{cases} \mathbf{u}_2^A = \mathbf{q}_2 \\ \mathbf{u}_2^B = \mathbf{q}_2 \end{cases} \quad (3.2)$$

The first notation clearly tells what is happening but is not the easiest form to implement in a systematic manner. The second form can be conveniently written using a *signed Boolean matrix* \mathbf{B} operating on the full set of DoFs \mathbf{u} . This notation was introduced in [105] and

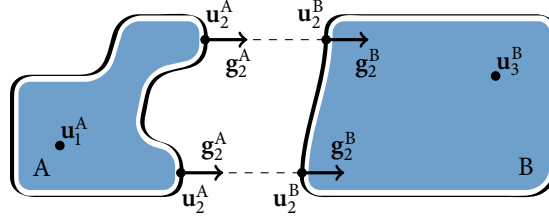


Figure 3.1: An assembly of two substructures A and B, connected at the interfacing nodes \mathbf{u}_2 .

leads for this example to the following condition:

$$\mathbf{B}\mathbf{u} = \mathbf{0} \quad \implies \quad \mathbf{u}_2^B - \mathbf{u}_2^A = \mathbf{0} \quad \text{with} \quad \mathbf{B} \triangleq \begin{bmatrix} \mathbf{0} & -\mathbf{I} & \mathbf{I} & \mathbf{0} \end{bmatrix} \quad (3.3)$$

Every pair of interface DoFs adds a row to the Boolean matrix (it is assumed that the DoFs have matching ordering, hence the identities). Considering that the full set of coordinates \mathbf{u} comprises n DoFs of which $2n_2$ pertain to the interface, the Boolean matrix \mathbf{B} has size $n_2 \times n$. The product of \mathbf{B} and \mathbf{u} thus yields n_2 equations, each one expressing the incompatibility or interface “gap” associated with a single pair of interface DoFs.

The third form of Eq. (3.2) is based on a coordinate substitution by a set of generalised coordinates \mathbf{q} , namely the set of unique coordinates that remain after assembly. This is related to the assembly procedure in FE modelling; the DoFs $\mathbf{u}^{(s)}$ can be considered as “super-element” coordinates pertaining to substructure $\Omega^{(s)}$ that need to be mapped to a global set of coordinates \mathbf{q} . For the example here, the following mapping can be defined:

$$\mathbf{u} = \mathbf{L}\mathbf{q} \quad \implies \quad \begin{cases} \mathbf{u}_1^A = \mathbf{q}_1 \\ \mathbf{u}_2^A = \mathbf{q}_2 \\ \mathbf{u}_2^B = \mathbf{q}_2 \\ \mathbf{u}_3^B = \mathbf{q}_3 \end{cases} \quad \text{with} \quad \mathbf{L} \triangleq \begin{bmatrix} \mathbf{I} & \mathbf{0} & \mathbf{0} \\ \mathbf{0} & \mathbf{I} & \mathbf{0} \\ \mathbf{0} & \mathbf{I} & \mathbf{0} \\ \mathbf{0} & \mathbf{0} & \mathbf{I} \end{bmatrix} \quad (3.4)$$

The *Boolean localisation matrix* \mathbf{L} maps the n physical DoFs \mathbf{u} of all substructures to $n - n_2 = m$ generalised DOFs \mathbf{q} . Matrix \mathbf{L} is thus of size $n \times m$.

A useful relation can be observed between the signed Boolean matrix and the Boolean localisation matrix. Because \mathbf{q} is the set of unique DoFs of an assembled system, the physical coordinates \mathbf{u} , as a result of Eq. (3.4), are compatible by definition. Hence the condition of Eq. (3.4) is satisfied automatically for all possible displacements of \mathbf{q} .

$$\mathbf{B}\mathbf{u} = \mathbf{B}\mathbf{L}\mathbf{q} = \mathbf{0} \quad \forall \mathbf{q} \quad \implies \quad \begin{cases} \mathbf{L} = \text{null}(\mathbf{B}) \\ \mathbf{B}^T = \text{null}(\mathbf{L}^T) \end{cases} \quad (3.5)$$

As it turns out, \mathbf{B} and \mathbf{L} are each other’s nullspaces, which allows to obtain one Boolean matrix from the other by Eq. (3.5). Aside from being a convenient property, it is essential for the definition of primal and dual assemblies, as will be discussed in Sec. 3.3.

3.2.2 Force equilibrium

The second condition for substructure assembly is the *force equilibrium* between matching interface DoFs. This condition is a direct result of Newton’s third law of motion, stating

Degree of freedom (DoF)	Displacements	Forces	# DoFs
All DoFs of A and B	\mathbf{u}	\mathbf{f}	n
- internal of substructure A	\mathbf{u}_1^A	\mathbf{f}_1^A	n_1
- interfaces of substructure A	\mathbf{u}_2^A	\mathbf{f}_2^A	n_2
- interfaces of substructure B	\mathbf{u}_2^B	\mathbf{f}_2^B	n_2
- internal of substructure B	\mathbf{u}_3^B	\mathbf{f}_3^B	n_3
Unique or generalised DoFs	\mathbf{q}	\mathbf{p}	m
- internal of substructure A	\mathbf{q}_1	\mathbf{p}_1	m_1
- interface of substructures A and B	\mathbf{q}_2	\mathbf{p}_2	m_2
- internal of substructure B	\mathbf{q}_3	\mathbf{p}_3	m_3
Interface DoFs	δ	λ	n_c, n_e

Table 3.1: Degrees of freedom and symbols as they appear in this chapter. The sets of coordinates and forces are vectorially associated and therefore comprise an equal number of DoFs.

that for every force vector, there must be another force vector with equal magnitude and opposing direction. It is used here to define a relationship between the interface forces \mathbf{g} between connected substructures A and B:

$$\mathbf{g}_2^A = -\mathbf{g}_2^B \quad \Leftrightarrow \quad \mathbf{g}_2^A + \mathbf{g}_2^B = \mathbf{0} \quad \Leftrightarrow \quad \begin{cases} \mathbf{g}_2^A = \lambda \\ \mathbf{g}_2^B = -\lambda \end{cases} \quad (3.6)$$

Again, three notations are provided of which the last two will be discussed further. The second form can be established by pre-multiplying the interface forces with the transpose of the Boolean localisation matrix \mathbf{L} and equating the resultant to zero:

$$\mathbf{L}^T \mathbf{g} = \mathbf{0} \quad \Rightarrow \quad \begin{cases} \mathbf{g}_1^A = \mathbf{0} \\ \mathbf{g}_2^A + \mathbf{g}_2^B = \mathbf{0} \\ \mathbf{g}_3^B = \mathbf{0} \end{cases} \quad (3.7)$$

The second line of Eq. (3.7) establishes the equilibrium condition on the DoFs of the interface. The first and last line act on the DoFs that have no associated interface force because they are uncoupled. Hence, they are redundant and harmless to the assembly equations.

Finally, a substitution is introduced for the interface forces. As \mathbf{g}_2^A and \mathbf{g}_2^B only differ in sign, they can be regarded as one set of DoFs rather than a dual set. Using the transpose of the signed Boolean matrix \mathbf{B} , the following substitution can be made:

$$\mathbf{g} = -\mathbf{B}^T \lambda \quad \Rightarrow \quad \begin{cases} \mathbf{g}_1^A = \mathbf{0} \\ \mathbf{g}_2^A = \lambda \\ \mathbf{g}_2^B = -\lambda \\ \mathbf{g}_3^B = \mathbf{0} \end{cases} \quad (3.8)$$

Here λ is a set of *Lagrange multipliers*, denoting the intensity of the interface forces. Every Lagrange multiplier is associated with a pair of interface DoFs in the assembly. By defining the interfaces forces according to Eq. (3.8), the equilibrium condition is automatically satisfied, as can be verified by substitution into Eq. (3.7):

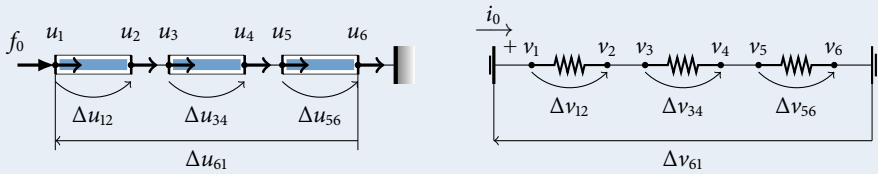
$$\mathbf{L}^T \mathbf{g} = -\mathbf{L}^T \mathbf{B}^T \lambda = \mathbf{0} \quad \forall \mathbf{g} \quad (3.9)$$

The nullspace property of Eq. (3.5) indeed proves that the equilibrium condition is satisfied for all possible interface forces built on Eq. (3.7).

► *Intermezzo: relation to Kirchhoff's laws*

The interface conditions expose an apparent balance or “symmetry” between the conditions of coordinate compatibility, described by Eq. (3.2)–(3.4), and force equilibrium, governed by Eq. (3.6)–(3.8). This symmetry can be understood if one regards force and displacement as a pair of input/output quantities, subject to *duality*, and a mechanical assembly as a network of lumped subsystems. Then it appears that an analogy exists with electric network theory [68, 109].

Let us review the interface conditions from the perspective of Kirchhoff’s laws for electrical circuits. The first law, known as *Kirchhoff’s current law*, states that all currents flowing in or out of a junction must sum up to zero. This is analogue to the equilibrium condition Eq. (3.7) between interface forces at a connecting node. The electromotive force or “voltage” at a junction is constant for all connected terminals, which is analogue to the compatibility condition of Eq. (3.3). The second law is *Kirchhoff’s voltage law* and states that the sum of potential drops and rises in any closed circuit must equal zero. This is lesser known in structural dynamics, but may be applied to the differences in displacements over the subsystems, as will be demonstrated.



An example of three bars in series is depicted, together with its electrical circuit analogy. Because of the series configuration, the junctions only have two terminals each. Application of the current law thus leads to a trivial result for interface forces / electric currents, which may also be obtained using the Boolean localisation matrix for this system:

$$\begin{array}{l}
 \text{Mechanic} \quad \begin{cases} g_2 + g_3 = 0 \\ g_4 + g_5 = 0 \end{cases} \implies \mathbf{L}^T \mathbf{g} = \mathbf{0} \\
 \text{Electric} \quad \begin{cases} i_2 + i_3 = 0 \\ i_4 + i_5 = 0 \end{cases} \implies \mathbf{L}^T \mathbf{i} = \mathbf{0}
 \end{array}
 \quad
 \mathbf{L} = \begin{bmatrix} 1 & 0 & 0 & 0 \\ 0 & 1 & 0 & 0 \\ 0 & 1 & 0 & 0 \\ 0 & 0 & 1 & 0 \\ 0 & 0 & 1 & 0 \\ 0 & 0 & 0 & 1 \end{bmatrix}$$

Next, constant displacement or voltage at each terminal can be obtained by application of the compatibility condition:

$$\begin{array}{l}
 \text{Mechanic} \quad \begin{cases} u_2 - u_3 = 0 \\ u_4 - u_5 = 0 \end{cases} \implies \mathbf{B} \mathbf{u} = \mathbf{0} \\
 \text{Electric} \quad \begin{cases} v_2 - v_3 = 0 \\ v_4 - v_5 = 0 \end{cases} \implies \mathbf{B} \mathbf{v} = \mathbf{0}
 \end{array}
 \quad
 \mathbf{B} = \begin{bmatrix} 0 & -1 & 1 & 0 & 0 & 0 \\ 0 & 0 & 0 & -1 & 1 & 0 \end{bmatrix}$$

Kirchhoff's second law applies to the differences in displacements / electric potential in a closed circuit. Note that the displacement u_1 and the rigid boundary condition at u_6 are in fact understood as a closed circuit here. Nevertheless, the following resulting equation is somewhat unfamiliar in mechanics:

$$\begin{aligned}(u_2 - u_1) + (u_4 - u_3) + (u_6 - u_5) + (u_1 - u_6) &= 0 \\ \implies \Delta u_{12} + \Delta u_{34} + \Delta u_{56} + \Delta u_{61} &= 0\end{aligned}$$

which means for the electrical system:

$$\begin{aligned}(v_2 - v_1) + (v_4 - v_3) + (v_6 - v_5) + (v_1 - v_6) &= 0 \\ \implies \Delta v_{12} + \Delta v_{34} + \Delta v_{56} + \Delta v_{61} &= 0\end{aligned}$$

In the presented analogy, voltage is substituted for displacement and current for forces. Intuitively, we are inclined to relate voltage with force, as the causes of flowing currents and moving structures, and thus write the analogy the other way around [109]. Historically, this so-called *impedance analogy* was accepted first, but received strong opposition because it conflicts with the rules of parallel and series addition [68]. What is used here is the *mobility analogy*, advocated by Firestone [61] in response to this issue.

Note that the \mathbf{L} and \mathbf{B} matrices may also be used to define a set of “generalised” currents and voltages, consisting of 4 DoFs (due to the number of columns of \mathbf{L}) for this example. This is left as an exercise to the interested reader. ◀

3.3 Substructure coupling

Let us now use the interface conditions to assemble the two dynamic systems from the example of Fig. 3.1. Without loss of generality, we choose to express the subsystem dynamics in the frequency domain, as this leads to the clearest notation. Note that the following assembly procedures are collectively referred to as frequency-based substructuring (FBS).

Following the definition of the subsystem DoFs by Eq. (3.1), the impedance and admittance matrices can be defined for subsystems A and B. The frequency dependency is omitted here to improve readability:

$$\begin{aligned}\mathbf{Z}^A &\triangleq \begin{bmatrix} \mathbf{Z}_{11}^A & \mathbf{Z}_{12}^A \\ \mathbf{Z}_{21}^A & \mathbf{Z}_{22}^A \end{bmatrix}; & \mathbf{Y}^A &\triangleq \begin{bmatrix} \mathbf{Y}_{11}^A & \mathbf{Y}_{12}^A \\ \mathbf{Y}_{21}^A & \mathbf{Y}_{22}^A \end{bmatrix}; & \mathbf{u}^A, \mathbf{f}^A &\in \mathbb{R}^{n^A} \\ \mathbf{Z}^B &\triangleq \begin{bmatrix} \mathbf{Z}_{22}^B & \mathbf{Z}_{23}^B \\ \mathbf{Z}_{32}^B & \mathbf{Z}_{33}^B \end{bmatrix}; & \mathbf{Y}^B &\triangleq \begin{bmatrix} \mathbf{Y}_{22}^B & \mathbf{Y}_{23}^B \\ \mathbf{Y}_{32}^B & \mathbf{Y}_{33}^B \end{bmatrix}; & \mathbf{u}^B, \mathbf{f}^B &\in \mathbb{R}^{n^B}\end{aligned}$$

Note that the subsystem admittance and impedance can be obtained from each other by matrix inversion. Next, the subsystem matrices can be put in block-diagonal form, to align

with to the full set of DoFs:

$$\mathbf{Z} \triangleq \begin{bmatrix} \mathbf{Z}_{11}^A & \mathbf{Z}_{12}^A & \mathbf{0} & \mathbf{0} \\ \mathbf{Z}_{21}^A & \mathbf{Z}_{22}^A & \mathbf{0} & \mathbf{0} \\ \mathbf{0} & \mathbf{0} & \mathbf{Z}_{22}^B & \mathbf{Z}_{23}^B \\ \mathbf{0} & \mathbf{0} & \mathbf{Z}_{32}^B & \mathbf{Z}_{33}^B \end{bmatrix}; \quad \mathbf{Y} \triangleq \begin{bmatrix} \mathbf{Y}_{11}^A & \mathbf{Y}_{12}^A & \mathbf{0} & \mathbf{0} \\ \mathbf{Y}_{21}^A & \mathbf{Y}_{22}^A & \mathbf{0} & \mathbf{0} \\ \mathbf{0} & \mathbf{0} & \mathbf{Y}_{22}^B & \mathbf{Y}_{23}^B \\ \mathbf{0} & \mathbf{0} & \mathbf{Y}_{32}^B & \mathbf{Y}_{33}^B \end{bmatrix}; \quad \mathbf{u}, \mathbf{f} \in \mathbb{R}^n$$

The zeros on the off-diagonal blocks indicate that the subsystems are so far uncoupled. The dynamic equations for the uncoupled system can now be expressed in both impedance and admittance form, employing the definitions of respectively Eq. (2.7) and (2.8):

$$\mathbf{Z}\mathbf{u} = \mathbf{f} + \mathbf{g} \quad (3.10a)$$

$$\mathbf{u} = \mathbf{Y}(\mathbf{f} + \mathbf{g}) \quad (3.10b)$$

Recall that in both equations the total number of DoFs \mathbf{u} is n and that the interface forces \mathbf{g} are yet undetermined. According to Eq. (3.1), vector \mathbf{g} has only $2n_2$ non-zero entries, bringing the total amount of unknowns in Eq. (3.10) to $n + 2n_2$. Eq. (3.10a–3.10b) only have n equations each, meaning that the systems are under-determined and thus unassembled. In order to couple the two substructures, the equations shall either be supplemented with additional equations governing the interface conditions, or the number of unknowns need to be reduced. Two standard approaches to do so are discussed next.

3.3.1 Primal assembly

The primal assembly is used to assemble subsystem impedance matrices. It starts with the definition of a unique set of coordinates \mathbf{q} . The physical DoFs \mathbf{u} of all substructures are mapped to \mathbf{q} using Eq. (3.4), hence by definition of an appropriate Boolean localisation matrix \mathbf{L} . This leaves a unique set of DoFs for which the compatibility condition is satisfied a priori. To enforce equilibrium of the interface forces, Eq. (3.7) is added to the equations of motion of Eq. (3.10a):

$$\begin{cases} \mathbf{Z}\mathbf{L}\mathbf{q} = \mathbf{f} + \mathbf{g} \\ \mathbf{L}^T\mathbf{g} = \mathbf{0} \end{cases} \quad (3.11)$$

Pre-multiplying the first line with \mathbf{L}^T , a system of m equations is obtained with m unknowns; the interface force term \mathbf{g} drops out due to the condition posed on the second line. This yields the assembled equations of motion for the generalised coordinate set \mathbf{q} and associated generalised forces $\mathbf{p} = \mathbf{L}^T\mathbf{f}$:

$$\hat{\mathbf{Z}}\mathbf{q} = \mathbf{p} \quad \text{with} \quad \hat{\mathbf{Z}} \triangleq \mathbf{L}^T\mathbf{Z}\mathbf{L} \quad (3.12)$$

Matrix $\hat{\mathbf{Z}}$ denotes the primally assembled impedance for the generalised coordinates. The matrix is square but not necessarily full; DoFs that are not directly connected to each other have zero entries in the matrix. Inversion of this matrix yields the more familiar admittance form, namely the matrix of FRFs for the primal coordinates:

$$\mathbf{q} = \hat{\mathbf{Y}}\mathbf{p} \quad \text{with} \quad \hat{\mathbf{Y}} \triangleq (\mathbf{L}^T\mathbf{Z}\mathbf{L})^{-1} \quad (3.13)$$

If required, the FRFs of the primal admittance matrix can be expanded to the original set of DoFs \mathbf{u} by pre- and post-multiplying with \mathbf{L} . This yields the so-called *dually assembled*

admittance (as further discussed in the next section), which shall be distinguished from primally assembled matrices by use of a tilde:

$$\mathbf{u} = \tilde{\mathbf{Y}}\mathbf{f} \quad \text{with} \quad \tilde{\mathbf{Y}} = \mathbf{L}(\mathbf{L}^T\mathbf{Z}\mathbf{L})^{-1}\mathbf{L}^T \quad (3.14)$$

Lastly the interface forces are not obtained as a by-product of the primal assembly process. They may be computed afterwards, for instance by substituting the assembled responses \mathbf{u} back into the original unassembled dynamic equation (3.10a):

$$\mathbf{g} = \mathbf{Z}\mathbf{u} - \mathbf{f} = [\mathbf{Z}\mathbf{L}(\mathbf{L}^T\mathbf{Z}\mathbf{L})^{-1}\mathbf{L}^T - \mathbf{I}]\mathbf{f} \quad (3.15)$$

A primal assembly is suitable if one has access to the subsystem dynamics in impedance form, for instance obtained from finite element modelling, see Sec. 2.2. For assembly of admittances, such as the FRFs obtained by experimental testing, a suitable approach is discussed in Sec. 3.3.2.

► Primal formulation in other domains

The primal assembly approach is similar to finite element assembly, which is normally performed on the system matrices directly. For instance, the equations of motion for a primal assembly in the physical domain can be formulated as follows:

$$\hat{\mathbf{M}}\ddot{\mathbf{q}}(t) + \hat{\mathbf{C}}\dot{\mathbf{q}}(t) + \hat{\mathbf{K}}\mathbf{q}(t) = \mathbf{p}(t) \quad \text{with} \quad \begin{cases} \hat{\mathbf{M}} = \mathbf{L}^T\mathbf{M}\mathbf{L} \\ \hat{\mathbf{C}} = \mathbf{L}^T\mathbf{C}\mathbf{L} \\ \hat{\mathbf{K}} = \mathbf{L}^T\mathbf{K}\mathbf{L} \end{cases} \quad (3.16)$$

These assembled system matrices can be used for transient simulation by any standard time-stepping algorithm.

If the subsystem matrices are modally reduced, i.e. defined for the modal coordinates $\boldsymbol{\eta}$ as discussed in Sec. 2.3, a primal assembly cannot be defined directly. Indeed, there is no logical choice for the operator \mathbf{L} , because there are generally no modes that appear uniquely in two different structures. Nevertheless we may require modal compatibility at the physical interface DoFs, namely by combining the definitions of Eq. (2.4) for modal coordinates $\boldsymbol{\eta}$ and the compatibility condition of Eq. (3.3):

$$\mathbf{B}\mathbf{R}\boldsymbol{\eta} = \mathbf{0} \quad \implies \quad \mathbf{B}_m\boldsymbol{\eta} = \mathbf{0} \quad \text{with} \quad \mathbf{B}_m \triangleq \mathbf{B}\mathbf{R} \quad (3.17)$$

Matrix \mathbf{B}_m constitutes the modal compatibility matrix; \mathbf{R} is the block-diagonal concatenation of the substructures' reduction matrices. Note that \mathbf{B}_m is no longer Boolean; nevertheless it has a null-space \mathbf{L}_m which gives rise to a new set of unique modal coordinates $\boldsymbol{\xi}$ for the primally assembled system (see also [101, 104]):


$$\begin{cases} \boldsymbol{\eta} = \mathbf{L}_m\boldsymbol{\xi} \\ \mathbf{B}_m\mathbf{L}_m\boldsymbol{\xi} = \mathbf{0} \quad \forall \boldsymbol{\xi} \end{cases} \quad \implies \quad \mathbf{L}_m = \text{null}(\mathbf{B}_m) \quad (3.18)$$

This newly obtained localisation matrix \mathbf{L}_m — although not Boolean and abandoned from any physical comprehension — may be used to assemble the modal system matrices in a fashion analogue to Eq. (3.16). We then obtain the following equations

of motion for the generalised modal coordinates ξ :

$$\begin{aligned} \hat{\mathbf{M}}_m \ddot{\xi}(t) + \hat{\mathbf{C}}_m \dot{\xi}(t) + \hat{\mathbf{K}}_m \xi(t) &= \hat{\mathbf{f}}_m(t) \\ \mathbf{u}(t) &= \mathbf{R} \mathbf{L}_m \xi(t) \end{aligned} \quad \text{with} \quad \begin{cases} \hat{\mathbf{M}}_m = \mathbf{L}_m^T \mathbf{M}_m \mathbf{L}_m \\ \hat{\mathbf{C}}_m = \mathbf{L}_m^T \mathbf{C}_m \mathbf{L}_m \\ \hat{\mathbf{K}}_m = \mathbf{L}_m^T \mathbf{K}_m \mathbf{L}_m \\ \hat{\mathbf{f}}_m = \mathbf{L}_m^T \mathbf{f}_m \end{cases} \quad (3.19)$$

Clearly, the approach of Eq. (3.17–3.16) is just a direct consequence of combining modal reduction techniques, i.e. Eq. (2.6), with the steps of primal assembly. Nevertheless the resulting methodology is quite profound, for instance: the assembled system's natural vibration modes and resonance frequencies are directly accessible from the eigenvalue problem of $\hat{\mathbf{K}}_m$ with $\hat{\mathbf{M}}_m$.

For completeness of this section, it is probably justified to explore the possibilities of primal assembly for the time and state-space domain. However there is no trivial impedance variant for the equations of motion in these two domains, which is a requirement for primal assembly. The concept of dual assembly suits these domains better, as will be discussed next. 

3.3.2 Dual assembly

A *dual assembly* starts with the admittance notation of Eq. (3.10b). Instead of eliminating the redundant DoFs, which is the principal idea of primal assembly, compatibility is enforced by adding the additional equations of Eq. (3.3). This adds n_2 equations to the original system of n equations. For the interface forces, Lagrange multipliers are substituted according to Eq. (3.8), hence the equilibrium condition is satisfied a priori.

$$\begin{cases} \mathbf{u} = \mathbf{Y} (\mathbf{f} - \mathbf{B}^T \boldsymbol{\lambda}) \\ \mathbf{B} \mathbf{u} = \mathbf{0} \end{cases} \quad (3.20)$$

The system Eq. (3.20) now has $n + n_2$ equations and an equal amount of unknowns. It can be solved by substituting the first line into the compatibility condition and solving for $\boldsymbol{\lambda}$:

$$\begin{aligned} \mathbf{B} \mathbf{Y} (\mathbf{f} - \mathbf{B}^T \boldsymbol{\lambda}) &= \mathbf{0} \\ \mathbf{B} \mathbf{Y} \mathbf{f} &= \mathbf{B} \mathbf{Y} \mathbf{B}^T \boldsymbol{\lambda} \\ \boldsymbol{\lambda} &= (\mathbf{B} \mathbf{Y} \mathbf{B}^T)^{-1} \mathbf{B} \mathbf{Y} \mathbf{f} \end{aligned} \quad (3.21)$$

The Lagrange multipliers $\boldsymbol{\lambda}$ are effectively the connecting forces that keep the two substructures together. Observe that the term $\mathbf{B} \mathbf{Y} \mathbf{f}$ represents the incompatibility caused by the uncoupled responses to the applied force \mathbf{f} , while $(\mathbf{B} \mathbf{Y} \mathbf{B}^T)^{-1}$ forms the combined dynamic stiffness experienced at the interfaces. The coupled response is obtained by substituting the Lagrange multipliers back into the first line of Eq. (3.20):

$$\begin{aligned} \mathbf{u} &= \mathbf{Y} (\mathbf{f} - \mathbf{B}^T \boldsymbol{\lambda}) \\ \mathbf{u} &= \mathbf{Y} \mathbf{f} - \mathbf{Y} \mathbf{B}^T (\mathbf{B} \mathbf{Y} \mathbf{B}^T)^{-1} \mathbf{B} \mathbf{Y} \mathbf{f} \end{aligned} \quad (3.22)$$

Collecting the admittance terms, the *dually assembled* FRF matrix can be obtained, which is again embellished by a tilde to discriminate the dual from the primally assembled matrix.

$$\mathbf{u} = \tilde{\mathbf{Y}}\mathbf{f} \quad \text{with} \quad \tilde{\mathbf{Y}} \triangleq \left[\mathbf{I} - \mathbf{Y}\mathbf{B}^T (\mathbf{B}\mathbf{Y}\mathbf{B}^T)^{-1} \mathbf{B} \right] \mathbf{Y} \quad (3.23)$$

Note that $\tilde{\mathbf{Y}}$ is an $n \times n$ matrix, meaning that the interface DoFs appear twice. The FRFs on the rows corresponding to $\mathbf{u}_2^A = \mathbf{u}_2^B$ and columns of $\mathbf{f}_2^A = \mathbf{f}_2^B$ are thus identical, which is characteristic for a dual FRF matrix. The redundant rows and columns may be removed if desired, for instance for storing size considerations. This yields the *primal* FRF matrix for the set of unique coordinates \mathbf{q} and loads \mathbf{p} . This may for instance be obtained in the following way:

$$\begin{cases} \mathbf{q} = \mathbf{L}^+ \mathbf{u} \\ \mathbf{p} = \mathbf{L}^+ \mathbf{f} \end{cases} \quad \implies \quad \hat{\mathbf{Y}} = (\mathbf{L})^+ \tilde{\mathbf{Y}} (\mathbf{L}^T)^+ \quad (3.24)$$

The pseudo-inverse operation effectively takes the average over the entries in the non-unique rows and columns, creating a new primal admittance matrix of $m \times m$. This has the same effect as manual selection of the unique rows and columns from the FRF matrix.

3.3.3 Lagrange-multiplier FBS

The coupling approach of Eq. (3.22–3.23) has first been proposed in [105] and has quickly gained popularity as the “one-liner” equation for Lagrange-multiplier frequency-based substructuring (LM-FBS). This method allows to assemble an arbitrary number of substructures in a highly systematic fashion. An LM-FBS procedure for assembly of N_s substructures consists of the following four steps:

1. Obtain the FRF matrix $\mathbf{Y}^{(s)}$ for each substructure. Make a distinction between DoFs that are internal to the structure and DoFs that need to be connected. The connecting DoFs should appear both as rows (responses \mathbf{u}_2) and columns (forces \mathbf{f}_2) in the FRF matrix. This implies for experimentally obtained FRFs that sufficient sensors and excitations need to be mounted and performed to determine the interface dynamics (see also Chap. 4).
2. Define a global set of DoFs, comprising the DoFs of all *separate* substructures. With regard to the interface DoFs, ensure that the positions and directions are defined uniquely for all substructures. The global set of coordinates, forces and matrix of unassembled FRFs are concatenated as follows:

$$\begin{cases} \mathbf{u} = \text{col}(\mathbf{u}^{(1)}, \dots, \mathbf{u}^{(N_s)}) \\ \mathbf{f} = \text{col}(\mathbf{f}^{(1)}, \dots, \mathbf{f}^{(N_s)}) \\ \mathbf{Y} = \text{diag}(\mathbf{Y}^{(1)}, \dots, \mathbf{Y}^{(N_s)}) \end{cases} \quad \text{total number of DoFs} \quad n = \sum_s n^{(s)}$$

3. Define the subsystem connectivity. This can be done in two ways: (a) by specifying the signed Boolean matrix \mathbf{B} with plus and minus ones for every connected DoF or (b) by defining the Boolean localisation matrix \mathbf{L} for the unique set of DoFs \mathbf{q} and computing \mathbf{B} from Eq. (3.5).

4. Apply the LM-FBS equation (3.23) for each frequency point in the FRF matrix. To eliminate the redundant rows/columns and end up with the primal FRF matrix, apply Eq. (3.24).

In practice of experimental FRF measurement, it is likely that the set of response DoFs \mathbf{u} is not fully aligned with the series of excitations points \mathbf{f} . For instance, some sensors (such as microphones) may function solely as reference points and need no force excitation, whereas some excitations may have been performed on positions without a sensor. As a result, the interface displacements in \mathbf{u} do not appear at the same indices as the associated interface forces in \mathbf{f} . Instead of altering the FRF matrices, it is more convenient to construct Boolean matrices for the conditions of compatibility and equilibrium separately. It can be verified that the LM-FBS equation of Eq. (3.23) changes accordingly:

$$\begin{cases} \mathbf{B}_c \mathbf{u} = \mathbf{0} \\ \mathbf{g} = -\mathbf{B}_e^T \boldsymbol{\lambda} \end{cases} \implies \mathbf{u} = \left[\mathbf{I} - \mathbf{Y} \mathbf{B}_e^T (\mathbf{B}_c \mathbf{Y} \mathbf{B}_e^T)^{-1} \mathbf{B}_c \right] \mathbf{Y} \mathbf{f} \quad (3.25)$$

Comparing with Eq. (3.23), this does not change anything to the matrix system to solve: it only provides means to keep the measured matrices in original format. In an attempt to further automatize the substructuring process, one could define the LM-FBS algorithm as follows:

$$\tilde{\mathbf{Y}} = \text{LM-FBS}(\mathbf{Y}, \mathbf{B}_c, \mathbf{B}_e) \iff \tilde{\mathbf{Y}} = \left[\mathbf{I} - \mathbf{Y} \mathbf{B}_e^T (\mathbf{B}_c \mathbf{Y} \mathbf{B}_e^T)^{-1} \mathbf{B}_c \right] \mathbf{Y} \quad (3.26)$$

In spite of the apparent freedom in the construction of the Boolean matrices, care should be taken to end up with an interface admittance matrix $\mathbf{Y}^{\text{int}} \triangleq \mathbf{B}_c \mathbf{Y} \mathbf{B}_e^T$ that is invertible and properly conditioned. In fact the conditioning of this term is highly defining for the success of the coupling procedure.

► Dual formulation in other domains

Like the primal formulation, the dual formulation also applies to the equations in the physical domain. Supplementing the equation of motion of Eq. (2.1) with the dual compatibility of Eq. (3.3) and substituting Eq. (3.8) for the interface forces, the following system is obtained:


$$\begin{cases} \mathbf{M} \ddot{\mathbf{u}}(t) + \mathbf{C} \dot{\mathbf{u}}(t) + \mathbf{K} \mathbf{u}(t) + \mathbf{B}^T \boldsymbol{\lambda}(t) = \mathbf{f}(t) \\ \mathbf{B} \mathbf{u}(t) = \mathbf{0} \end{cases} \quad (3.27)$$

Note that the Lagrange multipliers are now moved to the left side of the differential equation, as they pertain to the unknowns in the system. Together, the following matrix system of equations is constructed:

$$\begin{bmatrix} \mathbf{M} & \mathbf{0} \\ \mathbf{0} & \mathbf{0} \end{bmatrix} \begin{bmatrix} \dot{\mathbf{u}}(t) \\ \boldsymbol{\lambda}(t) \end{bmatrix} + \begin{bmatrix} \mathbf{C} & \mathbf{0} \\ \mathbf{0} & \mathbf{0} \end{bmatrix} \begin{bmatrix} \dot{\mathbf{u}}(t) \\ \boldsymbol{\lambda}(t) \end{bmatrix} + \begin{bmatrix} \mathbf{K} & \mathbf{B}^T \\ \mathbf{B} & \mathbf{0} \end{bmatrix} \begin{bmatrix} \mathbf{u}(t) \\ \boldsymbol{\lambda}(t) \end{bmatrix} = \begin{bmatrix} \mathbf{f}(t) \\ \mathbf{0} \end{bmatrix} \quad (3.28)$$

This formulation is sometimes found in literature on parallel finite element solvers, see for instance the finite element tearing and interconnecting (FETI) method [59].

Dual assembly in the modal domain is not discussed here but relates to many popular techniques; see for instance literature on component mode synthesis (CMS) [35, 36,

219] and the dual Craig-Bampton method [165]. Dual assembly of time-domain IRFs is known as impulse-based substructuring (IBS). This was proposed in 2010 by Rixen [166, 170] as the time-domain counterpart of FBS and has recently gained interest in the substructuring community [168, 189, 211, 212, 215]; see also Sec. 2.5. 

3.4 Substructure decoupling

In the previous two sections the basic tools have been outlined for substructure assembly, i.e. coupling of component models. It was demonstrated for coupling of substructures A and B or, written using the plus sign as a systematic coupling operator: $AB = A + B$. If one would imagine a reverse operation of substructure coupling, it would probably perform something like $AB - B = A$. Such operation indeed exists and has fittingly been coined substructure *decoupling*¹.

Decoupling is an essential tool in the field of experimental substructuring. In practice it often occurs that a substructure cannot be measured in the exact configuration as desired. Added mass from sensors is an obvious example, but one could also imagine the need for temporary fixtures in order to constrain the substructure properly for measurement or be able to measure and excite rotational dynamics. In all cases these “residual” structures may have a significant contribution to the dynamics, which needs to be removed after measurement on the component by means of decoupling.

The basic concepts of substructure decoupling are presented in this section. It is assumed that the concepts of substructure coupling are well understood. As will be demonstrated, decoupling can be applied using very similar techniques. The interested reader is further referred to [43, 44, 220] for an overview of techniques and [40, 73, 86, 193] for some historical background.

3.4.1 Primal disassembly

Like substructure coupling, decoupling can be expressed in a primal and dual fashion. The primal approach is easily understood if one recalls the conceptual similarity with FE assembly. In both cases, one is allowed to sum the impedances of the substructures' interfaces with respect to their mapping in the global system matrix. Hence the addition could be reversed by simple subtraction of the substructure's impedance, as will be demonstrated.

Let us illustrate substructure decoupling using the same example structure, which is now depicted in Fig. 3.2. The same definitions apply for the DoFs, i.e. Eq. (3.1) and Table 3.1. The following system matrices are identical, as it might be the result of primal assembly of

¹The term *inverse substructuring* also appears in literature, but often raises confusion. In some cases it is used to refer to the same decoupling techniques as treated here. The original meaning however concerns the identification of the structural properties in the presence of flexible mounts (e.g. A and B in an assembly $A - k - B$), yet without knowledge of one of the substructures' dynamics. For such techniques and applications (many of which relating to the automotive industry), see [116, 224, 225, 240, 241]. Finally, a mobility-based method equivalent to decoupling has been found in [83].

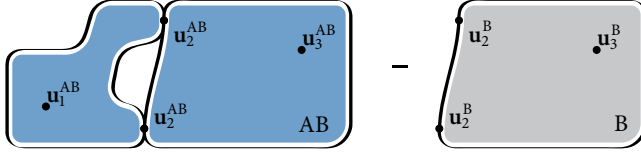


Figure 3.2: Decoupling of substructure B from the assembly AB.

substructures A and B using Eq. (3.12):

$$\mathbf{Z}^{AB} \triangleq \begin{bmatrix} \mathbf{Z}_{11}^{AB} & \mathbf{Z}_{12}^{AB} & \mathbf{Z}_{13}^{AB} \\ \mathbf{Z}_{21}^{AB} & \mathbf{Z}_{22}^{AB} & \mathbf{Z}_{23}^{AB} \\ \mathbf{Z}_{31}^{AB} & \mathbf{Z}_{32}^{AB} & \mathbf{Z}_{33}^{AB} \end{bmatrix} = \begin{bmatrix} \mathbf{Z}_{11}^A & \mathbf{Z}_{12}^A & \mathbf{0} \\ \mathbf{Z}_{21}^A & \mathbf{Z}_{22}^A + \mathbf{Z}_{22}^B & \mathbf{Z}_{23}^B \\ \mathbf{0} & \mathbf{Z}_{32}^B & \mathbf{Z}_{33}^B \end{bmatrix}$$

Note that most of the impedance terms are in fact a sole property of one of the substructures; interaction only occurs at the connecting DoFs. Hence, to obtain the impedance of substructure A from AB and B, the following trivial subtraction operation suffices:

$$\begin{bmatrix} \mathbf{Z}_{11}^A & \mathbf{Z}_{12}^A & \mathbf{0} \\ \mathbf{Z}_{21}^A & \mathbf{Z}_{22}^A + \mathbf{Z}_{22}^B & \mathbf{Z}_{23}^B \\ \mathbf{0} & \mathbf{Z}_{32}^B & \mathbf{Z}_{33}^B \end{bmatrix} - \begin{bmatrix} \mathbf{0} & \mathbf{0} & \mathbf{0} \\ \mathbf{0} & \mathbf{Z}_{22}^B & \mathbf{Z}_{23}^B \\ \mathbf{0} & \mathbf{Z}_{32}^B & \mathbf{Z}_{33}^B \end{bmatrix} = \begin{bmatrix} \mathbf{Z}_{11}^A & \mathbf{Z}_{12}^A & \mathbf{0} \\ \mathbf{Z}_{21}^A & \mathbf{Z}_{22}^A & \mathbf{0} \\ \mathbf{0} & \mathbf{0} & \mathbf{0} \end{bmatrix}$$

Let us generalise this by writing the impedances \mathbf{Z}^{AB} and \mathbf{Z}^B in block-diagonal form and defining an appropriate Boolean localisation matrix. The impedance of B needs to be supplied with a minus-sign to account for the subtraction operation:

$$\mathbf{Z} \triangleq \begin{bmatrix} \mathbf{Z}^{AB} & \mathbf{0} \\ \mathbf{0} & -\mathbf{Z}^B \end{bmatrix} = \begin{bmatrix} \mathbf{Z}_{11}^{AB} & \mathbf{Z}_{12}^{AB} & \mathbf{Z}_{13}^{AB} & \mathbf{0} & \mathbf{0} \\ \mathbf{Z}_{21}^{AB} & \mathbf{Z}_{22}^{AB} & \mathbf{Z}_{23}^{AB} & \mathbf{0} & \mathbf{0} \\ \mathbf{Z}_{31}^{AB} & \mathbf{Z}_{32}^{AB} & \mathbf{Z}_{33}^{AB} & \mathbf{0} & \mathbf{0} \\ \mathbf{0} & \mathbf{0} & \mathbf{0} & -\mathbf{Z}_{22}^B & -\mathbf{Z}_{23}^B \\ \mathbf{0} & \mathbf{0} & \mathbf{0} & -\mathbf{Z}_{32}^B & -\mathbf{Z}_{33}^B \end{bmatrix}; \quad \mathbf{L} \triangleq \begin{bmatrix} \mathbf{I} & \mathbf{0} & \mathbf{0} \\ \mathbf{0} & \mathbf{I} & \mathbf{0} \\ \mathbf{0} & \mathbf{0} & \mathbf{I} \\ \mathbf{0} & \mathbf{I} & \mathbf{0} \\ \mathbf{0} & \mathbf{0} & \mathbf{I} \end{bmatrix}$$

It can be verified that the required decoupling is performed by application of the same equation as used for the primal coupling, namely (3.12):

$$\hat{\mathbf{Z}} = \mathbf{L}^T \mathbf{Z} \mathbf{L}$$

Hence, the primal disassembly can be understood as the assembly of structure AB with the *negative impedance of substructure B*, with respect to the DoFs that appear in both structures. A requirement is that all DoFs of the substructure to decouple are exactly represented in the assembled situation, such that the excess impedance of B can indeed be subtracted from AB. This shall not pose limitations if the matrices are obtained from numerical modelling, but can be troublesome in the experimental practice. Again a dual approach offers more flexibility for decoupling of experimental substructures, which is discussed next.

3.4.2 Dual disassembly

The dual disassembly method approaches the decoupling problem from the admittance of the assembled system AB — which is assumed to be known — and the hypothetical

presence of a substructure B that needs to be decoupled. It was seen that process of primal disassembly is effectively equal to primal assembly with the negative admittance of the residual substructure. In a dual formulation, this translates to finding interface forces that ensure coordinate compatibility, but act in *opposite direction* on system AB. Hence these forces remove the influence of B on AB, leaving one with the uncoupled response of A².

As a start, the equations of motion can be written for the assembled system AB and substructure B. Observe the minus sign for the interface forces in the second equation:

$$\begin{cases} \mathbf{u}^{AB} = \mathbf{Y}^{AB}\mathbf{f}^{AB} + \mathbf{Y}^{AB}\mathbf{g}^{AB} \\ \mathbf{u}^B = -\mathbf{Y}^B\mathbf{g}^B \end{cases} \quad (3.29)$$

The aim is now to write the dynamics of both systems in one equation, yet to remain compatible with the LM-FBS assembly notation. The following matrix definitions are therefore introduced for this example:

$$\mathbf{Y} \triangleq \begin{bmatrix} \mathbf{Y}_{11}^{AB} & \mathbf{Y}_{12}^{AB} & \mathbf{Y}_{13}^{AB} & \mathbf{0} & \mathbf{0} \\ \mathbf{Y}_{21}^{AB} & \mathbf{Y}_{22}^{AB} & \mathbf{Y}_{23}^{AB} & \mathbf{0} & \mathbf{0} \\ \mathbf{Y}_{31}^{AB} & \mathbf{Y}_{32}^{AB} & \mathbf{Y}_{33}^{AB} & \mathbf{0} & \mathbf{0} \\ \mathbf{0} & \mathbf{0} & \mathbf{0} & -\mathbf{Y}_{22}^B & -\mathbf{Y}_{23}^B \\ \mathbf{0} & \mathbf{0} & \mathbf{0} & -\mathbf{Y}_{32}^B & -\mathbf{Y}_{33}^B \end{bmatrix}; \quad \mathbf{u} \triangleq \begin{bmatrix} \mathbf{u}_1^{AB} \\ \mathbf{u}_2^{AB} \\ \mathbf{u}_3^{AB} \\ \mathbf{u}_2^B \\ \mathbf{u}_3^B \end{bmatrix}; \quad \mathbf{f} \triangleq \begin{bmatrix} \mathbf{f}_1^{AB} \\ \mathbf{f}_2^{AB} \\ \mathbf{0} \\ \mathbf{0} \\ \mathbf{0} \end{bmatrix}; \quad \mathbf{g} \triangleq \begin{bmatrix} \mathbf{0} \\ \mathbf{g}_2^{AB} \\ \mathbf{0} \\ \mathbf{g}_2^B \\ \mathbf{0} \end{bmatrix}$$

The compatibility matrix for this disassembly is constructed similar as for any assembly task, namely with plus and minus identities that sum up to zero for each row:

$$\mathbf{B} \triangleq \begin{bmatrix} \mathbf{0} & -\mathbf{I} & \mathbf{0} & \mathbf{I} & \mathbf{0} \end{bmatrix}$$

Note that applied forces \mathbf{f} only need to be defined for the DoFs of substructure A in AB, because all DoFs pertaining to B will ultimately be removed from the system. Furthermore, interface forces appear for the respective interface DoFs of the two systems with the same sign. The minus-sign in the second line of Eq. (3.29) is accounted for in the global admittance matrix \mathbf{Y} , because the admittance of B is added negatively. This allows to write the following system, which is in fact a repetition of the dual assembly equation (3.20):

$$\begin{cases} \mathbf{u} = \mathbf{Y}(\mathbf{f} + \mathbf{g}) = \mathbf{Y}(\mathbf{f} - \mathbf{B}^T\boldsymbol{\lambda}) \\ \mathbf{B}\mathbf{u} = \mathbf{0} \end{cases} \quad (3.30)$$

Without further development of the equations, we can thus conclude that the LM-FBS equation of Eq. (3.23) as used for coupling is equally applicable for substructure decoupling. The only difference lies in the definition of the global admittance matrix, which accepts negative admittances for the substructures to decouple:

$$\mathbf{Y} \triangleq \begin{bmatrix} \mathbf{Y}^A & \mathbf{0} \\ \mathbf{0} & \mathbf{Y}^B \end{bmatrix} \quad \text{for coupling of } A + B = AB, \quad (3.31a)$$

or

$$\mathbf{Y} \triangleq \begin{bmatrix} \mathbf{Y}^{AB} & \mathbf{0} \\ \mathbf{0} & -\mathbf{Y}^B \end{bmatrix} \quad \text{for decoupling of } AB - B = A. \quad (3.31b)$$

²This is more thoroughly discussed in [220].

Each one of these block-diagonal admittance definitions can be fed into the LM-FBS algorithm of Eq. (3.26), that returns the dually (dis)assembled admittance \tilde{Y} . Note that the compatibility matrix is defined in a straightforward fashion regardless the operation. If preferred, one could however define the localisation matrix \mathbf{L} and obtain \mathbf{B} from Eq. (3.5).

► *A side-note on dual disassembly*

In the example above, the residual subsystem admittance \mathbf{Y}^B comprises FRFs for the interface DoFs \mathbf{u}_2 and some DoFs \mathbf{u}_3 internal to B. After decoupling, one ends up with a dually disassembled matrix for the coordinate space of \mathbf{u} as defined above, which contains a lot of redundant information. On one hand, the internal DoFs \mathbf{u}_3 are nowhere involved in the decoupling process. As we wish to retain just the DoFs in the domain of substructure A, i.e. the first two rows and columns of \mathbf{Y} , all references to \mathbf{u}_3 can be swept from the disassembled admittance matrix.

On the other hand, one may wonder how the FRFs associated with the resulting “dual” pairs $(\mathbf{u}_2^{AB}, \mathbf{u}_2^B)$ and $(\mathbf{u}_3^{AB}, \mathbf{u}_3^B)$ interrelate. As a consequence of the LM-FBS equation and the definition of \mathbf{B} , the entries on the rows and columns of \mathbf{u}_2^{AB} and \mathbf{u}_2^B are an exact match. This is indeed the result of requiring strong compatibility and equilibrium on the interface DoFs \mathbf{u}_2 . In the absence of errors, the associated FRFs can be shown to be exactly \mathbf{Y}_{22}^A , i.e. the desired interface admittance of substructure A.

However, the two rows and columns for \mathbf{u}_3 are not clearly defined and it is doubtful whether they are of any use. Presumably, they would be equal if the FRFs of the structures involved are free of noise. This would imply that, although compatibility is not explicitly required on these DoFs, they are in fact compatible due to the equilibrium forces acting on \mathbf{u}_2 . If this were true, one could also imagine a set of interface forces that is “extended” to these internal DoFs, i.e. \mathbf{g}_3 , assisting in establishing compatibility on some set of DoFs that are shared between AB and B.

Any further thoughts here may appear speculative without mathematical proof, but are in fact a result of considering the *observability* (by some coordinates \mathbf{u}) and *controllability* (by forces \mathbf{g}) of the vibrations that occur at the substructure’s interfaces. The important concepts of observability and controllability in structural dynamics are thoroughly discussed in Part II of this thesis. With regard to substructure decoupling, they are employed to set up alternative interface conditions that may improve performance when dealing with experimental FRFs. The concepts as presented next are a selection of ideas obtained from the (ongoing) research of D’Ambrogio and Fregolent [41] and the decoupling framework of Voormeeren and Rixen [220]. ◀

3.4.3 Decoupling with alternative interface definitions

The general LM-FBS definition of Eq. (3.25) provides means to specify two distinct signed Boolean matrices, namely \mathbf{B}_c for coordinate compatibility and \mathbf{B}_e for interface force equilibrium. This is useful in substructure coupling to ensure that the coordinates of the interface (matrix rows) match with the forces (matrix columns), which is often needed if the FRF matrices are obtained by measurement. Still, the matrices function just as “bookkeepers” to align all DoFs correctly.

For substructure decoupling, this mechanism offers an additional possibility, namely to

extend the interface by some internal DoFs \mathbf{u}_3 of the residual structure that appear equally in both FRF matrices. Although their corresponding decoupled FRFs may not be of interest at the end procedure, they may appear helpful to improve the conditioning of the decoupling process.

Interface ingredients

Let us assume that appropriate measurements have been conducted on AB and B to obtain FRFs for coordinates ($\mathbf{u}_2, \mathbf{u}_3$) and forces ($\mathbf{g}_2, \mathbf{g}_3$). Logically, with these sets of DoFs, one could imagine a total of nine different decoupling variants. For instance, the options for coordinate compatibility are:

1. *Standard interface*: the standard set of n_2 interface DoFs \mathbf{u}_2 is used. The compatibility matrix reads:

$$\mathbf{B}_c \triangleq \begin{bmatrix} \mathbf{0} & -\mathbf{I} & \mathbf{0} & \mathbf{I} & \mathbf{0} \end{bmatrix}$$

2. *Extended interface*: The interface \mathbf{u}_2 is extended by n_3 internal DoFs \mathbf{u}_3 , requiring compatibility for a total of $n_2 + n_3$ DoFs. The compatibility matrix reads:

$$\mathbf{B}_c \triangleq \begin{bmatrix} \mathbf{0} & -\mathbf{I} & \mathbf{0} & \mathbf{I} & \mathbf{0} \\ \mathbf{0} & \mathbf{0} & -\mathbf{I} & \mathbf{0} & \mathbf{I} \end{bmatrix}$$

3. *Internal*: the interface DoFs \mathbf{u}_2 are not used/measured but instead compatibility is required at n_3 internal DoFs \mathbf{u}_3 . The compatibility matrix reads:

$$\mathbf{B}_c \triangleq \begin{bmatrix} \mathbf{0} & \mathbf{0} & -\mathbf{I} & \mathbf{0} & \mathbf{I} \end{bmatrix}$$

A similar reasoning holds for the three variants of \mathbf{B}_e for force equilibrium, bringing the number of possible combinations to nine. Of these nine however, only a few combinations are effective in practice. To discuss this, let us denote by n_c the total number of coordinate compatibility equations, i.e. the number of rows in \mathbf{B}_c , and by n_e the number of rows in the equilibrium matrix \mathbf{B}_e . We assume that, in the assembled structure AB, the physical interaction between A and B is constituted by no more than n_2 DoFs. In other words, structure AB could have been the result of coupling of A and B with n_2 interface DoFs.

Decoupling strategies

As stated before, the success of LM-FBS (dis)assembly is largely subject to the conditioning of the terms to be inverted, given by $\mathbf{Y}^{\text{int}} \triangleq \mathbf{B}_c \mathbf{Y} \mathbf{B}_e^T$. According to the definitions above, this is an matrix of $n_c \times n_e$ FRF functions. In light of this interface admittance, let us discuss the following decoupling approaches:

1. *Standard interface*: $n_c = n_e = n_2$. The interface admittance is a square matrix and is of full rank. Strong compatibility and equilibrium is thus required on the interface DoFs.
2. *Extended interface*: $n_c = n_e > n_2$. The interface admittance is a square matrix with $n_2 + n_3$ singular values. In the absence of noise, the matrix is singular because the number of singular values is larger than the number of actual interface “modes” present in the system. In the presence of noise, the matrix is probably invertible but

badly conditioned. A singular value decomposition should thus be performed to find the number of significant modes in \mathbf{Y}^{int} and perform a truncated inversion.

3. *Non-collocated overdetermined*: $n_c = n_2 + n_3$; $n_e = n_2$. The interface admittance is a non-square overdetermined matrix, meaning that the solution can be found in a least-square sense: $(\mathbf{Y}^{\text{int}})^+$. Hence the number of singular values is n_2 , but the Lagrange multipliers (and thereby the interface forces \mathbf{g}_2) are sought in such a way that the norm of the compatibility error is minimised:

$$\lambda = \underset{\lambda}{\operatorname{argmin}} \|\mathbf{B}_c \mathbf{u}\| \quad \lambda \in \mathbb{R}^{n_e}$$

This proves to be an effective method in practice [45, 186, 220], provided that the positions of the sensors on test structures AB and B are replicated very accurately.

4. *Non-collocated internal*: $n_c = n_2$; $n_e = n_3$. The interface is fully instrumented to obtain \mathbf{u}_2 but the excitation points \mathbf{g}_3 are somewhat away from the interface. This may be a practical approach when the interfaces of AB are not accessible for excitation. It is required to overdetermine the problem, by exciting sufficient points that ensure $n_3 > n_2$. Note that the solution is not unique, like the previous case, but now the forces are found as the minimal-quadratic set to realise $\mathbf{B}_c \mathbf{u} = \mathbf{0}$. A crucial requirement is to have full controllability of the interface from the chosen excitation points \mathbf{g}_3 .

This overview can be used as a guideline for decoupling; however, the relative success of one method or another remains strongly case-specific. Sec. 8.5 presents an application of coupling and decoupling techniques and briefly touches on some advanced strategies and alternative methods in this field.

3.5 Summary

In this chapter the basic tools have been outlined for dynamic substructuring. It has been shown that substructuring is not a single method on its own, but can in fact be applied to a large range of domains, as long as the interface dynamics of a structure can be clearly described. One can then implement the two principal conditions of substructuring, being displacement compatibility and force equilibrium on the coordinates that constitute the interfaces between two substructures.

For the assembly of substructures, a primal and a dual approach have been discussed. The primal approach relates to impedance addition as seen in FE assembly: it literally assembles the substructures by mapping the matching DoFs to the same coordinate in a unique set of DoFs. From here on, matrix inversion and coordinate expansion may provide access to a force response solution in the full coordinate space.

The approach of dual assembly finds a coupled solution in the same coordinate space as the unassembled system. To do so, additional Lagrange multipliers are introduced that represent the magnitude of the connecting forces. These forces, applied to the interfaces of the separate substructures, render the interface DoFs compatible. The dual approach employs subsystem admittances rather than impedances and is therefore a popular choice in the field of experimental substructuring. The frequency-domain variant, commonly known as Lagrange multiplier frequency-based substructuring or LM-FBS in short, is shown to be a highly versatile algorithm.

Besides assembly of component models, similar procedures can be employed to disassemble or decouple residual substructures from a system. Decoupling can be performed in a primal and dual fashion, highly analogue to the coupling procedures. The dual approach offers additional control over the conditioning of the problem by extending the decoupling conditions to points beyond the physical interface. The advantages herein are mostly of practical nature: it allows (for instance) to substitute the interface forces by an overdetermined set of forces somewhat remote from the interface, easier accessible for measurement.

Dynamic substructuring can thus be contemplated as a collection of assembly and disassembly tools, performing similar tasks as an FE model assembler. It applies to any modelling domain that has a clear definition of input-output relations between the terminals. In the particular case of frequency-based substructuring, the assembly equations can be performed per frequency and the steps of dynamic substructuring reduce to simple linear matrix operations.

More than just a modelling tool, substructuring allows to look into the chain of vibration transmission from one point to another and understand how substructures interact. This is a crucial advantage in transfer path analysis as discussed in Part II of this thesis.

4

Obtaining dynamic models by experiment

chapter contents:

4.1 Introduction	45
4.1.1 Interface modelling	46
4.1.2 Discrete interface modelling	47
4.1.3 Towards collocated virtual point dynamics	48
4.2 Virtual point transformation	49
4.2.1 Interface displacement reduction	50
4.2.2 Interface force reduction	51
4.2.3 Virtual point assembly	52
4.2.4 Virtual point coupling vs. virtual point FRFs	54
4.3 Interface displacement modes	55
4.3.1 Displacement IDM	55
4.3.2 Force IDM	57
4.4 Measurement quality indicators	58
4.4.1 Sensor consistency	58
4.4.2 Impact consistency	59
4.4.3 Virtual point reciprocity & passivity	60
4.5 Instrumentation in practice	61
4.5.1 Sensor placement	61
4.5.2 Excitation positions	62
4.6 Example	63
4.6.1 Modelling of a simple beam	64
4.6.2 Inspection of measured FRFs	65
4.6.3 Transformation to virtual point FRFs	66
4.7 Summary	67

4.1 Introduction

Whenever consigned with the task of numerical modelling of a substructure, one would probably devote as much attention to modelling of the internal features as to the connection points. This is based on the righteous assumption that, for correct modelling of a numerical structure, every feature matters: all mass, damping and stiffness in the structure contribute to the global dynamics. Indeed, a numerical model is inherently impedance-based: one cannot solely model the impedance at the interface DoFs in order to portray the dynamics

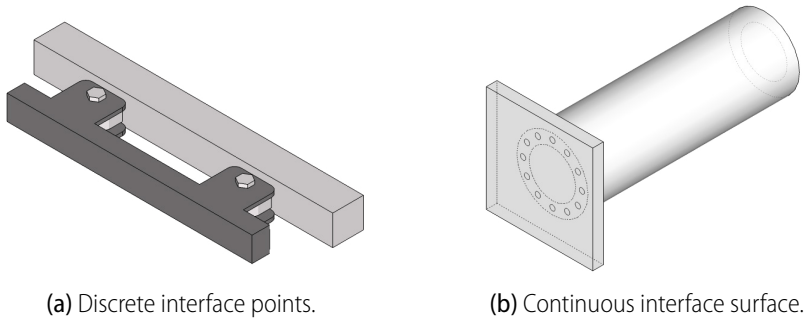


Figure 4.1: Two examples of substructure connectivity.

of the structure in its entirety¹.

In contrast, experimental modelling mostly concentrates on describing the dynamics at the interfaces; the internal points are of minor interest. The standard practice of admittance measurement yields independent observations of the global dynamics on the points of measurement, e.g. in the form of admittance FRFs. The effects of the internal dynamics are already incorporated in these functions. Hence, for implementation of the model in a dynamic simulation (think of dynamic substructuring or TPA), measurement is required only on the points that interact in some way. These points can function as an output (response point of interest), input (as a terminal for external excitation) or both (for the purpose of substructuring, for instance). A certain level of component abstraction is thus tolerated, allowing us to contemplate complex dynamical systems as simple potato-shaped structures — so dearly beloved by academic dynamicists — with just a limited number of input/output terminals.

Interaction with other substructures can be correctly established if the dynamics are properly described at these connecting terminals. The word “properly” is yet undefined here, and it shall be the aim of this chapter to investigate what this implies. In particular, the experimental procedures will be looked upon from the perspective and requirements of substructure assembly. A nodal model, obtained by experiment, is considered the end result of applying these procedures.

4.1.1 Interface modelling

Dynamic substructuring requires that compatibility is satisfied between the displacement of the interfaces of two components, and that the interconnecting forces are in equilibrium. This is easily established for a discrete dynamical system using the coupling equations as outlined in Chap. 3, namely by imposing the two conditions described in Sec. 3.2 on the respective coupling nodes of the substructures. In practice however, components are often connected by bolts, welds or adhesives, that physically show more resemblance to a line or surface connection than to a single point. Modelling such connectivity by experimental measurements requires more thoughtful contemplation of what is really going on at the interfaces between two structures.

¹In fact, one would need to condense the internal dynamics onto the nodes that are appointed as interface nodes, creating a super-element; see Sec. 2.4.2.

In general, one can distinguish two categories of connectivity between substructures, of which one is normally the most appropriate for a given case:

1. The components are connected at a handful of points, that can be regarded as discrete nodes (Fig. 4.1a). These points are permitted to displace with respect to each other, thereby allowing for significant deformations in the structures. The connection points themselves however behave fairly rigid in the area near the interfaces. Deformations in the connecting points are of minor order and not contributing to the coupled vibrations. Examples are truss structures in bridges and a steering system mounted in a vehicle subframe.
2. The interface resembles a continuous line or surface (Fig. 4.1b). The deformation of the interface is strongly coupled to the internal vibrations of the structure, and can therefore not be discretised to a small number of nodes. Examples include the coupling of a gearbox to an engine, glued carbon-fiber panels of a vehicle's bodywork and the partitions of an aircraft's fuselage.

4.1.2 Discrete interface modelling

Let us consider a single bolted connection as illustrated in Fig. 4.2. The pretension in the bolt causes friction to occur at the interfaces, which prohibits the two structures to have relative motion with respect to each other. If both structures were represented by an FE model, the substructuring task amounts to coupling the displacements and interface forces of the coinciding nodes, as illustrated in Fig. 4.2b. By coupling a sufficient number of nodes over a larger area, any rotational coupling is implicitly accounted for.

Let us now consider the procedure of experimental modelling. An admittance measurement needs to be conducted on each substructure in order to obtain the respective FRF matrices. To facilitate substructure coupling, the simplest way would be to mount a single tri-axial accelerometer on the connection point of each substructure and excite in X, Y and Z direction close to the sensor. This yields a 3-DoF description which is sometimes called a single-point connection (SPC). In this way, one obtains a 3×3 FRF matrix for the substructure's interfaces, which can be used for substructure coupling.

The SPC method does not account for rotational coupling, which is known to be essential in many cases of substructuring [117, 131]. Measurement and excitation (or in fact observation and controllability) of rotations has been an active topic of research amongst experimentalist and has led to several approaches:

1. *Direct measurement.* Rotation sensors and transducers can be thought of, but have not been the practical standard over the past. Some examples of unconventional hardware for rotation measurement or excitation can be found in [13, 115, 150].
2. *Modal expansion.* If modal information of the structure is available, for instance from static FEM analysis, rotations can be obtained from extrapolation of the measured data. This is the concept of the system equivalent reduction and expansion process (SEREP) [143].
3. *Finite differences.* Rotations can be approximated from translations measured at known distances from each other [29, 47]. Simple finite difference approaches such as $\theta = (u_0 - u_d)/d$ may suffice for simple plate or beam problems [51, 176], but can be cumbersome for obtaining full 6-DoF kinematics.

4. *Multiple translations.* The equivalent multi-point connection (EMPC) method [106, 147] accounts for the rotations *implicitly*, by coupling translational FRFs of multiple points in the proximity of the interface. This is illustrated by Fig. 4.2c. In practice, a minimum of 3 tri-axial accelerometers (not in line) is sufficient to couple all translational and rotational directions², introducing a total of 9 DoFs per coupling point. However, this condition can be too stringent: if the structure between the 3 connections point is very stiff, any discrepancy in motion (due to measurement errors) will be overcompensated for in the coupling equations. This unwanted “stiffening” of the interface results in spurious peaks in the coupled FRFs [169].
5. *IDM filtering.* By defining 6 rigid interface displacement modes³ (IDMs) per connection point and projecting the 9-DoF (or more) admittance matrix onto this subspace, one only retains the dynamics that load the interface area in a rigid manner [80, 106]. If substructuring is now performed with this “filtered” receptance, one only imposes compatibility and equilibrium on the motion of those 9 or more DoFs that obey local rigid behaviour, while the residual flexible motion is left uncoupled. The interface problem is thereby “weakened” and, due to the least-square reduction step, measurement errors are averaged out.

A common problem of abovementioned methods is the practical difficulty to collocate applied forces with measured displacements/accelerations. Indeed, one can never excite exactly at the point where a sensor is located, which is required to measure a true “driving-point” FRF. This already poses a problem for the class of academic structures, as reported for instance in [78, 138–140], making real-life structures even more formidable. In addition, it is difficult to define measurement points in such way that they appear identically on both structures *and* can be measured and excited in all required directions.

Concluding, it seems justified to not question if, but rather how much uncertainty is introduced in the experimental determination of substructure FRFs [6, 56, 107]. One assurance is that the effects of experimental errors become more apparent at higher frequencies⁴. Hence, it stands to reason to first “massage” the raw FRF data of a measurement into a format that is better suited for substructuring.

4.1.3 Towards collocated virtual point dynamics

Let us look at the previously discussed IDM filtering method from a modal reduction point of view. By defining the IDMs for a single connection point, one confines the dynamics to 6-DoF-per-node kinematics instead of the 9 or more DoFs of the measured FRFs (rows of the matrix). In particular, if the IDMs are defined to represent the 3 translations (X , Y , Z) and 3 rotations (θ_X , θ_Y , θ_Z) with respect to a single point in a global coordinate system, this kinematic description is similar to a node in an FE model. In that case, the IDMs can be used to transform the measured translational displacements to 6-DoF motion of a single point. A similar approach can be followed to extract concentrated 6-DoF forces and moments from the excitation forces of the FRF measurement (columns of the matrix).

The concept is illustrated by Fig. 4.2d. The resulting 6×6 FRF matrices describe the dy-

²This is a similar reasoning as a chair being stable on three legs.

³The original definition of IDM is interface *deformation* mode [106]. However, as we are primarily interested in the modes for which the interface behaves rigid, the wording interface *displacement* seems more appropriate.

⁴This applies to most sources of errors. An example of a frequency-independent error is an offset in sensor sensitivity due to bad calibration.

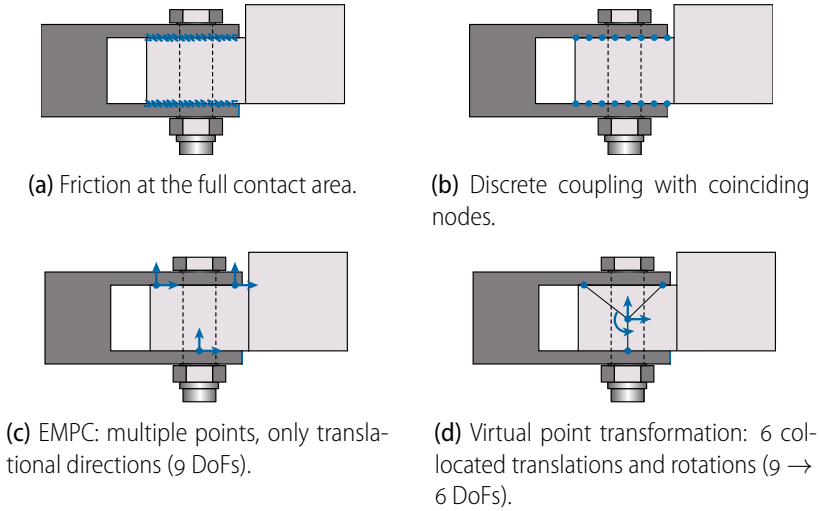


Figure 4.2: A bolted connection: four ways to consider the interface problem.

dynamic responses of so-called *virtual point motion* to *virtual point loads*, or in other words the admittance of an interface concentrated in a *virtual point*. The point is said to be virtual, because no actual measurements need to be performed on the point itself. In fact, it can be chosen anywhere in the proximity of the interface, allowing to locate the virtual points *identically* for two substructures to couple.

Interesting is now how to set up an experiment that leads to a complete and reciprocal 6×6 virtual point FRF matrix, including proper driving-point admittance on the diagonal. The next two sections propose a methodology to achieve this, based on [106, 184]. Sec. 4.4 introduces useful quality assurance criteria and Sec. 4.5 addresses practicalities such as sensor placement and impact locations. The complete methodology is demonstrated in Sec. 4.6 based on a simulated measurement.

4.2 Virtual point transformation

For the derivation of the virtual point transformation, let us consider the coupling problem of two experimental substructures A and B as illustrated in Fig. 4.3. The substructures have non-collocated interface DoFs by nature: neither sensors nor excitation points appear identically. The measured FRF matrices are denoted by $\mathbf{Y}^A(\omega)$ and $\mathbf{Y}^B(\omega)$. The governing equation of the uncoupled dynamics is of the admittance FRF form:

$$\mathbf{u} = \mathbf{Y}(\mathbf{f} + \mathbf{g}) \quad (4.1)$$

We shall concentrate on the interface DoFs, respectively denoted by \mathbf{Y}_{22}^A and \mathbf{Y}_{22}^B . As the interface DoFs are non-collocated, they can not be equated directly by definition of a Boolean matrix. In other words, there is no direct relation between $\mathbf{u}_2^A \Leftrightarrow \mathbf{u}_2^B$ and $\mathbf{g}_2^A \Leftrightarrow \mathbf{g}_2^B$. In what follows, the assumption is used that the structures behave rigidly in the area close to the coupling point. The derivation focuses on the interface DoFs of a single substructure, denoted for simplicity by $\mathbf{u} \in \mathbb{R}^n$.

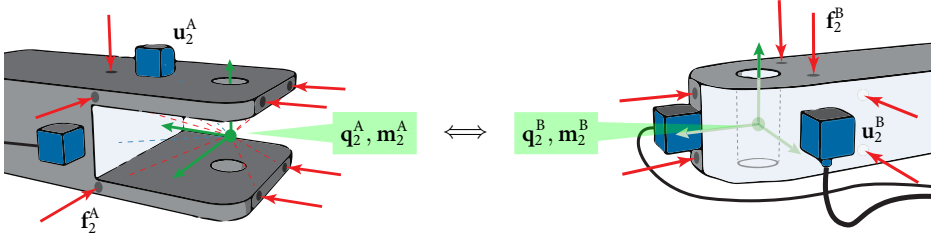


Figure 4.3: The virtual point transformation workflow for coupling of substructure A (left) and B (right). Both substructures are instrumented by acceleration sensors (blue). The excitations of the FRF measurements are depicted by red arrows.

4.2.1 Interface displacement reduction

Let us express the n interface displacements \mathbf{u} by $m < n$ interface deformation modes (IDMs) \mathbf{q} . The IDMs are contained in the columns of the $n \times m$ matrix \mathbf{R} , which is a frequency-independent mode shape matrix (the actual construction of the IDMs is discussed in Sec. 4.3). As the number of IDMs is smaller than the number of interface DoFs, a residual on the displacements is added, denoted by $\boldsymbol{\mu}$. This residual captures all displacements not in the subspace of the IDMs, which is normally the “flexible” motion.

$$\mathbf{u} = \mathbf{R}\mathbf{q} + \boldsymbol{\mu} \quad \mathbf{q} \in \mathbb{R}^m \quad (4.2)$$

To find \mathbf{q} in a minimal-quadratic sense, one could apply the standard Moore-Penrose pseudo-inverse of \mathbf{R} , minimising the norm of the residuals on the displacements and enforce $\mathbf{R}^T\boldsymbol{\mu} = \mathbf{0}$. To gain more flexibility, we introduce a symmetric weighting matrix \mathbf{W} acting on the measured set of DoFs. The residual displacement shall then satisfy:

$$\mathbf{R}^T\mathbf{W}\boldsymbol{\mu} = \mathbf{0} \quad \mathbf{W} \in \mathbb{R}^{n \times n} \quad (4.3)$$

The coordinate transformation $\mathbf{u} \rightarrow \mathbf{q}$ follows from standard application of a weighted least-square procedure, namely by pre-multiplying Eq. (4.2) by $\mathbf{R}^T\mathbf{W}$ and solving for \mathbf{q} . In addition to the IDM coordinates \mathbf{q} , the “filtered” displacement can be retrieved by substituting \mathbf{q} back into Eq. (4.2). The resulting displacement is denoted by $\tilde{\mathbf{u}}$. The residual, finally, is simply the remainder of \mathbf{u} minus $\tilde{\mathbf{u}}$:

$$\begin{cases} \mathbf{q} = (\mathbf{R}^T\mathbf{W}\mathbf{R})^{-1}\mathbf{R}^T\mathbf{W}\mathbf{u} & (4.4a) \end{cases}$$

$$\begin{cases} \tilde{\mathbf{u}} = \mathbf{R}(\mathbf{R}^T\mathbf{W}\mathbf{R})^{-1}\mathbf{R}^T\mathbf{W}\mathbf{u} & (4.4b) \end{cases}$$

$$\begin{cases} \boldsymbol{\mu} = [\mathbf{I} - \mathbf{R}(\mathbf{R}^T\mathbf{W}\mathbf{R})^{-1}\mathbf{R}^T\mathbf{W}]\mathbf{u} & (4.4c) \end{cases}$$

To simplify notation, let us introduce the following two substitutions:

$$\begin{cases} \mathbf{q} = \mathbf{T}\mathbf{u} & \text{with } \mathbf{T} \triangleq (\mathbf{R}^T\mathbf{W}\mathbf{R})^{-1}\mathbf{R}^T\mathbf{W} & (4.5a) \end{cases}$$

$$\begin{cases} \tilde{\mathbf{u}} = \mathbf{F}\mathbf{u} & \text{with } \mathbf{F} \triangleq \mathbf{R}\mathbf{T} & (4.5b) \end{cases}$$

$$\begin{cases} \boldsymbol{\mu} = (\mathbf{I} - \mathbf{F})\mathbf{u} & (4.5c) \end{cases}$$

Matrix \mathbf{T} is the essential operator of the virtual point transformation. It performs a linear combination of the n measured DoFs so that m virtual point coordinates are retained. A

minimum condition for the existence of \mathbf{T} is to have an IDM matrix of rank m , which can theoretically be realised by $n = m$ displacement DoFs. This implies in practice that the physical DoFs \mathbf{u} are located and orientated properly to describe all m modes independently⁵. As a consequence, $\boldsymbol{\mu} = \mathbf{0}$ and $\tilde{\mathbf{u}} = \mathbf{u}$, meaning that no filtering is applied.

Any $n > m$ implies that modal filtering is performed on the displacement space, which means that the residual $\boldsymbol{\mu}$ may become non-zero. The filtered displacement $\mathbf{u} \rightarrow \tilde{\mathbf{u}}$ can be obtained directly using the $n \times n$ filter matrix \mathbf{F} defined by Eq. (4.5b), which differs from identity if $n > m$. The virtual point transformation procedure becomes a least-square fit that minimises the weighted error in the residuals:

$$\mathbf{q} = \underset{\mathbf{q} \in \mathbb{R}^m}{\operatorname{argmin}} (\boldsymbol{\mu}^T \mathbf{W} \boldsymbol{\mu}) \quad (4.6)$$

If \mathbf{W} is chosen to be identity, the standard pseudo-inverse is found, which leads to a minimisation of the quadratic residuals of the displacements. In general, if \mathbf{W} is a diagonal matrix, it assigns weighting to the individual displacements in the error minimisation. This provides control over the importance of a certain measured sensor DoF for the transformation, or allows to temporarily exclude a particular DoF by setting its weighting to zero. Alternatively, if \mathbf{W} is chosen to represent a (dynamic) stiffness matrix, one is nullifying some local residual energy. Finally it shall be noted that \mathbf{W} can be defined per frequency line, allowing to make different choices for the low, medium and high frequency range, for instance.

Most important is that the virtual point motion \mathbf{q} can be obtained from an overdetermined set of measured translations \mathbf{u} using an IDM matrix \mathbf{R} . The transformation employs a spatial reduction that does not require inversion of measurement data. Several properties can be assigned to the quality of the transformation, which is further elaborated in Sec. 4.5.

4.2.2 Interface force reduction

The reduction of interface forces follows a similar procedure, although in a reversed manner. Unlike displacements, forces are not uniquely defined by virtual point forces and moments \mathbf{m} (from here on simply called virtual loads). In fact, the other way around is true.

► To exemplify this, consider a rigid beam hinged around a point of rotation, i.e. the virtual point. If the beam rotates, every point on the beam has a displacement \mathbf{u} which can be uniquely determined from the rotation of the virtual point \mathbf{q} . In other words, $\mathbf{q} \rightarrow \mathbf{u}$ is a unique transformation, whereas \mathbf{q} can be determined/averaged from \mathbf{u} , provided that a sufficient amount of displacements is measured (two in case of a simple rotation).

Let us now consider a set of forces acting on the same beam. If a resultant moment \mathbf{m} is known in the virtual point, there is no unique transformation $\mathbf{m} \rightarrow \mathbf{f}$, as multiple combinations of forces exist that generate the same moment. However, one can always calculate a resultant moment \mathbf{m} in the virtual point due to the applied forces \mathbf{f} , if their locations and directions are known. ◀

⁵To determine a 6-DoF virtual point with just $n = 6$ translations, one should consider a triad of points and register for instance the directions XYZ, XY and Z, respectively.

Hence, the reduction of forces is performed inversely. A similar IDM matrix can be constructed, relating the measured forces to virtual point loads. This is again denoted by \mathbf{R} ; distinction with the displacement IDMs will be made later on. Note however that the matrix needs to be transposed in order to write the relation between m virtual loads and n (interface) forces⁶:

$$\mathbf{m} = \mathbf{R}^T \mathbf{f} \quad (4.7)$$

As m is typically smaller than n , Eq. (4.7) is underdetermined and the inversion shall take the form of a weighted right-inverse of \mathbf{R}^T . This inverse seeks for the minimum-quadratic set of forces that realises a given vector \mathbf{m} . In order to prioritise the elements in the force vector, a symmetric weighting matrix \mathbf{W} is again introduced:

$$\tilde{\mathbf{f}} = \mathbf{W} \mathbf{R} (\mathbf{R}^T \mathbf{W} \mathbf{R})^{-1} \mathbf{m} \quad (4.8)$$

The resulting set of forces $\tilde{\mathbf{f}}$ is automatically admissible, i.e. in the space of \mathbf{R} . Analogue to the displacements, let us introduce the following substitutions:

$$\left\{ \begin{array}{ll} \tilde{\mathbf{f}} = \mathbf{T}^T \mathbf{m} & \text{with } \mathbf{T}^T \triangleq \mathbf{W} \mathbf{R} (\mathbf{R}^T \mathbf{W} \mathbf{R})^{-1} \\ \tilde{\mathbf{f}} = \mathbf{F} \mathbf{f} & \text{with } \mathbf{F} \triangleq \mathbf{T}^T \mathbf{R}^T = \mathbf{R} \mathbf{T} \\ \mathbf{v} = (\mathbf{I} - \mathbf{F}) \mathbf{f} & \end{array} \right. \quad (4.9a)$$

$$\quad \quad \quad (4.9b)$$

$$\quad \quad \quad (4.9c)$$

Eq. (4.9b) and (4.9c) allow to calculate the IDM-filtered forces and residuals (here denoted by \mathbf{v}) in case that the forces are the input. For the virtual point transformation of admittance, these are normally not used.

4.2.3 Virtual point assembly

The interface reduction steps as derived above allow us to assemble only the part of the dynamics of substructure A and B that can be described by the subspaces of their respective IDMs. The remaining displacements and forces are left free. From here on, the transformation matrices for the displacements and forces are clearly denoted by \mathbf{T}_u and \mathbf{T}_f .

Let us now continue the assembly of Eq. (4.1) by coupling only the part of the displacements and forces that is admissible with respect to the IDMs. The following definitions are used:

$$\mathbf{u} = \begin{bmatrix} \mathbf{u}_2^A \\ \mathbf{u}_2^B \end{bmatrix}; \quad \mathbf{g} = \begin{bmatrix} \mathbf{g}_2^A \\ \mathbf{g}_2^B \end{bmatrix}; \quad \mathbf{Y} = \begin{bmatrix} \mathbf{Y}_{22}^A & \mathbf{0} \\ \mathbf{0} & \mathbf{Y}_{22}^B \end{bmatrix}$$

$$\mathbf{q} = \begin{bmatrix} \mathbf{q}_2^A \\ \mathbf{q}_2^B \end{bmatrix}; \quad \mathbf{m} = \begin{bmatrix} \mathbf{m}_2^A \\ \mathbf{m}_2^B \end{bmatrix}; \quad \mathbf{T}_u = \begin{bmatrix} \mathbf{T}_u^A & \mathbf{0} \\ \mathbf{0} & \mathbf{T}_u^B \end{bmatrix}; \quad \mathbf{T}_f = \begin{bmatrix} \mathbf{T}_f^A & \mathbf{0} \\ \mathbf{0} & \mathbf{T}_f^B \end{bmatrix}$$

The virtual point transformations of Eq. (4.5a) and Eq. (4.9a) are now used to write compatibility and equilibrium. Whereas the measured displacements $\mathbf{u}_2^A, \mathbf{u}_2^B$ are incompatible by nature, the virtual points are in fact compatible so it is permitted to require $\mathbf{q}_2^A = \mathbf{q}_2^B$. This means that the IDMs used to express the kinematics of substructure A and B are defined

⁶The calculation of \mathbf{m} in Eq. (4.7) shows resemblance with the modal participation factor calculated from a vector of applied forces; see Eq. (2.6) in Sec. 2.3.2 on modal reduction.

the same way, for instance: both describe 3 global-frame translations and 3 rotations with respect to a unique point in space, i.e. the virtual point. The virtual point DoFs are collocated and can thus be used to write compatibility and equilibrium.

The same holds for the virtual interface loads, allowing to write the following dual coupling equations:

$$\begin{cases} \mathbf{u} = \mathbf{Y}(\mathbf{f} + \mathbf{g}) = \mathbf{Y}(\mathbf{f} - \mathbf{T}_f^T \mathbf{B}^T \boldsymbol{\lambda}) \\ \mathbf{B} \mathbf{q} = \mathbf{B} \mathbf{T}_u \mathbf{u} = \mathbf{0} \end{cases} \quad \text{with} \quad \mathbf{B} \triangleq \begin{bmatrix} -\mathbf{I} & \mathbf{I} \end{bmatrix} \quad (4.10)$$

Lagrange multipliers are substituted for the virtual point interface forces of A and B, enforcing equilibrium on the (rigid) part of the forces in the subspace of the IDMs. Likewise, compatibility is enforced by the second equation onto the admissible displacements. The assembly procedure continues in a familiar LM-FBS fashion, namely by solving for $\boldsymbol{\lambda}$:

$$\begin{aligned} \mathbf{B} \mathbf{T}_u \mathbf{Y}(\mathbf{f} - \mathbf{T}_f^T \mathbf{B}^T \boldsymbol{\lambda}) &= \mathbf{0} \\ \mathbf{B} \mathbf{T}_u \mathbf{Y} \mathbf{f} &= \mathbf{B} \mathbf{T}_u \mathbf{Y} \mathbf{T}_f^T \mathbf{B}^T \boldsymbol{\lambda} \\ \boldsymbol{\lambda} &= (\mathbf{B} \mathbf{T}_u \mathbf{Y} \mathbf{T}_f^T \mathbf{B}^T)^{-1} \mathbf{B} \mathbf{T}_u \mathbf{Y} \mathbf{f} \end{aligned} \quad (4.11)$$

Now that the virtual point coupling forces are known, the full virtual-point coupled solution is found by substitution back into Eq. (4.10):

$$\mathbf{u} = \mathbf{Y} \mathbf{f} - \mathbf{Y} \mathbf{T}_f^T \mathbf{B}^T (\mathbf{B} \mathbf{T}_u \mathbf{Y} \mathbf{T}_f^T \mathbf{B}^T)^{-1} \mathbf{B} \mathbf{T}_u \mathbf{Y} \mathbf{f} \quad (4.12)$$

Let us now examine Eq. (4.12). At first sight, one recognises the same ingredients as for standard LM-FBS coupling, stated by Eq. (3.25). The response consists of an uncoupled response, i.e. the first term on the right-hand side, and a coupled response to the applied forces \mathbf{f} . The coupling, however, takes a “detour” through a total of four virtual point transformation matrices. To better comprehend this procedure, let us expand Eq. (4.12):

$$\mathbf{u} = \underbrace{\mathbf{Y} \mathbf{f}}_{\text{uncoupled response}} - \underbrace{\mathbf{Y} \mathbf{T}_f^T \mathbf{B}^T}_{\text{response to virt. point } \boldsymbol{\lambda}} \underbrace{(\mathbf{B} \mathbf{T}_u \mathbf{Y} \mathbf{T}_f^T \mathbf{B}^T)^{-1}}_{\substack{\text{virt. point} \\ \text{int. admittance}}} \underbrace{\mathbf{B} \mathbf{T}_u \mathbf{Y} \mathbf{f}}_{\substack{\text{incomp.} \\ \text{in } \mathbf{q}}}$$

Reading from right to left, we first recognise the incompatibility caused by the uncoupled responses. These are transformed to the virtual point space by the operator \mathbf{T}_u . Between the brackets, we observe the combined interface admittance. This is put in the virtual point space by pre- and post-multiplication of the measured FRFs by \mathbf{T}_u and \mathbf{T}_f^T . Hence, the term in the centre constitutes the *virtual point admittance* of the interface, which will be elaborated on later. The Boolean matrices on both sides of this term function as expected, namely to select and sum up the admittance at the interface DoFs in the virtual point space. Lastly, the term to the left of the inverted admittance governs the response to the virtual point interface forces that are in front of it. These forces are transformed back to the measured DoF-space by the operator \mathbf{T}_f^T .

4.2.4 Virtual point coupling vs. virtual point FRFs

Sec. 4.2.3 has demonstrated how interface FRFs, incompatible by the nature of experimental measurement, can be coupled by use of appropriate virtual point transformations. Having clarified all the terms in Eq. (4.12), let us now define two approaches to proceed.

Virtual point coupling

The coupling detour explained above can be simplified by grouping the respective pairs of \mathbf{B} and \mathbf{T} matrices. This yields two new, yet familiar operators that carry out the actions of virtual point transformation and DoF-selection at once:

$$\left\{ \begin{array}{ll} \mathbf{B}_c \triangleq \mathbf{B}\mathbf{T}_u & \text{compatibility at virtual point} \\ \mathbf{B}_e \triangleq \mathbf{B}\mathbf{T}_f & \text{equilibrium at virtual point} \end{array} \right. \quad (4.13a)$$

$$(4.13b)$$

Note that these matrices can be fed straight into the LM-FBS algorithm of Eq. (3.26). The substructures' admittance matrices can be left untouched and, as a consequence, the resulting coupling FRFs are found in the original dual space of the measured DoFs.

Virtual point FRFs

In the introduction of this chapter, the need for a nodal model was highlighted: a dynamic model, composed from collocated FRFs, that is compatible for coupling with FE or other experimental models. Indeed, for the purpose of dynamic substructuring or transfer path analysis, it may be preferred to transform the entire measurement into a virtual point admittance matrix. Such matrix can be stored in a database and easily retrieved for modelling purposes, in the capacity of a dynamic super-element.

The virtual point admittance was already identified above, namely as the combined subsystems' admittances pre- and post-multiplied with their respective transformation matrices. This may as well be computed on a substructure level, for instance to obtain the nodal admittance FRFs of substructure s :

$$\mathbf{Y}_{\text{qm}}^{(s)} = \mathbf{T}_u^{(s)} \mathbf{Y}^{(s)} \mathbf{T}_f^{(s)T} \quad (4.14)$$

The subscript \star_{qm} is used here to denote the virtual point DoF-space of the new admittance matrix. As will be demonstrated later, the IDM matrices \mathbf{R} have a block-diagonal structure and so do their resulting \mathbf{T} matrices. This means that, given an arbitrary structure s , the subset of FRFs used for transformation of coupling point 1 is not being reused for transformation of coupling point 2. In addition, the block-diagonal structure makes it easy to keep measured points of interest or additional excitation points untouched, by mixing in identity elements in the substructure's transformation matrices. Let us demonstrate this for the DoFs of substructures A and B from the example of Sec. 3.2:

$$\begin{bmatrix} \mathbf{u}_1^A \\ \mathbf{q}_2^A \end{bmatrix} = \begin{bmatrix} \mathbf{I} & \mathbf{0} \\ \mathbf{0} & \mathbf{T}_{u_2}^A \end{bmatrix} \begin{bmatrix} \mathbf{u}_1^A \\ \mathbf{u}_2^A \end{bmatrix} \quad \Longrightarrow \quad \mathbf{q}^A = \mathbf{T}_u^A \mathbf{u}^A$$

$$\begin{bmatrix} \mathbf{q}_2^B \\ \mathbf{u}_3^B \end{bmatrix} = \begin{bmatrix} \mathbf{T}_{u_2}^B & \mathbf{0} \\ \mathbf{0} & \mathbf{I} \end{bmatrix} \begin{bmatrix} \mathbf{u}_2^B \\ \mathbf{u}_3^B \end{bmatrix} \quad \Longrightarrow \quad \mathbf{q}^B = \mathbf{T}_u^B \mathbf{u}^B$$

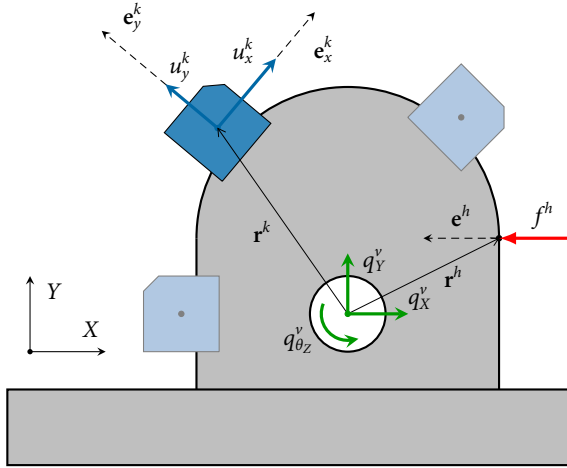


Figure 4.4: The IDMs associated with the virtual point (green) can be constructed from the positions and directions of the measured displacements (blue) and impacts (red).

The coordinate sets \mathbf{q}^A and \mathbf{q}^B now contain a mix of original internal DoFs and virtual point interface DoFs. With respect to the interface conditions, one can now define Boolean matrices in the traditional fashion, as all interface DoFs are already collocated due to their matching IDMs. The principles as demonstrated here can be employed in a customised fashion to serve the needs of the substructuring or TPA job in prospect.

4.3 Interface displacement modes

In the preceding section it was shown that the virtual point transformation relies on a spatial reduction of coordinates. The interface connectivity is reduced to virtual points using a predetermined set of interface displacement modes (IDMs) \mathbf{R} . This section elaborates on the construction of the 6-DoF IDMs for a virtual point. The example of Fig. 4.4 is used to illustrate the theory. Virtual point v is surrounded by $n_k = 3$ triaxial acceleration sensors, registering a total of 9 translational displacements⁷ in the local (x, y, z) frame of the sensors. A hammer impact is indicated by a thick red arrow.

4.3.1 Displacement IDM

The sensor IDM matrix \mathbf{R} (the subscript is dropped in this section) translates the local frame displacements to 6 virtual point displacements and rotations plus a residual. Let us write out this equation for a single triaxial sensor k . The orientation of the sensor is determined by three measurement directions, specified as orthonormal unit vectors:

$$[\mathbf{e}_x^k \ \mathbf{e}_y^k \ \mathbf{e}_z^k] = \mathbf{E}^k$$

The distance from the sensor to the virtual point is given by vector \mathbf{r}^k . The respective local displacements along these directions are denoted by \mathbf{u}^k . The 6 DoFs of virtual point v are comprised by the set \mathbf{q}^v . The following kinematic relation can be established between the

⁷In fact the sensors measure accelerations, but for simplicity of notation displacements are considered here.

virtual point \mathbf{q}^v and the sensor displacements \mathbf{u}^k :

$$\begin{bmatrix} u_x^k \\ u_y^k \\ u_z^k \end{bmatrix} = \begin{bmatrix} e_{x,X}^k & e_{x,Y}^k & e_{x,Z}^k \\ e_{y,X}^k & e_{y,Y}^k & e_{y,Z}^k \\ e_{z,X}^k & e_{z,Y}^k & e_{z,Z}^k \end{bmatrix} \begin{bmatrix} 1 & 0 & 0 & 0 & r_Z^k & -r_Y^k \\ 0 & 1 & 0 & -r_Z^k & 0 & r_X^k \\ 0 & 0 & 1 & r_Y^k & -r_X^k & 0 \end{bmatrix} \begin{bmatrix} q_X^v \\ q_Y^v \\ q_Z^v \\ q_{\theta_X}^v \\ q_{\theta_Y}^v \\ q_{\theta_Z}^v \end{bmatrix} + \begin{bmatrix} \mu_x^k \\ \mu_y^k \\ \mu_z^k \end{bmatrix} \quad (4.15)$$

This relation states how much displacement is measured on the channels of sensor k for a given displacement and rotation of the corresponding virtual point v . Any residual displacement ends up in $\boldsymbol{\mu}$.

Introducing $\bar{\mathbf{R}}^{kv}$ as the 3×6 global-frame IDM matrix associated with sensor k and virtual point v , we can write this relation for each sensor:

$$\begin{aligned} \mathbf{u}^k &= \mathbf{E}^{kT} \bar{\mathbf{R}}^{kv} \mathbf{q}^v + \boldsymbol{\mu}^k \\ \mathbf{u}^k &= \mathbf{R}^{kv} \mathbf{q}^v + \boldsymbol{\mu}^k \quad \text{with} \quad \mathbf{R}^{kv} \triangleq \mathbf{E}^{kT} \bar{\mathbf{R}}^{kv} \end{aligned} \quad (4.16)$$

\mathbf{R}^{kv} is the local-frame IDM matrix. For a typical configuration of 3 sensors per virtual point, the \mathbf{R}^{kv} matrices can be stacked to form the following system of equations:

$$\mathbf{u} = \mathbf{R} \mathbf{q} + \boldsymbol{\mu} \quad \text{with} \quad \mathbf{R} = \begin{bmatrix} \mathbf{R}^{1,1} \\ \mathbf{R}^{2,1} \\ \mathbf{R}^{3,1} \\ & \mathbf{R}^{4,2} \\ & \mathbf{R}^{5,2} \\ & \mathbf{R}^{6,2} \\ & & \ddots \\ & & & \mathbf{R}^{n_k, n_v} \end{bmatrix} \quad (4.17)$$

Eq. (4.17) has the same form as Eq. (4.2). Alternatively, one may prefer to describe the virtual point relation for each measurement channel individually. A single displacement DoF u_i^k with local direction vector \mathbf{e}_i^k can be related to the associated set of virtual point coordinates in \mathbf{q}^v :

$$u_i^k = \left[\mathbf{e}_i^{kT} \quad (\mathbf{r}_i^k \times \mathbf{e}_i^k)^T \right] \mathbf{q}^v + \mu_i^k = \mathbf{R}_i^{kv} \mathbf{q}^v + \mu_i^k \quad (4.18)$$

The single-DoF row-vector between the block brackets is of size 1×6 . The full matrix \mathbf{R} can be constructed row-wise per sensor channel i and column-wise for the different virtual points.

Regardless of the construction method, the resulting IDM matrix \mathbf{R} is block-diagonal, or at least contain IDMs that are uncoupled with respect to the various virtual points and sensor groups. Although not treated here, \mathbf{R} may be augmented with flexible IDMs if desired. In any case, care should be taken that \mathbf{R} is full rank, which implies that sufficient measurement points are considered to compute an inverse or pseudo-inverse \mathbf{T} using Eq. (4.5a).

4.3.2 Force IDM

The transformation of the forces can be performed in an analogue way. The following relation can be written for the set of virtual forces \mathbf{m}^v as a result of a single impact f^h in the direction of \mathbf{e}^h and at a distance \mathbf{r}^h from the virtual point v :

$$\begin{bmatrix} m_X^v \\ m_Y^v \\ m_Z^v \\ m_{\theta_X}^v \\ m_{\theta_Y}^v \\ m_{\theta_Z}^v \end{bmatrix} = \begin{bmatrix} 1 & 0 & 0 \\ 0 & 1 & 0 \\ 0 & 0 & 1 \\ 0 & -r_Z^h & r_Y^h \\ r_Z^h & 0 & -r_X^h \\ -r_Y^h & r_X^h & 0 \end{bmatrix} \begin{bmatrix} e_X^h \\ e_Y^h \\ e_Z^h \end{bmatrix} f^h \quad (4.19)$$

Note that the virtual point forces are indeed the direct result of applied forces, hence we do not need to add a residual.

Now, to remain consistent with Eq. (4.18), the transpose of \mathbf{R}^{hv} is defined:

$$\mathbf{m}^v = \begin{bmatrix} \mathbf{e}^h \\ \mathbf{r}^h \times \mathbf{e}^h \end{bmatrix} f^h = \mathbf{R}^{hvT} f^h \quad (4.20)$$

Every impact adds a single column to the transposed IDM matrix \mathbf{R}^T . Assuming 9 impacts per virtual point, the system for the complete set of DoFs reads:

$$\mathbf{m} = \mathbf{R}^T \mathbf{f} \quad \text{with} \quad \mathbf{R} = \begin{bmatrix} \mathbf{R}^{1,1} \\ \vdots \\ \mathbf{R}^{9,1} & \mathbf{R}^{10,2} \\ & \vdots \\ & \mathbf{R}^{18,2} \\ & \ddots \\ & & \mathbf{R}^{n_h, n_v} \end{bmatrix} \quad (4.21)$$

Note that the IDM matrix of the forces takes the same form as the IDM matrix of the displacements from Eq. (4.17). In fact, if one decides to excite only on the sensor faces (which is generally not advised, see section 4.5.2), one has obtained the exact same IDM matrix, apart from some sign changes.

With more than six independent excitations per virtual point, Eq. (4.21) becomes underdetermined, which means that there is no unique combination of the excitation forces \mathbf{f} from which a certain \mathbf{m} can be constructed. The solution is found using the pseudo-inverse of Eq. (4.9a). Instead of minimising a residual (which was the case for the displacements), this operation finds a set of excitation forces that minimises the \mathbf{W}^{-1} -norm of \mathbf{f} :

$$\mathbf{f} = \operatorname{argmin} \|\mathbf{f}^T \mathbf{W}^{-1} \mathbf{f}\|$$

This again has advantageous properties for interface weakening and error suppression, as discussed in Sec. 4.2.

4.4 Measurement quality indicators

An important feature of the virtual point transformation is the ability to quantify the consistency of the measurement. Note that the classical coherence function can be used to assess properties of single FRFs, but does not tell if a set of n FRFs is dynamically plausible. The quality functions introduced here are a by-product of the transformation and reveal important practical aspects of the whole measurement.

4.4.1 Sensor consistency

The sensor consistency function is an indicator of the consistency of the measured response channels with respect to a certain load case. It compares the measured responses with the responses after projection onto the IDMs. It was originally proposed in [106] as an indicator of the “rigidness” of the interface, but has additional, generally useful properties.

For the evaluation of the consistency of the sensors around virtual point 1, let us consider their responses to a load case \mathbf{f}_2 , denoted by $\mathbf{u}_{1,2}$. This load vector is composed from one or more excitations at coupling point 2, reasonably distant from virtual point 1. This way, the responses in \mathbf{u}_1 due to \mathbf{f}_2 are probably more global (showing some signal in all directions) than when considered for one or more excitations near the sensors around point 1. The filtered responses are found by pre-multiplying the responses with the IDM projection matrix \mathbf{F}_u for the respective coordinates:

$$\left\{ \begin{array}{l} \mathbf{u}_{1,2} \triangleq \mathbf{u}_{1,\mathbf{f}_2} = \mathbf{Y}_{12}\mathbf{f}_2 \\ \tilde{\mathbf{u}}_{1,2} \triangleq \tilde{\mathbf{u}}_{1,\mathbf{f}_2} = \mathbf{F}_{11}\mathbf{Y}_{12}\mathbf{f}_2 \end{array} \right. \quad (4.22a)$$

$$\left\{ \begin{array}{l} \mathbf{u}_{1,2} \triangleq \mathbf{u}_{1,\mathbf{f}_2} = \mathbf{Y}_{12}\mathbf{f}_2 \\ \tilde{\mathbf{u}}_{1,2} \triangleq \tilde{\mathbf{u}}_{1,\mathbf{f}_2} = \mathbf{F}_{11}\mathbf{Y}_{12}\mathbf{f}_2 \end{array} \right. \quad (4.22b)$$

As mentioned before, \mathbf{F}_u is a rank- m filter operator. It differs from identity if the transformation is overdetermined, namely for $n > m$. The filtered responses are in that case limited by the m modes of the IDM; \mathbf{F}_u implements the reduction and expansion step, Eq. (4.5a–4.5b) in a single operator.

The responses $\tilde{\mathbf{u}}_{1,2}$ shall now be compared with $\mathbf{u}_{1,2}$ to evaluate to what extent the responses are affected by IDM filtering. Two criteria are discussed next.

Overall sensor consistency

To get a quick feeling of the consistency of all sensor channels, the norm of both vectors can be compared. This yields a frequency-dependent function bounded by zero (no consistency) and one (full consistency):

$$\rho_{\mathbf{u}_{1,2}}(\omega) = \frac{\|\tilde{\mathbf{u}}_{1,2}(\omega)\|}{\|\mathbf{u}_{1,2}(\omega)\|} \quad (4.23)$$

A function value $\rho(\omega) = 1$ means that the amplitude of all filtered sensor channels is left unchanged, suggesting that all sensor responses can be fully described by the m IDMs (6 for a rigid interface) at the specified frequency. Mathematically, it implies that the singular value decomposition $\mathbf{Y}_{12} = \mathbf{U}_{11}\boldsymbol{\Sigma}_{12}\mathbf{V}_{22}^T$ only comprises m significant singular values and that the associated left singular modes \mathbf{U}_{11} are all in the subspace of \mathbf{R}_u . In practice, it indicates that all sensors are correctly positioned, aligned and calibrated, as otherwise at least one channel would “swing” out of line and reduce the overall value of ρ .

If the value drops down above a certain frequency, it is often an indication of the presence of a flexible interface mode. This can be verified by looking at mode $m + 1$ in \mathbf{U}_{11} . If the associated singular value is significant, one could consider to augment the IDM basis by a flexible mode, e.g. based on mode $m + 1$ in \mathbf{U}_{11} .

Specific sensor consistency

For evaluation of the consistency per measurement channel, we introduce a variation of the spectral coherence function. Essentially, this is an expansion of the spectral coherence function [17] when evaluated for a total of two spectra:

$$\text{coh}(x, y) \triangleq \frac{(x + y)(x^* + y^*)}{2(xx^* + yy^*)} \quad x, y \in \mathbb{C} \quad \implies \quad \begin{cases} 1 & \text{if } x = y \\ \frac{1}{2} & \text{if } x \perp y \\ 0 & \text{if } x = -y \end{cases} \quad (4.24)$$

This equation compares two values with respect to their amplitude and phase. It is again bounded between zero and one and can thus be used to objectively compare two complex response spectra with each other. For evaluation of the specific consistency of measurement channel u_i , we write:

$$\rho_{u_{i,2}}(\omega) = \text{coh}(\tilde{u}_{i,2}(\omega), u_{i,2}(\omega)) \quad u_i \in \mathbf{u}_1 \quad (4.25)$$

If the overall sensor consistency is poor over the full frequency range, it may very well be a problem of just one incorrect sensor direction or calibration value⁸. Eq. (4.25) allows to evaluate the consistency of each measurement channel with respect to the full transformation. This way, the problematic sensor can be identified and the entries in \mathbf{R}_u corrected if needed.

4.4.2 Impact consistency

Similar to the sensor consistency, it is possible to define a consistency function for the applied forces. This value is particularly useful to assess the accuracy of the excitation positions and directions — crucial aspects in impact hammer measurement.

We now consider the effect of the force filter matrix \mathbf{F}_f on the responses. In order to provide a methodology analogue to the sensor consistency, a linear combination of responses is considered for the evaluation, denoted by scalar y_2 . Vector \mathbf{w}_2 is introduced to compute a (weighted) sum over the response channels of virtual point 2:

$$y_2 = \mathbf{w}_2^T \mathbf{u}_2 \quad \mathbf{w}_2 \in \mathbb{R}^{n_2}$$

Note that the quantity y_2 has very little dynamical significance; it only allows to assess the effect of the force filtering with respect to some responses in \mathbf{u}_2 , selected and combined using \mathbf{w}_2 . Let us again define an original and force-filtered set of responses, namely for all forces $f_j \in \mathbf{f}_1$ corresponding to virtual point 1:

$$\begin{cases} \mathbf{y}_{2,1} \triangleq [\dots y_{2,f_j} \dots] = \mathbf{w}_2^T \mathbf{Y}_{21} & (4.26a) \\ \tilde{\mathbf{y}}_{2,1} \triangleq [\dots \tilde{y}_{2,f_j} \dots] = \mathbf{w}_2^T \mathbf{Y}_{21} \mathbf{F}_{11} & (4.26b) \end{cases}$$

⁸For instance: if one sensor is rotated by 90 degrees along the z-axis, a rigid interface motion in the x, y-plane will appear as a partly flexible motion. The effect will be visible as a low consistency over the full frequency range.

Here, $y_{2,1}$ is a row vector comprising the summed responses as a result of all singleton impacts associated with the columns of Y_{21} . Row vector $\tilde{y}_{2,1}$ comprises a similar set of responses, yet for the forces filtered by the force IDM matrix. This can be reasoned as follows: for every single impact $f_j \in \mathbf{f}_1$, F_{1l} looks for an equivalent combination of impacts \mathbf{f}_1 that produces the same load on the virtual point. This allows to evaluate if there is any difference in response between the direct application of a single impact and the compound excitation suggested by the IDM matrix.

Overall impact consistency

Comparing the norm of the original and filtered set of responses, a measure is obtained for the overall consistency of the impacts:

$$\rho_{f_i,2}(\omega) = \frac{\|\tilde{y}_{2,1}^T(\omega)\|}{\|y_{2,1}^T(\omega)\|} \quad (4.27)$$

This frequency-dependent function quantifies how well the full set of impact forces \mathbf{f}_1 can be represented by 3 translational forces and 3 moments (in case of a 6-DoF IDM matrix). If some excitations points have been positioned too far away from the virtual point, they may load the interface in a flexible manner, which is reflected by a low value. More often actually, the value drops because of position and direction errors in the impacts.

Specific impact consistency

The specific impact consistency is used to spot individual impacts that are “non-consistent” with respect to the transformation. Using the definitions of Eq. (4.24) and Eq. (4.26a–4.26b), the following function can be defined:

$$\rho_{f_j,2}(\omega) = \text{coh}(\tilde{y}_{2,j}(\omega), y_{2,j}(\omega)) \quad f_j \in \mathbf{f}_1 \quad (4.28)$$

A low consistency value can have multiple causes, for instance:

- ▶ The impact position was off;
- ▶ The impact was not in the expected direction;
- ▶ The impact was not properly executed (e.g. double pulse, too little energy);
- ▶ The impact resulted in a signal overload at one or more channels in \mathbf{u}_2 .

Like the specific sensor consistency, the specific impact consistency may assist in finding troublesome impacts and fixing entries in the force IDM matrix. This can greatly improve the transformation results, as will be demonstrated in Sec. 4.6.

4.4.3 Virtual point reciprocity & passivity

Evaluating sensor and impact consistency is useful to troubleshoot errors in the measurement setup and validation of the assumptions with respect to interface rigidity. However, a high sensor / impact consistency does not guarantee a truthful virtual point FRF matrix Y_{qm} . Two additional properties are discussed for quality assessment of the two-sided transformed data.

FRF reciprocity

Reciprocity of the original measurement data is in most cases not very meaningful as the location of sensors and impact positions do not nicely coincide. In contrast, the virtual point motion and loads are actually collocated, meaning that the virtual point FRF matrix should be reciprocal. Reciprocity can thus be used to assess the transformation quality.

Let i and j denote two different DoFs from the set of virtual point DoFs. Then a frequency-dependent reciprocity function between zero and one is defined by:

$$\chi(\omega)_{ij} = \text{coh}(Y_{ij}(\omega), Y_{ji}(\omega)) \quad Y_{ij}, Y_{ji} \in \mathbf{Y}_{\text{qm}} \quad (4.29)$$

This function quantifies the similarity in both amplitude and phase between the two reciprocal virtual point FRFs. Note that for the diagonal of the matrix, $i = j$ and $\chi_{ii} = 1$ by definition. The reciprocity function is therefore only useful for evaluation of the off-diagonal terms.

Driving point passivity

One of the lesser known properties of the FRF matrix is driving point passivity. Driving-point FRFs, i.e. the FRFs on the diagonal of the matrix, need to be minimum-phase functions. This means that an applied force at DoF i shall always result in a displacement *in the same direction* at that point⁹. If the function is not minimum-phase, it implies that energy is added after the impulse, which contradicts system passivity [113, 192]. As a consequence, the phase of driving-point FRFs shall be bounded as follows:

$$\angle \mathbf{Y}_{ii} \begin{cases} \in [-180, 0] & \text{for receptance FRFs} \\ \in [-90, 90] & \text{for mobility FRFs} \\ \in [0, 180] & \text{for accelerance FRFs} \end{cases} \quad (4.30)$$

This property allows to assess the diagonal of the virtual point FRF matrix, which are the only entries that must demonstrate minimum-phase responses. Conveniently, those are also the only entries for which the reciprocity criterion does not apply. Hence the two criteria are complementary, in some practical way.

4.5 Instrumentation in practice

This section discusses some more practical issues related to the virtual point experiment. Proper positioning of the measurement and excitation points is essential to obtain a high-quality model. Care should be taken to ensure that all 6 DoFs per virtual point can be described independently. This has implications for both sensor placement and impact positions. The following preparation and post-processing steps are presented in the order as they normally appear in time.

4.5.1 Sensor placement

The use of tri-axial accelerometers has become standard practice in experimental testing. A single accelerometer hosts 3 sensing devices in orthogonal directions, that can be assumed

⁹Sign changes only occur at a minimum distance of half the wave-length of the underlying modes. This can be understood from modal synthesis, for instance Eq. (2.19).

to be collocated. Although one pair of those sensors measures a total of 6 channels, it is normally not sufficient to describe all 6 DoFs of the virtual point. One linear dependence will appear in the virtual points DoFs: the tri-axial sensors are unable to describe the rotation over the axis spanned between both sensors, as illustrated by Fig. 4.5a. This is regardless of the position of the sensors relative to the virtual point. Introduction of a third tri-axial sensor, such that the three sensors span a surface (Fig. 4.5b), enables the three sensors with a total of 9 DoFs to describe all 6 DoFs of the virtual point properly.

The additional benefit of the third tri-axial sensor is the overdetermination of the interface problem. Applying the virtual point transformation as discussed in Sec. 4.2, the effects of uncorrelated measurement noise, as well as bias errors due to misalignment of the sensors are reduced, which is generally considered as good practice [48, 106, 186]. The use of at least three tri-axial sensors per virtual point can therefore be held as rule of thumb, if the aim is to describe the virtual point by 6 independent coordinates.

Finally, considering the rigid interface assumption, it seems logical to place the sensors as close as possible to the virtual point. The smaller the distances are, the lesser the effects of flexible interface motion compared to the rigid interface motion. On the other hand, for smaller distances, the virtual point transformation gets more sensitive to absolute errors on the position. In general, one should approach this aspect with some engineering judgement or foreknowledge about the system and measurement equipment.

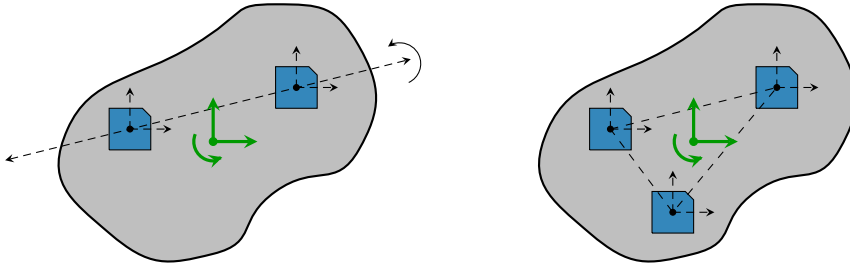
► *Shaker vs. impact hammer excitation*

In the field of experimental (modal) analysis, there are two main movements with regard to excitation of the structure^a [10]. For testing of civil and aeronautical structures, shaker excitation is the most common method. The relatively large and heavy structures need quite a bit of excitation energy to get acceptable signal-to-noise (SNR) ratios on the measurement. For testing of more modest structures, i.e. anything from hand-held components to passenger cars, impact hammer testing is more common. Impact hammers are supplied with a load-cell, registering the force history of the impact. This technique has become popular, especially in the substructuring community, because of the ability to perform a “roving-hammer” test on many measurement points in relatively short time. The following guidelines, although generally applicable, are oriented towards impact hammer excitation. ◀

^aThis concerns the experimental techniques with known excitation forces. A third movement could be the output-only techniques pertaining to the domain of operational modal analysis (OMA), which assume broad-band natural excitation spectra provided by wave or wind currents, for instance.

4.5.2 Excitation positions

Unlike the 6 accelerations measured by 2 tri-axial sensors, 6 well-positioned hammer impacts are potentially sufficient to fully determine the 6 generalised loads of the virtual point. Still, for the same reason, it is preferable to use more excitation points and overdetermine the force transformation. Similar to the sensor placement, three impacts in each direction (x, y, z) can be used as minimum, creating 9 columns in the FRF matrix for each coupling point. However, as one is not restricted by the available measurement equipment (as is the case for the simultaneous sensor positions), it is advised to excite at much more points.



(a) Two sensors spanning a line: one dependency exists between the rotational axes. (b) Three sensors spanning a surface: all rotations are fully determined.

Figure 4.5: Sensor placement for measurement of accelerations in an arbitrary structure.

Care should be taken to include excitation directions that do not point straight to the virtual point, in order to generate “moment” along the rotational axes.

In some previous studies, the faces of the acceleration sensors were suggested as possible impact locations [101, 186]. As the impact locations and directions are equal to the locations and orientations of the measured responses of the sensor, the same IDM matrix can potentially be used for both transformations. However, practice shows that FRFs obtained at the sensors’ faces exhibit poor coherence, especially for the cross-directional FRFs of one sensor. Also, the sensor is easily driven in overload. As the virtual point transformation does not require physical driving-point measurement (driving-point FRFs are correctly rendered by the two transformations), this type of excitation is discouraged.

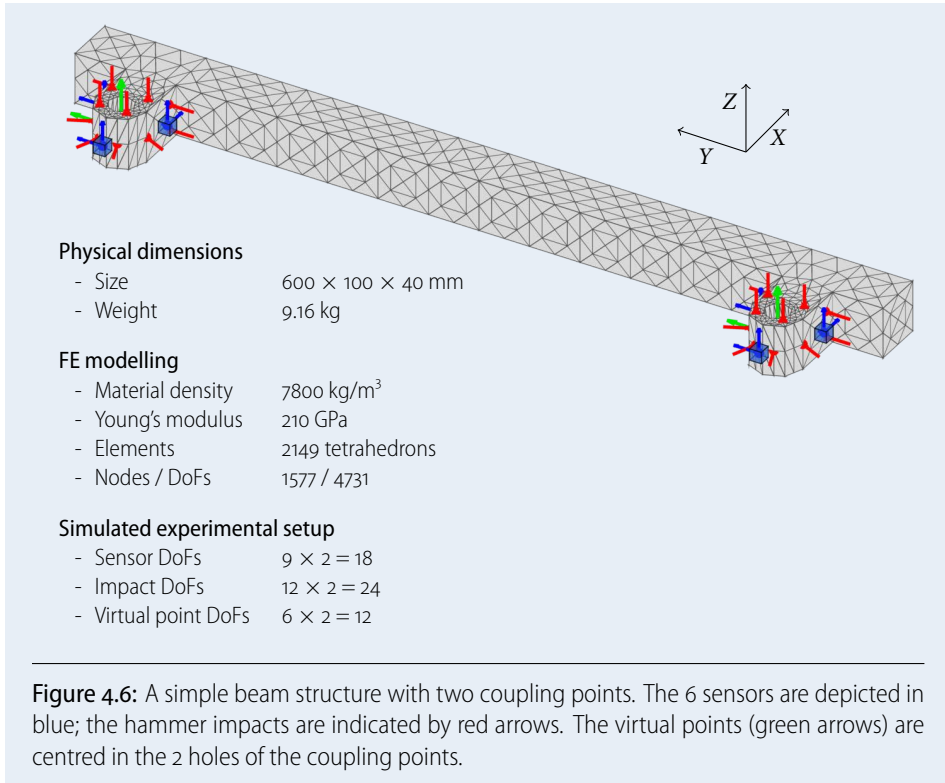
With respect to the distance of impact points from the virtual point, a similar reasoning applies as for the sensors. However, remind that the uncertainty of hammer impacts is highly subject to the skill of the experimentalist¹⁰. Position errors are always made, typically in the order of a few millimetres. To minimise their effect for the transformation, it is advised to excite at some more distance from the virtual point. This is possible as long as the local rigidity assumption is still justified, which is normally a matter of the targeted frequency bandwidth.

4.6 Example

This section demonstrates the application of the virtual point transformation based on a “simulated” measurement. The application on actual experimental structures is demonstrated in Sec. 8.3 for determination of structural-acoustic FRFs of the vehicle. However, there is no “truth model” to compare the experimental results with.

The aim of this section is to clearly demonstrate some important aspects of the virtual point transformation, using simulated data that is free from noise or measurement errors. This example can thus be regarded as a verification of the methodology rather than an experimental validation. Nonetheless, the structure used for the example bears a strong resemblance with a substitute beam, as encountered in Sec. 8.5.

¹⁰This only applies to manual impact hammer testing. Automated hammer or shaker measurements probably reduce these uncertainties, but are far more elaborate in practice. Considering the substantial amount of measurement points for our applications, impact hammer measurement has been the preferred method.

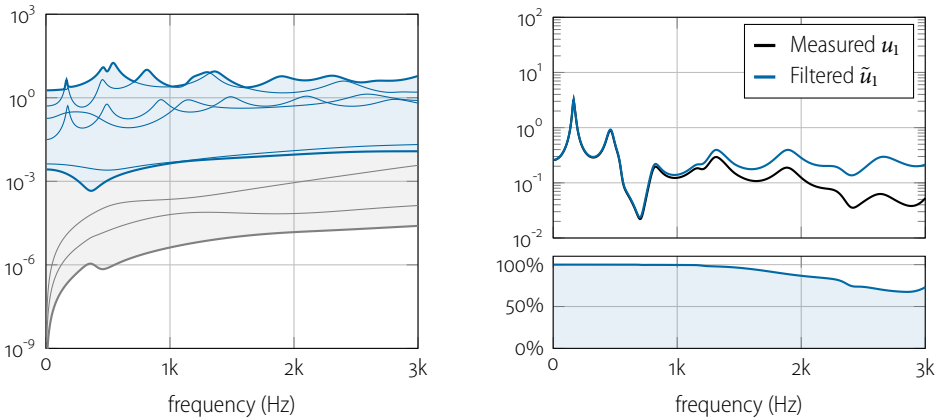


4.6.1 Modelling of a simple beam

A model of a simple beam structure is displayed in Fig. 4.6. The structure comprises two coupling points; a virtual point is put in the centre of the hole of each coupling point. The aim of a measurement would be to model the dynamics of these coupling points by experiment, using the proposed procedures of the virtual point transformation. These points could not be measured nor excited in practice, hence driving point FRFs would not be obtained by direct measurement.

A finite element model has been created using 2150 tetrahedron elements¹¹. The system's mass and stiffness matrix have been constructed for a total of 4731 DoFs; modal damping of $\zeta = 5\%$ was assigned to all the modes. To mimic an experimental measurement campaign, accelerance FRFs have been synthesised by modal superposition using the method of Eq. (2.19). A total of 40 vibration modes has been used in the mode synthesis (including six rigid body modes), stretching a frequency bandwidth from zero to 6 kHz. FRFs have been evaluated for 18 response channels and 24 hammer impacts in a frequency range of 0–3000 Hz. The so-obtained FRF matrix would be a typical result of an experimental measurement campaign: the sensor and impact locations are spread throughout the interface structure, i.e. not collocated. A virtual point transformation shall therefore be performed to obtain collocated 6-DoF FRFs, suitable for dynamic substructuring.

¹¹The mesh size appears a bit coarse in the Z-direction on the curved side of the coupling points, which is probably bad practice in FE modelling. However, considering the purpose of this example, it was decided not to focus too much on creating an accurate numerical model.



(a) Singular values of a subset of the FRF matrix \mathbf{Y}_{12} , indicating that the interface behaves rigidly.

(b) Consistency of response DoF u_1 . Above: measured and filtered response; below: specific sensor consistency $\rho_{u_{1,2}}$.

Figure 4.7: Assessment of measured FRF matrix and the sensor consistency.

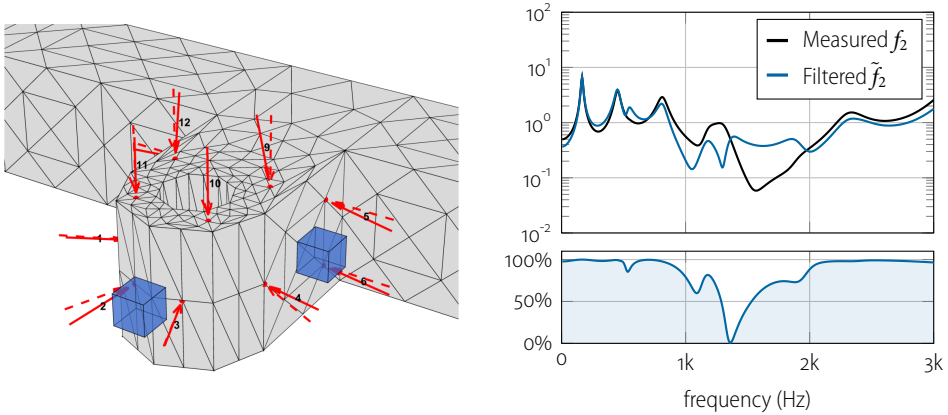
4.6.2 Inspection of measured FRFs

Let us first discuss the measured FRF matrix. Fig. 4.7a shows the singular values of a subset of the FRF matrix \mathbf{Y}_{12} , namely for the 9 responses at point 1 due to 12 excitations around point 2. The total amount of singular values is 9, limited by the number of response DoFs u_i in the matrix. If the interface behaves rigidly, no more than 6 significant singular values shall be present. This is confirmed by Fig. 4.7a; the blue part represents the first six singular values which make up more than 99% of the responses (in fact, the first 4 singular values clearly take the majority).

Next, the sensor consistency is assessed, evaluated for the responses of point 1 to excitations around point 2. As expected from the singular value evaluation, the overall consistency value is close to one over the full frequency range. Fig. 4.7b shows the the specific sensor consistency of DoF u_1 , i.e. the X-direction of the sensor on the curved surface, together with the original and filtered response. This is the only channel that exhibits non-consistent (non-rigid) behaviour: the filtered response starts to deviate from the measurement above 1000 Hz. On all other DoFs (u_2, \dots, u_9), the filtered responses are an almost perfect match with the measured responses. This means that the motion can be very well described by the 6 IDMs, hence the interface rigidity assumption is justified.

A similar procedure was performed for the 12 hammer impacts near virtual point 1. The impacts as defined in Fig. 4.6 were verified to produce near perfect impact consistency. However in practice, it is likely to make small position and angle errors in the impacts. Therefore, a small random error is introduced in the angle, in the order of 10 degrees. The “misaligned” impact vectors are shown in Fig. 4.8a. The corresponding FRFs are calculated by linearly combining the orthogonal X,Y, and Z FRFs available from the FE model.

The effect of simulated measurement errors on the specific impact consistency is shown in Fig. 4.8b for force DoF f_2 . It can be observed that the error in the direction yields a reduced consistency, mainly in the region between 1000 and 2000 Hz. Although not further



(a) Small errors in the direction of the impacts (thick arrows), compared to the intended impacts (dashed).

(b) Consistency of force DoF f_2 . Above: measured and filtered response; below: specific impact consistency $\rho_{f_{i,2}}$.

Figure 4.8: Assessment of the consistency of the hammer impacts. A slight deviation in the direction of the impacts has been introduced to simulate typical measurement errors.

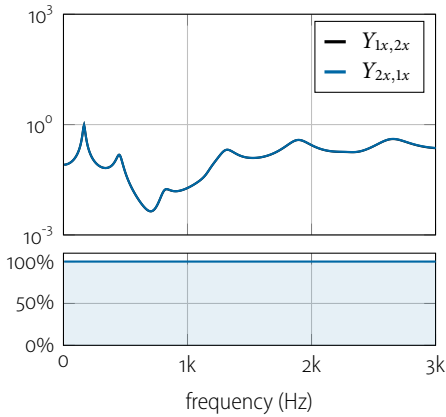
analysed here, this can be understood by looking at the modal content of the structure in this frequency range. In practice, one could try and fine-tune the definition of direction and position in the IDM matrix, in order to optimise for the highest consistency values.

4.6.3 Transformation to virtual point FRFs

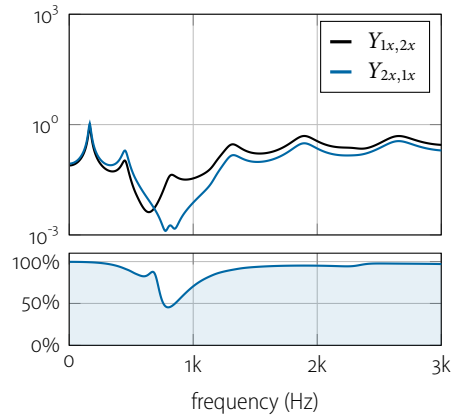
The two transformations are now applied to transform the 18×24 measured FRF matrix \mathbf{Y} into a 12×12 virtual point FRF matrix \mathbf{Y}_{qm} . This is the FRF matrix for collocated virtual motion and loads, concentrated in the two coupling points. The quality of the transformed FRFs can be evaluated by determining the reciprocity of the FRFs using Eq. (4.29).

Two results of the transformation are considered: one created with the exact impact locations and a second with the slight direction errors. Fig. 4.9 shows the virtual point FRFs for the x -directions of point 1 to point 2, together with their reciprocal FRF. The frequency-averaged reciprocity of the full 12×12 virtual point admittance matrix is shown in Fig. 4.10. The results on the left (Fig. 4.9a and 4.10a) show a perfect match, which can be concluded from their reciprocity function. The average reciprocity over the full bandwidth is above 99%, while all FRFs on the diagonal are strictly passive, i.e. phase between 0 and 180° . This represents the optimal case: all FRFs are reciprocal and perfectly conditioned for substructure coupling.

The results on the right (Fig. 4.9b and 4.10b) clearly show the propagation of experimental errors in the transformation. The average reciprocity of the virtual point FRFs is only 78%. The largest reciprocity errors are observed for the Z -directions and rotations about the θ_X and θ_Y axis. This is understandable given the example: an excitation in an X or Y -direction should in theory not induce motion in the Z -direction; any offset in direction or position will immediately deviate from zero cross-response. This is reflected by the reduced values for DoF 3–5 and 9–11. In such case, it is suggested to either fix the directions in the IDM matrix, or add more impact points in order to increase the overdetermination.

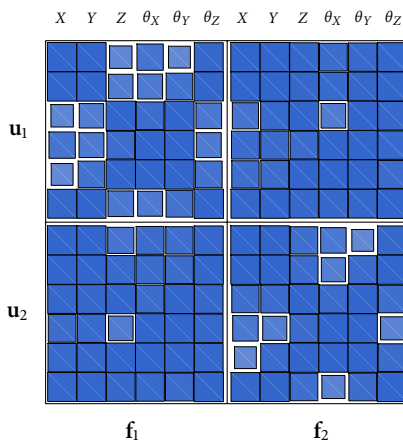


(a) Exact impact directions.

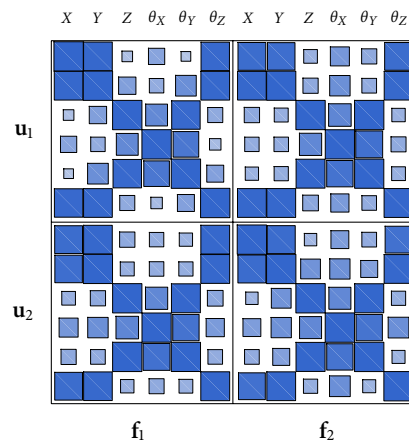


(b) Slight errors in the impact directions.

Figure 4.9: Virtual point FRFs for the X-directions of point 1 to point 2, together with their reciprocal FRF. The reciprocity criterion function is shown below.



(a) Exact impact locations.



(b) Slight errors in the impact directions.

Figure 4.10: Mean reciprocity of the full virtual point admittance matrix. The coordinates are grouped per virtual point and denote the three translations and three rotations in the global coordinate system.

4.7 Summary

The real art of experimental modelling is to define, perform and post-process a measurement such that an accurate and compatible model is obtained, capturing all the dynamics needed for the analysis of choice. In this chapter, the methodology of the virtual point transformation has been presented. Starting from the perspective of interface reduction, it has been discussed how multiple translational responses and forces can be mapped to generalised motion and loads in a virtual point. Interface displacement modes (IDMs) describe the kinematics of the measured DoFs as seen from this virtual point. The IDMs allow to couple two measured sets of FRFs by means of virtual point compatibility and

equilibrium conditions. Alternatively, the transformation can be applied to the full FRF matrices, creating an FRF matrix in a FEM-compatible fashion.

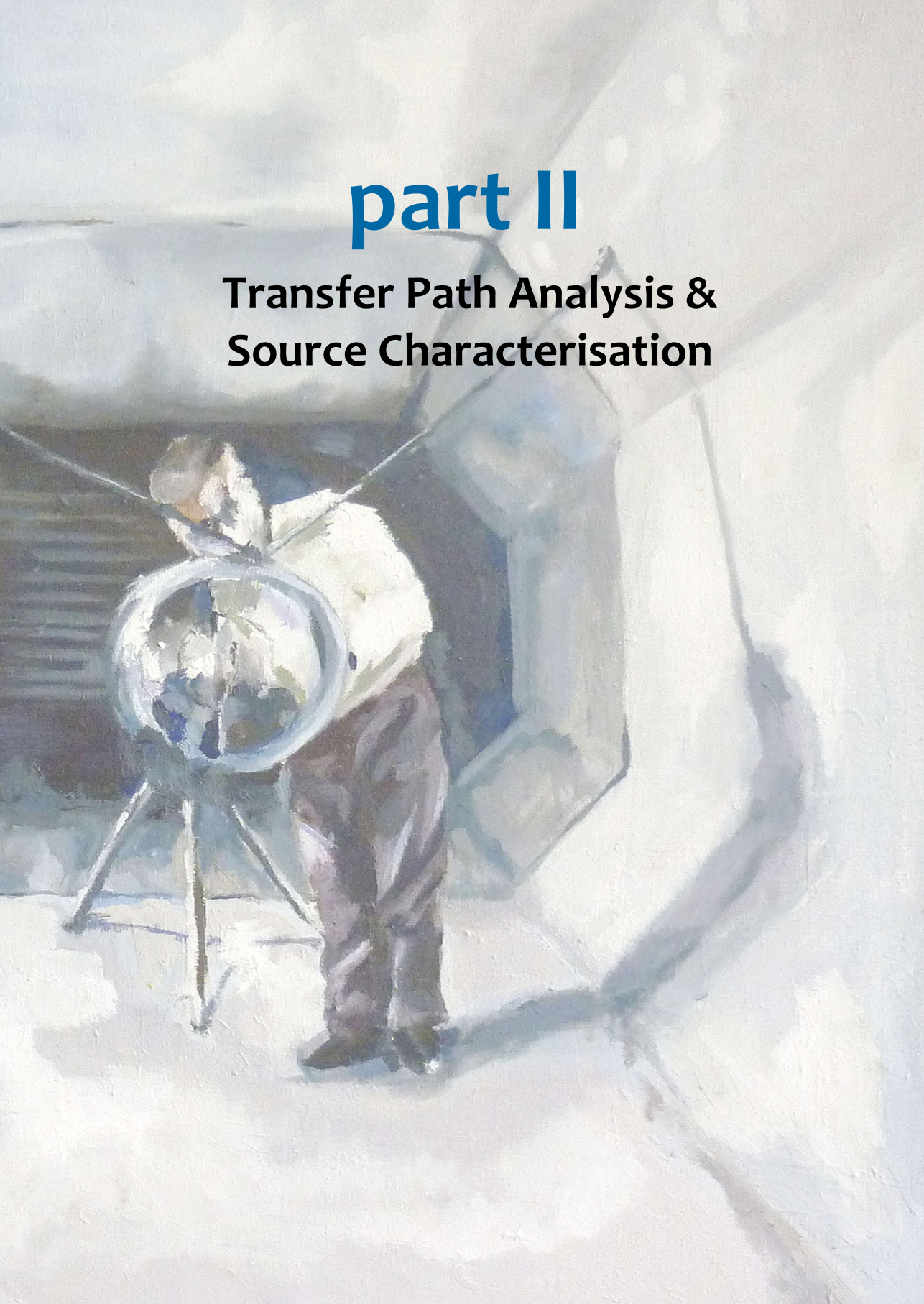
Whenever the set of measured DoFs is larger than the number of IDMs, the transformation is overdetermined and the measured FRFs are projected onto the subspace of the IDMs. This has several advantages. Typically, 6 IDMs are constructed that govern the translational and rotational rigid modes of the interface, while more than 6 response and force DoFs are obtained from measurement. This allows to couple only the rigid motion of the interface, whereas flexible phenomena, often due to measurement errors, end up in the residual and are filtered out.

Some practical aspects have been discussed that one may encounter when doing an experimental measurement. Sensor and impact positioning should be thought out carefully beforehand. Yet, many aspects can be evaluated afterwards based on a number of non-dimensional quality indicators. Consistency, reciprocity and passivity functions may help to assess the quality of the obtained FRF matrix.

A simulated measurement has been presented to demonstrate the process of transformation and quality monitoring. Perfect, reciprocal 6-DoF FRFs can be obtained through careful execution of the experimental steps. Altogether, the results should encourage the reader to try and model components by experiment, using the tools offered in this chapter.

part II

Transfer Path Analysis & Source Characterisation



5

Introduction to Transfer Path Analysis

chapter contents:

5.1 Introduction	71
5.1.1 The role of TPA in sound & vibration engineering	71
5.1.2 The TPA workflow	72
5.1.3 Outline of part two	73
5.2 History of TPA techniques	73
5.2.1 Impedance and mobility concepts	73
5.2.2 Advancing experimental techniques	74
5.2.3 Towards general TPA methodologies	75

5.1 Introduction

Transfer Path Analysis (TPA) has been a valuable engineering tool for as long as noise and vibrations of products have been of interest. A TPA concerns a product's actively vibrating components (such as engines, gearing systems or turbochargers) and the transmission of these vibrations to the connected passive structures. TPA is particularly useful when the actual vibrating mechanisms are too complex to model or measure directly, as it allows to represent a source by forces and vibrations displayed at the interfaces with the passive side. In this way the *source excitations* can be separated from the structural/acoustic *transfer characteristics*, allowing to troubleshoot the dominant paths of vibration transmission. The engineer can then anticipate by making changes to either the source itself or the receiving structures that are connected to it.

5.1.1 The role of TPA in sound & vibration engineering

A TPA often rises from the need to reduce some sort of undesired noise or vibration, for instance to improve product comfort or lifetime, ensure safety or preserve stealthiness. Aside from automotive development, applications are also seen in industries such as marine and aeroplane engineering, building acoustics and acoustic modelling of musical instruments. A TPA is generally motivated by one of the following desires:

1. *Secrecy*: perhaps the earliest TPA studies were triggered by the need to reduce the transmission of engine vibrations in military ships and submarines in order to make them stealthy. Many publications in the 1950s and 1960s document on isolation of ship engines by means of absorbers and decoupling mechanisms [77, 153, 196, 198, 208] to minimise the transmission through the interfaces.

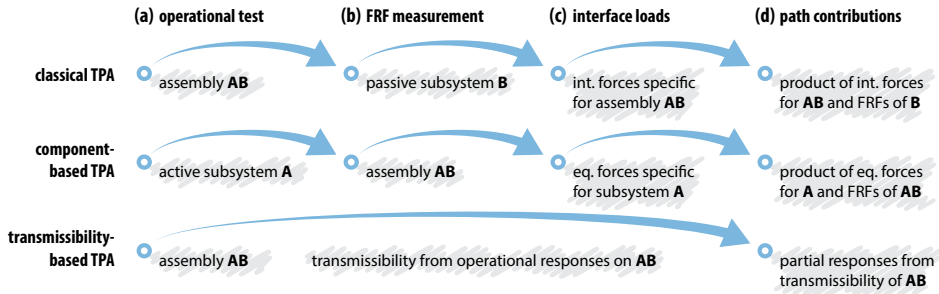


Figure 5.1: The TPA workflow, depicted stepwise for the three TPA families.

2. *Safety*: along with the rapid development of aeroplanes and spacecraft in the 1960s, TPA concepts started to be of use to study fatigue and stability (flutter) problems due to active or induced vibrations. As sources of vibrations are much more persistent in aeronautics – think of vortex-induced vibrations – focus was on characterising the passive transfer paths by means of modal analysis [21, 145].
3. *Comfort*: over the last decades TPA tends to be particularly associated with noise, vibration and harshness (NVH) engineering as commonly encountered in the automotive industry. The majority of recent developments and commercial solutions have been tailored towards this engineering society or related industries, driven by the increasing customer expectations on acoustic comfort [9, 30, 149, 155, 239].

In response to the evolving demands, TPA methods have been under continuous development and their family members have grown numerous. Some designations that found their way into literature include Operational TPA (OTPA), Operational Path Analysis with exogenous inputs (OPAX), blocked-force TPA, Gear Noise Propagation, in-situ Source Path Characterisation and Virtual Acoustic Prototyping. Very often those methods are presented from highly case-specific derivations. Not surprisingly, as the underlying physical concepts are similar, some of the above-mentioned show strong similarities or are even identical.

5.1.2 The TPA workflow

A TPA workflow can typically be subdivided in the following steps:

- (a) operational measurement on the active component;
- (b) determination of the passive (sub)system characteristics, often by means of FRFs;
- (c) determination of the operational interface loads;
- (d) identification of path contributions.

The steps are shown schematically in Fig. 5.1, from left to right and further categorised into three families (these will be clearly defined in the next chapter). Depending on the TPA method at hand, some or all of these steps may be performed in arbitrary order. The optimisation actions that follow from such an analysis are generally not considered part of the workflow.

5.1.3 Outline of part two

This part of this thesis is dedicated to transfer path analysis and source characterisation. It is mainly based on the publication [185], however slightly adjusted to improve consistency within this thesis. Also, new insights have been added with regard to component-based TPA and observability and controllability.

Sec. 5.2 of this chapter presents an account of some early developments and their relation to currently established TPA methods. This should by no means be regarded as a complete historical overview; rather it was chosen to highlight some key publications that have inspired the methodological developments in different ways.

Chap. 6 presents a unified framework for derivation of a large range of TPA methods. Sec. 6.1 introduces a general notation, starting by depicting the transfer problem using the dynamic substructuring paradigm, as introduced by Chap. 3. Hereafter the TPA methods are derived and classified along three families, namely the *classical* (Sec. 6.2), *component-based* (Sec. 6.3) and *transmissibility-based* (Sec. 6.4) TPA methods, as depicted vertically in Fig. 5.1. Sec. 6.5 concludes the chapter with a summary of the framework.

Chap. 7 comprises a collection of discussions and ideas, presented in random order. Some of these aspects are of more practical nature or application-specific; others provide new angles to further understand the transfer path problem.

5.2 History of TPA techniques

Transfer Path Analysis has been developed mostly during the second half of the 20th century, although some fundamental concepts date back to the 1880s. As often occurs in science, inspiration was found in different fields of research. This section starts with describing the adaptation of linear electric network theory to describe the transfer of structural vibrations. These form the foundations on which many analytical, and later also experimental TPA techniques have been built.

5.2.1 Impedance and mobility concepts

The inherent task of analysing a transfer problem is to describe the relation between the inputs and outputs of systems, preferably in a systematic or lumped way. Some of the major contributions in system theory originate from electric network science, founded on the laws for electric circuits of Kirchhoff [100], the superposition principle and the definitions of electric quantities such as admittance and impedance by Heaviside [79]. The equivalent source theorems of Thévenin [203] and Norton [141] were stated¹ by the turn of the 20th century, allowing to substitute a group of active and passive components by an equivalent voltage / current and a single impedance. Altogether these discoveries provided a handful of tools to depict complex electrical systems as a set of lumped subsystems, characterised by frequency dependent properties (e.g. impedance, admittance) and interacting by so-called “through” and “across” quantities, e.g. current and voltage.

The electric network principles appeared equally useful to describe structural vibrations

¹Actually it was Helmholtz who posed the equivalent source theorem already in 1853 in one of his fundamental works [81]. Like many scientist in that time, Thévenin was not aware of this early finding, as can be read in [96, 97].

of mechanical systems. Gardonio and Brennan published an extensive review [68] of the system description based on impedance and mobility (admittance) concepts in structural dynamics. They regard the article of Webster in 1914 [226] as the first effort to demonstrate analogies between electrical and mechanical impedance properties. In an attempt to describe the acoustic pressure in horns and musical instruments, Webster defined the acoustical impedance as the complex frequency-dependent ratio between pressure and volume of flowing air. From thereon analogies have been derived for mechanical systems², which is thoroughly reviewed in [67, 68].

Impedance and mobility have since been well established as concepts to model and understand all sorts of vibratory systems [37, 62, 82, 202]. The adaptation of the four-pole matrix method [195] furthermore introduced means to model systems consisting of a larger sequence of subsystems. However, most applications remained limited to fairly analytic cases [153, 198, 208]. In particular, the topic of experimental source characterisation has received little attention until the 1970s.

5.2.2 Advancing experimental techniques

Between 1971 and 1981 Bendat and Piersol provided a comprehensive set of spectral correlation and coherence functions with special attention for digital data acquisition [14–17]. These publications have empowered multiple-input / multiple-output (MIMO) measurement techniques that are instrumental to many advanced analyses, such as multi-reference modal testing [53]. Indeed the engineers were now given the chance to analyse vibration problems in their full complexity (e.g. multi-path, multi-DoF) rather than by simplified or analytical descriptions.

During the decades that followed, various simultaneous developments have been observed that led to a rapid expansion of practical TPA methods:

- ▶ The first exploration of techniques nowadays denoted by *classical TPA* is often attributed to the work of Verheij around 1980 who studied the transmission of ship machinery vibrations through resilient mounts [217, 218]. Although theory on mount stiffness had been around already for years [196], Verheij was one of the first to successfully determine interface forces and moments by experiment. Although attractive from an academical point of view, practical engineering called for less elaborate force determination methods. The matrix-inverse technique proved to be a good alternative [46, 157, 204, 205] and is up to today one of the most popular classical TPA methods in practice. The theory of classical TPA is presented in Sec. 6.2.
- ▶ In 1981 Magrans proposed a general method of measuring transmissibility between terminals in a network [123]. The so-called Global Transfer Direct Transfer (GTDT) method was further explored by Guasch [74–76] and later put into practice as the Advanced TPA [124]. Independently, Liu & Ewins [118] and Varoto & McConnell [216] explored properties of transmissibility matrices for structural vibrational problems, followed up by Ribeiro, Maia, Silva and Fontul [63, 125, 163, 164]. Surprisingly though, the transmissibility-based method known as *Operational TPA* was first

²The initial analogy regarded force analogous to voltage, which seemed the most intuitive choice. Firestone however disqualified this mechanical-impedance analogy in 1933 [61], arguing that it infringes Kirchoff's definitions of the terms *through* and *across*. The mechanical-mobility analogy, linking force with electrical current, is indeed the correct analogy for drawing mechanical circuits using parallel and series addition [144]. Nevertheless, the terms impedance and mobility have never changed definition in common use.

presented (again independently) by Noumura and Yoshida in Japan [142]. Sec. 6.4 discusses the theory and related techniques; reviews and benchmark studies are found in [64, 102, 120, 179].

- ▶ Inspired on acoustics, Mondot and Petersson proposed a method in 1987 to depict the vibration transfer problem using the characteristic power of the source itself (the so-called source descriptor) and a coupling function accounting for the added dynamics of the receiving structure [130]. This triggered the idea to characterise a source by means of blocked forces or free velocities [132, 151, 152], as seen in e.g. the *in-situ* method by Moorhouse and Elliott [49, 134] and *pseudo-forces* method by Janssens and Verheij [92, 94]. These and other strategies based on source component description are discussed in Sec. 6.3.
- ▶ Most TPA methods require admittance of either the source, receiver or assembled structure. Dynamic substructuring is particularly useful for this purpose: it allows to assemble systems from the dynamics of its substructures (see Chap. 3). The first DS techniques emerged in the 1960 and were focused on computation of natural vibration modes and frequencies and applied to aerospace structures. This perhaps explains why DS techniques were hardly ever brought in context with TPA³. Yet with the introduction of Frequency Based Substructuring (FBS) [39, 95], methods became available to assemble multiple substructures from FRFs, either obtained from numerical modelling or admittance tests [105]. In fact, DS theory appeared very convenient to derive hybrid numerical/experimental TPA schemes and perform component optimisation [154, 156]. This is particularly effective in combination with component-based TPA schemes [101, 103], as discussed in Sec. 6.3.

5.2.3 Towards general TPA methodologies

The abundance of developments brought prosperity to the engineering community, yet at the same time raised misunderstanding about the interrelations between the methods. In 1980 the ISO work group TC43/SC1/WG22 was established, dedicated to investigating and standardising the present technologies for structure-borne TPA [87, 88]. An intermediate report [233] already presented a comprehensive overview, addressing aspects such as the required number of DoFs, source description by means of equivalent quantities (forces, velocities, power), reciprocal measurement techniques and potential integration of Statistical Energy Analysis (SEA) principles. Although well accepted by acoustical engineers, the standardisations failed to gain broad popularity in the field of structure-borne TPA.

Popular methods such as operational TPA and matrix-inverse TPA have nowadays been integrated into many commercial noise and vibration solutions. Extensive literature is currently available, often discussing the application of a particular technique in a case-specific fashion. From such perspective the relation with other TPA techniques can be vague. In the next chapter it is attempted to review the landscape of TPA techniques in a unified way, namely from the proposed general framework.

³Early examples that suggest relations between TPA and dynamic substructuring are papers of Rubin [173, 174] (who later published an important modal reduction method [172]) and a NASA report [145].

6

General framework for Transfer Path Analysis

chapter contents:

6.1 The transfer path problem	77
6.1.1 Transfer path from assembled admittance	78
6.1.2 Transfer path from subsystem admittance	79
6.2 Classical TPA	80
6.2.1 Direct force	81
6.2.2 Mount stiffness	81
6.2.3 Matrix inverse	82
6.3 Component-based TPA	84
6.3.1 The equivalent source concept	84
6.3.2 Blocked force	85
6.3.3 Free velocity	86
6.3.4 Hybrid interface	87
6.3.5 In-situ	88
6.3.6 Pseudo-forces	90
6.3.7 Relation to LM-FBS	92
6.4 Transmissibility-based TPA	95
6.4.1 The transmissibility concept	96
6.4.2 Operational TPA	98
6.4.3 Operational mount identification (OPAX)	100
6.5 Summary	104

This chapter presents a unified framework for derivation of a large range of TPA methods. It is chosen to present and classify the methods separate from their typical fields of application, such that the underlying physical concepts are exposed and may be compared.

In Sec. 6.1 the framework for TPA is introduced, starting by depicting the transfer problem using the dynamic substructuring paradigm. Hereafter the TPA methods are derived and classified along three families, namely the *classical* (Sec. 6.2), *component-based* (Sec. 6.3) and *transmissibility-based* (Sec. 6.4) TPA methods. Concluding remarks and a summary are presented in Sec. 6.5.

6.1 The transfer path problem

Let us consider the dynamic system AB as schematically depicted in Fig. 6.1a. Two subsystems can be distinguished: an active subsystem A containing an excitation at node 1 and

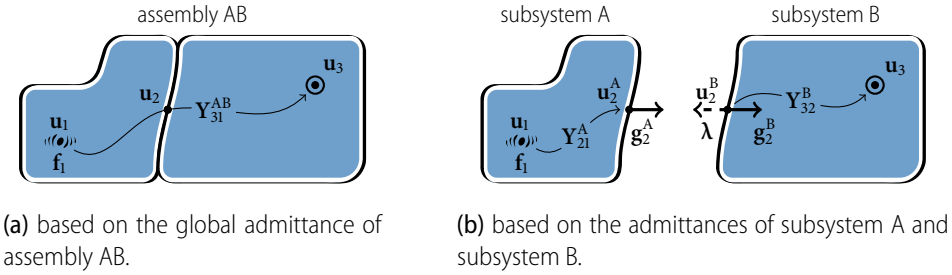


Figure 6.1: The transfer path problem.

a passive subsystem B comprising the responses of interest at node 3. The subsystems are rigidly interconnected at the interface node 2. For simplicity of derivation, the Degrees of Freedom (DoFs) in this example are restricted to three distinct nodes. These may however represent a larger set of DoFs, representing respectively:

- u₁ source:** internal DoFs belonging to the active component that cause the operational excitation but are unmeasurable in practice;
- u₂ interface:** coupling DoFs residing on the interface between the the active and passive component;
- u₃ receiver:** response DoFs at locations of interest at the passive component, possibly including acoustic pressures and other physical quantities.

Hence, the example of Fig. 6.1a is illustrative for a wide range of practical problems, provided that the structure of interest can be decomposed into an active and passive part. In what follows, all methods assume that the operational excitation at node 1 is unmeasurable in practice, but transmits vibrations through the interfaces at node 2 to receiving locations at node 3. The responses shall then be built up from a certain description of the vibrations measured at the interface (node 1 → 2) and an appropriate set of transfer functions relating these vibrations to the receiving responses (node 2 → 3). The fundamental choices herein dictate to which TPA family the method is classified.

6.1.1 Transfer path from assembled admittance

Let us first approach the transfer problem top-down for the assembled system AB, see Fig. 6.1a. We are interested in the response spectra at the receiving locations $\mathbf{u}_3(\omega)$ for source excitations at node 1, given by the force spectra $\mathbf{f}_1(\omega)$. For the assembled problem, this is simply obtained from a superposition of the individual contributions, i.e. the excitation force spectra multiplied with their respective linear(ised) transfer functions, contained in the columns of admittance FRF matrix $\mathbf{Y}^{AB}(\omega)$.

$$\mathbf{u}_i(\omega) = \sum_j Y_{ij}^{AB}(\omega) \mathbf{f}_j(\omega) \quad \implies \quad \mathbf{u}_3(\omega) = \mathbf{Y}_{31}^{AB}(\omega) \mathbf{f}_1(\omega) \quad (6.1)$$

In the equations that follow, the explicit frequency dependency $\star(\omega)$ will be omitted to improve legibility. Also note that the response set \mathbf{u} can include displacements, velocities, accelerations or any other quantity, provided that the rows of the FRF matrices are obtained accordingly. Furthermore, in order to keep the derivations brief and understandable, it is chosen to only consider the structure-borne paths. Nevertheless, Eq. (6.1) can easily be

extended to include contributions of airborne paths if the application so requires. In that case \mathbf{Y} and \mathbf{f} need to be augmented with a set of (responses to) acoustic loads such as volume velocities (m^3/s), as further discussed in Sec. 7.3.

6.1.2 Transfer path from subsystem admittance

The same transfer function is now derived for an assembly of the individual subsystems, as depicted in Fig. 6.1b. Let us first put the subsystem's FRF matrices \mathbf{Y}^A and \mathbf{Y}^B in a block-diagonal format. The force vector comprising the excitation force is augmented with interface forces \mathbf{g}_2 for both sides of node 2, that are yet to be determined. The obtained system of equations resembles the admittance variant of dual assembly, which is a standard form of dynamic substructuring as discussed in Sec. 3.3.2.

$$\begin{bmatrix} \mathbf{u}_1 \\ \mathbf{u}_2^A \\ \mathbf{u}_2^B \\ \mathbf{u}_3 \end{bmatrix} = \begin{bmatrix} \mathbf{Y}_{11}^A & \mathbf{Y}_{12}^A & \mathbf{0} & \mathbf{0} \\ \mathbf{Y}_{21}^A & \mathbf{Y}_{22}^A & \mathbf{0} & \mathbf{0} \\ \mathbf{0} & \mathbf{0} & \mathbf{Y}_{22}^B & \mathbf{Y}_{23}^B \\ \mathbf{0} & \mathbf{0} & \mathbf{Y}_{32}^B & \mathbf{Y}_{33}^B \end{bmatrix} \left(\begin{bmatrix} \mathbf{f}_1 \\ \mathbf{0} \\ \mathbf{0} \\ \mathbf{0} \end{bmatrix} + \begin{bmatrix} \mathbf{0} \\ \mathbf{g}_2^A \\ \mathbf{g}_2^B \\ \mathbf{0} \end{bmatrix} \right)$$

$$\mathbf{u} = \mathbf{Y}(\mathbf{f} + \mathbf{g}) \quad (6.2)$$

The following physical explanation can now be reasoned to solve Eq. (6.2). The excitation force at node 1 induces a motion at node 2 of subsystem A. As subsystem B is not directly affected by forces at A (due to the block-diagonal form of the global FRF matrix), an incompatibility is caused between \mathbf{u}_2^A and \mathbf{u}_2^B . This is denoted by the interface ‘‘gap’’ δ , which can conveniently be written using a signed Boolean matrix¹ \mathbf{B} as shown by Eq. (6.3a) and (6.3c). Next, assuming that no additional mass is present between the subsystems, the *equilibrium condition* is satisfied, requiring the interface forces \mathbf{g}_2 on both sides to be equal in magnitude and opposing in sign. The interface forces are expressed by Eq. (6.3b) and (6.3c), using a set of Lagrange multipliers λ for the magnitude and the transposed Boolean matrix to account for the interface force directions.

$$\delta = \mathbf{u}_2^B - \mathbf{u}_2^A \quad \text{or} \quad \delta \triangleq \mathbf{B}\mathbf{u} \quad (6.3a)$$

$$\mathbf{g}_2^A = -\mathbf{g}_2^B = \lambda \quad \text{or} \quad \mathbf{g} \triangleq -\mathbf{B}^T\lambda \quad (6.3b)$$

$$\text{with} \quad \mathbf{B} = \begin{bmatrix} \mathbf{0} & -\mathbf{I} & \mathbf{I} & \mathbf{0} \end{bmatrix} \quad (6.3c)$$

The interface forces λ that pull the two subsystems together can be determined from Eq. (6.3a) by requiring $\delta = \mathbf{0}$, which enforces the *compatibility condition* $\mathbf{u}_2^A = \mathbf{u}_2^B$. Considering Eq. (6.3b), the interface forces that ensure compatibility can be determined by equating the second and third line of Eq. (6.2) and solving for λ :

$$\begin{aligned} \mathbf{Y}_{21}^A \mathbf{f}_1 + \mathbf{Y}_{22}^A \mathbf{g}_2^A &= \mathbf{Y}_{22}^B \mathbf{g}_2^B \\ -(\mathbf{Y}_{22}^A + \mathbf{Y}_{22}^B) \lambda &= \mathbf{Y}_{21}^A \mathbf{f}_1 \\ -\lambda &= (\mathbf{Y}_{22}^A + \mathbf{Y}_{22}^B)^{-1} \mathbf{Y}_{21}^A \mathbf{f}_1 = \mathbf{g}_2^B \end{aligned} \quad (6.4)$$

¹The signed Boolean matrix \mathbf{B} establishes the relations for all interface DoFs of A and B that are vectorially associated, e.g. u_{2x}^A and u_{2x}^B . Guidelines on the construction and properties of the signed Boolean matrix are found in Sec. 3.2 and [104].

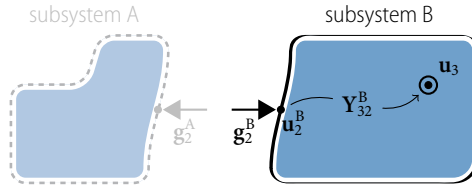


Figure 6.2: Classic TPA: application of interface forces, representing the operational excitation to the passive subsystem B. The interface forces are measured under operation of the assembled system AB.

Eq. (6.4) provides the interface forces at the coinciding interface DoFs caused by the operational excitation \mathbf{f}_1 inside subsystem A. The response at the receiving side \mathbf{u}_3^B is found by substituting Eq. (6.4) into the last line of Eq. (6.2):

$$\mathbf{u}_3 = \mathbf{Y}_{32}^B \mathbf{g}_2^B = \underbrace{\left[\mathbf{Y}_{32}^B (\mathbf{Y}_{22}^A + \mathbf{Y}_{22}^B)^{-1} \mathbf{Y}_{21}^A \right]}_{\mathbf{Y}_{31}^{AB}} \mathbf{f}_1 \quad (6.5)$$

Comparing with Eq. (6.1), it follows that the terms between the brackets indeed represent the admittance of the assembly \mathbf{Y}_{31}^{AB} by coupling of the subsystems' admittances. It can be verified that this result is in accordance with Lagrange multiplier frequency-based substructuring (LM-FBS) assembly, as discussed in Chap. 3 of this thesis.

So far it has been assumed that the excitation at node 1 is measurable. In reality however it is impossible or impractical to identify the exact force loading. This is solved in TPA by assuming that the dynamics at the interface node 2 due to this excitation are measurable and may very well represent the source excitation. In what follows, different approaches are examined to describe the transmission of vibrations, or rather, the response at the passive subsystem B for a non-measurable excitation somewhere inside (or on) the active subsystem A. The notation of dynamic substructuring is used to reveal the relations between the different approaches.

6.2 Classical TPA

The family of *Classical TPA* methods is essentially intended to identify transfer path contributions in *existing products*. They have nowadays become standard practice to troubleshoot NVH problems in automotive engineering [9, 155]. A classical TPA performs operational tests on the assembled product AB to obtain interface forces between the active and passive side, namely λ in Eq. (6.4). It can be verified from Eq. (6.2) and (6.5) that these interface forces fully determine the responses at the passive side and are thus representative for the effects of the source vibrations at the receiver locations \mathbf{u}_3 . To calculate the receiver responses², the passive-side interface forces $\mathbf{g}_2^B = -\lambda$ are applied to the interfaces of subsystem B, as shown in Fig. 6.2.

$$\mathbf{u}_3 = \mathbf{Y}_{32}^B \mathbf{g}_2^B \quad (6.6)$$

²In this framework the resulting responses \mathbf{u}_3 are formulated as a matrix-vector product, namely the sum of the partial responses. Techniques to evaluate the individual transfer paths contributions are discussed in Sec. 7.6.

Both steps pose some challenges in practice. The FRFs of the passive side are typically determined from impact or shaker tests, or in a reciprocal fashion using for instance an acoustic source at the receiving location and accelerometers at the interface nodes [57, 58, 231, 232, 234]. Either way it requires *dismounting* of the active part(s) from the passive side. With respect to the determination of operational interface forces \mathbf{g}_2^B , it could be impractical to mount force sensors between the active and passive part. Therefore a number of indirect methods have been developed to circumvent direct force measurement. Hence, the variants of classical TPA are defined according to how \mathbf{g}_2^B is obtained from operational tests, which are discussed next.

6.2.1 Classical TPA: direct force

The most straightforward technique to obtain the interface forces is from force transducers mounted directly between the active and passive side, as depicted in Fig. 6.3a. It was demonstrated by Eq. (6.4) that the interface force caused by the operational excitation is given by:

$$-\lambda = (\mathbf{Y}_{22}^A + \mathbf{Y}_{22}^B)^{-1} \mathbf{Y}_{21}^A \mathbf{f}_1 \quad \implies \quad \mathbf{g}_2^B = -\lambda \quad (6.7)$$

This is valid under the assumption that $\mathbf{u}_2^B = \mathbf{u}_2^A$, which requires the stiffness of the transducers to be high enough (relative to the stiffness of the actual subsystems) in the frequency range of interest. In fact, the main drawback of the method is the inconvenience of placing the transducers between the active component and the receiving structure. Lack of space, distortion of the original mounting situation and the incapability to measure all desired degrees of freedom at a connection point render the method impractical, especially for typical automotive applications. In case of large-scale systems such as ship machinery, this method may still be preferred [218].

6.2.2 Classical TPA: mount stiffness

An effective way of reducing vibration transmission is by placing resilient mounts between the components instead of rigid fixtures, as illustrated in Fig. 6.3b. By proper tuning of the mount flexibility (stiffness) and absorption (damping) properties, a high level of vibration suppression can be achieved. The mount stiffness method uses these mount properties to determine the interface forces. Assumed that the added mass of the mounts is negligible, the interface force equilibrium condition Eq. (6.3b) is still satisfied. However, the compatibility condition of Eq. (6.3a) is “weakened”, hence $\mathbf{u}_2^B - \mathbf{u}_2^A$ is no longer zero. Instead the m interface forces and coordinate incompatibilities are related by the dynamic stiffnesses of the mounts, denoted by z_{jj}^{mt} , j representing a single interface DoF:

$$\begin{bmatrix} g_j^A \\ g_j^B \end{bmatrix} = -z_{jj}^{\text{mt}} \begin{bmatrix} 1 & -1 \\ -1 & 1 \end{bmatrix} \begin{bmatrix} u_j^A \\ u_j^B \end{bmatrix} \quad \implies \quad g_j^B = z_{jj}^{\text{mt}} (u_j^A - u_j^B) \quad j \in 1, \dots, m$$

A spring-like stiffness matrix can be recognised, however with a minus sign because the interface forces g_j act on the connected subsystems A and B instead of the mount. Introducing the diagonal mount stiffness matrix \mathbf{Z}^{mt} , the full set of m interface forces \mathbf{g}_2^B can be estimated from the differential interface displacements between the source and receiver side, i.e. the measured displacements at both sides of the mounts:

$$\mathbf{g}_2^B = \mathbf{Z}^{\text{mt}} (\mathbf{u}_2^A - \mathbf{u}_2^B) \quad \text{with} \quad \mathbf{Z}^{\text{mt}} = \text{diag}(z_{11}^{\text{mt}}, \dots, z_{mm}^{\text{mt}}) \quad (6.8)$$

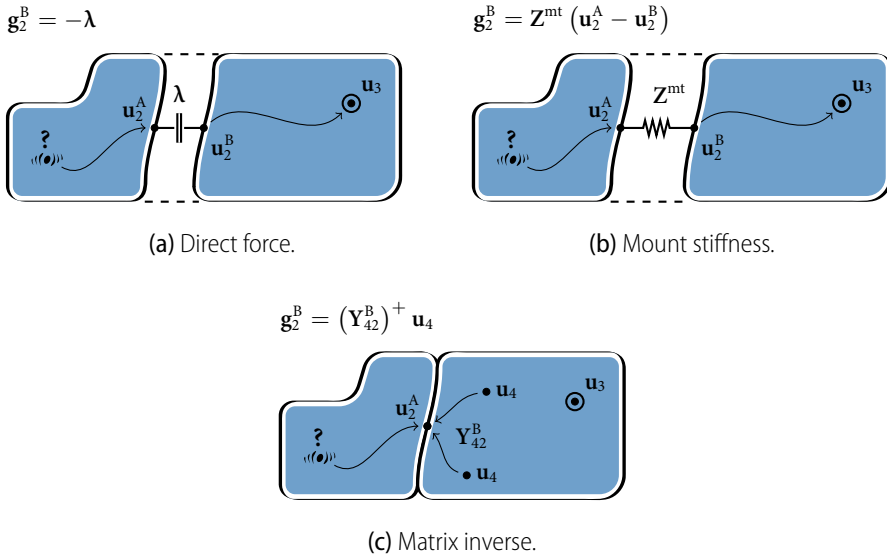


Figure 6.3: Three approaches to determine the operational interface forces in Classic TPA.

In most cases the flexible mounts are already integrated in the design to attenuate the vibration transmission. If they are however placed in the system for the mere purpose of TPA, it can be shown that the interface forces and thus the vibrations of the coupled system are altered significantly [12, 162], namely:

$$\mathbf{g}_2^B = (\mathbf{Y}_{22}^A + \mathbf{Y}_{22}^B + \mathbf{Y}^{mt})^{-1} \mathbf{Y}_{21}^A \mathbf{f}_1 \quad \text{with} \quad \mathbf{Y}^{mt} = (\mathbf{Z}^{mt})^{-1}$$

Although the mount stiffness method can be powerful and easy to conduct, the accuracy is highly subject to the terms³ in \mathbf{Z}^{mt} . Typical absorbers exhibit amplitude-dependent nonlinearities and directional characteristics [77, 207, 208]. An advanced TPA method that estimates the mount properties from operational tests is discussed in Sec. 6.4.3.

6.2.3 Classical TPA: matrix inverse

The third and perhaps most popular classical TPA member is the matrix-inverse method [46, 157, 204, 205]. It was observed from Eq. (6.6) that responses at the passive side are found from application of the interface forces to the passive subsystem's FRFs. Recalling these responses from Eq. (6.2):

$$\begin{bmatrix} \mathbf{u}_2^B \\ \mathbf{u}_3 \end{bmatrix} = \begin{bmatrix} \mathbf{Y}_{22}^B \\ \mathbf{Y}_{32}^B \end{bmatrix} \mathbf{g}_2^B$$

This problem can be inverted if the left-hand side contains sufficient independent responses to describe all m interface forces and moments in \mathbf{g}_2^B . The set of receiver responses \mathbf{u}_3 is typically too small in number and too distant from the interfaces to be suitable for

³Note that the terms in the dynamic stiffness matrix \mathbf{Z}^{mt} correspond to differential displacements of the associated interface DoFs $\mathbf{u}_2^A - \mathbf{u}_2^B$ and not the coordinates of both A and B. Some implications of the terms in \mathbf{Z}^{mt} are discussed in [12, 221].

inversion. Inversion of the first row is theoretically sufficient, but requires complete instrumentation of the assembled structure's interfaces to measure all DoFs \mathbf{u}_2^B associated with \mathbf{g}_2^B . In addition, a symmetric FRF matrix \mathbf{Y}_{22}^B would be required for the passive subsystem's interfaces, which is challenging to obtain accurately⁴.

In practice, the passive side is equipped with so-called *indicator responses* \mathbf{u}_4 as shown in Fig. 6.3c. An amount of $n \geq m$ responses shall be located in the proximity of the interfaces, such that the full set of m interface forces is properly *observable* from these points (this is addressed below). As these indicator DoFs merely assist in the determination of the interface forces, the sensor type can be chosen rather arbitrarily, although (tri-axial) accelerometers are the most common choice.

Two sets of measurements are now required to reconstruct the interface force spectra. First, responses \mathbf{u}_4 are measured on the assembled system AB during operational tests. These can be expressed in terms of subsystem admittances, similar to Eq. (6.5):

$$\mathbf{u}_4 = \mathbf{Y}_{41}^{AB} \mathbf{f}_1 = \mathbf{Y}_{42}^B \underbrace{(\mathbf{Y}_{22}^A + \mathbf{Y}_{22}^B)^{-1} \mathbf{Y}_{21}^A}_{\mathbf{g}_2^B} \mathbf{f}_1 \quad (6.9)$$

Next, FRFs need to be measured for the passive subsystem B, relating the motion at these indicator points to forces at the interface, namely \mathbf{Y}_{42}^B . Note that this requires dismounting of the active components from the assembly. Nevertheless, the FRFs \mathbf{Y}_{42}^B (needed for the matrix-inverse force determination) and \mathbf{Y}_{32}^B (to calculate responses at the target locations, Eq. (6.6)) can be obtained from the same FRF measurement campaign, as it only involves mounting of additional sensors. The operational interface forces can be reconstructed from a pseudo-inverse of the indicator response spectra \mathbf{u}_4 with the subsystem FRFs:

$$\mathbf{g}_2^B = (\mathbf{Y}_{42}^B)^+ \mathbf{u}_4 \quad (6.10)$$

If \mathbf{Y}_{42}^B is full rank, it holds that $(\mathbf{Y}_{42}^B)^+ \mathbf{Y}_{42}^B = \mathbf{I}$, such that in theory the correct interface forces from Eq. (6.4) are obtained by subsequent application of Eq. (6.9) and (6.10). Hence the conditioning of the FRF matrix is crucial, which should have (a) sufficient rank to describe all interface forces \mathbf{g}_2^B independently from the set \mathbf{u}_4 and (b) a reasonably low condition number in order not to amplify measurement errors in the inversion. As a rule of thumb, it is common to use at least twice as many response DoFs as strictly required to fully determine the interface forces. Much attention has been devoted to improving the conditioning of the inverse problem by means of singular value decomposition, see for instance the work of Thite and Dobson [31, 46, 204–206] or an early review of techniques [126]. Time domain implementations have also been developed, such as the inverse structural filtering methods described in [99, 157].

Recently there has been interest in application of strain gages instead of the commonly used accelerometers at the indicator points. It is argued that strain responses possess a more direct relation to interface forces and are better able to capture the local phenomena of the structure. Consequently it is expected that strain measurements lead to better conditioning of the matrix to be inverted [175, 177]. More research is currently needed to further verify this assumption.

⁴See Chap. 4 and Sec. 7.4 for a discussion on obtaining a full and reciprocal set of translational and rotational DoFs.



(a) Application of equivalent forces to the passive system AB, representing the operational excitation.

(b) Application of equivalent forces to the active system AB in opposing direction, cancelling the active operational excitation.

Figure 6.4: Component-based TPA: two explanations of the equivalent source concept.

6.3 Component-based TPA

A fundamentally different class of methods is that of the *component-based TPA*. As shown in Eq. (6.7), the interface forces obtained from a classical TPA are not a characteristic of the source alone but of the assembled dynamics. For that reason, a classical TPA cannot predict the effects of subsystem modification, as one would need to conduct a new operational test for every change in design. In other words, the interface forces measured in an assembly AB are not transferable to an assembly with another receiving side B.

Component-based TPA tries to characterise the source excitation by a set of equivalent forces or velocities that are an inherent property of the active component itself. The responses at the receiving side can be simulated by applying these forces to the FRFs of an assembled system with the active part shut down, as illustrated in Fig. 6.4a. Hence, the dynamic interaction with the passive side is accounted for in a later stage, at least not during operational measurements. This allows defining a testing environment⁵ that is ideal for operational measurement on the active component, explaining the denotation *component-based*.

Interestingly, with respect to the origin of component-based TPA theory, literature has been very ambiguous. As mentioned in Sec. 5.2, some researchers have found inspiration in acoustics or electronic network theory (particularly the equivalent source identities of Thévenin and Norton), such as [25, 49, 130, 132, 134, 151, 152]. Others derived similar theories from a structural-mechanical point of view [69, 92, 94] or dynamic substructuring techniques [101, 103]. As a consequence, a wide variety of component-based TPA methods have been derived, largely independent of each other. This section presents a more generic derivation in order to unite all component methods and compare the various concepts.

6.3.1 The equivalent source concept

Approaching the problem top-down, one is looking for a set of equivalent forces f_2^{eq} that, applied to the interface of the assembled system AB at rest, yields the correct responses at u_3 . This can be directly formulated using the admittance of the assembly Y_{32}^{AB} , or expanded in terms of its subsystem admittances:

$$u_3 = Y_{32}^{AB} f_2^{eq} = \left[Y_{32}^B (Y_{22}^A + Y_{22}^B)^{-1} Y_{22}^A \right] f_2^{eq} \tag{6.11}$$

⁵The dependency of the source excitation on the mounting conditions is discussed in Sec. 7.1.

The response \mathbf{u}_3 , as a result of the equivalent forces, should equal the response obtained when the active component is running in the same assembly, caused by \mathbf{f}_1 in Eq. (6.5). Comparing this with Eq. (6.11), it follows naturally that the equivalent forces should take the form:

$$\begin{aligned} \mathbf{Y}_{32}^B (\mathbf{Y}_{22}^A + \mathbf{Y}_{22}^B)^{-1} \mathbf{Y}_{22}^A \mathbf{f}_2^{\text{eq}} &= \mathbf{Y}_{32}^B (\mathbf{Y}_{22}^A + \mathbf{Y}_{22}^B)^{-1} \mathbf{Y}_{21}^A \mathbf{f}_1 \\ \implies \mathbf{f}_2^{\text{eq}} &= (\mathbf{Y}_{22}^A)^{-1} \mathbf{Y}_{21}^A \mathbf{f}_1 \end{aligned} \quad (6.12)$$

An alternative explanation would be that the equivalent forces, applied in the *opposite direction* to the assembly with the source in operation, must cancel out all vibrations “down-stream” of \mathbf{u}_2 . This is illustrated by Fig. 6.4b and formulated as follows:

$$\mathbf{u}_2 = \mathbf{Y}_{21}^{\text{AB}} \mathbf{f}_1 - \mathbf{Y}_{22}^{\text{AB}} \mathbf{f}_2^{\text{eq}} = \mathbf{0} \quad (6.13)$$

Development of Eq. (6.13) leads to the same equivalent force definition. Eq. (6.12) shows that the equivalent forces are indeed a property on the active component A only. The existence of such an equivalent source problem offers tremendous potential for practical component-based TPA methods. There is however one important limitation:

The equivalent forces only properly represent the operational source excitations for responses on the receiving structure or on the interface. Responses obtained on the source will be different and therefore of no use.

This limitation was already mentioned in [101, 103] and can be understood by examining the system of Eq. (6.2): responses at the passive side B are caused only by forces through or onto the interface, whereas the responses at the source side A are a result of both the direct contribution of \mathbf{f}_1 and its reflection through the coupled subsystem B.

In the next sections, several approaches are discussed that yield a set of equivalent forces from operational tests, following the definition of Eq. (6.12).

6.3.2 Component TPA: blocked force

Consider the case where the boundary of subsystem A is rigidly fixed, as depicted in Fig. 6.5a. The operational excitation \mathbf{f}_1 is entirely portrayed by the reaction forces at the “blocked” interface \mathbf{g}_2^{bl} , such that the interface displacements $\mathbf{u}_2^A = \mathbf{0}$.

$$\begin{bmatrix} \mathbf{u}_1 \\ \mathbf{u}_2 = \mathbf{0} \end{bmatrix} = \begin{bmatrix} \mathbf{Y}_{11}^A & \mathbf{Y}_{12}^A \\ \mathbf{Y}_{21}^A & \mathbf{Y}_{22}^A \end{bmatrix} \begin{bmatrix} \mathbf{f}_1 \\ \mathbf{g}_2^A = -\mathbf{g}_2^{\text{bl}} \end{bmatrix}$$

A direct relation is found, leading to the following equivalent force:

$$\mathbf{g}_2^{\text{bl}} = (\mathbf{Y}_{22}^A)^{-1} \mathbf{Y}_{21}^A \mathbf{f}_1 \implies \mathbf{f}_2^{\text{eq}} = \mathbf{g}_2^{\text{bl}} \quad (6.14)$$

The so-called *blocked-force TPA* is perhaps the most commonly known variant of component-based TPA methods because of its straight-forward applicability. It can be seen as an application of the Thévenin equivalent source problem [203], that found its way into popular mechanics halfway the 20th century [82, 174, 208]. Mathematically one can regard the blocked-force method as imposing a Dirichlet boundary condition on the active subsystem’s interface.

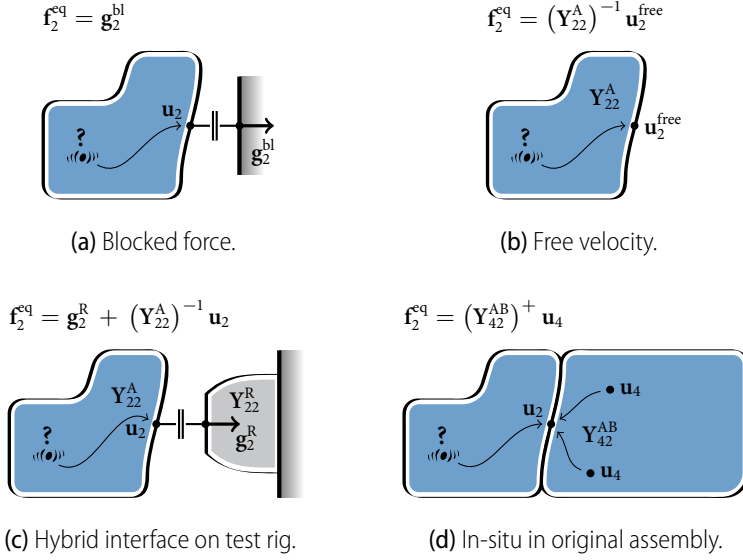


Figure 6.5: Component-based TPA methods: various approaches to obtain equivalent forces representing the excitation.

The blocked-force method assumes the boundary to be infinitely stiff in all directions, which is in practice rarely the case⁶. Hence the accuracy of the blocked forces is highly subject to the stiffness of the boundary relative to the component at hand [26, 101, 187]. An additional difficulty is the measurement of rotational moments, as most commonly used sensors are unable to measure collocated 6-DoF interface loads. As a consequence, the blocked-force method is expected to perform best at the low frequency end for which the rigid boundary assumption is most valid and rotational effects are in practice least prominent.

6.3.3 Component TPA: free velocity

The direct counterpart of the blocked-force method is the *free-velocity TPA* as depicted in Fig. 6.5b. In this case the component’s interfaces are left free, such that all vibrations are seen as “free displacements” $\mathbf{u}_2^{\text{free}}$ at the interface DoFs.

$$\begin{bmatrix} \mathbf{u}_1 \\ \mathbf{u}_2^{\text{A}} = \mathbf{u}_2^{\text{free}} \end{bmatrix} = \begin{bmatrix} \mathbf{Y}_{11}^{\text{A}} & \mathbf{Y}_{12}^{\text{A}} \\ \mathbf{Y}_{21}^{\text{A}} & \mathbf{Y}_{22}^{\text{A}} \end{bmatrix} \begin{bmatrix} \mathbf{f}_1 \\ \mathbf{g}_2^{\text{A}} = \mathbf{0} \end{bmatrix}$$

From here on, equivalent forces⁷ can be calculated by inverting the admittance measured at the free subsystem’s interfaces, which can be understood by comparing the free displacements with the blocked force definition of Eq. (6.12):

$$\mathbf{u}_2^{\text{free}} = \mathbf{Y}_{21}^{\text{A}} \mathbf{f}_1 \implies \mathbf{f}_2^{\text{eq}} = (\mathbf{Y}_{22}^{\text{A}})^{-1} \mathbf{u}_2^{\text{free}} \tag{6.15}$$

⁶For numerical analysis, the blocked-force concept can be particularly effective to reduce a distributed load on the active component to fewer DoFs of the interfaces. This was demonstrated for transient simulation of offshore structures [210].

⁷If the admittances of the subsystems are available separately, one may also apply the free velocities directly, as shown in [167, 182].

Analogue to the blocked-force TPA, this method can be seen as a strict application of a Neumann boundary condition and is furthermore related to Norton's equivalent source theorem for electric networks [141]. Again, imposing free boundary conditions can be troublesome as the vibrating system often needs to be mounted at one or more connection points to be able to run in operation. Therefore the method is in practice expected to perform best for frequencies well above the rigid body modes of the structure. Also note that effects such as friction and damping, which would occur at the interfaces of the assembled system, are absent in the operational measurement on the free component.

► *Origin of the free velocity concept*

The fact that the method makes reference to free velocities rather than free displacements has an historical motive, as the former quantity is commonly applied in acoustical engineering in combination with acoustic pressure. For such acoustic problems, dynamic coupling of admittance is normally discarded. This is a fair assumption, considering that the impedance of the radiating source is much larger than the impedance of the receiving surrounding fluid, i.e. air. In structure-borne vibrations the source and receiving system often exhibit similar dynamics, hence explicit coupling is needed. This was realised for a single-DoF problem by means of a non-dimensional coupling function in [130]. Extensions to multi-DoF systems and further discussion of this topic are found in [132, 151, 152]. Finally, it is worth mentioning that the free-velocity concept has been standardised into an ISO norm for characterisation of structure borne sound sources [88].

6.3.4 Component TPA: hybrid interface

As both above-mentioned methods pose their limitations in practice, one often prefers to conduct operational tests on an appropriate support structure. Such a coupled structure unavoidably displays its own dynamics on the interfaces, which need to be accounted for in order to render the equivalent forces independent of any connected part. Let us therefore imagine the active component fixed onto a test bench or test rig R as illustrated in Fig. 6.5c. Denoting the interface admittance of the test rig by Y_{22}^R , we obtain for the extended system of equations:

$$\begin{bmatrix} \mathbf{u}_1^A \\ \mathbf{u}_2^A \\ \mathbf{u}_2^R \end{bmatrix} = \begin{bmatrix} Y_{11}^A & Y_{12}^A & \mathbf{0} \\ Y_{21}^A & Y_{22}^A & \mathbf{0} \\ \mathbf{0} & \mathbf{0} & Y_{22}^R \end{bmatrix} \begin{bmatrix} \mathbf{f}_1 \\ \mathbf{g}_2^A \\ \mathbf{g}_2^R \end{bmatrix} \quad (6.16)$$

The following interface conditions apply:

$$\begin{cases} \mathbf{u}_2^A = \mathbf{u}_2^R \\ \mathbf{g}_2^A = -\mathbf{g}_2^R \end{cases}$$

After enforcing the compatibility and equilibrium conditions on the interface DoFs, a derivation similar to Sec. 6.1.2 can be followed to find the operational interface forces \mathbf{g}_2^R . These forces are now dependent on the properties of both the active component A and the test rig R. Substituting the forces back into the second row of Eq. (6.16), the corresponding

interface displacements \mathbf{u}_2 are obtained as well (the superscript on \mathbf{u}_2 has been dropped because of compatibility):

$$\begin{cases} \mathbf{g}_2^R = (\mathbf{Y}_{22}^A + \mathbf{Y}_{22}^R)^{-1} \mathbf{Y}_{21}^A \mathbf{f}_1 & (6.17a) \end{cases}$$

$$\begin{cases} \mathbf{u}_2 = [\mathbf{I} - \mathbf{Y}_{22}^A (\mathbf{Y}_{22}^A + \mathbf{Y}_{22}^R)^{-1}] \mathbf{Y}_{21}^A \mathbf{f}_1 & (6.17b) \end{cases}$$

Eq. (6.17a–6.17b) hold for any \mathbf{Y}_{22}^R , as long as no external force is acting on the test rig. The desired set of equivalent forces Eq. (6.12) is obtained by combining Eq. (6.17a) and (6.17b) in such way that the dynamics of the test rig \mathbf{Y}_{22}^R are eliminated.

$$\mathbf{f}_2^{\text{eq}} = (\mathbf{Y}_{22}^A)^{-1} \mathbf{Y}_{21}^A \mathbf{f}_1 \iff \mathbf{f}_2^{\text{eq}} = \mathbf{g}_2^R + (\mathbf{Y}_{22}^A)^{-1} \mathbf{u}_2 \quad (6.18)$$

As it turns out, Eq. (6.18) forms the sum of contributions of both the blocked force and the free velocity experiment, respectively Eq. (6.14) and Eq. (6.15). One could therefore speak of a *hybrid interface* condition, or Robin boundary condition in a mathematical sense. It can indeed be verified that Eq. (6.17a–6.17b) converge⁸ to the blocked forces for $\mathbf{Y}^R \rightarrow \mathbf{0}$ and to free velocities when $\mathbf{Y}^R \rightarrow \infty$.

The hybrid interface approach combining force and motion was originally published in [103]; the displacement term was regarded in this work as the “non-rigid test bench compensation” to the imperfect blocked forces. Although generally applicable in theory, it should be mentioned that the method can be rather costly and time-consuming in practice, as one needs to explicitly measure collocated forces and motion in all directions for every interface node [26].

In lack of force measurement, one may substitute the third row of Eq. (6.16) for \mathbf{g}_2^B . The so obtained approach was suggested in [187] and takes displacement measurement only:

$$\mathbf{f}_2^{\text{eq}} = (\mathbf{Y}_{22}^R)^{-1} \mathbf{u}_2 + (\mathbf{Y}_{22}^A)^{-1} \mathbf{u}_2 \quad (6.19)$$

The price for not having to measure interface forces is that separate FRF measurements should now be conducted, to obtain the subsystem admittances of the active component and the test rig.

6.3.5 Component TPA: *in-situ*

Looking again at Eq. (6.19), we observe that the two inverted admittance FRF matrices in fact represent the dynamic stiffness matrices of respectively structure A and R for the same set of collocated interface DoFs. They can be combined by simple impedance addition, as is standard practice for primal impedance assembly (see Sec. 3.3.1):

$$\mathbf{f}_2^{\text{eq}} = (\mathbf{Z}_{22}^R + \mathbf{Z}_{22}^A) \mathbf{u}_2 = \mathbf{Z}_{22}^{\text{AR}} \mathbf{u}_2 \quad (6.20)$$

The result of Eq. (6.20) is indeed indifferent to the dynamics of R or any other mounting structure that component A is connected to.

Transforming back to admittance notation, we find that the blocked forces can be calculated inversely from the combined admittance of the assembly’s interface. Alternatively, it

⁸A intuitive presentation of the range between the two limit cases is given in [132].

can be posed in an overdetermined fashion using a sufficient set of indicator DoFs \mathbf{u}_4 on the receiving subsystem:

$$\mathbf{f}_2^{\text{eq}} = (\mathbf{Y}_{22}^{\text{AR}})^{-1} \mathbf{u}_2 \quad \text{or} \quad \mathbf{f}_2^{\text{eq}} = (\mathbf{Y}_{42}^{\text{AR}})^+ \mathbf{u}_4 \quad (6.21)$$

Obtained from a different derivation, the approach of Eq. (6.21) has first been proposed by Moorhouse & Elliott as the *in-situ* method [49, 134]. As the name implies, the operational measurement may even be conducted in the target assembly AB, avoiding dismounting of any part, namely:

$$\mathbf{f}_2^{\text{eq}} = (\mathbf{Y}_{22}^{\text{AB}})^{-1} \mathbf{u}_2 \quad \text{or} \quad \mathbf{f}_2^{\text{eq}} = (\mathbf{Y}_{42}^{\text{AB}})^+ \mathbf{u}_4 \quad (6.22)$$

The equivalent forces resulting from application of Eq. (6.22) are nonetheless a property of component A only and thus transferable to an assembly with another passive side.

The in-situ force determination procedure is illustrated in Fig. 6.5d. Indeed, Eq. (6.22) represents the inverse of Eq. (6.11), yet with an extended set of response DoFs in order to render the system (over)determined and thus invertible. As a consequence, the method shows great resemblance with the classical matrix-inverse method of Eq. (6.10), the difference being the choice for the assembled admittance instead of the passive subsystem's admittance. Similar techniques regarding matrix conditioning (e.g. overdetermination, singular value rejection) apply as well to the in-situ method. Most remarkable is that the receiving side can be chosen arbitrarily, as the equivalent forces identified by Eq. (6.21) or (6.22) are theoretically invariant of any subsystem coupled to it. In that respect, two important conditions need to be kept in mind:

1. Operational excitations \mathbf{f}_1 may only originate from the domain of component A. Any excitation coming from the passive side will disturb the determination of equivalent forces.
2. Although the responses used for the matrix inversion (\mathbf{u}_2 or \mathbf{u}_4) can be positioned rather arbitrarily, they are bounded to the domain of the interface and the passive side. This relates back to the remark made after Eq. (6.12): vibrations at the source structure are not only caused by the interface forces but also by the source excitations directly.

Physically one could interpret the in-situ method as follows: knowing the transfer functions from the interface DoFs to several points on the passive side, Eq. (6.21) or (6.22) seeks for a set of equivalent forces \mathbf{f}_2^{eq} that, applied to the interface DoFs of the assembled structure, generates the same responses \mathbf{u}_4 at the passive side. Given that this response set is overdetermined, the equivalent forces are calculated such that they minimise the sum of the squared errors (or l^2 -norm) in the extended set \mathbf{u}_4 . Similar ideas are used in the field of experimental substructure decoupling [42, 193, 220]: the identification of the forces that decouple the residual substructure can be improved by defining an “extended interface”, adding some additional DoFs on the structure of interest distant from the interface. This method has been discussed in Sec. 3.4.3.

Several numerical and experimental studies of in-situ source characterisation have been reported [25, 50, 52, 112, 122, 187, 188]. A time-domain force reconstruction algorithm was proposed by Sturm [199, 200]; see also Sec. 7.6. Further generalisation of the in-situ concept can be found in the pseudo-forces method that is discussed next.

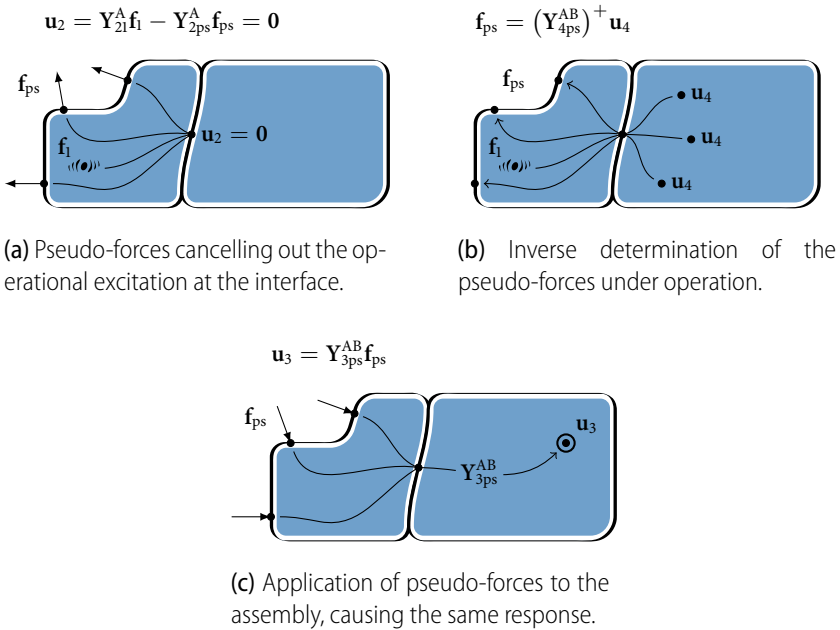


Figure 6.6: The concept of the pseudo-forces component TPA method.

6.3.6 Component TPA: pseudo-forces

The last member of the component-based TPA family to discuss is the *pseudo-forces* method as proposed by Janssens and Verweij in the late 1990s [92–94]. It assumes the existence of a non-unique set of pseudo-forces acting on the outer surface of the active component, cancelling out the effect of the operational vibrations transmitted through the interface to the passive side. This is illustrated in Fig. 6.6a. If those forces are now applied in opposite direction to the assembly with the source shut-down, an identical response at the receiving side should be obtained, see Fig. 6.6c. In other words, the pseudo-forces are supposed to represent the source excitation for responses at the passive side.

The fact that it can be regarded as a component TPA method lies in the former assumption: if there exists a set of pseudo-forces that cancels out the operational dynamics at the interface, the responses beyond this interface shall be zero as well, hence these forces are invariant of any structure attached to it. A similar reasoning may be applied to the previously discussed equivalent force methods, yet the locations of the pseudo-forces are not bounded to the interface but extend to the full domain of the active component.

The actual determination of the pseudo-forces is carried out slightly differently. The first step is to define a set of s pseudo-forces \mathbf{f}_{ps} on the active component that is

- (a) sufficient to represent the excitation source;
- (b) easily accessible for impact or shaker measurement.

One could think of a minimum of $s = 6$ forces when the interface behaviour can be considered as rigid, or a larger number in case of more intricate connectivity. Secondly, a set of $n \geq s$ indicator response DoFs has to be chosen on the passive side from which the operational excitation is monitored. These responses are denoted by \mathbf{u}_4 and can be written

as a result of \mathbf{f}_1 , similar to Eq. (6.9):

$$\mathbf{u}_4 = \mathbf{Y}_{41}^{AB} \mathbf{f}_1 = \mathbf{Y}_{42}^B (\mathbf{Y}_{22}^A + \mathbf{Y}_{22}^B)^{-1} \mathbf{u}_{2,\mathbf{f}_1}^{\text{free}} \quad \text{with} \quad \mathbf{u}_{2,\mathbf{f}_1}^{\text{free}} \triangleq \mathbf{Y}_{21}^A \mathbf{f}_1 \quad (6.23a)$$

A substitution is made here using the free velocity caused by the excitation \mathbf{f}_1 , or in other words: the theoretical motion at the interface of component A if the interfaces were left free, see also Sec. 6.3.3. This is by no means a quantity that needs to be measured, but will prove useful for the derivation later on.

The next step is to determine pseudo-forces \mathbf{f}_{ps} that best recreate the operational responses at the indicator DoFs \mathbf{u}_4 when the source excitation is shut down. Note that the assumption is similar to the equivalent forces problem stated in Sec. 6.3.1, yet the pseudo-forces act on the outer surface of the active component rather than its interfaces. Similar to Eq. (6.23a), the response at the indicator DoFs as a result of the pseudo-forces reads:

$$\mathbf{u}_4 = \mathbf{Y}_{4\text{ps}}^{AB} \mathbf{f}_{\text{ps}} = \mathbf{Y}_{42}^B (\mathbf{Y}_{22}^A + \mathbf{Y}_{22}^B)^{-1} \mathbf{u}_{2,\mathbf{f}_{\text{ps}}}^{\text{free}} \quad \text{with} \quad \mathbf{u}_{2,\mathbf{f}_{\text{ps}}}^{\text{free}} \triangleq \mathbf{Y}_{2\text{ps}}^A \mathbf{f}_{\text{ps}} \quad (6.23b)$$

Now, the pseudo-forces \mathbf{f}_{ps} that best describe the operational source excitations are found from solving an overdetermined system with the response set \mathbf{u}_4 that was measured under operation (see Fig. 6.6b):

$$\mathbf{f}_{\text{ps}} = (\mathbf{Y}_{4\text{ps}}^{AB})^+ \mathbf{u}_4 \quad (6.24)$$

It can be shown that these forces, under certain conditions, are a property of component A only. A sufficient condition is that the free interface velocities $\mathbf{u}_2^{\text{free}}$ as a result of the original source excitation can be fully represented by the set of pseudo-forces determined from Eq. (6.24). In that case the definitions of Eq. (6.23a) and Eq. (6.23b) may be equated and one finds that the pseudo-forces are specific to the source component:

$$\mathbf{u}_{2,\mathbf{f}_{\text{ps}}}^{\text{free}} = \mathbf{u}_{2,\mathbf{f}_1}^{\text{free}} \quad \implies \quad \mathbf{f}_{\text{ps}} = (\mathbf{Y}_{2\text{ps}}^A)^+ \mathbf{Y}_{21}^A \mathbf{f}_1 \quad (6.25)$$

Applying these pseudo-forces to the FRFs of an assembled system of interest, i.e. $\mathbf{Y}_{3\text{ps}}^{AB}$, it can be verified that the correct receiver responses \mathbf{u}_3 at the passive side are obtained:

$$\mathbf{u}_3 = \mathbf{Y}_{3\text{ps}}^{AB} \mathbf{f}_{\text{ps}} = \left[\mathbf{Y}_{32}^B (\mathbf{Y}_{22}^A + \mathbf{Y}_{22}^B)^{-1} \mathbf{Y}_{2\text{ps}}^A \right] (\mathbf{Y}_{2\text{ps}}^A)^+ \mathbf{Y}_{21}^A \mathbf{f}_1 = \mathbf{Y}_{31}^{AB} \mathbf{f}_1 \quad (6.26)$$

The pseudo-forces determined from Eq. (6.24) are indeed transferable to an assembly with another passive side. Eq. (6.26) yields the responses for this new assembly, provided that the columns of the FRF matrix $\mathbf{Y}_{3\text{ps}}^{AB}$ correspond to the same pseudo-forces, i.e. excitation points at the source.

The previously discussed in-situ method can be regarded as a special case of the pseudo-force method, namely for the case where the pseudo-forces are really located at the interfaces. The pseudo-forces calculated from Eq. (6.24) shall then equal the equivalent (blocked) forces from Eq. (6.12), namely $\mathbf{f}_{\text{ps}} = \mathbf{f}_2^{\text{eq}}$. With regard to the positioning of the indicator DoFs \mathbf{u}_4 , the same restriction holds as for the in-situ method, namely that they must be located at the passive system B or at the interface⁹.

⁹The contrary was erroneously stated in the original work [92].

A related idea was proposed [103] to calculate pseudo-forces (or *substitute forces* in the original work) from equivalent forces, in turn obtained from test bench measurements:

$$\mathbf{f}_{ps} = (\mathbf{Y}_{2ps}^A)^+ \mathbf{Y}_{22}^A \mathbf{f}_2^{eq}$$

To find the receiver responses \mathbf{u}_3 , Eq. (6.26) can now be applied instead of Eq. (6.11). This is useful if \mathbf{Y}_{32}^{AB} is unmeasurable, namely when the interfaces of the assembled system AB are inaccessible for FRF measurement.

► A short discussion on component TPA terminology

This section on component-based TPA designates five practical methods to obtain an equivalent force description of a source. The forces are, according to the theory, independent of any structure that was mounted to it under measurement. This principle on its own is sometimes referred to as *source characterisation*; see for instance [25, 72, 112, 152]. In that respect, source characterisation can be seen as part of a transfer path analysis, namely the activity of describing the source; whereas the full analysis is completed by adding the transfer characteristics of the targeted assembly.

Another ambiguity lies in the wordings *equivalent force*, *blocked force* and *pseudo-force*. In a most general contemplation, we have considered the component-based TPA as the structural-mechanical analogue of the equivalent source problem of Thévenin [203] and Norton, as previously mentioned in Sec. 5.2.1, 6.3.2 and 6.3.3. The term *equivalent force* is thereby justified as a general set of forces that can be substituted for the operational excitation. *Blocked force* is on one hand the logical structural-mechanical interpretation of the equivalent force, but on the other hand only concerns the forces that act on the interface DoFs and consequently block them. In other words, the blocked-forces can be seen as a subclass of equivalent forces, namely those that act at the interface. This allows us to define the other subclass, namely the *pseudo-forces*, as forces applied elsewhere on the active structure, causing some other responses in the passive structure to become zero.

This quibble in terminology is mostly an unintended side-effect of re-interpreting a couple of practical TPA methods from very different origins. In order to further generalise the component TPA theory, the following section proposes an alternative interpretation, inspired on the LM-FBS notation of Sec. 3.3.3. ◀

6.3.7 Component TPA: relation to LM-FBS

The methods in the family of component-based TPA, as outlined in Sec. 6.3, can be used to measure the operational excitation of an active system in a test assembly and simulate for an assembly with a different passive side. It was shown that any influence of the test structure can be cancelled out by appropriate matrix-inverse operations, i.e. Eq. (6.18) for the mixed interface, Eq. (6.21) for the in-situ and Eq. (6.24) for the pseudo-forces approach. In general, it can be stated that the active component with dynamics \mathbf{Y}^A can be measured in some alternative test assembly \mathbf{Y}^{AR} , to simulate the passive-side response in a different target assembly \mathbf{Y}^{AB} .

Let us illustrate this by looking at the governing equations of the in-situ application, or more specifically the test rig variant of Eq. (6.21) with indicator responses \mathbf{u}_4 . The full

This leads to the following choices for \mathbf{B}_c and \mathbf{B}_e :

$$\begin{cases} \mathbf{B}_c \triangleq \begin{bmatrix} \mathbf{0} & \mathbf{0} & -\mathbf{I} & , & \mathbf{0} & \mathbf{0} & \mathbf{0} \end{bmatrix} \\ \mathbf{B}_e \triangleq \begin{bmatrix} \mathbf{0} & -\mathbf{I} & \mathbf{0} & , & \mathbf{0} & \mathbf{I} & \mathbf{0} \end{bmatrix} \end{cases} \quad (6.29b)$$

Let us now examine the consequences of the definitions above. First, the compatibility condition sets the displacements of the indicator DoFs of AR to zero, but leaves all DoFs of AB free:

$$\mathbf{B}_c \mathbf{u} = \mathbf{0} \quad \implies \quad -\mathbf{u}_4^{\text{AR}} = \mathbf{0} \quad (6.30)$$

This means that the incompatibility is fully determined by the responses measured on AR. Next, this incompatibility must be resolved by a set of forces, determined by the choice for \mathbf{B}_e . In this particular case, these are forces on the interface \mathbf{g}_2 . Let us continue by following the standard procedures of LM-FBS to determine the Lagrange multiplier forces:

$$\boldsymbol{\lambda} = (\mathbf{B}_c \mathbf{Y} \mathbf{B}_e^T)^+ \mathbf{B}_c \mathbf{Y} \mathbf{f}$$

Taking note of the current choices for the Boolean matrices, we can write out the operations above and obtain the following expression for $\boldsymbol{\lambda}$:

$$\boldsymbol{\lambda} = -(\mathbf{Y}_{42}^{\text{AR}})^+ \mathbf{Y}_{41}^{\text{AR}} \mathbf{f}_1 \quad \implies \quad \boldsymbol{\lambda} = -\mathbf{f}_2^{\text{eq}} \quad (6.31)$$

It appears that the Lagrange-multiplier forces, computed by application of LM-FBS, equal the equivalent force as a result of Eq. (6.27a) and (6.27b), yet with a minus sign. In other words, the equilibrium forces computed using LM-FBS with the definitions of Eq. (6.29) yield equivalent forces that describe the source system A, determined in test environment AR.

To finalise the substructuring procedure, let us continue by applying the Lagrange multipliers to the “uncoupled” block-diagonal admittance of Eq. (6.29a):

$$\mathbf{u} = \mathbf{Y} \mathbf{f} + \mathbf{Y} \mathbf{g} = \mathbf{Y} \mathbf{f} - \mathbf{Y} \mathbf{B}_e^T \boldsymbol{\lambda}$$

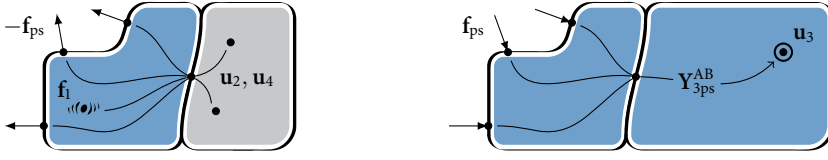
Writing out the operation for the current Boolean matrices, the following expression is obtained for prediction of the receiver responses in the targeted assembly AB:

$$\mathbf{u}_3^{\text{AB}} = \mathbf{0} + \mathbf{Y}_{32}^{\text{AB}} \mathbf{f}_2^{\text{eq}} = \mathbf{Y}_{32}^{\text{AB}} (\mathbf{Y}_{42}^{\text{AR}})^+ \mathbf{Y}_{41}^{\text{AR}} \mathbf{f}_1 \quad (6.32)$$

The expression on the right-hand side is identical to Eq. (6.28). This demonstrates that the in-situ determination on a test structure AR, as well as the application of the equivalent forces to a target assembly AB, can be written in a single step using familiar LM-FBS notation:

$$\mathbf{u}^{\text{pred}} = \mathbf{u}^{\text{meas}} - \mathbf{Y} \mathbf{B}_e^T (\mathbf{B}_c \mathbf{Y} \mathbf{B}_e^T)^+ \mathbf{B}_c \mathbf{u}^{\text{meas}} \quad (6.33)$$

Here, \mathbf{u}^{meas} is the input vector of the operational measurement, comprising non-zero terms on the first three elements related the test assembly AR and zeros on the elements of AB; \mathbf{u}^{pred} is the TPA prediction vector which is only valid for the elements that belong to the passive side of the target assembly AB, i.e. the responses of interest. The only difference with Eq. (3.25) is that operational responses \mathbf{u}^{meas} are substituted for the terms $\mathbf{Y} \mathbf{f}$, as the excitation forces \mathbf{f}_1 are never explicitly obtained by measurement.



(a) Source characterisation in AR by means of pseudo-forces, determined on a test rig (grey). (b) Application of pseudo-forces to targeted assembly AB to predict the receiver responses.

Figure 6.7: The LM-FBS generalisation of the in-situ and pseudo-force concept for source characterisation on a test rig.

A general component TPA notation

The notation of Eq. (6.33) offers a convenient mechanism to overdetermine the problem, or rather, control the observability and controllability of the transfer path problem. For instance, let us consider the following choice for the Boolean matrices, with regard to the matrix definitions of Eq. (6.29):

$$\left\{ \begin{array}{l} \mathbf{B}_c \triangleq \begin{bmatrix} \mathbf{0} & -\mathbf{I} & \mathbf{0} & , & \mathbf{0} & \mathbf{0} & \mathbf{0} \\ \mathbf{0} & \mathbf{0} & -\mathbf{I} & , & \mathbf{0} & \mathbf{0} & \mathbf{0} \end{bmatrix} \\ \mathbf{B}_e \triangleq \begin{bmatrix} \mathbf{0} & \mathbf{0} & -\mathbf{I} & , & \mathbf{0} & \mathbf{0} & \mathbf{1} \end{bmatrix} \end{array} \right.$$

This choice uses both \mathbf{u}_2^{AR} and \mathbf{u}_4^{AR} to estimate a set of pseudo-forces \mathbf{f}_{ps} in an overdetermined fashion. More precisely, the pseudo-forces are found as the set that does the best job in cancelling out the operational excitation (this is a similar reasoning as Eq. (6.13)):

$$\mathbf{f}_{ps} = \underset{\mathbf{f}_{ps} \in \mathbb{R}^s}{\operatorname{argmin}} \left(\boldsymbol{\delta}^T \boldsymbol{\delta} \right) \quad \text{with} \quad \boldsymbol{\delta} = \begin{bmatrix} \mathbf{u}_2^{AR} \\ \mathbf{u}_4^{AR} \end{bmatrix}^{\text{meas}} - \begin{bmatrix} \mathbf{Y}_{2ps}^{AR} \\ \mathbf{Y}_{4ps}^{AR} \end{bmatrix} \mathbf{f}_{ps}$$

These pseudo-forces are equivalently represented in the system definition of AB, hence can be transported to the targeted assembly in a physically correct way. Fig. 6.7 illustrates both steps. Essentially, the concept of overdetermination with internal points is applied similarly in substructure decoupling. This particular case could be referred to as the *non-allocated overdetermined* interface definition, see Sec. 3.4.3.

Concluding, we can state that Eq. (6.33) generalises the in-situ as well as the pseudo-force method. The free velocity method can also be performed, namely by replacing the test assembly AR by the free source component A. Note that, although \mathbf{u}_2^A is the only possible choice regarding the responses, pseudo-forces \mathbf{f}_{ps} can in fact be used to replace equivalent interface forces \mathbf{f}_2 , which was not yet observed in Sec. 6.3.3.

6.4 Transmissibility-based TPA

The two previously discussed families of TPA have in common that they attempt to model the vibration transmission in a physically correct sense, namely by determining as many forces and moments as required to describe the subsystem connectivity in full. Consequently, both families require measurement of the corresponding FRFs for the interface DoFs to the receiving response locations. It is evident that this approach ultimately reveals

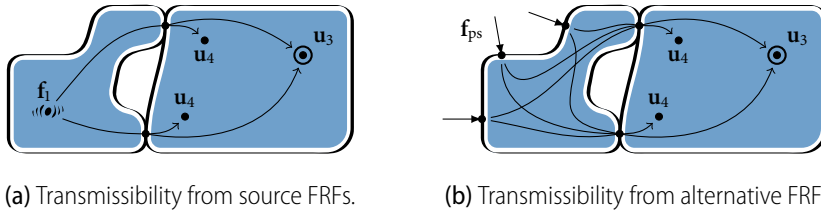


Figure 6.8: The transmissibility concept for an example with two connection points.

a wealth of information on the particular functioning of the active component, force distribution over the interface, resonances in the structure, etc. If however the mere purpose of a TPA is to identify the dominant path contributions in the assembled product, the efforts to set up and conduct the full experiment can be fairly disproportionate and costly. This is especially the case when multiple incoherent vibration sources are to be investigated.

The last family to discuss avoids the stage of explicit force determination. Instead the path contributions are determined from so-called “transmissibilities” between sensors, possibly calculated from operational measurements. Various methods are discussed in the following sections, that share the following properties:

1. Measurements are conducted on the assembled product only, saving time to dismount the active components. In fact the interfaces between the active and passive components are no longer of principal interest.
2. Path contributions are determined from well-chosen indicator points around the sources or connections. These indicator points function as inputs to the TPA.
3. The result of the analysis is highly subject to the choice for these indicator points; care should therefore be taken to include all transmission paths.

The family of *transmissibility-based TPA* methods indeed departs from the traditional source-transfer-receiver model that assumes a physically meaningful set of loads, FRFs and responses. Although potentially less accurate, methodologies derived from this concept tend to be easy to set up, versatile concerning sensor type and particularly effective for ranking contributions from several sources. From a practical point of view, transmissibility-based TPA tries to outrun the physically correct methods by its ability to conduct multiple cycles in shorter time. Nevertheless, under certain conditions, results of similar (or even equivalent) accuracy can be achieved in comparison with classical and component-based TPA methods.

6.4.1 The transmissibility concept

To discuss the theoretical concepts behind transmissibility-based methods, consider an assembled system AB with two connection points¹⁰ as shown in Fig. 6.8a. The active side contains a vibration mechanism that is characterised by internal forces f_1 ; the receiver responses at the passive side are denoted by n_3 DoFs in u_3 . To monitor the vibrations transmitted across the interfaces, n_4 indicator DoFs u_4 are positioned around the connection

¹⁰An example with two connection points was chosen here merely to provide better insight into some important cross-correlation properties. There is no fundamental consequence for the generality of the methods derived.

points.

Let us first assume that the source excitation \mathbf{f}_1 can be described by n_1 forces (or independent force distributions) and that FRFs are measurable for all of the above-mentioned DoFs in the assembly. The equations for the passive-side responses then read:

$$\begin{cases} \mathbf{u}_3 = \mathbf{Y}_{31}^{\text{AB}} \mathbf{f}_1 & \text{for } n_3 \text{ receiver DoFs} \\ \mathbf{u}_4 = \mathbf{Y}_{41}^{\text{AB}} \mathbf{f}_1 & \text{for } n_4 \text{ indicator DoFs} \end{cases} \quad (6.34\text{a})$$

$$\quad (6.34\text{b})$$

Provided that $n_4 \geq n_1$ and $\mathbf{Y}_{41}^{\text{AB}}$ is full rank, all excitation forces \mathbf{f}_1 are observable from \mathbf{u}_4 . Hence Eq. (6.34b) can be inverted and substituted into Eq. (6.34a). The responses \mathbf{u}_3 are now expressed in terms of the DoFs \mathbf{u}_4 that can be measured under operation:

$$\mathbf{u}_3 = \mathbf{T}_{34, \mathbf{f}_1}^{\text{AB}} \mathbf{u}_4 \quad \text{with} \quad \mathbf{T}_{34, \mathbf{f}_1}^{\text{AB}} \triangleq \mathbf{Y}_{31}^{\text{AB}} (\mathbf{Y}_{41}^{\text{AB}})^+ \quad (6.35)$$

The so obtained transmissibility matrix relates motion at the indicator DoFs \mathbf{u}_4 (the inputs) to the receiver DoFs \mathbf{u}_3 (the outputs) for excitation forces \mathbf{f}_1 . Interestingly, the size of the transmissibility matrix has become $n_3 \times n_4$, obfuscating the n_1 excitations associated with the original FRFs. This raises the question which excitations are really needed to construct the transmissibility matrix and to what extent this matrix is generally valid for the problem ($\mathbf{u}_4 \rightarrow \mathbf{u}_3$) under different excitations of the source structure.

To gain more insight in the transmissibility problem stated by Eq. (6.35), let us expand Eq. (6.34a) and (6.34b) in terms of the subsystems' admittances. As seen in previous derivations, the forces that couple the subsystems are identical for all responses at the passive side due to excitation at the active side. This property can be utilised in the expansion of Eq. (6.34a) and (6.34b):

$$\begin{bmatrix} \mathbf{u}_3 \\ \mathbf{u}_4 \end{bmatrix} = \begin{bmatrix} \mathbf{Y}_{31}^{\text{AB}} \\ \mathbf{Y}_{41}^{\text{AB}} \end{bmatrix} \mathbf{f}_1 = \begin{bmatrix} \mathbf{Y}_{32}^{\text{B}} \\ \mathbf{Y}_{42}^{\text{B}} \end{bmatrix} (\mathbf{Y}_{22}^{\text{A}} + \mathbf{Y}_{22}^{\text{B}})^{-1} \mathbf{Y}_{21}^{\text{A}} \mathbf{f}_1$$

In other words, the above equations are identical up to the admittance term that concerns the propagation in B from the interface \mathbf{u}_2 to respectively \mathbf{u}_3 and \mathbf{u}_4 . Recalling now the expressions for the interface force and free velocity, respectively Eq. (6.4) and Eq. (6.15), the following substitutions can be made:

$$\begin{bmatrix} \mathbf{u}_3 \\ \mathbf{u}_4 \end{bmatrix} = \begin{bmatrix} \mathbf{Y}_{32}^{\text{B}} \\ \mathbf{Y}_{42}^{\text{B}} \end{bmatrix} \mathbf{g}_2^{\text{B}} \quad (6.36)$$

with $\begin{cases} \mathbf{g}_2^{\text{B}} = (\mathbf{Y}_{22}^{\text{A}} + \mathbf{Y}_{22}^{\text{B}})^{-1} \mathbf{u}_2^{\text{free}} & \text{for } n_2 \text{ interface forces} \\ \mathbf{u}_2^{\text{free}} = \mathbf{Y}_{21}^{\text{A}} \mathbf{f}_1 & \text{for } n_2 \text{ free velocities} \end{cases}$

Hence, Eq. (6.36) shows that the transmission of vibrations from n_1 forces \mathbf{f}_1 to n_4 responses \mathbf{u}_4 is limited by the number of DoFs of the interface forces / displacements n_2 . This means that the interface acts as a *bottleneck*: it limits the effective rank of the transmissibility problem to a maximum of n_2 . Furthermore, Eq. (6.36) exposes two interesting properties of the transmissibility concept:

1. Regarding the source excitation, Eq. (6.36) shows a direct relation between the interface forces \mathbf{g}_2^{B} of the coupled system and the theoretical free velocities $\mathbf{u}_2^{\text{free}}$ at the

disconnected interfaces of component A. As understood from the component-based TPA methods, various sets of forces can be defined that equivalently produce these free interface velocities $\mathbf{u}_2^{\text{free}}$, such as the pseudo-forces of Eq. (6.23b). This is illustrated in Fig. 6.8b. In fact, any set of forces on the source that renders the interface fully *controllable* will guarantee convergence to a transmissibility matrix that generally captures the transmission of vibrations caused in component A. This property is used in the operational TPA method as discussed in the next section.

2. Regarding the transmissibility, the problem ($\mathbf{u}_4 \rightarrow \mathbf{u}_3$) is in fact *specific to the passive side only*, provided that the interface forces \mathbf{g}_2^{B} are fully observable from \mathbf{u}_4 . That means that the second line of Eq. (6.36) can be inverted, which is equivalent to Eq. (6.10) from the classical matrix-inverse method. With respect to transmissibility-based TPA, it implies that if \mathbf{u}_4 is chosen in such way that all interface forces are *observable*, \mathbf{g}_2^{B} can be eliminated from Eq. (6.36) and the transmissibility matrix becomes a property of the passive side only:

$$\mathbf{u}_3 = \mathbf{T}_{34}^{\text{B}} \mathbf{u}_4 \quad \text{with} \quad \mathbf{T}_{34}^{\text{B}} \triangleq \mathbf{Y}_{32}^{\text{B}} (\mathbf{Y}_{42}^{\text{B}})^+ \quad (6.37)$$

An elegant duality can be observed here with the component-based TPA concept that characterises the excitation as a property of the source component. More properties of the transmissibility matrix are discussed in [75, 227].

Summarising, it can be stated that the controllability is a property of the source component A, whereas the observability is specific to the receiving structure B. If both conditions are satisfied, Eq. (6.35) and (6.37) generate the same transmissibility matrix, so $\mathbf{T}_{34}^{\text{AB}} = \mathbf{T}_{34}^{\text{B}}$ or simply \mathbf{T}_{34} . The pseudo-inversion step involved in Eq. (6.35) or (6.37) “decorrelates” the transmissibility columns associated with \mathbf{u}_4 into linearly independent contributions to the receiver DoFs \mathbf{u}_3 , such that an element of \mathbf{T}_{34} is defined as follows:

$$T_{ij} \triangleq \left. \frac{u_i}{u_j} \right|_{u_{k \neq j} = 0} \quad \begin{cases} u_i \in \mathbf{u}_3 \\ u_j, u_k \in \mathbf{u}_4 \end{cases}$$

This process is often referred to as cross-talk cancellation (CTC). Note that this concerns a spatial or “modal” decorrelation¹¹ only, just like other methods involving FRF matrix inversion. It should therefore by no means be understood as some special signal processing step.

In practice, to obtain \mathbf{T}_{34} from FRFs as illustrated by Fig. 6.8a or 6.8b, one requires sufficient excitations and indicator DoFs to respectively *control* and *observe* the dynamics at the interface (this is further discussed in Sec. 7.5). However, the foremost reason for using a transmissibility-based TPA method is to identify source path contributions without the need to conduct a tedious FRF measurement campaign. The next section discusses how to obtain \mathbf{T}_{34} from operational responses only.

6.4.2 Operational transfer path analysis (OTPA)

The transmissibility matrix \mathbf{T}_{34} can be estimated statistically from the correlation between \mathbf{u}_3 and \mathbf{u}_4 when monitored under a variety of operational test conditions. The fundamental

¹¹This decorrelation has been approached in several ways: for instance based on so-called global and direct transmissibility functions (GTDf) in the work of Magrans and Guasch [74–76, 123] or by means of conventional FRFs as seen in Varoto & McConnell and Ribeiro et al. [125, 163, 164, 216].

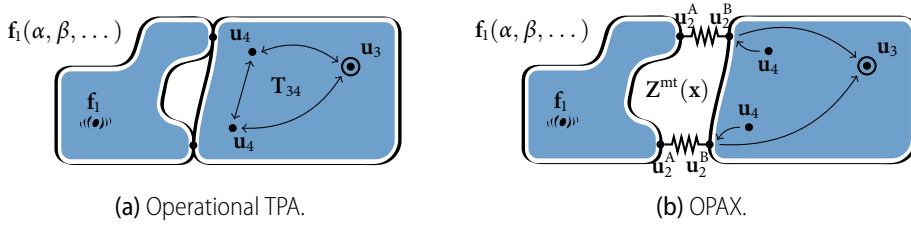


Figure 6.9: Transmissibility-based TPA approaches; the source excitation \mathbf{f}_1 depends on operational parameters (α, β, \dots) such as engine speed or torque.

assumption is that, by testing the vibration source under different operational conditions (e.g. a motor operating at different speeds or torques), multiple load cases are exercised that are slightly independent. However, as seen in the previous section, the effect of these load cases across the interface is theoretically limited to a maximum of $m = n_2$ independent modes of vibration at the passive side, because of the bottleneck-effect of the interface. This is further discussed below.

Let us assume that the operational excitation is able to generate sufficient independent load cases $\mathbf{f}_1(\alpha, \beta, \dots)$, where α and β represent independent operational parameters¹². This is illustrated in Fig. 6.9a. Eq. (6.35) or (6.37) can be established for r sets of measured responses obtained under varying operational conditions, e.g. the sliced time-blocks of an engine run-up measurement. This amounts to stacking the r measured responses of the receiving DoFs and indicator DoFs column-wise into arrays \mathbf{U}_3 and \mathbf{U}_4 to construct the following system of equations (the superscript on \mathbf{u} indicates the measurement block number):

$$\underbrace{\begin{bmatrix} \mathbf{u}_3^{(1)} & \mathbf{u}_3^{(2)} & \dots & \mathbf{u}_3^{(r)} \end{bmatrix}}_{n_3 \times r} = \underbrace{\mathbf{T}_{34}}_{n_3 \times n_4} \underbrace{\begin{bmatrix} \mathbf{u}_4^{(1)} & \mathbf{u}_4^{(2)} & \dots & \mathbf{u}_4^{(r)} \end{bmatrix}}_{n_4 \times r} \implies \mathbf{U}_3 = \mathbf{T}_{34} \mathbf{U}_4 \quad (6.38)$$

Note that is repeated for each frequency point individually. When sufficient measurement data has been acquired to ensure $r \geq n_4$, the problem of Eq. (6.38) can be made invertible by post-multiplying with the conjugate transposed matrix \mathbf{U}_4^H . The transmissibility matrix is then found from solving this system or, more conveniently, from the H_1 estimator¹³ of the cross-power spectra (CPS) and auto-power spectra (APS) of the measured DoFs:

$$\mathbf{T}_{34} = \mathbf{U}_3 \mathbf{U}_4^H (\mathbf{U}_4 \mathbf{U}_4^H)^{-1}$$

$$\mathbf{T}_{34} = \mathbf{S}_{34} \mathbf{S}_{44}^{-1} \quad \text{with} \quad \begin{cases} \mathbf{S}_{34} = \frac{1}{r} \mathbf{U}_3 \mathbf{U}_4^H \\ \mathbf{S}_{44} = \frac{1}{r} \mathbf{U}_4 \mathbf{U}_4^H \end{cases} \quad (6.39)$$

Eq. (6.39) performs cross-talk cancellation similar to Eq. (6.35). Now that the transmissibility matrix \mathbf{T}_{34} has been estimated globally, the actual path contributions can be analysed

¹²In [171] it is suggested that external excitation on the source structure, e.g. by use of a non-instrumented hammer, leads to better conditioning of the transmissibility matrix compared to a sequence of operational excitations. This resembles the approach depicted by Fig. 6.8b.

¹³The H_1 estimator is a well-known principle in experimental modal analysis to determine FRFs from a multiple input-output (MIMO) test, see for instance [17, 53]. Alternative ways to obtain the transmissibility matrix have recently been explored, such as the H_2 or H_s estimator to balance the error contributions between the inputs and outputs [110].

for each measurement cycle. If performed correctly (i.e. all transfer paths were included) and the vibration transfer can be assumed to be linear, the reconstructed response spectra equal the response spectra that were measured directly:

$$\mathbf{u}_3^{(l)} = \mathbf{T}_{34}\mathbf{u}_4^{(l)} \quad l \in \{1, \dots, r\} \quad (6.40)$$

The approach governed by Eq. (6.38–6.40) is generally known as *Operational Transfer Path Analysis* (OTPA) [142]. Clearly, the performance of this method is subject to the choice and positioning of the indicator sensors \mathbf{u}_4 , that function as “inputs” to the analysis. Too few sensors (or too distant from the source connections) could lead to neglecting important transmission paths, resulting in unrealistic prognoses [66]. On the other hand, having too many sensors (or too near to each other) complicates the inversion of \mathbf{S}_{44} due to poor conditioning, resulting in amplification of measurement noise [65].

Theoretically, the rank of \mathbf{U}_4 is limited by the number of DoFs at the interface $m = n_2$. This implies that, if $n_4 > n_2$, \mathbf{U}_4 and thus \mathbf{S}_{44} is rank deficient, even if $r > n_4$. It is therefore common practice to perform a Principal Component Analysis (PCA) in order to identify how many independent modes of vibration are present in the system and transferred across the interfaces. Principle components are calculated from the singular value decomposition of \mathbf{U}_4 . The transmissibility matrix can be built as follows:

$$\mathbf{U}_4 = \mathbf{U}_{u_4} \Sigma_{u_4} \mathbf{V}_{u_4}^H \quad \implies \quad \mathbf{T}_{34} = \mathbf{U}_3 \mathbf{V}_{u_4} \Sigma_{u_4}^+ \mathbf{U}_{u_4}^H \quad (6.41)$$

The left-singular vectors represent the vibration mode shapes that build up the vibrations in the indicator DoFs, sorted from the largest contribution to the smallest. By controlling the amount of principle components that are used in the computation of the transmissibility, the condition number can be kept low such that one balances between the completeness of path descriptions and attenuation of measurement noise. This is not discussed in detail here; guidelines can be found in specific literature on OTPA [102, 142, 158]. With regard to the controllability and observability of the transmissibility matrix, some more insight is provided in Sec. 7.5.

Another strong advantage of OTPA is the ease of combining various types of sensors, both for the input (indicator) and output (receiver) DoFs. Quantities such as accelerations, velocities, sound pressures and even forces and strains can be used in a mixed fashion, as long as proper scaling (unit normalisation) is taken into account [142]. This makes OTPA a suitable method to quickly investigate the proportion of structure-borne and airborne contributions [108]. Other related extensions or applications include Response Modification Analysis (RMA) for providing structural sensitivities to the target responses [179], pass-by analysis of road vehicle noise [89, 159] and time-domain auralisation of OTPA, sometimes referred to as Transfer Path Synthesis (TPS) [223].

6.4.3 Operational mount identification (OPAX)

The Operational Path Analysis with eXogenous Inputs (OPAX) [90, 91] is a hybrid TPA method that aims at combining the physical understanding gained from classical TPA methodology with the identification potential of operational TPA principles. OPAX combines the classical mount-stiffness and matrix-inverse TPA principles as discussed in Sec. 6.2.2 and 6.2.3, but adds the ability to estimate mount stiffness parameters from operational tests. Regarding these mount parameters, a mount model can be selected that

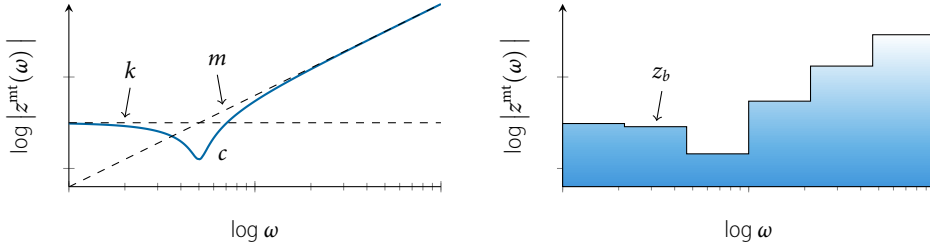


Figure 6.10: Two mount models: based on m, c, k properties (left) and multi-band (right).

fits the system under test and yields the right balance between analysis time/accuracy that was targeted for. This way the OPAX method can be adjusted to suit systems with resilient mounts as well as rigid connections and include airborne paths in the analysis with similar ease.

In what follows, an interpretation of the original publication [91] is presented step-by-step, such that it fits in the proposed framework. A schematic overview of the subsystems' instrumentation is provided in Fig. 6.9b.

Classical mount-stiffness scheme

Central to the OPAX method stands the classical TPA assumption, stating that passive side responses are obtained by application of operational interface forces to the FRFs of subsystem B, similar to Eq. (6.6). The interface forces are modelled as the product of mount-stiffnesses in \mathbf{Z}^{mt} and the differential interface displacements between the active and passive side, as in Eq. (6.8). Let us write the corresponding equations for the receiver responses \mathbf{u}_3 and additional indicator DoFs \mathbf{u}_4 :

$$\begin{bmatrix} \mathbf{u}_3 \\ \mathbf{u}_4 \end{bmatrix} = \begin{bmatrix} \mathbf{Y}_{32}^{\text{B}} \\ \mathbf{Y}_{42}^{\text{B}} \end{bmatrix} \mathbf{g}_2^{\text{B}} \quad (6.42)$$

and for the interface forces:

$$\mathbf{g}_2^{\text{B}} = \mathbf{Z}^{\text{mt}} (\mathbf{u}_2^{\text{A}} - \mathbf{u}_2^{\text{B}}) \quad (6.43a)$$

One of the aims of OPAX is to identify the mount stiffnesses \mathbf{Z}^{mt} from operation tests. It is assumed that the mounts do not exhibit cross-directional effects, such that \mathbf{Z}^{mt} is a diagonal matrix. Eq. (6.43a) can therefore be reformulated using the element-wise or Hadamard product of the set of n_2 single-DoF mount stiffnesses and the differential displacements across the mounts in the corresponding directions:

$$\mathbf{g}_2^{\text{B}} = (\mathbf{u}_2^{\text{A}} - \mathbf{u}_2^{\text{B}}) \circ \mathbf{z}^{\text{mt}} \quad \text{with} \quad \mathbf{z}^{\text{mt}} = [z_1^{\text{mt}} \quad \dots \quad z_{n_2}^{\text{mt}}]^T \quad (6.43b)$$

Mount parametrisation

The next step is to define a model to parametrise the mount stiffnesses in $\mathbf{z}^{\text{mt}}(\omega)$. As suggested in the original work [91], one can choose a single-DoF mount model consisting of linear mass, damping and stiffness terms (m, c, k) or a frequency-dependent model that accommodates for constant dynamic stiffness (z_b) in selected frequency bands. Both models are illustrated in Fig. 6.10.

Let us continue the discussion with the single-DoF mount model. This model introduces $q = 3$ unknowns per interface DoF, contained in the parameter set $\mathbf{x}^{(1)}$:

$$z_1^{\text{mt}}(\omega) = f(\omega, \mathbf{x}^{(1)}) = [-\omega^2 \quad j\omega \quad 1] \begin{bmatrix} m \\ c \\ k \end{bmatrix}^{(1)} = \Psi(\omega) \mathbf{x}^{(1)} \quad (6.44a)$$

It is important to note that $\mathbf{x}^{(1)}$ is a *frequency independent* parametrisation of the stiffness $z_1^{\text{mt}}(\omega)$ of mount DoF with index 1; the frequency dependent part is governed by $\Psi(\omega)$ which is common for all DoFs. Extending now for all n_2 interface forces, the system reads:

$$\underbrace{\begin{bmatrix} z_1^{\text{mt}}(\omega) \\ \vdots \\ z_{n_2}^{\text{mt}}(\omega) \end{bmatrix}}_{n_2 \times 1} = \underbrace{\begin{bmatrix} -\omega^2 & j\omega & 1 & & & \\ & & & \ddots & & \\ & & & & -\omega^2 & j\omega & 1 \end{bmatrix}}_{n_2 \times qn_2} \underbrace{\begin{bmatrix} \mathbf{x}^{(1)} \\ \vdots \\ \mathbf{x}^{(n_2)} \end{bmatrix}}_{qn_2 \times 1} \quad (6.44b)$$

$$\mathbf{z}^{\text{mt}}(\omega) = \Psi(\omega) \mathbf{x}$$

Different mount models can be imagined, such as the multi-band model as mentioned before, functions of higher-order polynomials, etc. as long as \mathbf{x} can be written as frequency-independent parameters. A priori available mount stiffness parameters can also be implemented in Eq. (6.44b).

Identification of mount parameters

Substituting Eq. (6.43b) and Eq. (6.44b) into the original classic TPA scheme of Eq. (6.42), a system of equations is obtained that includes the parametrised mount model:

$$\begin{bmatrix} \mathbf{u}_3(\omega) \\ \mathbf{u}_4(\omega) \end{bmatrix} = \begin{bmatrix} \mathbf{Y}_{32}^{\text{B}}(\omega) \\ \mathbf{Y}_{42}^{\text{B}}(\omega) \end{bmatrix} \underbrace{\left(\mathbf{u}_2^{\text{A}}(\omega) - \mathbf{u}_2^{\text{B}}(\omega) \right) \circ \Psi(\omega) \mathbf{x}}_{\approx \mathbf{g}_2^{\text{B}}} \quad (6.45)$$

The aim is now to construct a standard linear system of equations that allows to solve for \mathbf{x} . Let us first collect all frequency-dependent terms into matrices $\mathbf{A}(\omega)$. These include the FRFs of the passive subsystem (that must be measured explicitly, unlike operational TPA) and the interface displacements measured under operational tests:

$$\begin{bmatrix} \mathbf{u}_3(\omega) \\ \mathbf{u}_4(\omega) \end{bmatrix} = \begin{bmatrix} \mathbf{A}_3(\omega) \\ \mathbf{A}_4(\omega) \end{bmatrix} \mathbf{x} \quad (6.46)$$

using the following definitions:

$$\begin{cases} \mathbf{A}_3(\omega) = \mathbf{Y}_{32}^{\text{B}}(\omega) \left(\mathbf{u}_2^{\text{A}}(\omega) - \mathbf{u}_2^{\text{B}}(\omega) \right) \circ \Psi(\omega) & [n_3 \times qn_2] \\ \mathbf{A}_4(\omega) = \mathbf{Y}_{42}^{\text{B}}(\omega) \left(\mathbf{u}_2^{\text{A}}(\omega) - \mathbf{u}_2^{\text{B}}(\omega) \right) \circ \Psi(\omega) & [n_4 \times qn_2] \end{cases}$$

Noticing the matrix dimensions, the system of Eq. (6.46) is likely to be underdetermined to estimate the full set of mount parameters \mathbf{x} , namely for $qn_2 < (n_3 + n_4)$. Fortunately the mount parameters in \mathbf{x} are assumed to be invariant of frequency and operational conditions. Hence the conditioning of the problem can be improved by stacking all acquired data vertically, namely for one of the following combinations of dimensions:

- ▶ frequency lines $(\omega_1, \dots, \omega_k)$ and measurement cycles $(1, \dots, r)$, in case of unprocessed measurement data;
- ▶ motor orders and RPM points, if available from post-processing or order analysis.

Stacking all information vertically renders the system of Eq. (6.46) sufficiently determined to solve for \mathbf{x} , for instance in a least-square¹⁴ sense which yields the best fit for all mount parameters. For instance, by stacking all $n_3 + n_4$ receiver and indicator DoFs, k frequency points and r measurements cycles, the obtained linear system to solve reads:

$$\begin{bmatrix} \mathbf{u}_3^{(1)}(\omega_1) \\ \vdots \\ \mathbf{u}_4^{(r)}(\omega_k) \end{bmatrix} = \begin{bmatrix} \mathbf{A}_3^{(1)}(\omega_1) \\ \vdots \\ \mathbf{A}_4^{(r)}(\omega_k) \end{bmatrix} \mathbf{x} \quad \Longrightarrow \quad \mathbf{x} = (\bar{\mathbf{A}})^+ \bar{\mathbf{u}} \quad (6.47)$$

The mount parameters \mathbf{x} fitted by Eq. (6.47) can be substituted back into Eq. (6.44b) to find the mount stiffnesses $\mathbf{z}^{\text{mt}}(\omega)$. These are normally assumed to be independent of the operational conditions and assembly under test, although one may prefer to consider multiple amplitude ranges when the mounts exhibit strong non-linear behaviour.

Operational loads & path contributions

Interface forces can be calculated for each operational test by substituting the estimated mount stiffnesses into Eq. (6.43b). The interface forces are finally multiplied with their respective FRFs of the passive side to compute the path contributions to the receiver DoFs of interest.

$$\mathbf{u}_3 = \mathbf{Y}_{32}^{\text{B}} \mathbf{g}_2^{\text{B}} = \mathbf{Y}_{32}^{\text{B}} (\mathbf{u}_2^{\text{A}}(\omega) - \mathbf{u}_2^{\text{B}}(\omega)) \circ \Psi(\omega) \mathbf{x} \quad (6.48)$$

Several variants and case studies of OPAX are discussed in [91]. Some special cases are noted here:

- ▶ In case that all mount parameters are available a priori, the mount identification steps can be skipped and no indicator DoFs are required. The interface forces can be calculated directly from Eq. (6.43a) or (6.43b). This results in the classical mount-stiffness TPA approach as discussed in 6.2.2.
- ▶ For systems with rigid connections, the differential displacement becomes zero. In other words, displacement compatibility is fully satisfied ($\mathbf{u}_2^{\text{A}} = \mathbf{u}_2^{\text{B}}$) such that Eq. (6.43a) or (6.43b) can no longer be used to determine the interface forces. For this particular case, it is suggested in [91] to use the passive-side interface displacement only in combination with a narrow-band mount model:

$$\mathbf{g}_2^{\text{B}} = \mathbf{Z}^{\text{mt}} \mathbf{u}_2^{\text{B}}$$

If the mount model bandwidth reduces to single frequency lines, this formulation is claimed to be equivalent to the classical matrix-inverse TPA (see Sec. 6.2.3), where \mathbf{Z}^{mt} now represents the impedance as experienced at the passive side's interfaces. In fact, to be exactly consistent, \mathbf{Z}^{mt} should equal $(\mathbf{Y}_{22}^{\text{B}})^{-1}$, as can be verified by comparing the interface force with Eq. (6.4). This matrix is generally non-diagonal and operational identification of all its elements can be cumbersome.

¹⁴Unit normalisation should be taken into account when responses of different quantities are used.

- Acoustic loads related to air-borne transmission paths cannot be described by Eq. (6.43a) or (6.43b). Each acoustic pressure p_2 (measured near the source) needs to be associated with a single volumetric velocity q_2 at the source structure. These are related through an acoustic impedance z^{air} which is best described using a multi-band model. The total system of acoustic load-pressure relations then reads:

$$\mathbf{q}_2 = \mathbf{Z}^{\text{air}} \mathbf{p}_2$$

The volumetric velocities \mathbf{q}_2 function as acoustic loads; they can be identified together with the structural interface forces \mathbf{g}_2^{B} by applying Eq. (6.45)–(6.47). Further remarks and guidelines with respect to air-borne transmission paths are provided in Sec. 7.3.

In summary, OPAX is a versatile method that can be adapted to a wide range of applications and adjusted for either quick troubleshooting or thorough analysis. The classification of the method as a transmissibility-based TPA method is however arguable. At all times, one requires the FRFs of the passive side $\mathbf{Y}_{32}^{\text{B}}$, which puts the method in the family of classical TPA. Also, the interface loads become an intermediate result of the analysis, which is not the case with other transmissibility-based methods. Therefore OPAX can be positioned as an intermediate method, combining advantages from both the classical and operational TPA genre.

6.5 Summary

In this framework, eleven TPA methods have been derived and classified into three families. A brief overview of the discussed methodologies is presented in Table 6.1 on page 106. All eleven methods prescribe a task of operational measurement. Various testing environments can be considered, namely the source in assembly with the targeted passive structure (AB), on a test rig (AR) or against fixed or free boundary conditions (A). Yet, as observed from Table 6.1, the chosen test environment and measurement equipment do not necessarily confine the choice of TPA family to be applied.

Let us substantiate this statement with the following example. Suppose one has conducted a series of operational tests on an assembled system AB that had been equipped with receiver DoFs \mathbf{u}_3 and indicator DoFs \mathbf{u}_4 , such as depicted by Fig. 6.3c. Naturally, after de-mounting the source component and measuring the passive side FRFs \mathbf{Y}^{B} (for instance by impact measurement), a *classical matrix-inverse TPA* (Sec. 6.2.3) can be performed, providing insight in the interface forces and path contributions for the particular assembly.

Alternatively, one could measure the assembled system FRFs \mathbf{Y}^{AB} , allowing to calculate source-specific equivalent forces by application of the *in-situ TPA* method (Sec. 6.3.5). If the geometry of the assembly prevents proper excitation at the interfaces, one might instead apply the *pseudo-force TPA* methodology (Sec. 6.3.6) and excite alternative points on the source. Still, the same operational response data \mathbf{u}_4 can be used here.

Yet, if one runs short on time or motivation, the *operational TPA* method (Sec. 6.4.2) would probably be appropriate. Transmissibility can be estimated purely from the available operational response data ($\mathbf{u}_3, \mathbf{u}_4$), provided that enough independent operational cycles were measured. The transmissibility \mathbf{T}_{34} allows to calculate partial responses corresponding to the indicator DoFs.

This framework and discussion above demonstrate that *the TPA classification ultimately determines how the source is characterised*. The methods pertaining to the family of classical TPA describe the source vibrations for a particular assembly with a passive receiving structure. The component-based approaches depict the source by forces that are a property of the source only. Lastly, the methods based on transmissibility skip the stage of source characterisation and only provide information on the source's path contributions.

With respect to the practical side of a TPA campaign, the next chapter presents several (mutually unrelated) aspects and in-depth discussions. The TPA applications performed for this research project are reported in Chap. 9.

Family	Method	Section	Operational measurement		Source characterisation		Apply to FRFs
			quantity	on system	quantity	using	
Classical	Direct force	6.2.1	\mathbf{g}_2^B	AB	interface force	\mathbf{g}_2^B	\mathbf{Y}_{32}^B
	Mount stiffness	6.2.2	$\mathbf{u}_2^A, \mathbf{u}_2^B$	AB	interface force	\mathbf{g}_2^B	\mathbf{Y}_{32}^B
	Matrix inverse	6.2.3	\mathbf{u}_4	AB	interface force	\mathbf{g}_2^B	\mathbf{Y}_{32}^B
Component-based	Blocked force	6.3.2	\mathbf{g}_2^{bl}	A (blocked)	equiv. force	\mathbf{f}_2^{sq}	\mathbf{Y}_{32}^{AB}
	Free velocity	6.3.3	\mathbf{u}_2^{free}	A (free)	equiv. force	\mathbf{f}_2^{sq}	\mathbf{Y}_{32}^{AB}
	Hybrid interface	6.3.4	$\mathbf{g}_2^R, \mathbf{u}_2$	AR	equiv. force	\mathbf{f}_2^{sq}	\mathbf{Y}_{32}^{AB}
	In-situ	6.3.5	$\mathbf{u}_2 (\mathbf{u}_4)$	AR / AB	equiv. force	\mathbf{f}_2^{sq}	\mathbf{Y}_{32}^{AB}
	Pseudo-forces	6.3.6	\mathbf{u}_4	AR / AB	pseudo force	\mathbf{f}_{ps}	\mathbf{Y}_{3ps}^{AB}
					(path contrib.)	-	$(\mathbf{Y}_{31}^{AB}, \mathbf{Y}_{41}^{AB})$
Transmissibility-based	OTPA	6.4.2	$\mathbf{u}_3, \mathbf{u}_4$	AB	(path contrib.)	-	\mathbf{T}_{34}
	OPAX	6.4.3	$\mathbf{u}_2^A, \mathbf{u}_2^B, \mathbf{u}_4$	AB	interface force	\mathbf{g}_2^B	\mathbf{Y}_{32}^B

Table 6.1: Summary and classification of eleven methods presented in the TPA framework.

7

Practical considerations & advanced strategies

chapter contents:

7.1	Source dependency on mounting conditions	107
7.2	Multiple simultaneous sources	108
7.3	Air-borne transmission paths	110
7.4	Interface description & rotational DoFs	111
	7.4.1 Determination of virtual point DoFs	112
	7.4.2 Inverse determination of rotational forces	113
	7.4.3 Continuous interfaces	113
	7.4.4 Round-trip determination of interface FRFs	114
7.5	Observability & controllability of the transfer problem	115
7.6	Evaluation of paths contributions	117
	7.6.1 Partial responses	117
	7.6.2 Power flow	117
	7.6.3 Auralisation	118

Key to conducting a successful TPA is understanding the conceptual basics of the applied methods. These theoretical concepts have been discussed in the previous chapter. In practice however, proper application of experimental techniques can be just as important. This chapter discusses a couple of practical aspects that are frequently — but certainly not always — encountered when conducting a TPA. Theoretical derivations have been kept brief; the intention is to address a couple of aspects and provide useful references to related literature.

7.1 Source dependency on mounting conditions

Several component TPA methods propose to perform the operational test in an environment different from the targeted assembly; see e.g. the hybrid interface method in Sec. 6.3.4 and thereafter. A crucial assumption herein is that the operational source excitation f_1 is independent of the mounting condition. This dependency only refers to the internal mechanisms creating the excitation f_1 . The effect of f_1 on the interface DoFs u_2 is governed by the transfer dynamics, which is correctly accounted for by each method¹.

¹It is arguable whether a vibrating mechanism is best characterised by applied forces or imposed displacements. Both cases are discussed in [167] and it is shown that a displacement source can be implemented with similar ease as an applied force.

The blocked-force and free-velocity methods constitute the two extreme boundary conditions for which the active system can be tested. The hybrid interface method imposes boundary conditions depending on the dynamic stiffness of the test rig. For all three cases, the excitation may thus be influenced by the different mounting stiffness. Note that the in-situ and pseudo-force method both allow to conduct operational measurement in the target assembly, such that the boundary condition is already the one aimed for.

Some typical sources of excitation and their potential sensitivity to the imposed boundary conditions are discussed below.

- ▶ *Rotational orders.* Excitations related to the speed of some rotating system are not expected to be influenced by the boundary conditions. Such excitations are typically identified as orders relative to the RPM, i.e. distinct harmonics in the frequency spectrum with a fixed ratio to the fundamental frequency of the rotational source. Orders arise whenever a periodic excitation is not purely sinusoidal, such as the combustions in an engine, unbalance of a shaft or the torque ripple related to the number of poles in an electric machine.
- ▶ *Pre-loading.* Gearing systems are known to be affected by pre-loading. For instance, if the housing of a gearbox is bent, a slight misalignment of the gears can occur which may result in a dramatic increase of the internal excitations. However pre-loading relates to the static mounting condition ($\omega = 0$) rather than the dynamic interaction. As long as the static stiffness of the testing environment is in the same order as the targeted passive system, the influence should be minimal [101].
- ▶ *Internal non-linearities.* Vibrations that are caused or influenced by internal non-linearities may be affected by dynamic interaction. Discussion of this topic is beyond the scope of this thesis.

In general, it is advised to design the mounting structure such that it exhibits similar dynamic behaviour on the interfaces. If the purpose of study is to investigate the actual influence of the mounting conditions on the excitation, one could for instance turn to hardware-in-the-loop (HiL) testing or real-time substructuring strategies, allowing to actively adjust the dynamic stiffness at the interfaces [22, 98, 178].

7.2 Multiple simultaneous sources

Many products contain multiple sources of vibration that operate simultaneously. To a large extent, these components can be analysed separately and their contributions superimposed. However separate analysis of components is not always possible in practice. Either the components require simultaneous operation for functionality (think of a gearbox driven by an engine), or secondary sources of vibration, not of interest for the analysis, can simply not be deactivated during operational test. In any event, one should pay special attention to make sure that contributions of one source do not spill over into the analysis of the other.

Imagine simultaneous operation of two sources A and A', as illustrated in Fig. 7.1. Although \mathbf{f}_1 and \mathbf{f}_1' may be the excitation forces of independent mechanisms, the resulting interface forces \mathbf{g}_2^B and $\mathbf{g}_2^{B'}$ comprise contributions of each other, being intrinsic to the total system ABA'. When the interface forces are measured directly (Sec. 6.2.1), the receiver responses

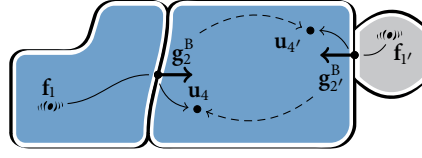


Figure 7.1: Multiple vibration sources A (left) and A' (right) operating simultaneously. The secondary transmission paths are dashed.

\mathbf{u}_3 (omitted in the figure) follow from simple superposition:

$$\mathbf{u}_3 = \mathbf{Y}_{32}^B \mathbf{g}_2^B + \mathbf{Y}_{32'}^B \mathbf{g}_{2'}^B \quad (7.1)$$

Hence, even when considering the contributions in Eq. (7.1) individually, effects of other sources are blended in, because the interface forces (\mathbf{g}_2^B) contain contributions of the other sources.

A second problem arises when determining interface forces indirectly from measured responses, for instance using the matrix inverse method (Sec. 6.2.3). Provided that both interfaces are sufficiently monitored by indicator DoFs, i.e. \mathbf{u}_4 and $\mathbf{u}_{4'}$, the correct interface forces can be retrieved by solving the following system for \mathbf{g}_2^B and $\mathbf{g}_{2'}^B$:

$$\begin{bmatrix} \mathbf{u}_4 \\ \mathbf{u}_{4'} \end{bmatrix} = \begin{bmatrix} \mathbf{Y}_{42}^B & \mathbf{Y}_{42'}^B \\ \mathbf{Y}_{4'2}^B & \mathbf{Y}_{4'2'}^B \end{bmatrix} \begin{bmatrix} \mathbf{g}_2^B \\ \mathbf{g}_{2'}^B \end{bmatrix} \quad (7.2)$$

Indeed, the crosstalk is cancelled due to inversion of the fully determined FRF matrix, that was obtained by exciting both interfaces of the *disassembled* receiving subsystem B. However, if the interfaces with source A' are not instrumented with indicator DoFs $\mathbf{u}_{4'}$ (perhaps because a vibration source was not recognised at all), one cannot distinguish the contributions of A from A'. This clearly leads to a contamination of the estimated interface force $\hat{\mathbf{g}}_2^B$ by application of Eq. (6.10), as only \mathbf{Y}_{42}^B and \mathbf{u}_4 are available:

$$\hat{\mathbf{g}}_2^B = (\mathbf{Y}_{42}^B)^+ \mathbf{u}_4 = \mathbf{g}_2^B + [(\mathbf{Y}_{42}^B)^+ \mathbf{Y}_{42'}^B] \mathbf{g}_{2'}^B \neq \mathbf{g}_2^B \quad (7.3)$$

Regarding component-based TPA, the blocked force, free velocity and hybrid interface method are essentially very well suited to consider multiple sources individually, as the methods' particular boundary conditions isolate the sources from each other. For the in-situ and pseudo-force method, a similar reasoning holds as for the classical matrix inverse discussion. FRFs of the fully assembled system \mathbf{ABA}' are required to construct the in-situ TPA problem (Sec. 6.3.5):

$$\begin{bmatrix} \mathbf{u}_4 \\ \mathbf{u}_{4'} \end{bmatrix} = \begin{bmatrix} \mathbf{Y}_{42}^{AB} & \mathbf{Y}_{42'}^{AB} \\ \mathbf{Y}_{4'2}^{AB} & \mathbf{Y}_{4'2'}^{AB} \end{bmatrix} \begin{bmatrix} \mathbf{f}_2^{\text{eq}} \\ \mathbf{f}_{2'}^{\text{eq}} \end{bmatrix} \quad (7.4)$$

Interestingly, if the problem is properly conditioned, solving of Eq. (7.4) leads to equivalent forces \mathbf{f}_2^{eq} and $\mathbf{f}_{2'}^{\text{eq}}$ that describe the sources independently. After all, the equivalent forces correspond to the theoretical blocked forces measured in separate isolated environments. Therefore, equivalent forces potentially yield a clearer, more distinct characterisation of the

separate source contributions than the classical TPA interface forces, which may be noted as an additional benefit of component-based TPA.

With respect to transmissibility-based TPA, sources can only be distinguished in terms of the monitored transition paths [103]. The main problem of neglecting such paths is that vibrations of source A' appear as contributions coming from source A . This is not easily recognised, as the summed contributions at \mathbf{u}_3 would probably match the measured \mathbf{u}_3 all the same [66].

In general, when performing tests in an assembled system, results should be interpreted with caution when active systems are present that are not considered in the analysis. Neglecting sources or paths results in incorrect estimation of forces and path contributions by applying matrix inversion. Nevertheless, when all sources are properly monitored, there is no fundamental restriction involved in simultaneous analysis of multiple sources.

7.3 Air-borne transmission paths

An essential question in NVH studies is the relative importance of structure-borne and air-borne paths. If the sound pressure at target locations is predominantly caused by radiation from parts at the passive side (e.g. panels in the interior of a vehicle), one can assume that the transfer problem is mainly of structure-borne nature. After all these parts radiate due to vibrations that are transmitted over the structural interfaces. The relation between acoustic pressure and forces is governed by structural-acoustic FRFs in [Pa/N]. As mentioned in Sec. 6.1, such response functions can straightforwardly be combined with structural response functions in an FRF matrix, since both types of responses are force-induced.

However when a significant part of the acoustic pressure is related to direct radiation of the source, air-borne paths should be analysed separately. Analogue to structural transfer functions \mathbf{Y} , acoustic transfer functions \mathbf{H} describe the responses of acoustic pressures to acoustic loads \mathbf{q} (not to be confused with generalised / virtual point coordinates in Chap. 2–4), commonly expressed as volume velocities in m^3/s . A typical situation is sketched in Fig. 7.2; the acoustic load generated by the source is denoted by \mathbf{q}_1 . The combined problem, including both structural and acoustic path contributions, reads:

$$\mathbf{p}_3 = \mathbf{Y}_{31}^{\text{AB}} \mathbf{f}_1 + \mathbf{H}_{31}^{\text{AB}} \mathbf{q}_1 \quad (7.5)$$

Analysis of air-borne transmission paths is a delicate task posing many practical challenges. First, a typical sound-radiating source cannot be modelled as an ideal mono-pole, meaning that one cannot easily characterise the radiation of the source \mathbf{q}_1 . Instead one has to surround the source component by a number of “substitute” mono-poles [18, 19], representing the spatial distribution of the radiated sound by multiple volume velocity DoFs \mathbf{q}_2^2 .

A second challenge lies in the measurement of the acoustic transfer paths $\mathbf{H}_{32}^{\text{AB}}$. Whereas impact hammers or shakers are very well capable of applying a concentrated force onto a structure, the acoustic counterpart requires excitation by a volume source which is far from trivial. Reciprocal measurement techniques are often used, reducing the required number of acoustic excitations. Theory and applications of reciprocity have been extensively studied, see for instance [57, 231, 234, 235] and reviews [58, 232].

²Note that this is conceptually analogue to the structure-borne TPA assumption, namely characterising the unmeasurable source vibrations \mathbf{f}_1 by means of forces at the interfaces \mathbf{g}_2 .

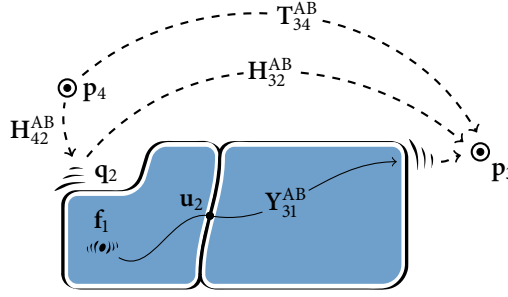


Figure 7.2: Various methods to consider air-borne transmission paths related to direct acoustic radiation of the source component.

Finally, not all TPA methods are suitable for air-borne problems in practice. Direct measurement of acoustic loads \mathbf{q}_2 has only recently been enabled by means of a directional particle velocity sensing device [27, 28] but practical TPA examples are rare [60]. It is more common to determine acoustic loads inversely, for instance from pressure indicator microphones \mathbf{p}_4 around the source [137, 237] or by use of advanced imaging techniques such as Near-field Acoustic Holography (NAH) [121, 129, 230]. For quick estimation of air-borne path contributions, transmissibility-based methods such as Operational TPA are suitable, avoiding explicit treatment of the acoustic loads. The various concepts are illustrated in Fig. 7.2 and formulated by Eq. (7.6a)–(7.6c).

$$\mathbf{p}_3 = \mathbf{H}_{32}^{AB} \mathbf{q}_2 \quad (\text{Direct measurement}) \quad (7.6a)$$

$$\mathbf{p}_3 = \mathbf{H}_{32}^{AB} \mathbf{q}_2 \quad \text{with} \quad \mathbf{q}_2 = (\mathbf{H}_{42}^{AB})^+ \mathbf{p}_4 \quad (\text{Matrix-inverse}) \quad (7.6b)$$

$$\mathbf{p}_3 = \mathbf{T}_{34}^{AB} \mathbf{p}_4 \quad \text{with} \quad \mathbf{T}_{34}^{AB} = \mathbf{S}_{34} \mathbf{S}_{44}^{-1} \quad (\text{Operational TPA}) \quad (7.6c)$$

The operational TPA method, when strictly applied to air-borne path analysis, requires APS and CPS spectra to be calculated from the operational pressure responses ($\mathbf{p}_3, \mathbf{p}_4$). When combined with structural indicator points \mathbf{u}_4 , a quick investigation can be made of the proportion between structure-borne and air-borne path contributions [102]. Note that the OPAX method actually implements the matrix-inverse concept of Eq. (7.6b), with the remark that the acoustical impedance, represented by the term $(\mathbf{H}_{42}^{AB})^+$, is parametrised and estimated during operational tests.

Regarding source characterisation in a component-TPA fashion, interesting equivalent source concepts have been explored such as *blocked pressure* and *surface impedance*; see for instance [23, 135, 148] and references therein.

7.4 Interface description & rotational DoFs

A crucial factor in TPA is correct and complete description of the interfaces that constitute the transfer paths from active to passive components. It is commonly known that omission of transfer paths can result in a highly distorted depiction of the transfer problem, especially for TPA methods that employ matrix-inversion techniques [9, 66]. So far it has been discussed how the seemingly complex problem of vibration transmission can

be analysed using a limited number of transfer functions and corresponding forcing degrees of freedom. Nonetheless, these DoFs must be sufficient to model the behaviour of the interface in full.

Interface modelling and measurement is an active research topic in the field of experimental dynamic substructuring. The requirements for TPA are in fact very similar. Some aspects related to interface modelling and rotational DoFs are addressed here.

7.4.1 Determination of virtual point DoFs

Chap. 4 is devoted to experimental modelling of components, with a particular interest in obtaining virtual point FRFs. The virtual point transformation correctly determines rotations from multiple translational measurements, under the conditions discussed in the chapter. In fact, the spatial reduction principles are not limited to the transformation of FRFs, but may as well be applied to operational measurements in TPA. Furthermore, as the reduction methods are indeed spatial, they may be applied to both time and frequency data.

► In Chap. 4, such virtual point DoFs are denoted \mathbf{q}_2 and can be determined by transformation of the *measured* DoFs \mathbf{u}_2 around the coupling points. In the context of this TPA framework however, we have consistently referred to *indicator* DoFs \mathbf{u}_4 whenever vibrations are observed by sensors close to the coupling points at the passive side. This is an unfortunate discrepancy in notation, as the sensor positions are in practice often the same. To preserve notational clarity and consistency with Chap. 4, the virtual point notation is adopted in the remaining section, notwithstanding the fact that indicator DoFs often appear in the capacity of “overdetermined responses in the vicinity of the interfaces”.

Let us recapitulate some of the virtual point theory for application in TPA. A typical example would be to determine full-state translational and rotational accelerations for the interfaces of a vibrating structure, denoted by \mathbf{q}_2 . For this purpose, sufficient responses \mathbf{u}_2 shall be measured in the rigid proximity of the interface, for which an IDM matrix \mathbf{R}_u can be constructed. According to the virtual point theory, a minimum of three tri-axial indicator sensors is required for the determination of the full 6-DoF set of translational and rotational accelerations. Note that the following operations apply to both time and frequency domain data and that the weighting matrix used in Chap. 4 is omitted here (which simply implies that $\mathbf{W} \triangleq \mathbf{I}$):

$$\begin{aligned} \mathbf{u}_2 &= \mathbf{R}_{u_2} \mathbf{q}_2 \\ \mathbf{q}_2 &= \mathbf{T}_{u_2} \mathbf{u}_2 \quad \text{with} \quad \mathbf{T}_{u_2} = (\mathbf{R}_{u_2}^T \mathbf{R}_{u_2})^{-1} \mathbf{R}_{u_2}^T \end{aligned} \quad (7.7a)$$

A similar procedure could be reasoned to transform multiple measured forces around an interface to virtual point (blocked) interface forces \mathbf{m}_2 . The following notation may appear a bit cryptic; nevertheless the concept of regarding measured forces as an overdetermined set of excitations, effectively creating 6 virtual point forces/moments on an interface, is

fairly straight-forward:

$$\begin{aligned} \mathbf{m}_2 &= \mathbf{R}_{\mathbf{f}_2}^T \mathbf{f}_2 \\ \mathbf{f}_2 &= \mathbf{T}_{\mathbf{f}_2}^T \mathbf{m}_2 \quad \text{with} \quad \mathbf{T}_{\mathbf{f}_2} = (\mathbf{R}_{\mathbf{f}_2}^T \mathbf{R}_{\mathbf{f}_2})^{-1} \mathbf{R}_{\mathbf{f}_2}^T \end{aligned} \quad (7.7b)$$

Again, it is important that the force positions are chosen in the philosophy of a virtual point measurement, i.e. in the rigid area near the interface and properly oriented to determine all moments and forces associated with the virtual point. Examples of this procedure have been reported in [26, 187, 188] and are applied in this thesis in Chap. 9.

7.4.2 Inverse determination of rotational forces

Several TPA techniques rely on matrix-inverse force determination schemes. If the application requires to consider both translations and rotations explicitly, 6 forces and moments per connection point are to be determined, for instance from the virtual point transformation as described above. Nevertheless, it is possible to retain the original FRFs for translational motion \mathbf{u}_4 and employ virtual point mapping for the forces only using Eq. (7.7b). Let us illustrate this for the case of virtual point interface force³ determination, based on Eq. (6.10):

$$\mathbf{m}_2^B = (\mathbf{Y}_{42}^B \mathbf{T}_{\mathbf{f}}^T)^+ \mathbf{u}_4$$

The part between the brackets forms the admittance FRFs relating the set of 6 virtual-point interface forces and moments to translational indicator DoFs \mathbf{u}_4 . The fundamental condition here is that the full set of interface loads in \mathbf{g}_2^B is *observable* from the set of indicator DoFs \mathbf{u}_4 ⁴.

7.4.3 Continuous interfaces

Not all interface problems can be properly described by a small number of connection points. Some systems (such as the interface between gearbox and engine of a vehicle or turbine blades and hub of a wind turbine) comprise larger connecting surfaces, flanges or patterns of closely spaced bolts. Hence, simplification of connectivity is no longer acceptable and the trivial 6 rigid interface modes need to be augmented by a number of flexible modes, which are not naturally obtained from measurement. Information from (static) FEM analysis can be used to extrapolate the measured points, for instance using the System Equivalent Reduction Expansion Process (SEREP) [143]. Another interesting concept is the temporary attachment of a flexible fixture, allowing to better measure and/or excite the rotational and flexible modes of a subsystem [7]. This concept, popularly known as the *transmission simulator*, has recently gained popularity in the field of dynamic substructuring [128]. Applications to TPA have not yet been reported; however the decoupling techniques involved [44, 220] are related to inverse source characterisation ideas as seen in e.g. the in-situ method.

³To avoid introducing yet another symbol, \mathbf{m}_2 is used here to denote interface forces in the virtual point space.

⁴Transmissibility-based techniques also benefit from double instrumentation along transmission paths, e.g. two tri-axial accelerometers close to each other. Although rotational moments are not explicitly being characterised, it can be reasoned that the *effects* are better observable from the increased set of indicator DoFs \mathbf{u}_4 , leading to a more truthful reconstruction of the target responses.

7.4.4 Round-trip determination of interface FRFs

Measurement of interface FRFs of assembled systems is sometimes complicated by the inaccessibility of the interfaces for excitation. Sensors may normally be glued to the structure, such that they register the accelerations in three orthogonal directions. Excitations, on the other hand, cannot always be applied in all required directions. An example is the excitation of the in-plane directions of a plate.

Recently, the *round-trip* method has been proposed by Moorhouse and Elliott [136] as an alternative to obtain interface FRFs in assembled systems, i.e. Y_{22}^{AB} . The method avoids direct excitation of the interface DoFs, but instead calculates the effective interface FRFs by making smart use of the blocked-force principle and FRF reciprocity. The method is briefly summarised here.

The aim is to determine Y_{22} (the AB-superscript is omitted in this section) from alternative excitation points. First, an alternative set of responses is considered due to the same excitation f_2 . These responses are on side B of the assembly and denoted by u_3 :

$$u_3 = Y_{32}f_2 \quad (7.8a)$$

Next, a different set of forces is sought that, applied to side A, render the same responses u_3 as caused by f_2 . This can be recognised as an equivalent source problem, hence such forces are denoted by f_1^{eq} :

$$\begin{cases} u_3 = Y_{32}f_2 \\ u_3 = Y_{31}f_1^{eq} \end{cases} \implies f_1^{eq} = (Y_{31})^+ Y_{32}f_2 \quad (7.8b)$$

According to the equivalent source theory, the forces f_1^{eq} are representative for the forces f_2 for what concerns the responses at the interface and/or side B. This means that the following two responses u_2 are also equivalent:

$$\begin{cases} u_2 = Y_{22}f_2 \\ u_2 = Y_{21}f_1^{eq} \end{cases} \implies u_2 = \underbrace{Y_{21} (Y_{31})^+ Y_{32}}_{Y_{22}} f_2 \quad (7.8c)$$

Eq. (7.8c) formulates the concept of the round-trip approximation. However, in this form it still requires excitation of the interfaces to obtain Y_{32} . This is solved by measuring its reciprocal Y_{23} , namely by exciting very close to the sensors and in the same directions as the axes of measurement. This is feasible as one has the liberty to position the sensors somewhat remotely from the interface. The practical round-trip formulation thus reads:

$$Y_{22} = Y_{21} (Y_{31})^+ Y_{23}^T \quad (7.9)$$

A requirement is to have $n_1 \geq n_3$; reciprocity furthermore suggests that $n_2 = n_3$. The identity holds because the transfer $f_1 \rightarrow u_3$ is channelled through the interfaces with lower “throughput” dimension (See the next section for a discussion on the bottleneck effect of the interface). In practice, f_1 must comprise sufficient excitations in all directions, in order to excite all independent excitation modes of the interface. This correlates with the idea of external excitation on the source structure to obtain an independent transmissibility matrix, which was discussed in Sec. 6.4.1 and 6.4.2. Indeed, a transmissibility term can be recognised in Eq. (7.9), which allows us to write:

$$Y_{22} = T_{23} Y_{23}^T \quad \text{with} \quad T_{23} \triangleq Y_{21} (Y_{31})^+ \quad (7.10)$$

This was also suggested in [136]. Finally, the original work shows that the round-trip concept can be employed to approximate FRFs of continuous interfaces. In that case, \mathbf{u}_2 can be chosen to represent the coordinates of some user-defined shape functions, whose effective excitations are realised by application of the round-trip principle.

7.5 Observability & controllability of the transfer problem

In Sec. 6.4.1 the concept of transmissibility was introduced, followed by the method of operational TPA in Sec. 6.4.2 to compute transmissibility from operational responses. This section elaborates a bit more on the observability and controllability of the transfer path problem, which may provide useful insight in the connectivity of the substructures. Note that the discussion applies to the workflow of operational TPA, yet the principles are fundamental to the transfer problem in general.

As stated before, the interface can be regarded as a bottleneck with “throughput” dimension m , i.e. the number of DoFs characterising the interface, which limits the amount of independent load cases that can be transmitted to the passive side. On the other hand, the amount of indicator DoFs n_4 at the passive side may also exceed m , such that a linear dependency exists between the indicator responses that can originate from excitations through the interface. Both phenomena have their implications for the numerical conditioning of the transmissibility. In fact, study of the controllability and observability may provide valuable insight in the system connectivity.

Let us consider an operational TPA campaign (see Sec. 6.4.2) for measurement of r test spectra, under operational excitation of the source A in an assembled product AB. The amount of r is so far left undefined; nevertheless it is assumed that all r sets of operational responses are a result of load cases \mathbf{f}_1 that are mutually independent:

$$\mathbf{F}_1 = \begin{bmatrix} \mathbf{f}_1^{(1)} & \mathbf{f}_1^{(2)} & \dots & \mathbf{f}_1^{(r)} \end{bmatrix} \quad \implies \quad \text{rank}(\mathbf{F}_1) = r$$

Note that this array of excitation forces cannot be measured in practice; it only serves a theoretical purpose here. Equally hypothetical are the r free velocity spectra, if the source structure were dismantled from the passive side:

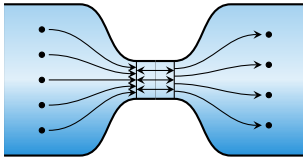
$$\underbrace{\mathbf{U}_2^{\text{A,free}}}_{n_2 \times r} = \underbrace{\mathbf{Y}_{21}^{\text{A}}}_{n_2 \times n_1} \underbrace{\mathbf{F}_1}_{n_1 \times r}$$

As seen before, the interface forces can be expressed using the free velocities of the source and the dynamic coupling with the passive structure. Consequently, for the n_4 indicator DoFs on the passive side, we find the following r response spectra:

$$\underbrace{\mathbf{U}_4}_{n_4 \times r} = \underbrace{\mathbf{Y}_{42}^{\text{B}}}_{n_4 \times n_2} \underbrace{\mathbf{G}_2^{\text{B}}}_{n_2 \times r} \quad \text{with} \quad \mathbf{G}_2^{\text{B}} = (\mathbf{Y}_{22}^{\text{A}} + \mathbf{Y}_{22}^{\text{B}})^{-1} \mathbf{U}_2^{\text{A,free}}$$

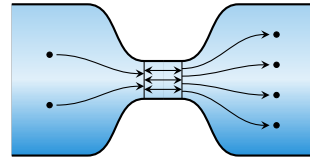
Array \mathbf{U}_4 is ultimately obtained from operational measurement and needs to be inverted for the computation of \mathbf{T}_{34} by Eq. (6.39)

Let us now investigate the rank of \mathbf{U}_4 , considering four different cases depending on r and n_4 . A schematic representation of the bottleneck problem is shown in Fig. 7.3. In what follows, m is used instead of n_2 to stress that excitation modes are considered rather than



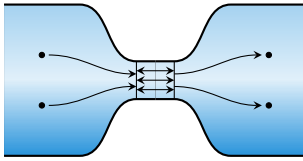
$r = 5$ $m = 3$ $n_4 = 4$

(a) Full controllability & full observability.



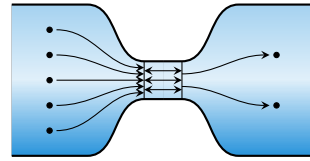
$r = 2$ $m = 3$ $n_4 = 4$

(b) Partial controllability & full observability.



$r = 2$ $m = 3$ $n_4 = 2$

(c) Partial controllability & partial observability.



$r = 5$ $m = 3$ $n_4 = 2$

(d) Full controllability & unobservability.

Figure 7.3: A schematic representation of the bottleneck problem: four situations with different implications for observability and controllability. The vibration is generated on the left side and propagates through the interface to the indicator DoFs on the right side.

physical DoFs. Controllability can be considered a property of the r columns of the source excitation spectra F_1 ; observability relates to the n_{n_4} rows of the indicator DoFs spectra U_4 .

- ▶ *Full controllability & full observability*, Fig. 7.3a. The rank of U_4 is m . The interface is fully excited and the set of indicator DoFs is overdetermined. Transmissibility T_{34}^B can be determined from the m principal components of U_4 . This system generally observes the effects of source excitations at the passive side, even those that were not part of the original set F_1 used for the transmissibility calculation. T_{34}^B becomes a property of the passive side only, although not a unique one because the set of u_4 is overdetermined.
- ▶ *Partial controllability & full observability*, Fig. 7.3b. The rank of U_4 is r . Not all interface modes have been excited, hence the interface did effectively not act as a bottleneck. The r force spectra in F_1 can be *detected* from U_4 using operational TPA, yet the obtained transmissibility is a property of the assembly and will not be able to describe arbitrary force loadings $f_1 \notin F_1$. More load cases are necessary to improve the transmissibility matrix, for instance using a non-instrumented hammer.
- ▶ *Partial controllability & partial observability*, Fig. 7.3c. The rank of U_4 is $n_4 = r$. The number of load cases is not limited by the interface, hence the bottleneck effect is not active. The indicator DoFs are insufficient to fully observe the interface, however the two load combinations are observable. In this case there is no effect of any interface. This means that the problem is reduced to a simple observability problem and that the transmissibility is a property of the assembly, hence not the receiving side alone.
- ▶ *Full controllability & unobservability*, Fig. 7.3d. The rank of U_4 is n_4 . The interface has been fully excited, so the number of independently transmitted modes is limited to m . However, the m effects cannot be fully observed at the passive side due to

insufficient indicator DoFs. As a result, \mathbf{U}_4 does not exhibit a large jump in singular values. The transmissibility is incomplete and, like above, becomes a property of the assembly. More indicator DoFs should be added to improve the observability.

Summarising, it is best practice to measure a matrix \mathbf{U}_4 such that $r > n_4$. If SVD analysis shows $m < n_4$ significant singular values, it either means that the interface is identified as a system having m DoFs, or that the source has not been able to excite more than m independent modes. To further verify this, it is suggested to apply some excitations manually, to see if the number of significant singular values increases. If it does not, it is a good indication that the transmissibility is a property of the passive side. If it does change, there is room for further improvement of the conditioning, however the matrix is already sufficient to observe the operational excitations of the OTPA campaign.

7.6 Evaluation of paths contributions

The set of receiver responses \mathbf{u}_3 are in this framework often considered as the end result of a TPA method. However, the actual purpose of a TPA is rather to identify the individual contributions that sum up to these responses, because these contributions reveal the amount of vibrations transmitted through each path. Transfer path contributions can be evaluated in various ways; some of the more common methods are summarised here.

7.6.1 Partial responses

Receiver response spectra are composed from the complex sum of the partial response spectra, i.e. the sum of all contributions over the considered transfer paths. To illustrate for classical TPA Eq. (6.6), the n_3 receiver response spectra u_i are composed from their m path contributions as follows:

$$u_{i,j}(\omega) = Y_{ij}^B(\omega)g_j^B(\omega) \quad \implies \quad u_i(\omega) = \sum_{j=1}^m u_{i,j}(\omega) \quad \begin{cases} i \in 1, \dots, n_3 \\ j \in 1, \dots, m \end{cases}$$

Partial responses are obtained for all three families of TPA methods and can thus be used to compare the results of various methods. They are typically visualised in 3D images with frequency ω on one axis and the m path contributions on the other axis. Such graphics allow for quick visual troubleshooting of the dominant transfer paths and critical frequency ranges. Other typical diagrams derived from partial responses include Campbell plots, n^{th} -octave plots, engine order plots, phase vector plots and sum levels over RPM; see for instance the graphics in [9, 108, 155, 239] and the ones presented in Chap. 9.

7.6.2 Power flow

Power flow investigations are used for instance to determine the activity of the source, localise energy concentrations or quantify damping over the interfaces [12, 228, 229, 236]. Complex power is commonly expressed as the conjugated product of force and velocity spectra, which can be related to AC current and voltage in electrical engineering. As velocity is a result of force times mobility (i.e. velocity FRF, denoted by $\dot{\mathbf{Y}}$), the phase of the power flow is directly related to the phase of the mobility FRFs:

$$\mathcal{P} = \frac{1}{2} \mathbf{f}^H \dot{\mathbf{u}} = \frac{1}{2} \mathbf{f}^H \dot{\mathbf{Y}} \mathbf{f}$$

The power flow of a single path contribution can be computed as follows:

$$\mathcal{P}_i = \frac{1}{2} f_i^* \dot{u}_i = \frac{1}{2} f_i^* \sum_{j=1}^m \dot{Y}_{ij} f_j$$

When considered for interface DoFs, the real part of \mathcal{P} represents the dissipated power over the interfaces whereas the imaginary part quantifies the dynamic interaction between the components [12]. As an explicit separation of forces and motion is required, transmissibility-based methods are not suitable for power flow analysis.

7.6.3 Auralisation

Auralisation is time-domain evaluation of path contributions by means of audible sound [222]. Some commercial packages offer the possibility to listen to partial responses, but the implementation often remains proprietary. In many cases, the essential TPA calculations are performed in the frequency domain. The outputs of the analysis, e.g. receiver responses $\mathbf{u}_3(t)$, are ultimately calculated in the time domain, for instance using approximated FIR filter banks or by convolution with impulse response functions (IRFs)⁵:

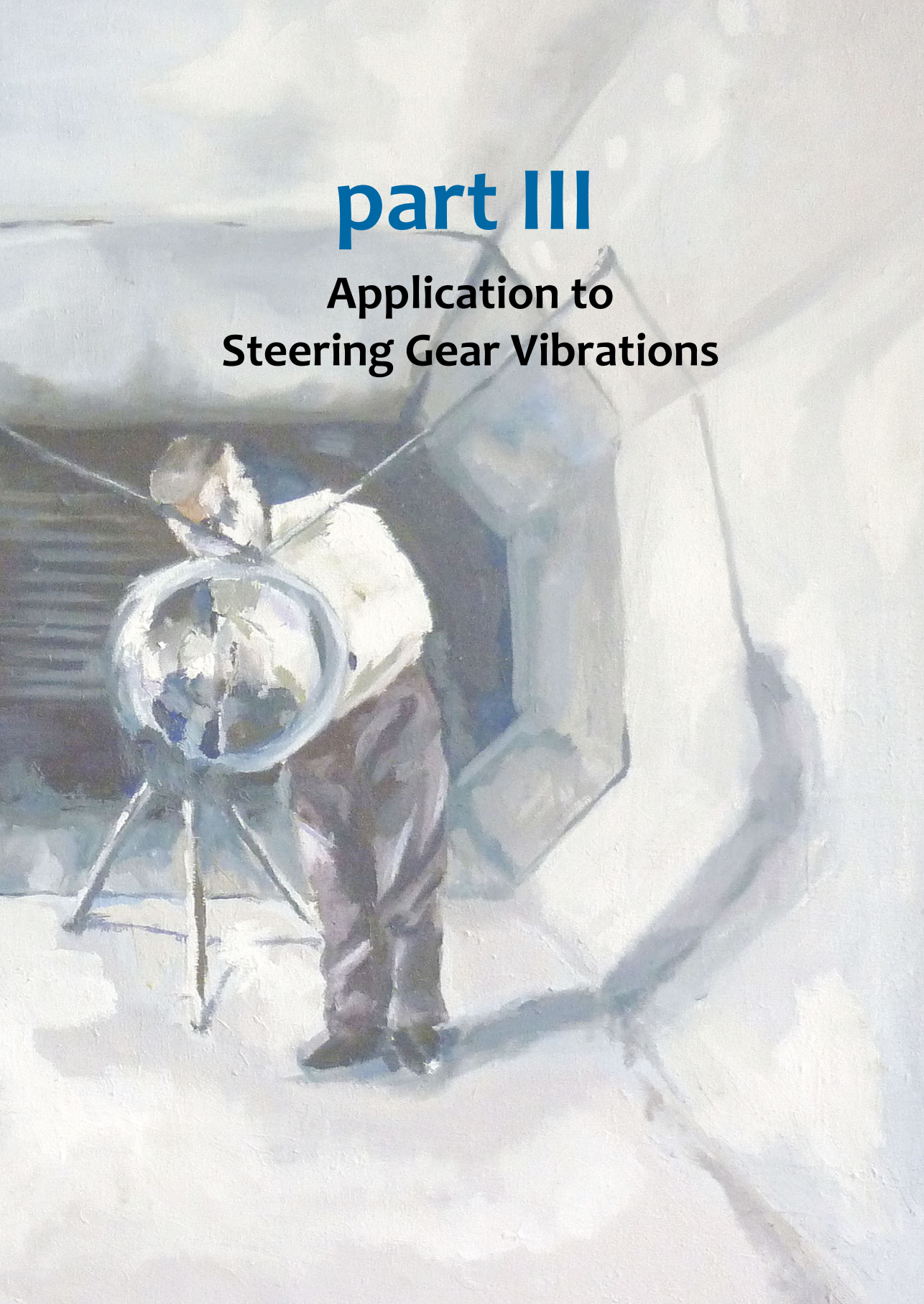
$$\mathbf{u}_3(t) = \int_0^t \mathbf{Y}_{32}^B(t - \tau) \mathbf{g}_2^B(\tau) d\tau$$

Some methods are specifically formulated for time-domain operation, such as the classical TPA force reconstruction algorithms proposed by [99, 157]. For the purpose of component-based TPA, an interesting blocked-force reconstruction technique was developed by Sturm et al. [199, 200] based on the in-situ TPA concept. This method is essentially a modification of the least mean square (LMS) algorithm and is inverse-free. Time-domain variants of operational TPA are often referred to as transfer path synthesis (TPS) [223] or time-domain independent component analysis (time-domain ICA) [238].

⁵Computation of structural responses by convolution of IRFs of substructures relates to the field of impulse-based substructuring (IBS) [168, 214], which solves the interface problem in the time-domain. See also Sec. 2.5.

part III

Application to Steering Gear Vibrations



8

Validation of frequency-based substructuring techniques

chapter contents:

8.1 Introduction	121
8.1.1 Measurement & methodology	122
8.1.2 Outline of part three	122
8.2 General subsystem description	123
8.2.1 Steering system	123
8.2.2 Subsystem connectivity	124
8.2.3 Front subframe & bodywork	124
8.3 Vehicle FRFs from experimental modelling	126
8.3.1 Impact hammer measurement	126
8.3.2 Analysis of FRF measurement	127
8.3.3 Virtual point transformation	130
8.3.4 Summary	132
8.4 FRF uncertainty & benchmark study	133
8.4.1 Benchmark on three similar cars	134
8.4.2 Conventional vs. virtual point approach	135
8.4.3 Comparison of structural FRFs	135
8.4.4 Comparison of structural-acoustic FRFs	136
8.4.5 Summary	137
8.5 Application of Dynamic Substructuring	138
8.5.1 Substitute coupling approach	138
8.5.2 Experimental & numerical modelling	140
8.5.3 Results of dynamic substructuring	141
8.5.4 Summary	142

8.1 Introduction

The third part of this thesis presents a selection of validation studies with application to the automotive industry. The studies have been carried out during a four-year collaboration project with the BMW group, organised at the research and development facility¹ in Munich, Germany. As introduced in Sec. 1.5, the applications focus on the structure-borne sound and vibration of the electric power steering (EPS) system. This engineering aspect belongs to the domain of the department specialised in acoustics of mechatronic components, denoted "Mechatronik, Absicherung".

¹Forschungs- und Innovationszentrum (FIZ), the heart of BMW's vehicle development since 1986, today hosting around 10.000 employees.

Over the course of four years, progress has been made in an iterative manner. Every new study has been defined as a follow-up of the preceding studies, gaining from practical “lessons learned” and newly discovered theorems along the way. Although the researched methods are kept general, different vehicles have been considered for application: a compact executive car, a medium-scale limousine and a large SUV. Test benches have been constructed and adapted each time to suit the various steering systems and intended TPA methodology².

8.1.1 Measurement & methodology

For the purpose of validation of the experimental methodology, several measurements campaigns have been conducted that fall into two categories:

- ▶ *FRF measurements* on both individual components and assemblies of the vehicle, EPS system, substitute beam (to be discussed later) and test bench. All FRFs are obtained from impact hammer measurements. The component FRFs are used for substructuring purposes, namely to construct vehicle FRFs by means of LM-FBS coupling and decoupling. The assembled FRFs are either used for validation of the substructuring results or as a direct input for TPA methods.
- ▶ *Operational measurements* consisting of a series of EPS-assisted steering cycles, both in-vehicle and on a test bench. The responses obtained from these campaigns are processed into measurement blocks with steady-state operational conditions, such as constant steering speed, constant EPS load etc. Frequency spectra are computed from these blocks using FFT, which form the input for source characterisation and transfer path analysis.

After each measurement campaign, the geometry of the instrumentation, e.g. position and orientation of sensors and impact positions, has been carefully registered and reproduced using photos and 3D CAD models of the components. The graphics shown in this part are snapshots taken from this virtual environment.

8.1.2 Outline of part three

This part intends to highlight those results that best reflect the implications of the theory as presented in Part I and II. This is organised as follows:

- ▶ Results related to the *passive dynamics* of the components and assemblies are presented in Chap. 8. This concerns the steps of FRF measurement, experimental modelling and examples of dynamic substructuring. The chapter also reports on a benchmark study of vehicle FRF measurements, demonstrating the advantages of the virtual point transformation for high-quality FRF determination.
- ▶ The applications related to the *active vibrations* of the EPS system are reported in Chap. 9. Several methods of source characterisation are discussed first. As will be shown, the method of source characterisation has implications for the design of the test bench used for component measurement. Thereafter, responses in the vehicle are predicted using component TPA theory. These responses are compared against a validation measurement.

²Intermediate results have been reported in [26, 186–188].

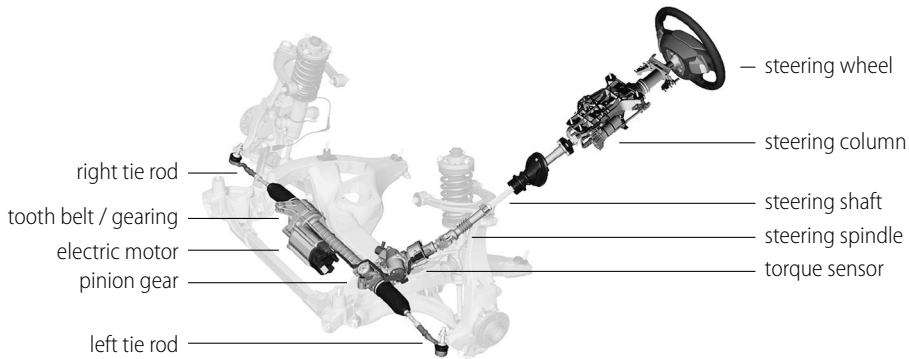


Figure 8.1: The steering system and suspension, illustrated based on the geometry of a 2010 5-series BMW [source: www.press.bmwgroup.com].

Note that the measurements presented here are sometimes obtained from different vehicles. Some studies have focused on validation of dynamic substructuring, whereas others have concentrated on application of TPA. All steps are, nonetheless, part of a workflow that is unique for all platforms. Besides, the individual results are sometimes at least as insightful as the final result of the analysis — an observation that is well reflected in the spirit of dynamic substructuring.

8.2 General subsystem description

Before discussing the applications, let us first introduce the relevant subsystems and their connectivity. Following the source-transmission-receiver model of Sec. 1.1.2, we focus on the subsystems that can be identified in the chain from steering gear to the driver's ear in the vehicle. This explanation is based on the 2010 BMW 5-series platform, however the other platforms have very similar configurations.

8.2.1 Steering system

The electric power steering (EPS) system [German: Lenkgetriebe] is the active system of interest in this thesis; see Fig. 8.1. The main vibrating mechanisms of the EPS system are the electric motor, tooth belt with planetary gearing and pinion gear. The electric motor emits harmonic vibrations related to the number of poles in the electric machine. This creates a characteristic high-frequent sound which is sometimes referred to as *whining* noise; see for instance [111]. The tooth belt, planetary gearing and pinion gear cause vibrations related to the number of teeth of the drive belt and gears. This causes harmonic orders synchronous to the speed of the electric motor, spanning a frequency range up to 3 kHz.

Because of the complexity of the internal mechanisms, it is difficult to pinpoint the sources of excitation individually. Moreover, the main concern of the conducted studies is the contribution of the EPS-related vibrations to the experienced sound *inside* the vehicle. It is therefore chosen to consider all EPS mechanisms as one collective source of vibrations, indicated as active subsystem A with excitation forces f_1 . These forces are unmeasurable indeed; we therefore focus on the vibrations that are transmitted across the interfaces u_2 with the vehicle.

Besides being an active source of excitation, the steering system also forms a passive dynamic contribution to the vehicle, due to its mass, stiffness and damping. The passive structural dynamics of the EPS system are denoted by the admittance FRF matrix \mathbf{Y}^A , which is partitioned as follows:

$$\mathbf{Y}^A = \begin{bmatrix} \mathbf{Y}_{11}^A & \mathbf{Y}_{12}^A \\ \mathbf{Y}_{21}^A & \mathbf{Y}_{22}^A \end{bmatrix}$$

Recall that, as introduced in Sec. 6.1, subscript 1 represents source excitation DoFs and 2 denotes interface DoFs. As discussed, the source excitation DoFs are unmeasurable, hence we only have access to the admittance of the interfaces \mathbf{Y}_{22}^A .

8.2.2 Subsystem connectivity

The steering system is rigidly connected to the front axle carrier [German: Vorderachsträger] at four bolted connection points, which in turn connects to the vehicle's bodywork; see also Fig. 8.3 and 8.4. Note that the steering system cannot be mounted resiliently (like the main engine that is supported by rubber engine mounts), as any added flexibility would reduce the lateral stiffness and compromise the handling of the vehicle. The four connection points of the EPS are therefore metal-on-metal mountings, which qualifies them as primary paths of structure-borne vibration transmission.

In addition to the primary paths, two types of secondary transmission paths can be identified (see Fig. 8.1 and 8.2 for reference):

- ▶ *Steering column assembly.* This path consists of the the steering spindle, shaft and column, that ultimately connects to the vehicle's bodywork and steering wheel. Depending on the platform, it comprises one or more Cardan joints and a sliding mechanism. From a kinematic point of view, the only DoF that is fixed in this path is the steering angle itself; all other DoFs are either hinged or decoupled. It has been confirmed in earlier studies that this path is of minor importance.
- ▶ *Wheels, tie rods, suspension.* The rack bar (inside the EPS housing) is connected to the wheels by tie rods. These tie rods are hinged by ball joints, which decouples all DoFs except for the lateral push-pull translation that make the wheels turn. Indeed, two vibration paths can be identified that run from the EPS system into the tie rods, wheels, suspension and finally the vehicle chassis. These paths, although important for low-frequency driving dynamics, have no significant contribution in the acoustic frequency range.

Summarising, the four connection points to the front axle carrier are considered the main connection points for substructuring and TPA. Their DoFs are therefore designated as 4×6 coupling DoFs, contained in \mathbf{u}_2 . The steering spindle is in some studies considered as an additional coupling point to assess its influence.

8.2.3 Front subframe & bodywork

The front axle carrier, or simply front subframe, is part of the vehicle's chassis. Because of its many functions, it is often designed in-house. Besides the steering system, it supports the main engine (in rubber engine mounts), part of the wheel suspension assembly and possibly other systems such as the stabilisation bar and front-drive differential. The front

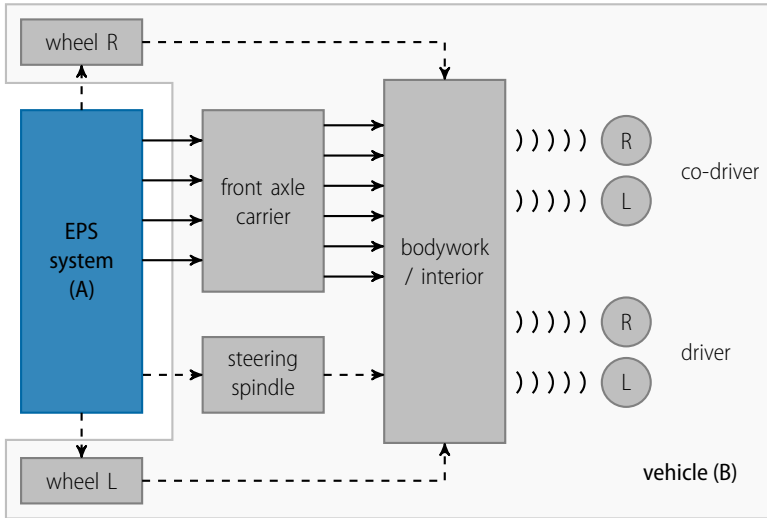


Figure 8.2: Schematic depiction of subsystems A and B and their connectivity. The primary paths and secondary paths are shown by respectively continuous and dashed lines.

subframe is typically machined from a single material such as alloy steel or aluminium. This makes it a potential candidate for numerical modelling, but this is not considered here.

The front axle carrier connects to vehicle's chassis and bodywork. The number of connection points vary per platform, typically between 6 and 10. From here on, the propagation problem becomes quite fuzzy, as vibrations may reach the interior via dozens of transfer paths. Correct description of these paths requires modelling of the acoustic radiation of interior panels, which is beyond the scope of this research.

Instead, the combined effects of structural/acoustic propagation are modelled as a number of structural/acoustic transfer paths, measured at the actual vehicle. This means that the passive subsystem B is defined as the entire vehicle without the EPS system, as indicated in Fig. 8.2. The coupling points to the EPS are assigned interface DoFs \mathbf{u}_2 ; the acoustic pressures at the driver's and passenger's ears are governed by the receiver DoFs \mathbf{u}_3 . Consequently, the following admittance³ matrix can be defined for subsystem B:

$$\mathbf{Y}^B = \begin{bmatrix} \mathbf{Y}_{22}^B & \mathbf{Y}_{23}^B \\ \mathbf{Y}_{32}^B & \mathbf{Y}_{33}^B \end{bmatrix}$$

All interface and receiver DoFs are measurable, however the receiver DoFs cannot be excited. We therefore only have access to the left column of the matrix.

Now that the subsystems and DoFs have been introduced, three applications of experimental modelling and substructuring techniques are discussed next.

³Some literature makes explicit difference between local mobility, structural transfer functions, acoustic noise transfer functions, etc. Here, all frequency-dependent functions are collectively referred to as admittance and denoted by \mathbf{Y} , respecting the fact that different quantities may appear in the columns and rows.

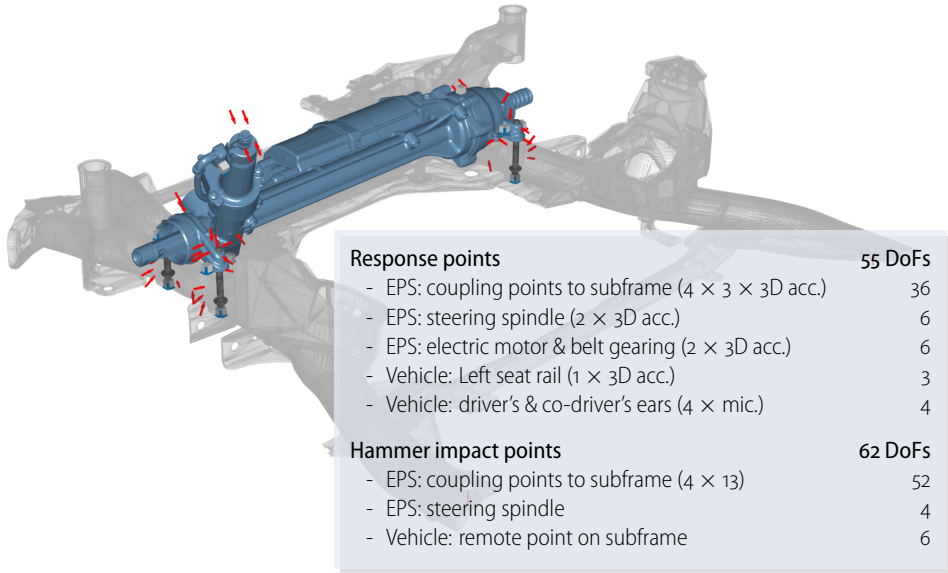


Figure 8.3: Impression of the EPS system (blue) mounted onto the front subframe of the BMW X5 series (translucent grey), supplied with tri-axial accelerometers (tiny grey cubes) and impact hammer excitation points (red arrows).

8.3 Vehicle FRFs from experimental modelling

This section discusses the procedure of experimental modelling of the dynamics of the assembled vehicle. This is an application of the theory presented in Chap. 4. The vehicle under test is a 2014 BMW X5 series. The EPS system is installed in the vehicle, hence the system is already in the desired configuration to measure the admittance of the assembled system.

The aim of this study is to obtain a virtual point admittance model of the assembled vehicle from a series of impact measurements, i.e. $Y_{uf}^{AB} \rightarrow Y_{qm}^{AB}$, meaning that measured displacements \mathbf{u} and forces \mathbf{f} are transformed to virtual point motion \mathbf{q} and loads \mathbf{m} . These virtual point FRFs will later be used in Chap. 9 for source characterisation and TPA. This section discusses the workflow of impact hammer measurement and virtual point processing. Note that substructuring is not yet part of this study; this will be discussed in Sec. 8.5 based on another vehicle platform.

8.3.1 Impact hammer measurement

The vehicle has been measured in an acoustic laboratory, resting on its four wheels on a test bench. Some cover parts at the bottom of the vehicle have been removed to gain access to the four coupling points of the EPS with the front subframe. The aim of the impact hammer measurement is to determine 6-DoF virtual point forces and moments for the interface DoFs by exciting sufficient points around the four coupling points. “Sufficient” is subject to the criteria as discussed in Chap. 4. For this experiment, about 13 points have been excited around each coupling point, offering a total of 52 excitation points for the transformation to 24 virtual point forces/moments: well overdetermined in theory.

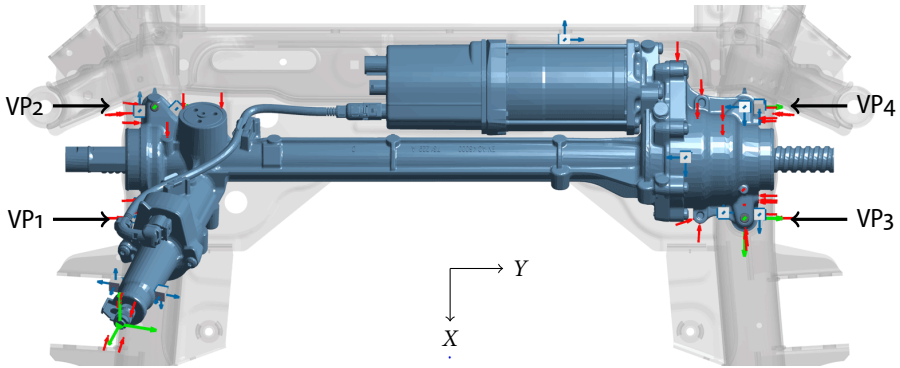


Figure 8.4: Top view of the EPS system. The sensors and impacts are concentrated around the left and right side of the structure. Virtual points (green arrows) are assigned to each coupling point.

Responses are measured from a total of 16 tri-axial accelerometers on and around the EPS system, plus 4 microphones and 1 accelerometer in the vehicle. Like the impact positions, the sensor positions are carefully chosen to enable calculation of 6-DoF virtual point accelerations. This means that each of the four coupling points is surrounded by three tri-axial accelerometers: two on the EPS system and one on the bolt head. The steering spindle has been instrumented by two sensors, to be able to quantify the rotational acceleration around the steering axis.

An overview of the geometry and measurement setup is shown in Fig. 8.3 and 8.4. The impact measurement was performed using a MKII acquisition front-end with associated PAK software from Müller-BBM VibroAkustik Systeme⁴. A sample frequency of 16384 Hz was used for measurement of 1 second time blocks. After windowing and FFT processing, FRF and coherence functions have been obtained in a frequency range of 0 to 6400 Hz with 1 Hz spacing. The size of the measured admittance matrix $Y^{AB}(\omega)$ is thus $55 \times 62 \times 6401$. All measurement and geometry data was converted to MATLAB for further processing and analysis.

8.3.2 Analysis of FRF measurement

In an attempt to analyse an FRF measurement consisting of a total of 3472 complex-valued transfer functions, it is probably not very compelling to randomly select a few and present them as “typical results”. Obviously, the individual FRFs should meet basic requirements, such as proper coherence and signal-to-noise ratio. Yet the measurement as a whole shall, above all, form a coherent entity that is meaningful from a structural-dynamic point of view. This means that evaluation tools must be able to assess whether the FRFs of a measurement are indeed a collection of observations of the expected structure, taking into account the geometry (i.e. the location and orientation of measurement points) and input-output behaviour of a linear dynamic system.

For modal-domain analysis (EMA), adequate tools are at our disposal such as the family of MAC functions [5]. However, for FRF-based substructuring and TPA, proper evaluation tools remain relatively scarce. This section analyses the vehicle measurement by evaluating

⁴See www.muellerbbm-vas.com or www.pakbybbm.com.

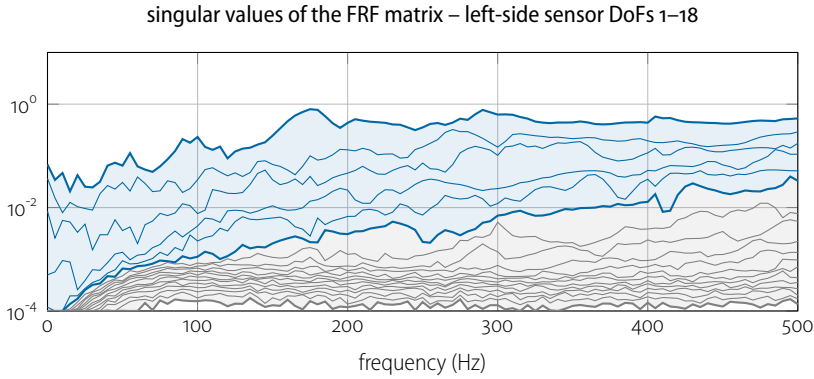


Figure 8.5: Singular values of a subset of the FRF matrix for response DoF 1–18, positioned at the left side of the steering system. The dominance of the first six modes suggests that the left side behaves rigidly in this frequency range.

the quality indicators introduced in Chap. 4, in order to investigate their use for large-scale FRF campaigns.

Singular value decomposition

A singular value decomposition (SVD), when performed on a frequency “cross-section” of the entire FRF matrix, exposes which response modes occur most dominantly and to what extent these modes are excited by each hammer impact⁵. The SVD of the admittance matrix at frequency ω_k is defined as follows:

$$Y(\omega_k) = U(\omega_k)\Sigma(\omega_k)V^T(\omega_k) \quad \text{with} \quad \begin{cases} U & \text{response modes in } \mathbf{u} \\ \Sigma & \text{overall dominance of the modes} \\ V & \text{excitation modes in } \mathbf{f} \end{cases}$$

A large part of the evaluation tools handled in Chap. 4 requires explicit information on the geometry of sensors and impact points, for instance to assess the sensor/impact consistency and thereby justify the rigidness assumption. Yet, without any knowledge of the geometry, an SVD reveals whether rigidness can be presumed at all. For instance: if the SVD at 200 Hz displays no more than 6 dominant singular values *and* the associated response modes in \mathbf{U} are predominantly synchronous in phase, the encompassed structure can be presumed to behave rigidly at 200 Hz.

Although this might be a rigorous assumption for the whole structure, it could provide some insight when computed for a subset of the admittance matrix. For example, Fig. 8.5 shows the singular values of a subset of the FRF matrix, namely for response DoF 1–18 associated with the 6 sensors on the left side of the EPS. Between 100–300 Hz, it can be observed that 99% of the energy is represented by the first six singular values and that these seem to depart from the noise floor. Using information on the sensor geometry, it was verified that these modes represent rigid motion indeed, namely the rigid body modes of the vehicle bouncing in its suspension.

⁵A related diagnostic tool is the complex mode indicator function (CMIF) [4], which effectively takes the (square of the) singular values on the diagonal of $\Sigma(\omega)$.

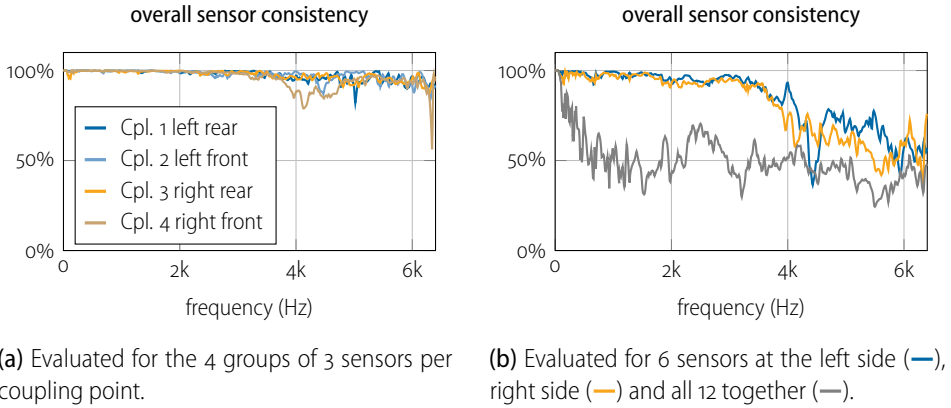


Figure 8.6: Several evaluations of the overall sensor consistency.

Sensor consistency

After the admittance test, the sensor positions and directions have been carefully measured and reproduced using the CAD geometry of the EPS system and the front subframe. This information is essential to construct the IDM matrix \mathbf{R}_u for transformation of the measured responses to responses at the virtual point, as indicated in Fig. 8.4.

To verify the sensor placement and identify potential flexibilities of the interface area, let us evaluate the overall sensor consistency using the functions introduced in Sec. 4.4. Several combinations are shown in Fig. 8.6. First, the overall sensor consistency is evaluated for each group of 3 sensors around the 4 coupling points. As shown in Fig. 8.6a, the consistency is high throughout most of the bandwidth, with some small effects of local flexibility kicking in around 4 kHz. This means that the area between each coupling point can be considered rigid.

Next, Fig. 8.6b shows two other variants: the combined consistency of the two groups of 6 sensors on the left side (—) and right side (—) and the combined consistency of all 12 sensors around the coupling points of the EPS system (—). For these cases, the location of the virtual point is respectively chosen in the middle of the two coupling points left and right and in the centre of the EPS. The coloured curves show that the left and right side behave as one rigid area up to approximately 2 kHz. For higher frequencies, the effect of flexibility becomes notable. The grey curve shows the rigidness when evaluated for the EPS as a whole. Clearly, the EPS system cannot be assumed to behave as a single rigid body, as the consistency drops rapidly beyond 100 Hz.

The following has been observed from the sensor consistency evaluations:

- ▶ Overall, the sensors are positioned and configured correctly around each coupling point. The effects of local flexibilities in the connection areas are very slight;
- ▶ If the interest is in frequencies up to 2 kHz, it might suffice to model the EPS system using two effective connections, namely for the left and right side. The two coupling points on each side are then considered as being part of a stiffened region that displaces as one point in the vehicle subframe. Yet, this would not impose any restrictions on the freedom of motion between the left and right side.

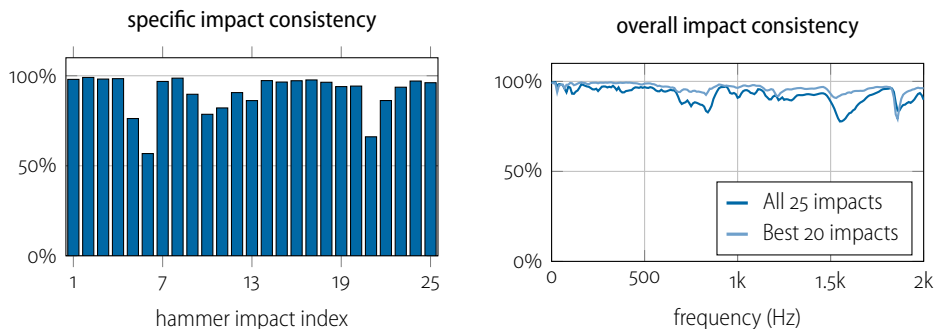


Figure 8.7: Evaluation of the frequency-averaged specific impact consistency (left) and overall impact consistency (right) of the 25 impacts on the left side.

- The EPS in the subframe cannot be considered as one rigidly moving system, except for frequencies below 100 Hz. This is expected: the first bending mode of the EPS structure itself was verified to appear around 150 Hz.

Impact consistency

The impact consistency could theoretically be used for the same purpose, namely to assess the rigidity of parts of the structure, but in practice serves a less sophisticated purpose: identifying and correcting erroneous definitions of the impact positions and directions. As demonstrated by the example in Sec. 4.6, the virtual point transformation is highly sensitive to deviations in the vector (i.e. position and direction) of hammer impacts. These deviations are likely to occur in practice, notwithstanding the fact that they are entirely subject to the skill and patience of the experimentalist.

Like the sensors, the impacts positions are mainly concentrated around the left and right side (see Fig. 8.3). From the sensor consistency, it was concluded that each side behaves rigidly up to 2 kHz. Similar behaviour can thus be required from the impact hammer consistency, which allows to evaluate a larger set of impacts when evaluated per side. The more impacts are considered in the consistency calculation, the better the chances are to spot incorrect impacts, as they appear as “outliers” in the least-square determination.

This is shown in Fig. 8.7: 25 impact points on the left side are considered in the calculation of specific and overall impact consistencies. A few outliers can be observed, most notably impact number 6, 5 and 21. A selection was made of the best 20 impacts: this results in somewhat higher overall consistency, shown by the light-blue curve.

A similar analysis was performed for the two coupling points of the right side. Consequently, the best impacts have been selected and the consistencies with respect to each of the four coupling points have been calculated. This is shown in Fig. 8.8. Coupling point 1 shows the lowest consistency with an average of 89%; the other three coupling points are around 94% over the full bandwidth.

8.3.3 Virtual point transformation

Let us now discuss the results of the full virtual point transformation. After removal of some columns in the FRF matrix corresponding to “bad” impacts, a matrix of 36×46

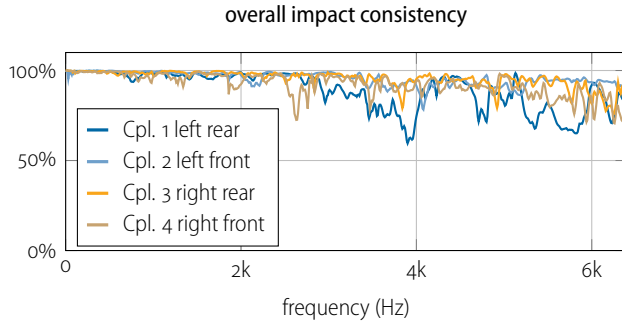


Figure 8.8: Overall impact consistency for the impacts grouped per coupling point.

measured FRFs remains for transformation to virtual point DoFs. Based on the previous discussion, two variants of virtual point assignment are suggested:

- (a) Each coupling point is considered as a separate virtual point. This creates a total of 24 interface DoFs for modelling up to 6 kHz.
- (b) The pairs of coupling points 1–2 and 3–4 are each assigned to a virtual point for respectively the left and right side. This yields a total of 12 virtual point interface DoFs, suitable for modelling up to 2 kHz.

It must be noted that, for the application of in-situ TPA in Chap. 9, a one-sided transformed admittance matrix suffices, i.e. $\mathbf{Y}_{\mathbf{u}\mathbf{m}}^{\mathbf{A}\mathbf{B}}$ for virtual point forces \mathbf{m} to measured accelerations \mathbf{u} . This is because the response DoFs are identical in both FRF measurements: the sensors that were used during vehicle FRF measurement have been kept mounted on the structure for the operational measurement, hence the DoFs \mathbf{u} are the same. Nevertheless it is interesting to discuss the results of the full virtual point analysis.

Virtual point admittance

After transformation to a 24×24 virtual point admittance matrix $\mathbf{Y}_{\mathbf{q}\mathbf{m}}^{\mathbf{A}\mathbf{B}}$, the total reciprocity averaged over the full bandwidth is 65%. This is not particularly great, but also not very surprising. The overdetermination of the impacts, when considering the four-point option, is not overabundant: around 11 impacts to 6 virtual point forces/moments. With this amount of impacts, it was already shown in Sec. 4.6 that minor deviations in the impact vector can have drastic effects for the reciprocity after transformation. For the experiment presented here, impact measurements have been performed in very tight enclosures of the vehicle chassis, often from uncomfortable positions. Hence, the odds of off-positioned and misaligned impacts are substantial.

Nevertheless, when looking at reciprocal FRFs individually, quite reasonable results can be found. Fig. 8.9 shows FRFs from coupling point 1 (left rear) to coupling point 3 (right rear) in four directions: translations in X, Y and Z and the rotation along the θ_X -axis. Clearly, the FRFs in Y and θ_X -direction show better reciprocity than X and Z. This can be understood from the measurement setup (see Fig. 8.3): most impacts are pointing in the Y-direction, which additionally creates moment about the X-axis of rotation. The impacts in the X and Z-direction are fewer in number and often positioned on curved surfaces, which makes it difficult to excite in the intended direction.

When the 2-point virtual point definition is adopted, the averaged reciprocity between 0 and 2 kHz is around 80%. Some pairs have exceptionally high reciprocity, for instance: the rotation about the θ_x -axis is now very well defined with 96%. Clearly, the increased amount of excitations in Y-direction benefits the estimation here, which confirms the assumption that overdetermination minimises the effect of errors in the impact vectors.

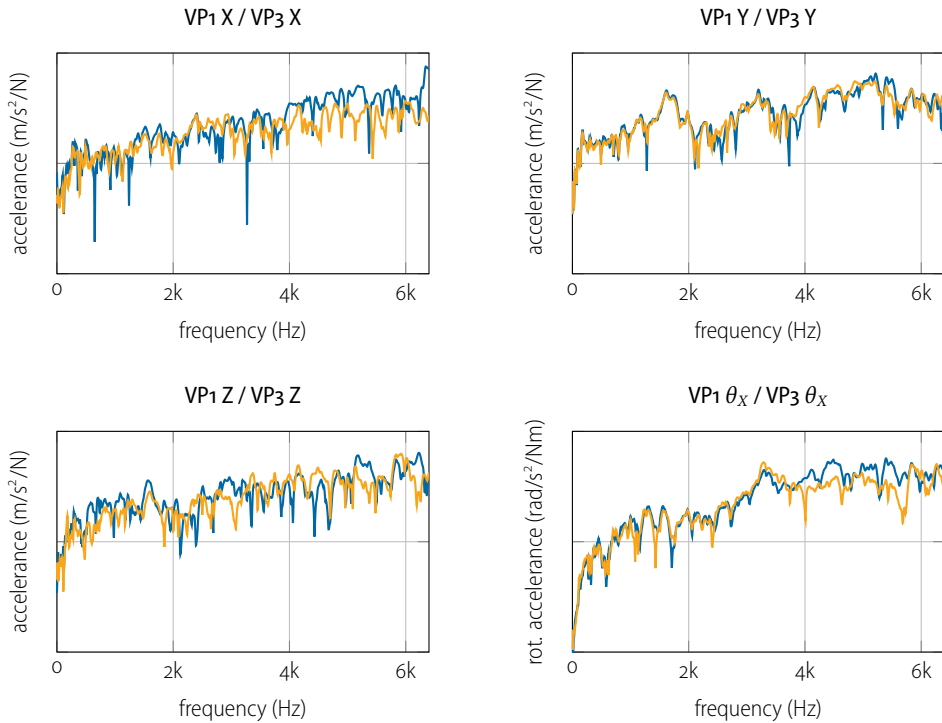


Figure 8.9: Virtual point FRFs for individual coupling points VP1/VP3 (—) and their reciprocal VP3/VP1 (—) in various directions: X, Y, Z acceleration and the rotational acceleration about the X-axis.

8.3.4 Summary

Let us summarize the steps that have been walked through in this analysis:

- ▶ The vehicle has been prepared for measurement and instrumented with acceleration sensors. Sufficient sensors have been put around each coupling point to be able to determine all translations and rotations through virtual point transformation.
- ▶ Impact positions have been defined that are — in theory — sufficient to determine all virtual point forces and moments.
- ▶ An SVD analysis has shown how the structure behaves at low frequencies. From this analysis, it was confirmed that rigid behaviour is indeed present, i.e. the responses corresponding to rigid motion exceed the noise floor.
- ▶ Evaluation of sensor consistency has revealed that the coupling points at the left and right side can in fact be considered as locally rigid structures. This allows to model the connectivity by two virtual points instead of four: one for the left and one for the

right side. However, the assumption only holds up to approximately 2 kHz.

- ▶ Impact consistency has assisted in spotting erroneous impacts, that can be considered as outliers and therefore excluded from further processing. Doing this, the overall impact consistency is improved; however one should treat this matter with care in order to preserve sufficient excitations for the virtual point transformation.
- ▶ Virtual point admittance was computed for the four coupling points, resulting in a 24-by-24 virtual point FRF matrix. Practice has shown that the overdetermination of impacts was not sufficient to overcome the influence of errors in the impact position and directions. Nonetheless, some FRFs can be assigned a high certainty because they show high correlation with their reciprocal.
- ▶ Transformation to combined left- and right-side virtual point FRFs further improves the overall reciprocity. However, as concluded from the sensor consistency, this type of modelling is only admissible up to 2 kHz.

The obtained admittances Y_{um}^{AB} and Y_{qm}^{AB} of the assembled vehicle with EPS are used in Chap. 9 for TPA purposes.

8.4 FRF uncertainty & benchmark study

FRF measurement is always accompanied by a number of experimental uncertainties, as was discussed in Sec. 1.3.2 and 4.5. Uncertainties can be attributed to a myriad of causes, such as the ones categorised here:

- ▶ *Experimental errors*, e.g. deviations in the position and direction of impact excitations, double pulses, influence of mounting or test bench conditions;
- ▶ *Instrumentation errors*, e.g. poor signal-to-noise ratio, sensor overload and cross-talk between channels, bias errors due to incorrect channel calibration, mass-loading of sensors and cabling;
- ▶ *Data acquisition errors*, e.g. signal distortion due to electromagnetic interference (e.g. 50/60 Hz hum), quantisation and sampling errors, aliasing, phase errors due to multiplexing between channels;
- ▶ *Signal processing errors*, e.g. spectral leakage and overestimation of damping due to incorrect windowing, phase distortion due to low-pass / high-pass filtering.

The previous application and the example of Sec. 4.6 have demonstrated how the quality of a complete impact measurement campaign can be evaluated based on structural-dynamic criteria, such as the sensor and impact consistency and reciprocity of a virtual point admittance matrix. Good performance on these criteria may partly eliminate the uncertainties associated with the FRF experiment.

In the automotive industry, an additional uncertainty of interest is the *production spread*, i.e. deviations in the assembled product as a result of production tolerances. Management of production tolerances is an important part of quality assurance, especially for aspects that involve safety and performance. A modern production-line vehicle, produced under tightly controlled circumstances, should in principle behave identically as any other vehicle of the same type and livery — although everyone is familiar with the occasional lemon [Dutch: “maandagmorgenproduct”] that beats the odds of the final acceptance test.

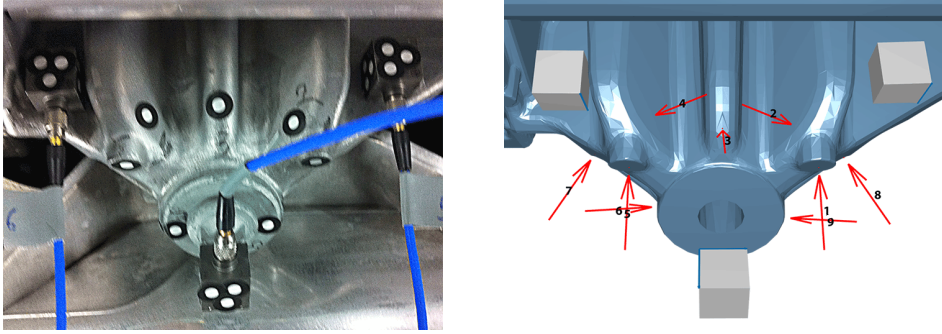


Figure 8.10: Rear-left coupling point of the EPS system: photo of the mounting in the vehicle (left) and a virtual reproduction (right). The dotted stickers are used for position measurement by photogrammetry software.

With regard to uncertainty in vehicle NVH engineering, the production spread is often indicated as a factor that limits the applicable frequency bandwidth of experimental techniques. After all, tiny differences in the construction have larger effects at higher frequencies. At the same time, it is hard to quantify which uncertainties belong to experimental measurement errors and which are related to production spread.

8.4.1 Benchmark on three similar cars

To investigate what this means for vehicle FRF measurement and test if the virtual point transformation performs better than conventional FRF measurement, a benchmark study has been conducted on three similar cars. The platform for application is the 2010 BMW 5-series. Two vehicles are of the edition “touring”, i.e. the station variant, and one vehicle is the limousine edition. It is worth noting that the assembly of the steering system and the front subframe is identical for all three cars; the difference between touring and limousine mainly concerns the interior compartment.

The purpose of measurement is to determine, for each of the three benchmark vehicles, a selection of structural-acoustic FRFs in a frequency range from 0 to 6000 Hz. The following FRFs have been chosen that are typical for applications in this project:

- ▶ The driving-point admittance FRFs of the rear-left coupling point of the steering system with the subframe, i.e. Y_{22}^{AB} . This type of FRFs could be considered for an application of dynamic substructuring;
- ▶ The structural-acoustic FRFs of this coupling point to the acoustic pressure at the left driver’s ear, i.e. Y_{32}^{AB} . These FRFs would be required for noise prediction using component-based TPA.

The FRFs of the three vehicles have been measured in different laboratories. The measurement equipment have been kept the same and it has been tried to use similar sensor and impact positions. After each measurement, photos have been shot from a multitude of angles for geometry analysis by photogrammetry software. This allows to accurately determine the position and orientation of the sensors and impact hammer excitation points, namely by reconstruction of the geometry using the identified dotted stickers and a CAD

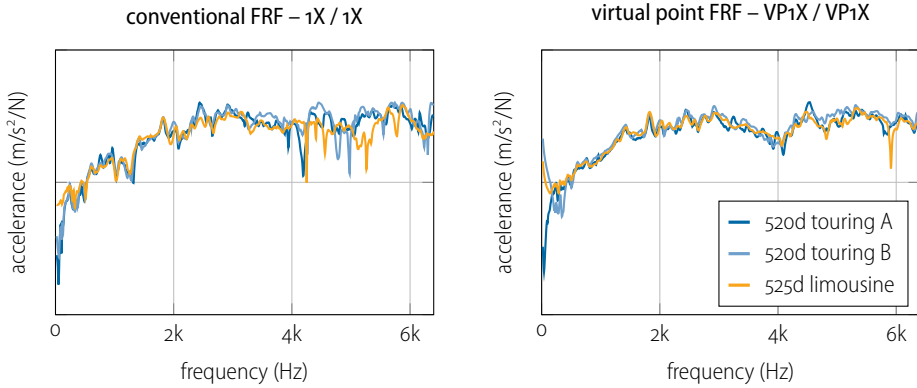


Figure 8.11: Comparison of the structural FRFs of three vehicles, obtained from conventional FRF measurement (left) and by application of the virtual point transformation (right).

model of the components under test. This is shown in Fig. 8.10 for the rear-left EPS system coupling point of interest.

8.4.2 Conventional versus virtual point approach

The conventional experiment consists of measurement of a single impact in one direction: the positive X -direction, indicated by impact number 3 in Fig. 8.10. To evaluate the driving-point FRF, the response of the bottom sensor is considered in the same direction. This corresponds to a single function in the measured FRF matrix \mathbf{Y}_{uf} .

The virtual point experiment employs, due to the transformation of 9 sensor responses and 10 impact forces, a total of 90 FRFs for each coupling point. Both IDM matrices are over-determined, which means that consistencies as well as reciprocity/passivity can be evaluated. For the comparison between vehicles, entry $[1, 1]$ was used from the virtual point FRF matrix \mathbf{Y}_{qm} , which corresponds to the driving-point FRF in translational X -direction. Note that the microphone at the driver's ear is a single response channel: it has no kinematic relation to other FRFs. This means that only the IDM matrix of the impact forces is used. Effectively, 10 FRFs are utilised to calculate the virtual-force transfer function to the microphone, which pertains to the right-sided transformed FRF matrix \mathbf{Y}_{um} .

8.4.3 Comparison of structural FRFs

Fig. 8.11 shows the results for the structural FRFs of the three vehicles. Let us discuss the performance of the two approaches for three frequency ranges.

- In the range from 0 to 200 Hz, both methods show high responses for one or two of the vehicles, whereas the response of the 520d touring A remains low. The high values are unrealistic: rigid body modes and low frequency responses shall remain low for systems that are not floating free. This was an artefact of measurement: in order to induce sufficient energy up to 6000 Hz, substantial impact force was used. This resulted in signal overloads at some of the sensor channels, which appears as a DC offset that diminishes for higher frequencies. To obtain better results at the low frequency end, it is suggested to use a softer tip at the impact hammer.

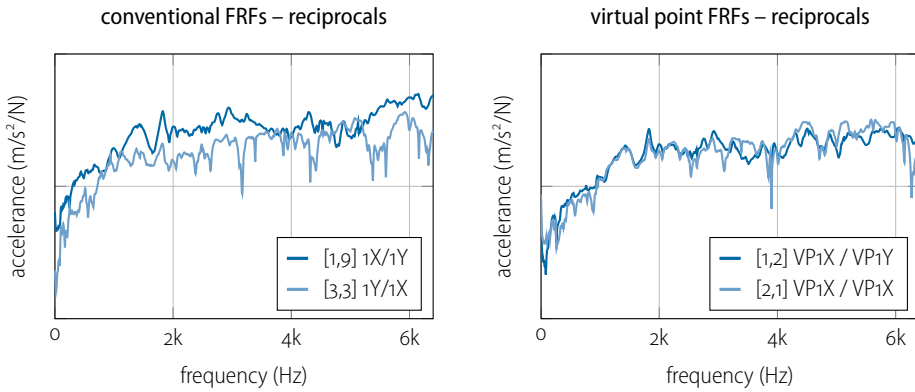


Figure 8.12: FRFs of an X-to-Y response and the reciprocal Y-to-X. The conventional experiment (left) shows two response functions of DoFs that should roughly be reciprocal; the virtual point FRFs (right) are correctly reciprocal as a result of the transformation.

- ▶ Between 200 and 2000 Hz, both methods show remarkably coherent responses. This implies that, at least locally, the three vehicles display almost identical dynamics. The average coherence⁶ of the virtual-point transformed determination is higher than the conventional measurement: an average of 95% against 87%.
- ▶ From 2000 to 6000 Hz, the virtual point method clearly outperforms the conventional method. Based on the conventional estimation, one could probably not tell with certainty whether the deviations are due to measurement errors or caused by production spread. The average coherence in this frequency range is 59%. The virtual point method returns very similar response functions, with an average coherence of 86%. From these results, one might indeed assume that the structural dynamics are similar.

The virtual point method also returns rotational FRFs and physically correct reciprocals, as the vectors of the virtual response and excitation DoFs are correctly associated. Obtaining a reciprocal from the conventional experiment is cumbersome, as can be observed from Fig. 8.10: most impact excitations are not in an orthogonal direction of one of the sensors. To illustrate this, Fig. 8.12 shows an attempt to compare reciprocals obtained by both approaches, namely for the measurement on the 520d touring A vehicle. For the conventional approach on the left, FRFs were selected of DoFs for which reciprocity should roughly be required. Clearly, this does not result in good reciprocity. The virtual point method shows more promising results⁷, with an average reciprocity of 80%.

8.4.4 Comparison of structural-acoustic FRFs

The structural-acoustic frequency response functions to the microphone at the driver’s ear are depicted in Fig. 8.13. Note that the vertical axis represents the sound pressure level (SPL) response in A-weighted decibels (dBa) as a result of a constant harmonic excitation force of one Newton (the grid lines represent steps of 20 dBa). The frequency axis shows

⁶Computed using the FRF coherence function. In this case it represents the similarity between the three FRFs, taking phase differences into account.

⁷Note that a similar analysis was shown in Fig. 8.9 for the virtual point FRFs of the X5 measurements.

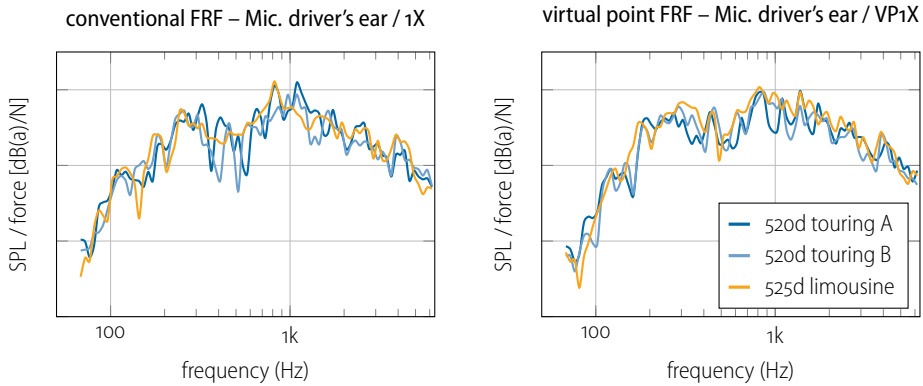


Figure 8.13: Structural-acoustic FRFs of three vehicles, obtained from conventional FRF measurement (left) and by application of the virtual point transformation to the forces (right).

a logarithmic scale: narrow frequency bands have been calculated using a twelfth-octave filter bank⁸.

In contrast to Fig. 8.12, the only difference between left and right is the force transformation of 10 impact force DoFs in the right diagram, which is the result of some kinematically sensible averaging. The microphone response remains a single channel in both cases. Although it has been positioned in each vehicle with utmost care, one should account for differences between the three vehicles in the order of 10 millimetres and angle differences in the order of 5 degrees.

The overall envelope of the response curves are comparable for both approaches. This implies that the response to excitations at the steering gear, even inside the vehicle, is rather independent of the vehicle type. However, any further conclusions of this nature are unsubstantiated based on the results presented here.

8.4.5 Summary

Three vehicles have been subjected to FRF determination according to two philosophies: conventional single-FRF measurement and virtual point FRF determination from multiple FRFs. In all cases, the virtual point methodology performed equally or better than the conventional approach, in the sense that less difference was observed between the determined FRFs belonging to the three vehicles. From the virtual point method, it could be concluded that the effects of spread in production properties, when considering local dynamics at the chassis, are negligible.

For determination of structural-acoustic FRFs, the two approaches show similar performance. Both methods show significant differences between the structural-acoustic responses of the three vehicles, which may be attributed to several factors such as uncertainties in microphone position and differences in interior configuration. Nonetheless, the overall envelopes follow the same trend, which is already valuable input for many engineering purposes.

⁸A twelfth-octave division correlates with the 12 semi-tones in a full octave, which amounts to a frequency ratio of $2^{1/12} = 1.0595$ or approximately 6% difference between each frequency band.

8.5 Application of Dynamic Substructuring

One of the very strengths of dynamic substructuring is the ability to predict structural-dynamic behaviour of an assembly based on the dynamics of its components. So far, it has been discussed how experimental measurement techniques can be employed to determine the dynamic behaviour, e.g. FRF functions, of an assembled system. However, this assumes that the assembly of interest is already available for measurement in the desired configuration, which it is typically not granted in the early phase of development.

This section discusses an application of experimental dynamic substructuring for assembly of vehicle FRFs from experimental and numerical models of its components. The focus is on the substructuring procedures rather than the measurement steps, as the applied experimental techniques are in line with the approach discussed in the previous two sections. In particular, it will be demonstrated how assemblies can be constructed by adding and subtracting substructures using the LM-FBS procedures described in Chap. 3.

This application concerns the BMW 3-series that was introduced to the market in 2012. Different to the previously discussed platforms, the EPS system of the 3-series has only two connection points to the subframe. Because of that, the steering spindle is considered as a third coupling point for substructuring. Note that the results presented in this section also appeared in [186].

8.5.1 Substitute coupling approach

The aim of the substructuring study presented here is to determine the coupled FRFs of the steering system – vehicle assembly from experimental models of the separate components. Naturally, the straightforward approach would be to measure the free dynamics of the EPS system suspended in a frame (subsystem A) and the “trimmed-body” vehicle without EPS (subsystem B) and assemble at the interfacing points to obtain the dynamics of AB. In a very systematic substructuring notation⁹, this would read:

$$\mathbf{Y}^{AB} = \mathbf{Y}^A + \mathbf{Y}^B \quad (8.1)$$

The *direct coupling* approach, schematically depicted in Fig. 8.14a, has several limitations in case of this construction. Most notably, the trimmed-body vehicle cannot be measured in the desired configuration: the steering column, which is hinged at the bodywork, is hanging unsuspended without the steering spindle connection.

To resolve this problem, a substitute part can be put in place as a temporary fixture. This is depicted in Fig. 8.14b. The substitute beam, denoted by subsystem C, is designed to have the same connecting points as the original structure. This can afterwards be removed by a substructure decoupling step, after which the original structure can be coupled. The two-step procedure reads:

$$\begin{cases} \mathbf{Y}^{B*} = \mathbf{Y}^{CB} - \mathbf{Y}^C \\ \mathbf{Y}^{AB} = \mathbf{Y}^{B*} + \mathbf{Y}^A \end{cases} \implies \mathbf{Y}^{AB} = \mathbf{Y}^{CB} - \mathbf{Y}^C + \mathbf{Y}^A \quad (8.2)$$

This approach is referred to as *substitute coupling*. Besides accommodating for a correct configuration of the relevant substructures, it offers other interesting advantages:

⁹A somewhat thicker plus and minus symbol are used to denote DS coupling and decoupling operations, respectively Eq. (3.31a) and (3.31b).

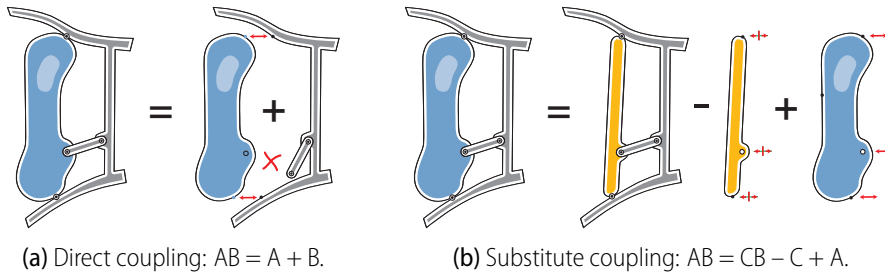


Figure 8.14: Two approaches for substructuring of the EPS system (A, blue) into the vehicle subframe (B, grey). Using a substitute beam (C, yellow) during measurement, the substructures can be measured in the correct configuration.

1. *Consideration of friction effects.* Using direct coupling, the interfaces of the separate substructures are measured in free conditions. Any effects of friction, that in reality occur at the coupled interfaces in the assembled configuration, are not included in either of the component models. This often causes an underestimation of damping in the assembled system, resulting in too prominent resonances and anti-resonances. Now, when measuring the vehicle with the substitute beam in place, the friction effects are included in the measured system BC and retained in B after decoupling of the free subsystem C. In other words, Y^{B^*} differs from Y^B insofar as the friction at the interface is only present in the former. Naturally, the interface surfaces of the substitute beam should resemble those of the EPS, as otherwise different friction effects can be expected.
2. *Modal conditioning.* Coupling of a structure between two relatively flexible bodies may increase the stiffness between coupling points substantially¹⁰. This changes the vibration modes of the assembled system, which is associated with very high coupling forces in the DS equations. Instead, if the structure is supplied with a temporary fixture that has comparable mass and stiffness, one measures the structure in a condition which is much closer to the targeted assembly. Consequently, the difference in dynamics is smaller, which potentially leads to better results in practice.
3. *Convenience of measurement.* Vehicle components such as the EPS system are often highly optimised structures full of curved surfaces, that are far from ideal for impact excitation. The accessibility of these surfaces is even worse when installed in the vehicle. If the aim of the experiment is to determine 6-DoF dynamics of system AB, the impact measurement is particularly challenging. A substitute beam can be tailored towards this goal, such that one has access to all required sensor and excitation points, even when installed in the vehicle.
4. *Hybrid modelling.* The dynamics of the substitute beam need to be decoupled from a measurement, which is known to be an error-prone operation. In order to have a very high-quality model of the substitute beam, one could calculate the modes by FE modelling and synthesise FRFs using experimentally identified poles. This is applied in the study presented here and uses the theory of Sec. 2.2, 2.3 and 2.7.

¹⁰For example, imagine a tuning fork with two slender legs: introduction of a rod in between changes the dynamics substantially.

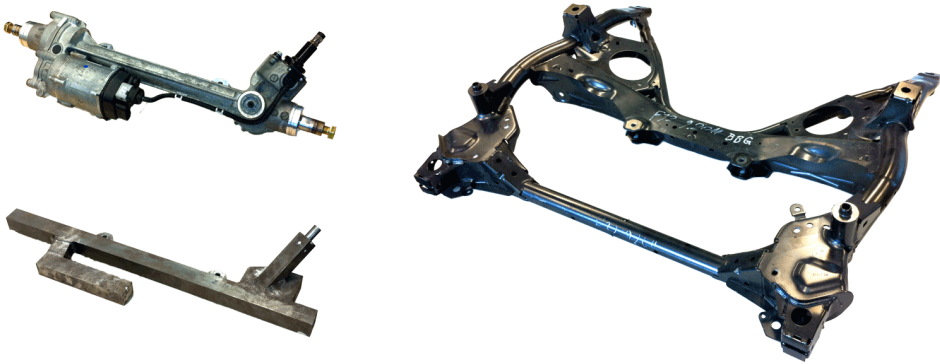


Figure 8.15: The three subsystems at hand: EPS system, substitute beam and vehicle subframe (as a representation of the trimmed-body vehicle).

Substitute coupling can be understood as the FBS interpretation of the method of modal constraints for fixtures and subsystems (MCFS) proposed by Allen & Mayes [7], which was later coined the transmission simulator method (TSM) [127, 128]. This method also employs a temporary fixture for measurement, but solves the decoupling and coupling steps in the modal domain. The aspect of modal conditioning is even more apparent, as the transmission simulator enables measurement of rotations and bending modes which would otherwise not be accessible.

Note that the abovementioned advantages of substitute coupling are by no means exact science. In theory, the two approaches yield identical results, provided that there are no unmodelled effects. In practice however, the substitute coupling approach proves to be a practical way of component measurement and an intuitive solution to include interface effects similar to how these occur in the targeted assembly. This is demonstrated next.

8.5.2 Experimental & numerical modelling

In order to compare the procedures of direct coupling and substitute coupling, a total of five assemblies and subsystems have been modelled experimentally from impact hammer measurements:

1. Assembly AB: vehicle with EPS system installed;
2. Assembly CB: vehicle with substitute beam installed;
3. Subsystem B: trimmed-body vehicle;
4. Subsystem A: EPS system in free conditions;
5. Subsystem C: substitute beam in free conditions.

The components of interest are shown in Fig. 8.15 (the picture of the front subframe represents the entire trimmed-body vehicle). The main coupling points for substructuring are the two connection points to the subframe. These have been measured and modelled according to 6-DoF virtual point methodology. A third coupling point is situated at the steering spindle: a local coordinate frame was defined here to express the local x, y, z translations and rotation about the steering axis. This adds another 4 DoFs, bringing the total

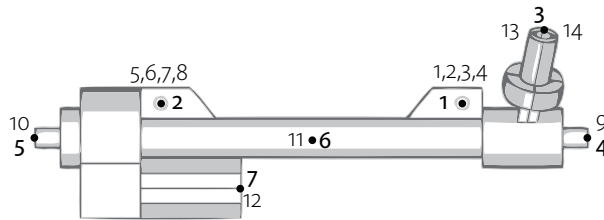


Figure 8.16: Schematic overview of the measurement points (light-face) and virtual points (bold-face) on the EPS system.

amount of interface DoFs \mathbf{u}_2 to 16.

In addition to interface DoFs, four internal points have been measured on the steering system and substitute beam, which are in this study denoted by \mathbf{u}_1 . The points on the substitute beam are used for the overdetermination of the decoupling process, as explained in Sec. 3.4.3, and are considered as 3-DoF virtual points. Two points are located on the left and right end of the rack bar, one point is positioned on the centre of the EPS housing and the fourth is attached to the EPS motor. Fig. 8.16 shows the location of sensor points (14 tri-axial accelerometers) and virtual points on the EPS system; similar locations have been used for the substitute beam.

In the interior of the vehicle, a microphone was positioned at the location of the driver's left ear, similar as for the previously discussed studies. Lastly, the vibration at the steering wheel has been measured using a single 3D accelerometer. These four responses are denoted \mathbf{u}_3 .

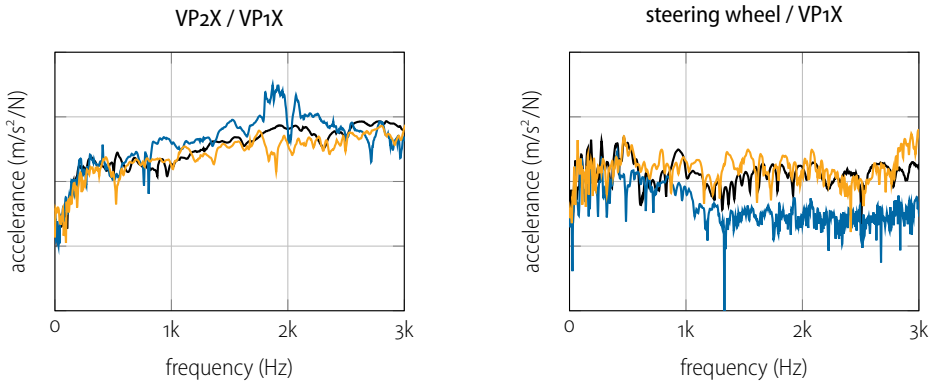
To refine the admittance of the substitute beam, an FE model was built in NASTRAN. 6 rigid body modes and 16 eigenmodes/frequencies have been computed, spanning a frequency range of 3400 Hz. From an EMA on the substitute beam, eigenmodes/frequencies have been extracted as well. The calculated frequencies and experimentally obtained frequencies match fairly well: the difference is below 5%. Consequently, FRFs have been synthesised using Eq. (2.19) from the experimentally estimated frequencies and damping values, while the modes have been adopted from the numerical model.

8.5.3 Results of dynamic substructuring

The two coupling procedures can now be compared with a validation measurement, i.e. direct coupling Eq. (8.1) and substitute coupling (8.2). For the first approach, coupling was established for the two bolted connections only. Coupling to the steering axis could not be achieved, as this point was not obtained during the trimmed-body impact measurement (recall the misconfiguration as illustrated in Fig. 8.14a). Hence, the number of interface DoFs for direct coupling amount to 12.

For the substitute coupling approach, two steps have been performed consecutively:

1. Decoupling of C from CB using the non-collocated overdetermined approach, i.e. 16 interface DoFs \mathbf{u}_2 plus 12 internal DoFs \mathbf{u}_1 for the compatibility condition and only 12 interface forces \mathbf{g}_2 for equilibrium. From the resulting dual set of DoFs, only the coordinates belonging to B^* are retained;
2. Coupling of A to B^* using 16 interface DoFs.



(a) Transfer between the left and right connecting points of the EPS to the subframe.

(b) Transfer from an EPS coupling point to the steering wheel.

Figure 8.17: Results of direct coupling (—) and substitute coupling (—) compared to a validation measurement (—). The grid lines on the acceleration axis represent steps of 10².

Two transfer functions are shown for comparison: Fig. 8.17a shows the FRF from one of the bolted connections to the other; Fig. 8.17b shows the transfer from one of the coupling points to the steering wheel in the vehicle. Unfortunately, a structural-acoustic transfer function to the driver's ear could not be compared due to calibration problems with the microphone in one of the vehicle measurements.

In both cases, substitute coupling shows the best results compared to the validation measurements. It can be seen from the Fig. 8.17a that the direct coupling yields an overestimation of the transfer between the coupling points. This may be due to the fact that the interface damping is neglected. The substitute coupling result displays the same trend, especially up to 1500 Hz, but leaves room for improvement.

Fig. 8.17b shows the response at the steering wheel due to excitation at the same coupling point of the EPS system. Clearly, the direct coupling approach cannot account for the vibration transfer through the steering spindle, as this connection could not be included in the coupling equations. For the substitute coupling approach, this path was indeed taken into account. The overall levels very well resemble the validation measurement.

8.5.4 Summary

The procedure of substitute coupling has been demonstrated and compared with direct coupling. It was shown how a temporary fixture can be used during measurement, to realise the correct connectivity and incorporate friction effects that occur at the interfaces. The FRFs of the substitute beam have been synthesised from numerically computed modes and experimentally obtained frequency and damping parameters. Results have indicated the benefits of substitute coupling over direct coupling, however the match with the validation measurement is not fully convincing over the full frequency range.

9

Steering noise prediction from test bench measurements

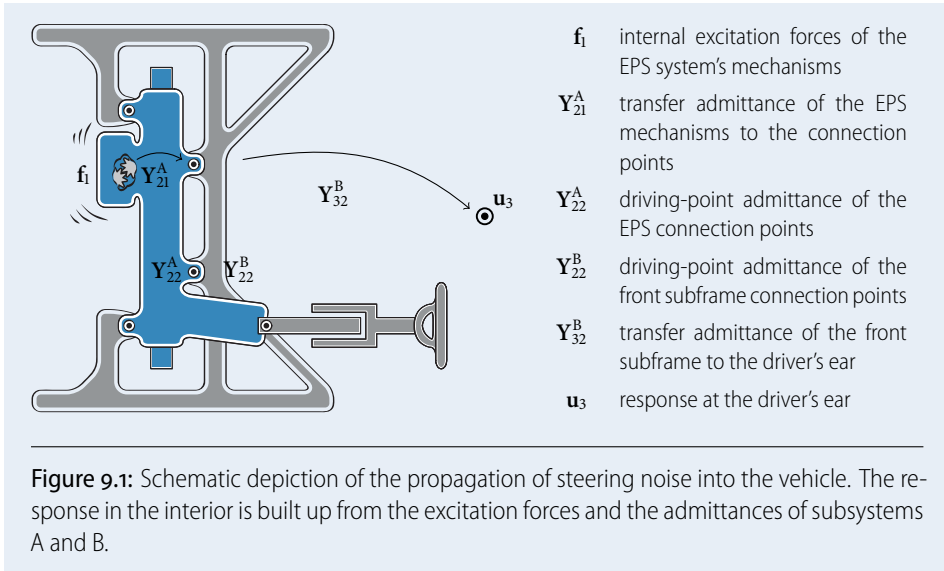
chapter contents:

9.1 Introduction	143
9.1.1 Propagation of steering noise	144
9.1.2 Characterisation of steering noise	144
9.1.3 Source characterisation on a test bench	145
9.1.4 Chapter outline	145
9.2 Development of component-based TPA approaches	145
9.2.1 Stiff support structures	146
9.2.2 Compliant support structures	148
9.2.3 Source characterisation on two test benches	149
9.2.4 Prediction of steering gear noise	150
9.2.5 Summary of presented methods	152
9.3 In-situ TPA from vehicle and test bench measurements	152
9.3.1 Purpose of study	152
9.3.2 In-situ TPA in the vehicle	153
9.3.3 In-situ TPA on a test bench	158
9.4 Summary	162

9.1 Introduction

This chapter discusses the studies of source characterisation and noise prediction of the steering system. The motivation for these studies has partly been covered in the introduction, Sec. 1.2. In summary, the steering system is an active mechatronic component that has an audible contribution in the vehicle's interior, especially when steering at high speed such as for a parallel parking manoeuvre. This might not be an immediate concern for combustion-engine vehicles, but becomes more relevant once changing to hybrid and full-electric drive-lines. After all, there is no engine noise at zero driving speed, leaving the driver fully exposed to all sorts of squeaks, rattles and other undesired sounds that may emanate from the steering system in operation.

Steering systems are often custom designed for a particular vehicle platform, with additional differentiation for various drive-lines, sport editions, variable steering speed ratio, etc. Experience has learned that these variants sometimes create different noise profiles in the vehicle that exceed the maximum level. However, if a different noise is experienced, this does not directly imply that the source excitation is different.



9.1.1 Propagation of steering noise

Let us recapitulate the governing equations of the transfer path problem, namely Eq. (6.1) for the assembled and Eq. (6.5) for the substructured problem:

$$\mathbf{u}_3 = \mathbf{Y}_{31}^{AB} \mathbf{f}_1 = \mathbf{Y}_{32}^B (\mathbf{Y}_{22}^A + \mathbf{Y}_{22}^B)^{-1} \mathbf{Y}_{21}^A \mathbf{f}_1 \tag{9.1}$$

In the second substructured equation, four subsystem admittances can be identified that determine the propagation of source excitations \mathbf{f}_1 to experienced sound \mathbf{u}_3 . This is illustrated in Fig. 9.1. In theory, one could use Eq. (9.1) to reason if an increase of each term correlates with higher or lower response at \mathbf{u}_3 . However, note that two admittance terms pertaining to respectively A and B are in some way dependent of each other. For example: it is almost impossible to change \mathbf{Y}_{22}^A without affecting \mathbf{Y}_{21}^A , as both are an observation of the same dynamic system¹.

9.1.2 Characterisation of steering noise

As discussed in Chap. 5, one of the principal motivations for a TPA is the fact that the source is unquantifiable. This implies that \mathbf{f}_1 and \mathbf{Y}_{21}^A cannot be measured and that the EPS system's activity must be characterised by alternative means. In the TPA framework of Chap. 6, three conceptual families have been discussed for this purpose:

- ▶ *Classical:* The EPS system's activity is described by the *interface forces* that occur in the connection points with the vehicle. As can be observed, the interface forces are a property of both the EPS system and the vehicle:

$$\mathbf{g}_2^B = (\mathbf{Y}_{22}^A + \mathbf{Y}_{22}^B)^{-1} \mathbf{Y}_{21}^A \mathbf{f}_1 \tag{9.2a}$$

- ▶ *Component-based:* The EPS system's activity is described by *equivalent forces*, such as blocked forces measured against a rigid boundary. These forces are a property of

¹In fact, one could use substructuring as well to investigate the effect of adding mass or stiffness to the terminals of each subsystem; see for instance [101].

the EPS system only:

$$\mathbf{f}_2^{\text{eq}} = (\mathbf{Y}_{22}^{\text{A}})^{-1} \mathbf{Y}_{21}^{\text{A}} \mathbf{f}_1 \quad (9.2b)$$

- *Transmissibility-based*: The EPS system's activity is described by *indicator responses* that are measured along the transmission paths of the EPS system in the vehicle:

$$\mathbf{u}_4 = \mathbf{Y}_{42}^{\text{B}} (\mathbf{Y}_{22}^{\text{A}} + \mathbf{Y}_{22}^{\text{B}})^{-1} \mathbf{Y}_{21}^{\text{A}} \mathbf{f}_1 \quad (9.2c)$$

9.1.3 Source characterisation on a test bench

Early on in the project, it was realised that the steering system would best be tested on a test bench, for optimal flexibility and controllability of the operational conditions. Also, the source characterisation should be independent of the dynamics of the vehicle or test bench, i.e. be a property of the EPS system only, to be able to predict the noise for assemblies with different vehicles. This way, the derived noise targets would be as much as possible a property of the EPS system itself.

Consequently, it was chosen to adopt and further explore the component-based TPA concept. The basic know-how of blocked force theory was obtained from [101, 103]. Over time, new force determination ideas have been explored and combined, inspired by new or related theories such as presented in [50, 92, 134, 182]. This has evolved towards a robust and easy to use component-based TPA strategy, which is the topic of this chapter.

9.1.4 Chapter outline

Sec. 9.2 presents the methodological developments in retrospect, namely on the basis of test bench iterations and theoretical explorations that have led to better comprehension of component-based TPA. Sec. 9.3 reports on the final iteration that was conducted to apply all “lessons learned” and, additionally, investigate some concepts adopted from other families of TPA.

9.2 Development of component-based TPA approaches

This section discusses several component-TPA approaches and (re)designs of test benches for the characterisation of steering system vibrations. It is a summary of studies, that have individually been presented in [26, 146, 188, 212]. Focus of this section is on the different methods for characterisation of the excitations of the EPS system. More specifically, the aim is to determine an equivalent set of forces \mathbf{f}_2^{eq} that can be used to predict the structure-borne noise of the EPS system inside the vehicle. This is the general concept of component-based TPA stated by Eq. (6.11):

$$\mathbf{u}_3 = \mathbf{Y}_{32}^{\text{AB}} \mathbf{f}_2^{\text{eq}} \quad (9.3)$$

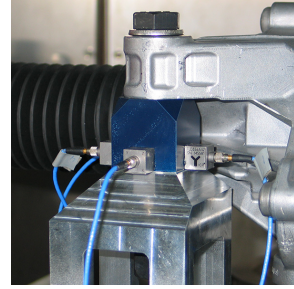
In order to impose realistic driving-like conditions onto the EPS system, several steering resistance mechanisms have been employed, such as wheels turning on stone tiles, hydraulic cylinders and servo-electric linear actuators. However, a discussion of these systems is not the aim of this chapter.



(a) Stiff test bench support with 3D force sensor clamped in near the interface.



(b) Stiff test bench support with four additional tri-axial accelerometers.



(c) Compliant test bench support with four tri-axial accelerometers.

Figure 9.2: Several designs of test bench supports for the EPS system of the 5-series platform. The fourth coupling point is shown, i.e. front right.

9.2.1 Stiff support structures

At first, a test bench was constructed for direct measurement of blocked forces according to Sec. 6.3.2. To establish the required rigid boundary condition, rocket-shaped support poles have been fabricated from solid cylindrical pieces of steel, as depicted by Fig. 9.2a and 9.3a. Each support comprises a 3D force transducer at the top near the connection point. This allows for direct measurement of a total of 12 blocked-force DoFs, namely the forces in orthogonal directions of the four coupling points of the EPS system:

$$\mathbf{f}_2^{\text{eq}} = \mathbf{g}_2^{\text{bl}} = \mathbf{g}_2^{\text{B}} \quad (9.4)$$

Soon enough, it was realised that the direct blocked force method is not applicable in the full bandwidth of interest. On one hand due to flexibility of the support pole above 1 kHz; on the other hand because of the inability to measure rotational moments. As a solution, each support rocket has been supplied with 4 accelerometers (Fig. 9.2b and 9.3b). These sensors span a sufficient space to determine the 6-DoF accelerations \mathbf{u}_2 at each coupling point, which can be used to compute a compensation term to augment the (not so) blocked forces \mathbf{g}_2^{R} . This corresponds to the hybrid interface method discussed in Sec. 6.3.4:

$$\mathbf{f}_2^{\text{eq}} = \mathbf{g}_2^{\text{R}} + (\mathbf{Y}_{22}^{\text{A}})^{-1} \mathbf{u}_2 \quad (9.5)$$

An impact measurement was performed on the free EPS system to obtain the required (virtual point) admittance at the EPS connection points $\mathbf{Y}_{22}^{\text{A}}$ to calculate the compensation term in 6 DoFs per point. However, the interface force term itself still lacks information on the rotational DoFs. It was therefore suggested to determine the interface moments from a matrix-inverse operation with the test bench admittance \mathbf{Y}^{R} , much like a classical TPA matrix inverse method. This allows for the following substitution in Eq. (9.5):

$$\mathbf{g}_2^{\text{R}} = (\mathbf{Y}_{22}^{\text{R}})^{-1} \mathbf{u}_2 \quad \implies \quad \mathbf{f}_2^{\text{eq}} = (\mathbf{Y}_{22}^{\text{R}})^{-1} \mathbf{u}_2 + (\mathbf{Y}_{22}^{\text{A}})^{-1} \mathbf{u}_2 \quad (9.6)$$

In addition, a mixed approach was considered that estimates the full interface force vector from a weighted least-square determination using the measured interface forces and the matrix-inverse acceleration term. This is not discussed here, see [26, 212] for details.

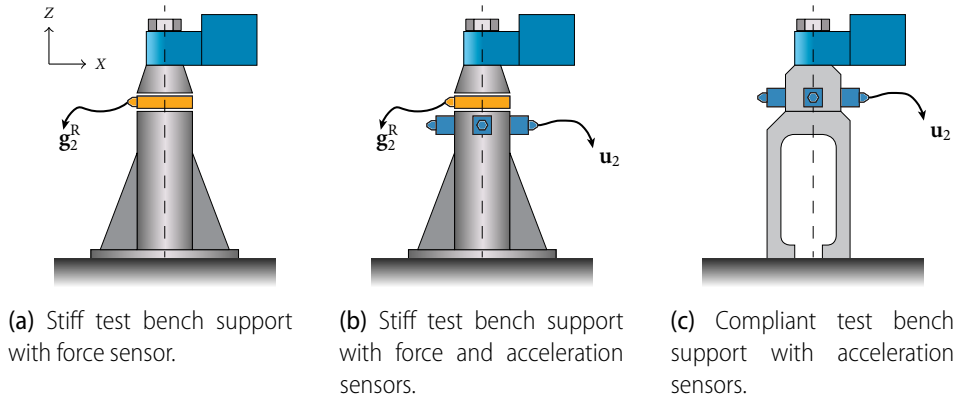


Figure 9.3: The two EPS support structures with three principles of instrumentation.

The aforementioned studies have provided the following insights:

- ▶ The direct blocked force approach of Eq. (9.4), using translational interface forces only, provided the best blocked force estimation. The compensation term of Eq. (9.5), computed from the interface accelerations, turned out to be much larger than the measured force term, which is not expected for this system. This was due to a poor signal-to-noise ratio (SNR) on the accelerometers, caused by the high stiffness of the steel supports poles. To improve the SNR, it would be justified to make the test bench more flexible, which appears contradictory considering the aim to determine “blocked” forces.
- ▶ The approach of Eq. (9.6), due to the two matrix inversions, effectively sums the stiffnesses of the EPS system (A) and the test bench (R) at their connection points, just like the primal stiffness assembly procedure of Sec. 3.3.1. It was concluded that the two matrix-inverse operations could be replaced by a single matrix inversion operation with the interface admittance of the assembly (AR). As discussed in Sec. 6.3.5, this leads to an approach which is also known as *in-situ* force determination.

The *in-situ* concept was originally proposed as a means to determine theoretical blocked forces in the originally targeted assembly [134], for instance to characterise the EPS system (A) from a measurement when mounted in the vehicle (B). However, as the resulting forces are an independent property of A , there is essentially no restriction in applying the methodology to an assembly with another passive side, such as the test bench (R):

$$\mathbf{f}_2^{\text{eq}} = (\mathbf{Y}_{22}^{\text{AR}})^{-1} \mathbf{u}_2 \quad (9.7)$$

In [187], the test bench *in-situ* approach of Eq. (9.7) has been compared with the previously discussed methods. It was learnt that the *in-situ* method, when applied to the stiff test bench, generally provides good estimates of the blocked-force, but suffers from SNR problems at low-frequencies. A robust estimation was obtained by comparing several force determination schemes and combining blocked force and *in-situ* estimates using a cross-over filter at 500 Hz. Fig. 9.4 presents a flowchart of the considered methods and their governing equations, together with the procedures of experimental subsystem modelling and vehicle validation (to be discussed later).

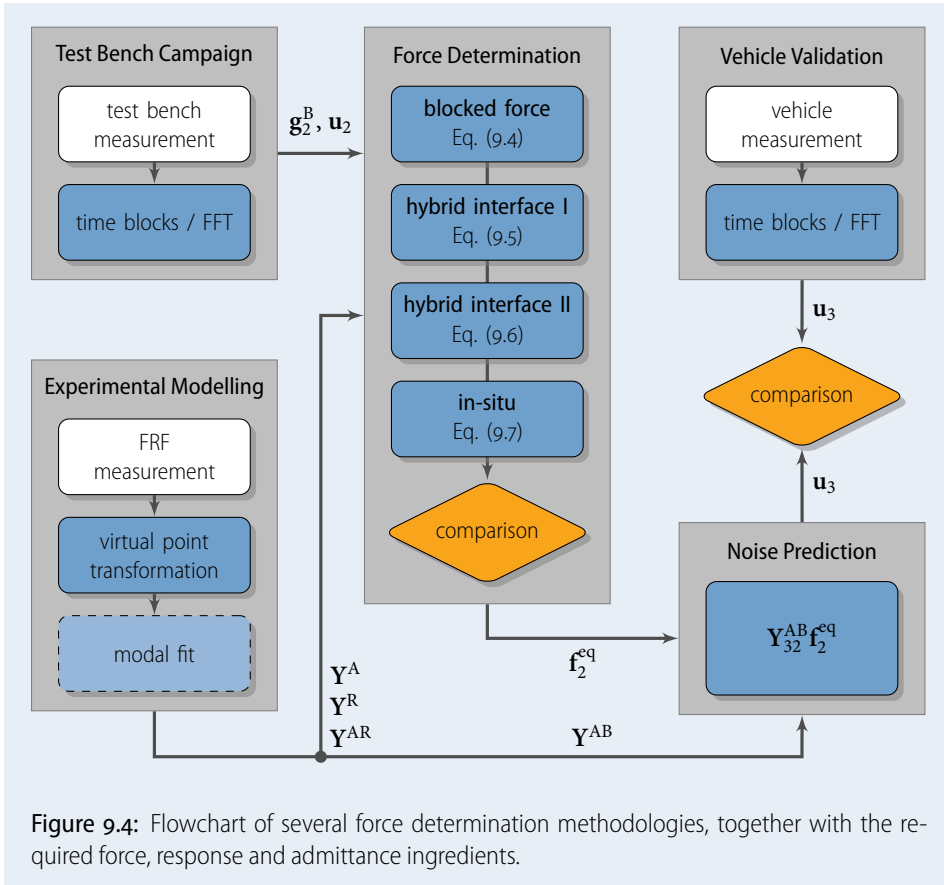


Figure 9.4: Flowchart of several force determination methodologies, together with the required force, response and admittance ingredients.

9.2.2 Compliant support structures

Based on promising results from the in-situ method, new support structures have been designed that are more compliant than the stiff poles; see Fig. 9.2c and 9.3c. The aim was to enable measurement of interface accelerations with sufficient SNR in the full bandwidth of interest of 0 to 6000 Hz. The new compliant supports are machined from solid blocks of aluminium and feature four slender legs for extra flexibility. An additional advantage of this design is the decoupling from vibrations at the base plate: crosstalk and disturbances originating from the test laboratory equipment are suppressed, just like any component suspended in soft springs².

Four tri-axial accelerometers per support were used to obtain an overdetermined set of interface responses \mathbf{u}_2 for computation of the virtual point interface accelerations. The sensors are put on a solid block of aluminium that only displaces rigidly. As a result, perfect sensor consistency was obtained.

Fig. 9.5 shows receptance FRFs \mathbf{Y}_{22}^R of both support structures, by conversion of the measured accelerance to receptance. Overall, the compliant test bench TB2 is roughly ten times more flexible than the stiff test bench TB1. This leads to higher SNR on the accelerometers and therefore better conditioning for the matrix inversion of Eq. (9.7).

²This decoupling however only occurs beyond the frequencies of the first resonance modes of the supports.

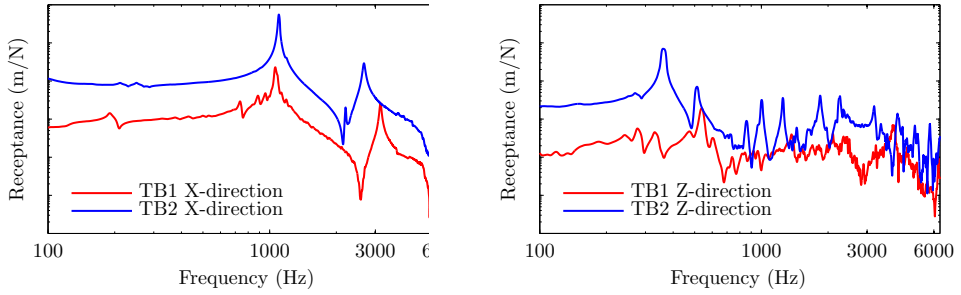


Figure 9.5: Receptance of the test bench supports in lateral (left) and vertical (right) direction.

9.2.3 Source characterisation on two test benches

Let us now discuss the application of source characterisation of the EPS system in operation. Two separate test bench campaigns have been conducted in different test facilities. All operational measurements result from a constant-speed steering manoeuvre, i.e. from maximum left to right at zero vehicle speed. This is comparable with a parallel parking manoeuvre. Steering wheel speeds of 100 to 600°/sec have been considered with increments of 100°/sec. All results presented in this chapter are obtained from the 600°/sec cycle. Each time, five identical cycles have been performed to assess the reproducibility of the measurement. Much care has been taken to provide similar operational conditions for the two test bench campaigns.

Equivalent forces f_2^{eq} are determined by application of the blocked force method on TB1 and the in-situ method on both TB1 and TB2. Fig. 9.6 shows series of equivalent forces in X and Z-direction of the first coupling point, as determined from three methods:

1. directly measured blocked interface forces g_2^B on stiff TB1;
2. in-situ force determination from measured accelerations u_2 on stiff TB1;
3. in-situ force determination from measured accelerations u_2 on compliant TB2.

Both the direct blocked force and the in-situ method are evaluated on the stiff test bench TB1. It was mentioned in Sec. 6.3.2 that the blocked force method constitutes a limit case, namely for an infinitely stiff boundary with zero interface displacement. However, the in-situ method merely exists by the sake of flexibility, as otherwise there would be no acceleration to use in the matrix-inverse operation of Eq. (9.7). As a consequence, strictly speaking, both methods cannot be true at the same time. Nonetheless, it is interesting to evaluate both methods on TB1 in comparison with the in-situ method of TB2.

Let us first discuss the equivalent forces in X-direction, depicted in Fig. 9.6 on the left. Results from the 5 cycles are depicted on top of each other; a high reproducibility can be observed. The blocked forces of TB1 (black) dive on three points clearly below the two in-situ determined forces (red). This can be explained by the dynamics of the support of TB1, that has a first bending mode around 1100 Hz. This means that the support structure displaces compliantly with the steering system, such that the interface force is no longer a blocked force. The peak of the TB1 in-situ curve at 4000 Hz can be assigned to the switching frequency of the external servo actuator used to operate the EPS system; this caused a distortion on the accelerometer measurement channels.

The equivalent forces in Z-direction determined by the in-situ method are shown in Fig. 9.6 on the right. The forces of TB1 show a significantly higher amplitude up to 3500 Hz com-

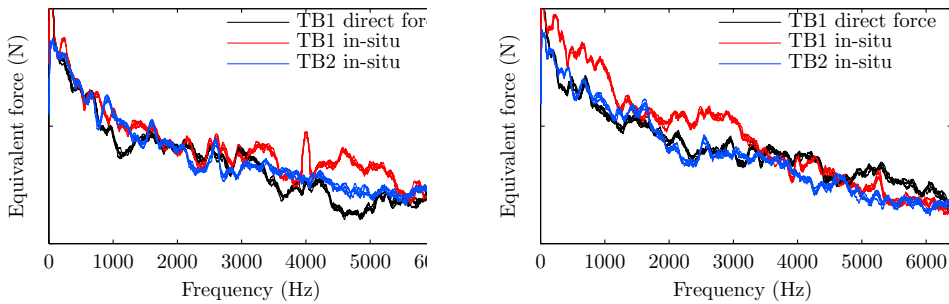


Figure 9.6: The equivalent forces in X-direction (left) and in Z-direction (right) on coupling point 1, determined on the two test benches from the directly measured interface forces and by the in-situ force determination method.

pared to the direct force measurement on TB1 and the in-situ method on TB2. A possible explanation of this overestimation could be the high stiffness of the assembly in Z-direction. As can be seen from Fig. 9.5 on the right, the measured admittance of the test bench support is very low, which turned out to be in the noise range of the acceleration sensors. This means that the admittance of the assembly EPS – TB2 was not properly measured in this direction. As a consequence, the operational accelerations are amplified in the inversion step of the in-situ method, resulting in an overestimation of the blocked-forces.

In general, care should be taken when drawing conclusions from equivalent force curves such as presented in Fig. 9.6. Let us remind that equivalent forces are a *representation* of the operational excitation of a source A, independent of any other connected component, but that this representation is not necessarily a unique one. Individual results in \mathbf{f}_2^{eq} may therefore differ. They are, however, equivalent with respect to their effect “downstream” of the interface, so for any response at the passive side of an assembly AB with arbitrary substructure B.

► In theory, the uniqueness can be related to the dimension of the equivalent force vector and the number of independent interface forces (or force modes) in the assembled system. For instance: it can be shown that in-situ determined equivalent force spectra equal those of the directly measured blocked forces, if the admittance matrix to invert by Eq. (9.7) is square and full rank and the measured blocked forces are indeed the full set of interface forces. In practice, this uniqueness is often not clearly defined, especially for active systems with multiple connection points and consequently many interface DoFs. Therefore, it is more meaningful to consider the *controllability* of a set of equivalent forces \mathbf{f}_2^{eq} , as will be discussed in Sec. 9.3. ◀

9.2.4 Prediction of steering gear noise

The steering gear noise at the driver’s left ear is synthesised by applying Eq. (9.3). Two sets of equivalent force spectra are considered and their noise prediction results are compared: (black) the results from application of the blocked force method on TB1 and (blue) the results from the in-situ method on TB2. The noise prediction was made by multiplying these spectra with the structural-acoustic FRFs of the assembled vehicle, i.e. $\mathbf{Y}_{32}^{\text{AB}}$, as depicted in Fig. 9.4. This matrix was obtained by experimental modelling of the 5-series vehicle FRFs,

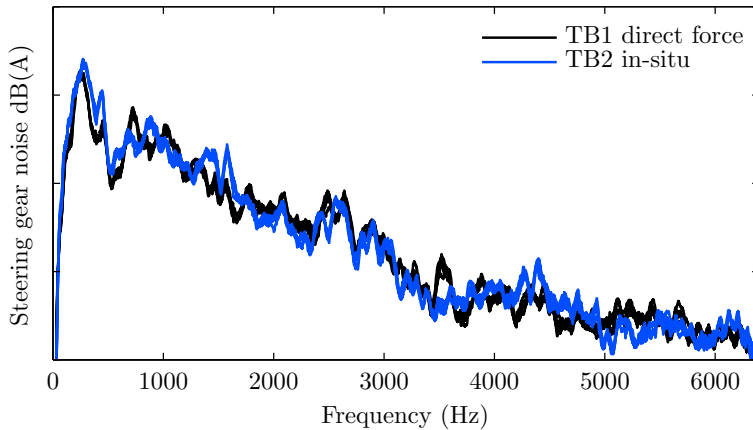


Figure 9.7: The prediction of the steering gear noise at the left driver's ear, based on two component TPA approaches.

which is not discussed here but follows from a similar procedure as the one presented in Sec. 8.3.

Fig. 9.7 shows the A-weighted acoustic pressures obtained by application of the two methods on two different test benches. The results are remarkably similar, even at high frequencies. This suggests that the equivalent forces, characterising the operational excitation of the EPS system, are independent of the dynamics of the test benches, considering their effect for responses at the passive side. Some observations and remarks:

- ▶ Up to 500 Hz, the response of the in-situ method is slightly higher than the response of the blocked force method. Over-estimation of the response in the low frequency band was already observed in earlier studies with matrix-inverse equivalent force determination schemes [26, 187]. It can be interesting to evaluate the conditioning of the FRF matrices used for inversion. Moreover, in light of the results of Sec. 8.3.2, it can be reasoned that 24 equivalent force DoFs are in fact too many to describe low-frequency behaviour. This is further discussed in Sec. 9.3.
- ▶ The blocked-force prediction of TB1 is computed using 12 translational forces only, as moments were not measurable with the available measurement equipment. This means that 12 of the 24 entries in the equivalent force vector for TB1 remain zero: rotational FRFs are thus not used in the matrix multiplication of Eq. (9.3). However, the predictions from in-situ methods are built from all 24 DoFs, i.e. 12 forces plus 12 moments. As those are determined from a matrix-inverse method, it would be interesting to investigate if the operational excitation could also be represented by fewer degrees of freedom. This is in fact a matter of controllability, which is addressed in the next section.

For the purpose of validation, steering cycles have been performed in the original vehicle using a servo motor on the steering wheel to provide constant steering speed. It turned out that this steering robot, although optimised for acoustic measurements, emitted noise that had a higher contribution on the microphones than the actual EPS system of interest. As a consequence, validation by comparison with the vehicle measurement was not possible.

9.2.5 Summary of presented methods

Let us briefly summarize the discussed TPA applications up to here. Several test benches have been constructed for component-based TPA measurements on the 5-series steering system. The blocked force, hybrid interface and in-situ methods have been explored and combined to obtain a robust characterisation of the source's activity, independent of the dynamics of the test bench. These methods are schematically depicted in Fig. 9.4. Based on the findings of the presented studies and the bandwidth requirements for analysis of EPS systems, it was chosen to further explore the in-situ method and apply the methodology to a new vehicle platform.

9.3 In-situ TPA from vehicle and test bench measurements

This section discusses the in-situ TPA applied to the EPS system of the 2014 BMW X5 SUV. An impression of the vehicle is shown in Fig. 9.8. The operational measurement campaign follows up on the FRF measurement and analysis described in Sec. 8.3. For a description of the relevant subsystems, their connectivity and the instrumentation in the vehicle, the reader is also referred to Sec. 8.1 and 8.2.

9.3.1 Purpose of study

The main purpose of this study is to explore the potential of in-situ TPA for characterisation of the EPS system in various testing environments. So far, the operational measurements have been conducted on test benches, whereas measurements in the vehicle only served the purpose of validation, namely to compare the in-vehicle measured \mathbf{u}_3 with those from TPA predictions. As concluded in the previous section, this comparison was compromised by the noise of the steering robot and the practical challenges in maintaining equal operational conditions. It was therefore suggested to also perform the in-situ measurements in the vehicle. In fact, this is the approach advertised by the method's original authors Moorhouse & Elliott [50, 52, 134]. This in-vehicle application is presented in Sec. 9.3.2, followed by a test bench campaign in Sec. 9.3.3.

Let us discuss a few general considerations and differences with the previous studies:

- ▶ *Virtual point DoFs vs. indicator DoFs.* A secondary goal of the new study was to investigate the minimum required instrumentation, in order to converge to a more “friendly” methodology in terms of measurement effort and financial means. For example, to determine all 24 interface acceleration DoFs of a system with 4-point connectivity, one is formally required to allocate 12 tri-axial accelerometers, occupying 36 channels on the data acquisition system. Note that this is a direct implication of the virtual point methodology: a minimum of three sensors per coupling point is needed to determine all 4×6 virtual point DoFs in \mathbf{u}_2^3 . The in-situ method as discussed in Sec. 6.3.5 does not explicitly require a full set of interface DoFs, but determines the equivalent forces of a source by means of observability in an assembly. This allows for more arbitrary positioning of sensors, that are now regarded as indicator DoFs \mathbf{u}_4 . As these \mathbf{u}_4 are liberated from the rules of virtual point theory (both in number and positioning), one is allowed to remove sensors that are redundant in terms of observability of the source system.

³This set of virtual point DoFs would be denoted \mathbf{q}_2 in Chap. 4.



Figure 9.8: Impression of the vehicle that was used for FRF and operational measurements. The photo on the right shows the four microphone positions in the interior.

- ▶ *Classical vs. component-based matrix inverse TPA.* Operational measurement in the vehicle has been common practice long before the in-situ method made its introduction. The classical TPA matrix-inverse method uses these operational spectra \mathbf{u}_4 in combination with the admittance of the passive subsystem \mathbf{Y}^B , estimating the *interface forces* specific to assembly AB; see Eq. (6.10). The in-situ method uses exactly the same operational measurement, but estimates source-intrinsic *equivalent forces* by solving a matrix system with the assembled admittance \mathbf{Y}^{AB} using Eq. (6.22). The difference between using the admittance of B or AB has profound implications for the kind of characterisation.
- ▶ *Automatic steering.* The EPS system of the X5 platform has the ability to actuate the EPS motor externally. This is particularly beneficial for this study, as no steering robot is required in the interior. Nonetheless, secondary noises occur that do not originate from the EPS system, namely the dry friction sound of the steering shaft when rotating in the steering column. This is an unidentified contribution to the microphone responses, which is discussed later on.

In the remainder of this section, two applications of in-situ TPA are presented, respectively from operational measurements in the vehicle, Sec. 9.3.2, and on a test bench, Sec. 9.3.3.

9.3.2 In-situ TPA in the vehicle

After measuring the FRFs as described in Sec. 8.3, an operational measurement campaign has been conducted in the vehicle. All sensors have been kept mounted on the structure, to eliminate offsets due to sensor placement. Besides the 4 microphone responses \mathbf{u}_3 in the interior as shown in Fig. 9.8, a total of 36 operational responses from 12 tri-axial accelerometers has been recorded around the coupling points of the EPS system. 8 of those sensors are positioned on the side of the steering system close to the connection points. The remaining 4 sensors are put on the head of the connecting bolts under the front axle carrier, somewhat away from the coupling point. The locations of these sensors are also shown in Fig. 8.3 and Fig. 8.4.

In this application, the first 8 sensors are designated as indicator DoFs \mathbf{u}_4 , being an input for the in-situ force determination, while the 4 sensors on the bolts are regarded as structure-borne receiver responses, i.e. part of \mathbf{u}_3 .

► *On-board validation*

The 12 responses \mathbf{u}_3 of the 4 accelerometers on the bolts allow for *on-board validation* of the TPA results: an assessment based on independent structure-borne responses near the location of the equivalent forces. The responses are independent, as they are not an input to the in-situ determination (unlike the other \mathbf{u}_4). They are positioned downstream of the interface, yet not too far away, to reduce the chances of being influenced by secondary sources of vibration. As such they qualify as perfect indicators of the completeness of the in-situ problem: any offset between the measured and TPA-predicted responses is most likely due to a deficiency in either the controllability (equivalent force definition) or observability (indicator DoFs) of the current problem definition. ◀

The following sections present several noise predictions that differ in the definition of the equivalent forces, namely: the full set of equivalent (blocked) forces determined from both a complete and a truncated inversion; a selection of translational forces only and a set of pseudo-forces. Remind that all variants are determined from the same in-vehicle operational measurement of \mathbf{u}_4^{AB} .

Full set of equivalent forces

Let us first consider the determination of 24 equivalent forces \mathbf{f}_2^{eq} . This corresponds to the full set of interface DoFs of the four coupling points, which means that these may be denoted as blocked forces. The “right-sided” transformed admittance matrix $\mathbf{Y}_{\text{um}}^{\text{AB}}$ is used, obtained from the analysis of Sec. 8.3:

$$\mathbf{Y}_{\text{um}}^{\text{AB}} = \mathbf{Y}_{\text{uf}}^{\text{AB}} \mathbf{T}_{\text{f}}^T$$

In the following context of TPA, this admittance is referred to as $\mathbf{Y}_{42}^{\text{AB}}$. The response DoFs \mathbf{u}_4 are the 24 accelerations from the 8 sensors surrounding the coupling points, untouched by any transformation. The excitation DoFs of \mathbf{f}_2 (or actually \mathbf{m}_2 in virtual point notation) are the 24 virtual point forces and moments, as a result of transformation of 52 impact hammer excitations around the interfaces. The admittance matrix is thus 24×24 , which means that the following complete inverse can be calculated:

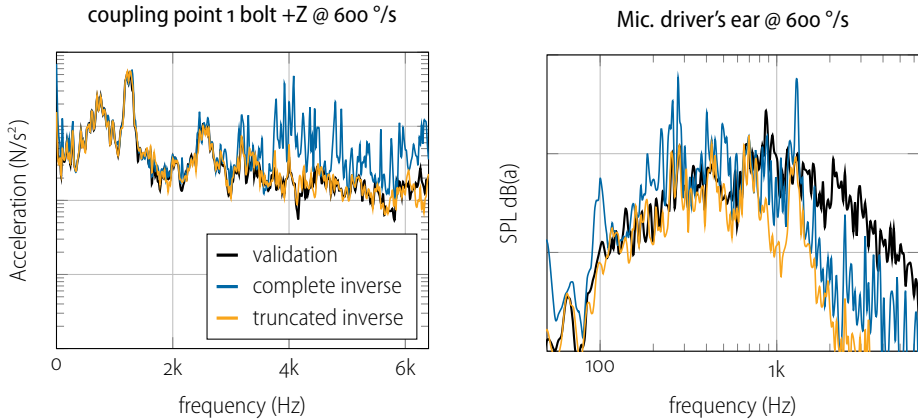
$$\mathbf{f}_2^{\text{eq}} = (\mathbf{Y}_{42}^{\text{AB}})^{-1} \mathbf{u}_4^{\text{AB}} \quad (9.8a)$$

Mathematically, this inverse determines 24 equivalent forces that *exactly* rebuild the responses \mathbf{u}_4 by a linear combination of the FRF columns of $\mathbf{Y}_{42}^{\text{AB}}$. This means that any noise in \mathbf{u}_4 ends up in the calculated forces as well, which is a reason to treat the results with caution.

As a second variant, the matrix has been regulated by means of a singular value truncation. The largest $n_s = 12$ singular values of $\mathbf{Y}_{42}^{\text{AB}}$ are retained in the inversion:

$$\mathbf{f}_2^{\text{eq}} = (\mathbf{Y}_{42}^{\text{AB}})^+ \mathbf{u}_4^{\text{AB}} \quad \text{with} \quad n_s = 12 \quad (9.8b)$$

These 12 singular values represent more than 95% of the energy in the FRF matrix over the full bandwidth. The two methods are used to calculate a set of 24 equivalent forces and moments. These forces are multiplied with the assembled vehicle FRFs to predict the receiver response, using the component-based TPA Eq. (9.3).



(a) Structure-borne response on a bolt underneath coupling point 1.

(b) Airborne response at the position of the driver's ear.

Figure 9.9: Noise prediction using 24 equivalent (blocked) forces as computed from the complete and truncated inverse, compared with the directly measured responses.

Fig. 9.9 shows the resulting receiver responses of the two variants, compared with the directly measured signals. In the figure on the left, a prediction is shown for a structure-borne response close to the coupling points where the equivalent forces are determined. The result of the truncated inverse best matches the validation curve. The curve generated by the complete inverse displays spurious peaks and generally overestimates the response. This can be explained by bad conditioning of the inverse problem: the condition number of the full matrix fluctuates between 10^3 and 10^5 , while the conditioning of the first 12 singular values is only around 10.

Fig. 9.9b shows the in-situ TPA prediction for the acoustic pressure inside the vehicle at the location of the driver's ear. Again, the truncated curve shows the best match, but deviates from the validation curve above 700 Hz. By listening to an auralisation of the spectra (by simple inverse FFT of the frequency spectra to time signals), it was verified that the missing sound originates from a secondary source not considered in the calculation of Eq. (9.8a–9.8b). The steering shaft, when rotating in the steering column, generates dry friction which emits a white noise. This source was not identified, as there are no sensors near the steering column that could “indicate” the vibration of this source. As a result, the predicted sound only exhibits spectral content that originates from the EPS system itself, i.e. passed through the indicators \mathbf{u}_4 . This is in fact a useful advantage of the method: it allows to concentrate on the EPS-specific noise contribution.

► Relation to operational TPA

Effectively, the in-situ operation as shown here functions as a filter, removing contributions from unidentified vibration sources. This filtering process has a clear parallel with operational TPA. Indeed, when combining the equivalent force determination of Eq. (9.3) with the TPA prediction of Eq. (9.8a) or Eq. (9.8b), a transmissibility matrix

is obtained:

$$\mathbf{u}_3 = \mathbf{T}_{34}^{\text{AB}} \mathbf{u}_4 \quad \text{with} \quad \mathbf{T}_{34}^{\text{AB}} = \mathbf{Y}_{32}^{\text{AB}} (\mathbf{Y}_{42}^{\text{AB}})^+$$

This transmissibility is calculated from columns of the FRF matrix \mathbf{Y}^{AB} , similar to what was discussed in Sec. 6.4.1. In this particular case, the transmissibility is generated from 24 virtual-point transformed interface excitations. Alternatively, one may leave out the virtual transformation here, as $\mathbf{Y}_{32}^{\text{AB}}$ and $\mathbf{Y}_{42}^{\text{AB}}$ are obtained from the same FRF measurement and thus use the same IDM matrix for the force transformation. ◀

Alternative set of equivalent forces

The 24 equivalent forces used above resemble the theoretical blocked forces that would have been measured if the interfaces were truly fixed on a rigid test bench. As such, they provide a suitable characterisation of the operational source excitation \mathbf{f}_i , but it is not the only possible one. Effectively, the in-situ method does not strictly determine the theoretical blocked forces, but rather calculates a set of equivalent forces that best resemble the operational responses at the indicator DoFs, as a linear combination of the available columns of the admittance matrix. For instance, if the matrix does not provide columns or “terminals” for rotational moments, the in-situ determination will seek for a combination of translational forces that result in the best possible (in a least-square sense) reproduction at \mathbf{u}_4 . In the general case, denoting the vector of available force DoFs by \mathbf{f}_a , this can be expressed as follows (recall that the location of \mathbf{f}_a must be at the active side A or interface):

$$\mathbf{f}_a^{\text{eq}} = \underset{\mathbf{f}_a}{\text{argmin}} \left\| \mathbf{u}_4 - \mathbf{Y}_{4a}^{\text{AB}} \mathbf{f}_a \right\| \quad \mathbf{f}_a \in \mathbf{f}^{\text{A}} \quad (9.9)$$

This generalised perspective on component-based TPA is discussed in Sec. 6.3.7 and applies to all methods involving matrix inversion, including the pseudo-forces method. In light of this, let us now examine the performance of these component-based TPA methods for two alternative sets of equivalent forces:

1. The 12 *translational equivalent forces* in \mathbf{f}_2^{eq} , obtained from 12 of the 24 columns of the right-sided transformed FRF matrix $\mathbf{Y}_{\text{um}}^{\text{AB}}$. This means that the linear system to solve is overdetermined: 12 translational virtual-point forces from 24 indicator responses. Hypothetically, these would be blocked forces in translational direction, in a mounting condition that leaves the coupling points free to rotate.
2. A set of 6 *pseudo-forces* $\mathbf{f}_{\text{ps}}^{\text{eq}}$, carefully selected from the impact excitations on the EPS system. Three forces are located on the left side and three on the right side of the EPS; the directions of excitation comprise both X, Y and Z components. These pseudo-forces can be computed with the same ease using Eq. (9.9); note however that the admittance matrix is now the originally measured one without any transformations, i.e. $\mathbf{Y}_{\text{uf}}^{\text{AB}}$, as the pseudo-force terminals are selected from the original impacts and not the virtual-point transformed forces.

The TPA predictions for the two equivalent force definitions are shown in Fig. 9.10. The 12 translational forces resemble the responses measured in the vehicle with similar accuracy as the SVD-truncated results of Fig. 9.9, both for structure-borne and airborne responses.

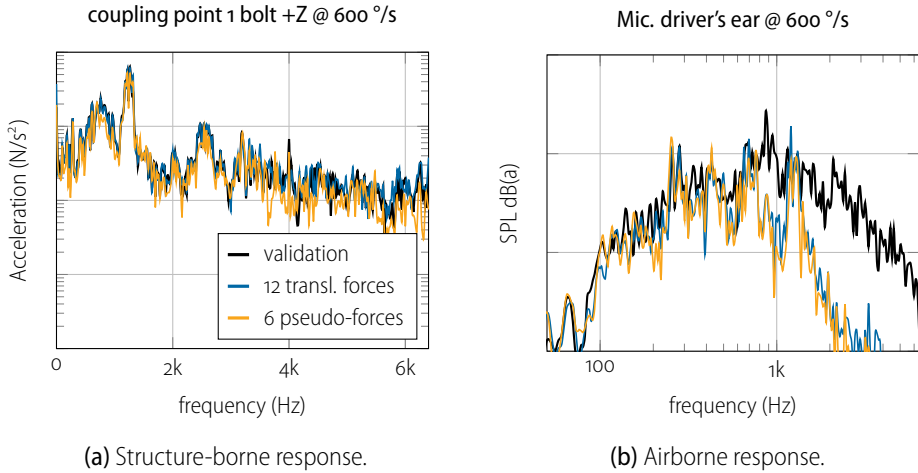


Figure 9.10: Noise prediction from alternative sets of equivalent forces: 12 translational forces at the interfaces and 6 pseudo-forces on the EPS system.

This implies that rotational forces are not explicitly required for the characterisation of the EPS system's activity. In other words: although the translational forces may not strictly represent the blocked-force experiment, they seem to provide a sufficient subspace to *characterise* the source excitation for responses at the passive side of the vehicle.

The prediction using 6 pseudo-forces is slightly less accurate but nonetheless promising: most of the response can be reconstructed using just these 6 forces. This indicates the potential of the pseudo-forces method for quick investigations in the original assembly. However, it is certainly not guaranteed that these forces are independent of the passive side and transferable to other assemblies. This would formally require to have full controllability from \mathbf{f}_{ps}^{eq} over all interfaces \mathbf{u}_2 , which is unlikely for this set of just 6 forces, taken into consideration the conclusions from the system analysis presented in Sec. 8.3.2.

Path contributions from equivalent forces

To illustrate the possibilities of the in-situ method for path ranking, the responses are split up in their contributions over the left and right side, i.e. coupling point 1+2 and 3+4 (see Fig. 8.4 for an overview). These have been referred to as *partial responses* in Sec. 7.6. For application of component-based TPA, the following summation can be used:

$$u_i(\omega) = \sum_j Y_{ij}^{AB}(\omega) f_j^{eq}(\omega) \quad \begin{cases} u_i \in \mathbf{u}_3 \\ f_j^{eq} \in \mathbf{f}_2^{eq} \end{cases} \quad (9.10)$$

Summation over j determines which paths and directions are considered together. For the example here, the two sets of six translational forces have been summed, respectively belonging to coupling point 1+2 and 3+4.

The two partial airborne responses are shown in Fig. 9.11. A 1/12-octave narrow band (semitones) division is used. Around 300 Hz, a dominant contribution of the right side can be observed. It was verified that these peaks correspond to motor and tooth belt orders, originating from mechanisms located on the right side of the EPS. At some frequencies,

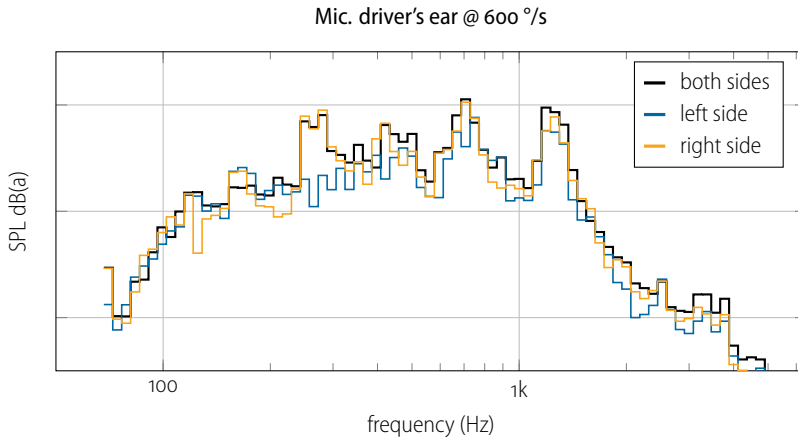


Figure 9.11: Partial responses of the left and right side contributions in 1/12-octave narrow bands.

e.g. around 180 Hz, the two partial contributions show higher individual levels than the combined SPL. Note that this is possible due to phase differences in the complex-valued terms: partial responses with opposing phase cancel each other out.

9.3.3 In-situ TPA on a test bench

After several investigations of in-situ TPA in the vehicle, a test bench was constructed for operational steering measurements with the same EPS system. Based on the studies discussed in Sec. 9.2, it was chosen to tailor the test bench support structures specifically for in-situ measurement. This means that force transducers are no longer part of the instrumentation. Apart from that, the considerations for design are comparable with those for the compliant test bench supports of the previous study; see Fig. 9.2c and 9.3c. A difference however is that the X5 test bench uses 2 combined support structures to accommodate the 4 bolted connection points instead of 4 separate poles. This was chosen because coupling points 1–2 and 3–4 are relatively close to each other.

The assembly of test bench and EPS system is shown in Fig. 9.12. The 4 coupling points are each surrounded by two tri-axial accelerometers instead of three, as illustrated by the photo in the close-up. It was learnt from the preceding in-situ studies that a smaller set of indicator DoFs suffices to determine (for instance) 12 translational equivalent forces. Moreover, the aim is not to explicitly determine 6-DoF accelerations \mathbf{u}_2 by virtual point transformation of the sensor accelerations, but to use the sensors as indicators that *observe* the vibrations of the EPS system, hence in the capacity of indicator DoFs \mathbf{u}_4 . Additional tri-axial accelerometers have been positioned at the EPS motor, planetary gearing, steering spindle and at the two tie-rods. These sensors have been used to investigate the source of some vibration orders and external disturbances in the measured spectra.

In order to simulate the resistance of the turning wheels, two electric linear servo-actuators have been installed on both sides of the EPS rack bar. The two linear actuators provide a combined load that resembles the actual force exerted on the EPS system when operating in the vehicle. However, as an unwanted side effect, the spindles of those actuators produce their own vibrations that get transferred through the rack bar and EPS system to the indicator sensors on the test bench supports. These vibrations mostly manifest below 500

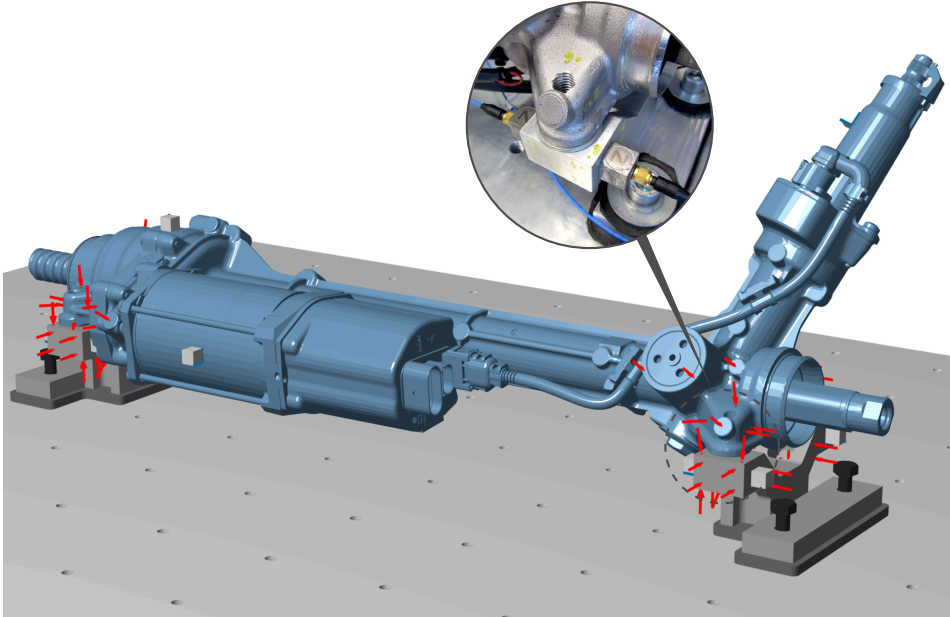


Figure 9.12: Impression of the EPS system mounted on the two support structures, in turn connected to a test table.

Hz, which invalidates the prediction in this frequency range.

In the remainder of this section, the FRF measurement of the test bench – EPS system assembly is presented, followed by an application of in-situ TPA. This allows to compare the results of in-situ characterisation on the test bench with the validation and in-situ application in the vehicle.

FRF measurement on the test bench

Application of the in-situ TPA on the test bench requires the FRF matrix $\mathbf{Y}_{42}^{\text{AR}}$, i.e. the assembly of the test bench and EPS system. Impact measurement has been performed on 80 points around the 4 interfaces, illustrated by the red arrows in Fig. 9.12. To transform the 80 impacts to 24 virtual point interface forces, an IDM matrix \mathbf{T}_f^T has been defined, compatible with the definitions for the virtual points of the vehicle measurement. A right-sided virtual-point transformed admittance matrix was determined for FRFs of the test bench – EPS assembly:

$$\mathbf{Y}_{\text{um}}^{\text{AR}} = \mathbf{Y}_{\text{uf}}^{\text{AR}} \mathbf{T}_f^T$$

Like for the in-vehicle TPA application, we continue to refer to this matrix as $\mathbf{Y}_{42}^{\text{AR}}$. Note that the matrix is square: 24 indicator responses by 24 virtual point DoFs. As a consequence, it is probably required to use either a singular value truncation or calculate equivalent forces using fewer DoFs, similar as for the in-vehicle characterisation.

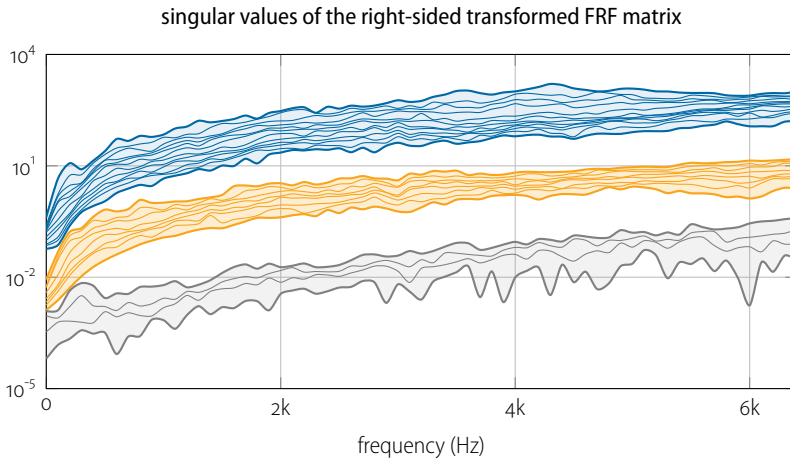


Figure 9.13: Singular value decomposition of the right-sided transformed admittance matrix $\mathbf{Y}_{42}^{\text{AR}}$, used for in-situ force determination on the test bench.

► pseudo-forces vs. virtual point forces

In theory, the measured admittance matrix can be used directly for source characterisation by a subset of the 80 original impacts. These forces then assume the role of pseudo-forces, similar as Eq. (9.9). However, in order to render such characterisation compatible with the vehicle FRFs, a mapping must be found between those forces (columns of $\mathbf{Y}_{42}^{\text{AR}}$) and the impacts on the vehicle (columns of $\mathbf{Y}_{32}^{\text{AB}}$) that share the *exact* same definitions of position and orientation. This could be feasible when both measurements are very carefully planned beforehand, but this was not intended here. Instead, by using the virtual point transformation, one has the freedom to choose impact points as desired and establish a compatible interface using their virtual points, uniquely defined for both assemblies.

Fig. 9.13 shows the singular values of the admittance matrix after right-sided transformation, which clearly fall into three bands. The first 12 singular values correspond to the 12 translational forces. The eight values thereafter are associated with responses to the moments about the X and Z-axes. The last 4 are moments about the Y-axes, which are not observable due to the current instrumentation of two sensors instead of three.

In-situ characterisation and TPA prediction

Steering cycles have been conducted on the test bench, resembling those of the vehicle measurements. A complete set of 24 equivalent forces is calculated from a truncated matrix inversion using the first 12 singular values of the matrix:

$$\mathbf{f}_2^{\text{eq}} = (\mathbf{Y}_{42}^{\text{AR}})^+ \mathbf{u}_4 \quad \text{with} \quad n_s = 12 \quad (9.11)$$

These forces are multiplied with the FRFs of the assembled vehicle $\mathbf{Y}_{32}^{\text{AB}}$ to obtain a prediction at \mathbf{u}_3 according to Eq. (9.3). Several structure-borne and airborne responses are considered and compared with results from the in-vehicle application.



Figure 9.14: TPA prediction of structure-borne responses at a sensor underneath coupling point 1 (top) and at the left seat rail inside the vehicle (bottom).

Fig. 9.14 shows structure-borne responses predicted from the test bench in-situ forces (—), compared with the validation measurement (—) and the application of in-situ characterisation in the vehicle (—), as already presented in Sec. 9.3.2. The top figures concern the sensor directly under coupling point 1, which is the same point as considered in the vehicle in-situ application shown in Fig. 9.9. This point is probably not of particular interest of a TPA, but provides a good insight in the performance of the methodology. The overall envelope of the responses is comparable between 500 and 4000 Hz, although some large deviations are observed. Below 500 Hz, it was concluded that the linear actuators of the test bench have a disturbing influence. Above 4000 Hz, there is no obvious explanation other than a myriad of experimental uncertainties in the measurement data.

The figures on the bottom of Fig. 9.14 show a prediction of structure-borne responses at a sensor in the interior, namely an accelerometer positioned at the outer rail of the left seat. Interestingly, the measured validation spectra reveal nothing but noise above 1000 Hz. This means that the signals measured during operation in the vehicle did not exceed the effective noise floor of approximately 1 mm/s^2 . However, both in-situ methods produce spectra that show a remarkably good agreement. This indicates that, although the operational excitation renders too little signal on \mathbf{u}_3 , the FRF measurement \mathbf{Y}_{32}^{AB} does pertain sufficient SNR on this position, which can be leveraged by application of component-based TPA.

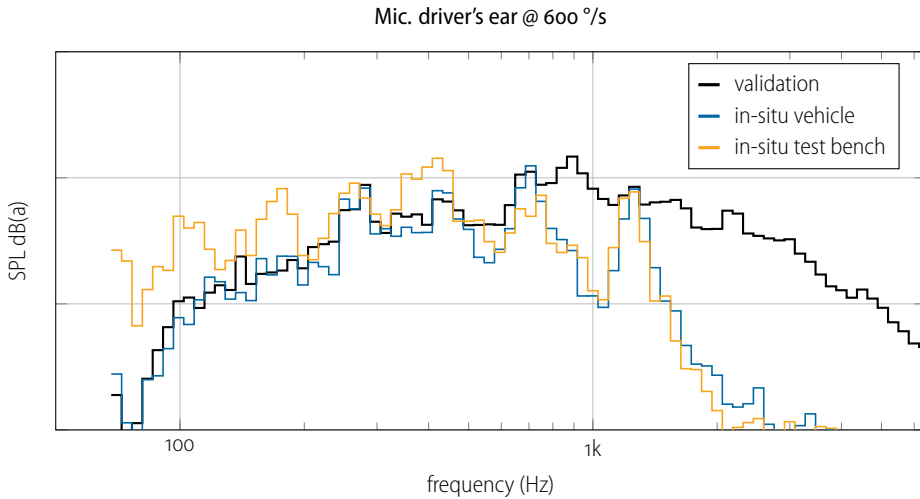


Figure 9.15: TPA prediction of airborne responses at the driver's ear inside the vehicle.

Fig. 9.15 demonstrates the performance for the airborne response at the driver's ear in 1/12-octave bands. Again, the prediction from test bench characterisation (—) is benchmarked against the vehicle validation (—) and in-situ characterisation (—). Below 500 Hz, the response is clearly dominated by the noise of the test bench equipment, that spills over into the indicator sensors on the test bench supports. This was verified by listening to the sound of the spectra. Above 500 Hz, the two in-situ methods match fairly well. The higher levels in the validation measurement were already attributed to the unidentified noise source in the steering column.

9.4 Summary

This chapter has presented a collection of applications in the field of component-based TPA. The goal of the applications is to characterise the activity of the EPS system by equivalent forces that are an system-intrinsic property, independent of the test bench or vehicle. The methods of blocked force, hybrid interface, in-situ and pseudo-forces characterisation have been explored for this purpose, alongside several iterations of test bench designs. The in-situ method has been identified as the most suitable method, given the system at hand and bandwidth of interest. A final application of in-situ, both in the original vehicle and on a test bench, has substantiated the idea that the source characterisation is independent and can be employed for noise prediction in assemblies with different vehicles. Although not considered here, the FRFs of such assemblies can be obtained by application of dynamic substructuring.

Throughout the studies, it was learnt that the EPS system is a most challenging component to control for operational trials and even harder to measure for validation in the vehicle. The speed of the EPS motor, which determines most of the orders in the excitation spectrum, is difficult to maintain perfectly constant. In addition, the excitation levels of the EPS are small and produce an almost negligible noise in the vehicle compared with other active systems.

Consequently, for what concerns the differences in prediction and validation, it is difficult to pinpoint the exact cause. Nonetheless, it is believed that the presented approach yields insightful results, is broadly applicable and provides a good basis for target setting in structural-acoustic problems.

part IV

Conclusions and Recommendations



10

Conclusions and recommendations

10.1 Conclusions

To answer to the technological advances and ever-increasing demands on NVH in the automotive industry, effective means are required to engineer and predict the experience of sound and vibrations. In this thesis, methods have been explored in the fields of dynamic substructuring and transfer path analysis, that together provide practical tools to analyse and simulate sound and vibrations of current-day vehicles. Emphasis is on the experimental side of dynamics, as it was identified that numerical modelling opportunities are rather limited given the complexity and high-frequency aspects of vehicle mechatronics.

In particular, the aim was to develop methods that allow to contemplate an experimentally characterised component as “just another FE model”, in the sense that it can be implemented in simulation environments with ease. The ramifications of this goal are twofold:

1. It concerns the method of virtual point transformation to express the passive dynamics of an experimentally measured structure by collocated nodal FRFs, compatible with FE models;
2. It applies to component-based TPA methods that characterise an active system as an independent source of vibrations by means of equivalent forces, which can be applied to arbitrary assemblies for prediction of sound and vibrations.

The following conclusions are presented separately for the topics covered in Part I and Part II, taking into account the relevant vehicle applications of Part III.

10.1.1 *Conclusions on dynamic simulation and substructuring*

One of the goals of this research is to be able to obtain the passive transmission characteristics of a vehicle for frequencies up to 6 kHz. As an introduction, Chap. 2 highlights five domains that can be considered when modelling the passive dynamics of a structure. Starting from the physical domain, governed by mass, damping and stiffness matrices, four domains are derived for representation in modal space, FRF, IRF and state-space parameters. It is indicated how one can convert between domains and how similar representations can be obtained from experimental testing. In light of substructuring — but also for general simulation purposes — the domains are presented as different means to describe the input-output behaviour between nodes, either in impedance or admittance form. This results in potentially very compact models, typically in matrix form, whose rows and columns represent the DoFs of the terminals that are considered as force input and response output, respectively.

Chap. 3 recapitulates the fundamental concepts of substructuring. It was concluded that coordinate compatibility and force equilibrium are in fact highly generic notions, that show similarity with Kirchhoff's laws for electricity. Using the Boolean compatibility and localisation matrices, these conditions can be imposed on various domains in a systematic way. This gives rise to the primal and dual assembly methods, which reveals some interesting symmetries between primal/impedance and dual/admittance notation. The concepts of primal and dual decoupling have been presented thereafter, with a short discussion on alternative interface definitions. As an application of frequency-based substructuring, the LM-FBS algorithm has been reformulated using a convenient notation that streamlines implementation of both coupling and decoupling procedures. This algorithm can be regarded as the general (dis)assembler of substructure FRFs, for instance obtained by experimental component modelling.

An application of dynamic substructuring has been presented in Sec. 8.5 for determination of the FRFs of the vehicle – steering system assembly, using experimentally obtained models of the vehicle and steering system and a numerical model of a temporary beam that was introduced for the purpose of substitute coupling. This method proposes to measure a larger substructure with a temporary fixture in place, followed by a decoupling step to remove the substitute fixture and a coupling step to add the substructure of interest. It was shown that substitute coupling outperforms the process of direct coupling, which may be due to the following reasons: paths comprising hinged connections are measured in the right configuration, friction and other interface effects are incorporated in the measurements; the modal conditioning is closer to the targeted assembly and the substitute beam can be optimised for convenience of measurement.

10.1.2 *Conclusions on experimental modelling*

Chap. 4 introduces the discipline of experimental modelling, which complements the task of admittance testing by all the steps from measurement preparation and instrumentation to post-processing and quality assessment. For this purpose, an integral methodology has been proposed that is centred around the virtual point transformation. It was shown that multiple sensors / excitation points can be assumed to displace / excite rigidly with respect to one another, if they are situated in a locally stiff region around a (coupling) point. Based on the location and direction of the associated response and force vectors, six interface displacement modes (IDMs) can be constructed that portray the rigid behaviour by three translations and three rotations with respect to a user-chosen virtual point. This point needs no explicit excitation or measurement, yet pertains correct driving-point properties and can thus be connected to other component (FE) models in a physically correct way.

In the preferred case that more than six responses / forces are considered as an input for the transformation, least-square averaging occurs, which additionally allows to determine quality indicators for the force and response transformations. Dimensionless notions for sensor and impact consistency have been proposed that evaluate either a group of DoFs or a specific DoF, allowing to trace back the sources of experimental errors responsible for the non-consistent dynamics. After two-sided transformation of the measured admittance matrix, a collocated virtual point matrix is obtained comprising 6-DoF nodal FRFs. These FRFs are subject to the principles of reciprocity and passivity, which can be employed as a final evaluation of quality, before storing the models for later use in a development or simulation process. Alternatively, if one prefers to use the virtual point transformation merely

to establish physically correct interface definitions in substructuring, it has been shown that the Boolean compatibility and equilibrium matrices can be augmented with the respective virtual point transformation matrices. This enables dual assembly with matching virtual point interfaces, yet retains the original DoF-space of the measurement.

A simulated experimental application to a beam structure has demonstrated the workflow of the transformation and potential of the quality indicators. It was concluded that offsets in the impact vector can drastically reduce the quality; hence overdetermination of the measurement, i.e. more than six inputs per coupling point, is at all times advised.

In Chap. 8, the same workflow has been applied to challenging real-life structures. It has been shown how the passive dynamics of a complex structure mounted in a vehicle frame can be obtained in terms of virtual point FRFs. Starting with a large matrix of impact measurements, it has been demonstrated how singular value decomposition and sensor / impact consistency can be utilised to get a better understanding of the system's dynamics and identify impacts that are defined or executed incorrectly. The virtual point transformation yielded FRFs with varying success: some directions were determined almost perfectly while others show worse reciprocity, for reasons that could be traced back to the experiment.

A particular interest in this project was the balance between uncertainty due to measurement errors and uncertainty as a result of production spread. To investigate this for an industrial case, the virtual point approach has been benchmarked on three identical cars. It has been shown that, better than conventional single-excitation measurement, the virtual point transformation produces highly coherent estimations of both structural and structural-acoustic FRFs in a bandwidth of 6 kHz. It was concluded that measurement uncertainty as well as production spread is low, even in the multi-kHz range. As an additional advantage over the conventional approach, uncertainties in the consecutive steps can be quantified using the quality indicators associated with the overdetermined virtual point transformation.

10.1.3 *Conclusions on transfer path analysis and source characterisation*

Part II concerns the characterisation of active vibrations and the corresponding propagation into a passive structure. This is the domain of transfer path analysis (TPA), for which a general framework has been proposed. Chap. 5 discusses the evolution of TPA, from early theoretical developments to the landscape of practical TPA methods that are nowadays being used in industry. A general framework for the derivation of these TPA methods has been presented in Chap. 6. The assembled transfer problem has been decomposed by considering the interaction between the active and passive subsystem as a substructuring problem. A classification has been proposed into the families of classical, component-based and transmissibility-based TPA. It has been shown that the classification defines the principle of source characterisation, but does not necessarily prescribe the environment for operational testing. Apart from similarities within a family, it was demonstrated that the three methodological families are highly interrelated.

Special attention has been devoted to the methods of component-based TPA. It has been demonstrated that the blocked-force problem can be considered as an equivalent force problem, analogue to the theorems of Thévenin and Norton for electric circuits. This offers potential for design purposes, as the source activity can be characterised by component-

specific forces and applied to an assembly with an arbitrary passive side. The component-based TPA family has further been generalised by combining elements of the in-situ and pseudo-forces method with Lagrange multiplier substructuring notation. Departing from the strict definition of blocked forces, equivalent forces are introduced as a general set of forces on the active side that represent the source activity by having controllability over the interface DoFs. The characterisation of such equivalent forces is in turn formulated as an observability problem from responses at the passive side.

Common practicalities and considerations of TPA have been discussed in Chap. 7, such as the problem of multiple sources, dependency on mounting conditions, inclusion of airborne transmission paths and determination of (rotational) interface DoFs. Also, a discussion on observability and controllability of the transfer path problem has been presented. It was concluded that the interface can be considered as a bottleneck, limiting the throughput of source excitation modes over the interface to the receiver side. This concept has been discussed for use in operational TPA, but is relevant for other TPA methods as well.

Chap. 9 presents a selection of TPA studies concerning the characterisation of steering vibrations and prediction of the experienced noise in the vehicle. For characterisation of steering vibrations on a test bench, the methods of blocked force, hybrid interface, in-situ and pseudo-forces characterisation have been explored. It was concluded that the in-situ method is the most suitable approach, considering the high-frequency excitation bandwidth of the steering system. It has been shown that singular value truncation of the matrix inversion problem improves the determination of equivalent forces, yet similar improvements could be obtained by determination of a smaller set of equivalent or pseudo-forces. This has substantiated the idea that equivalent forces are not necessarily a depiction of the theoretical blocked-forces, but rather the best combination of forces that, given the available “control vectors” (columns in the FRF matrix), best represent the vibrations as observed downstream of the interfaces. This again demonstrates that controllability and observability are key concepts in TPA.

A final application has demonstrated how the source vibrations of the steering system can be characterised from both in-vehicle operational measurements and operational trials on a test bench. By proper transposition of the component-based TPA theory to practice, it has been shown how structure-borne and airborne contributions in the vehicle can be predicted from measurements on a test bench. Together with the potential of experimental substructuring for assembly of vehicle FRFs, the presented methodology offers great opportunities for early-phase engineering of sound and vibration problems.

10.2 Recommendations

Over the course of this four-year project, we have had the wonderful opportunity to try and apply theoretical concepts to complex real-life systems. It is believed that proof on such real-life problems is instrumental to shift the classical preconception of “numerical models are for smart development and experiments for ignorant validation” towards a more neutral connotation, making use of the possibilities that experimental dynamic substructuring has to offer for hybrid modelling. Nonetheless, some fields covered in this thesis could benefit from more scientific proof and additional theoretical elaborations.

In retrospect of this project, the following topics are identified as potentially interesting directions for future research:

- ▶ *Application of substructuring to a larger/heavier component.* A typical steering system weighs around 15 kg, which makes up roughly one percent of the total mass of the vehicle. This means that the contribution to the dynamics of the complete vehicle is very modest, especially when considering the influence on transfer functions into the interior of the vehicle. In order to clearly demonstrate the potential of substructuring, the difference between an assembled and trimmed-body vehicle, i.e. AB and B, must be larger. Interesting substructures could for example be the main engine or parts of the vehicle chassis.
- ▶ *Application of TPA to an active component with higher excitation levels.* It was concluded in Chap. 9 that the acoustic levels produced by the steering gear in the vehicle are very low, typically not exceeding 35 dB(a). This is, admittedly, desirable from an NVH engineering point of view, but makes validation in the vehicle cumbersome. In addition, keeping the EPS motor at perfect constant speed turned out to be very challenging. This is required in order to recognise the engine orders as distinct peaks in the frequency spectra. Therefore it is suggested to apply the TPA methodology to another active component that has a higher noise and/or vibration contribution in the vehicle and can be controlled at perfect steady-state operation.
- ▶ *Investigation into the transferability of equivalent forces.* In Chap. 9, equivalent forces for the EPS system's activity have been determined in test assembly AR and transferred to the targeted vehicle assembly AB. This requires that the equivalent forces are a sole property of the active system A; a very important assumption which is supported by some of results presented in Fig. 9.14. However, comparison of the predicted vibration levels has mostly been hindered by practical limitations, such as the inability to provide the exact same operational excitation (in order words, $f_1^{AB} \neq f_1^{AR}$) and external disturbances in both test bench and vehicle measurements. Application of the theory to a more academical structure could provide more conclusive proof of this assumption.
- ▶ *Investigation of observability and controllability.* Observability and controllability are recurring concepts in this thesis, that may yield insights in the throughput behaviour of the interface. However, to clearly expose the bottleneck effect of an interface, it should first be investigated for a simpler structure. It is probably worthwhile to experiment with a single coupling point, for which it can be assumed that no more than six independent modes of vibration throughput be present.
- ▶ *Round-trip FRF quality assessment.* The round-trip method for FRF determination [136] has briefly been discussed in Sec. 7.4. It provides an alternative for obtaining a subset of an FRF matrix, namely the interface FRFs Y_{22} in case that both sides A and B of the interface can be measured. Perhaps this round-trip identity can be utilised to assess the quality or *truthfulness* of an experimentally obtained FRF matrix, by comparing the directly measured FRFs Y_{22} with the independent result of the round-trip procedure: $Y_{21} (Y_{31})^+ Y_{32}$.
- ▶ *Specification of the virtual point weighting matrix.* The virtual point transformation presented in Chap. 4 allows to specify a weighting matrix, which gives control over the relative importance of the measured DoFs in the least-square determination. This thesis does not further elaborate on the potential gain of specifying individual weightings to DoFs; more research is needed to understand the capabilities and define guidelines for effective use.

List of personal publications

Journal publications

M. V. van der Seijs, D. de Klerk, and D. J. Rixen. ‘General Framework for Transfer Path Analysis: History, Theory and Classification of Techniques’. In: *Mechanical Systems & Signal Processing* 68–69 (2016), pp. 217–244.



D. J. Rixen, A. Boogaard, M. V. van der Seijs, G. van Schothorst, and T. van der Poel. ‘Vibration source description in substructuring: A theoretical depiction’. In: *Mechanical Systems & Signal Processing* 60–61 (2015), pp. 498–511.



Conference publications

M. V. van der Seijs, E. A. Pasma, D. de Klerk, and D. J. Rixen. ‘A Comparison of Two Component TPA Approaches for Steering Gear Noise Prediction’. In: *Dynamics of Coupled Structures*. Vol. 4. Proceedings of the 33rd IMAC, A Conference and Exposition on Structural Dynamics. Springer New York, 2015. Chap. 7, pp. 71–79.



M. V. van der Seijs, E. A. Pasma, D. de Klerk, and D. J. Rixen. ‘A robust Transfer Path Analysis method for steering gear vibrations on a test bench’. In: *Proceedings of the International Conference on Noise and Vibration Engineering (ISMA), Leuven, Belgium*. 2014.



M. V. van der Seijs, P. L. C. van der Valk, T. van der Horst, and D. J. Rixen. ‘Towards Dynamic Substructuring Using Measured Impulse Response Functions’. In: *Dynamics of Coupled Structures*. Vol. 1. Proceedings of the 32nd IMAC, A Conference and Exhibition on Structural Dynamics. Springer New York, 2014. Chap. 6, pp. 73–82.



D. D. van den Bosch, M. V. van der Seijs, and D. de Klerk. ‘Validation of Blocked-Force Transfer Path Analysis with Compensation for Test Bench Dynamics’. In: *Dynamics of Coupled Structures*. Vol. 6. Proceedings of the 32nd IMAC, A Conference and Exposition on Structural Dynamics. Springer New York, 2014. Chap. 4, pp. 37–49.



E. Barten, M. V. van der Seijs, and D. de Klerk. ‘A Complex Power Approach to Characterise Joints in Experimental Dynamic Substructuring’. In: *Dynamics of Coupled Structures*. Vol. 6. Proceedings of the 32nd IMAC, A Conference and Exposition on Structural Dynamics. Springer New York, 2014. Chap. 27, pp. 281–296.



M. V. van der Seijs, D. D. van den Bosch, D. J. Rixen, and D. de Klerk. ‘An improved methodology for the virtual point transformation of measured frequency response functions in dynamic substructuring’. In: *4th ECCOMAS Thematic Conference on Computational Methods in Structural Dynamics and Earthquake Engineering (COMPdyn)*. Ed. by M. Papadrakakis, V. Papadopoulos, and V. Plevris. Kos Island, Greece, 2013, pp. 4334–4347.



M. V. van der Seijs, D. de Klerk, D. J. Rixen, and S. Rahimi. 'Validation of current state Frequency Based Substructuring Technology for the characterisation of Steering Gear – Vehicle Interaction'. In: *Topics in Experimental Dynamic Substructuring*. Vol. 2. Proceedings of the 31st IMAC, A Conference on Structural Dynamics. Springer New York, 2013. Chap. 20, pp. 253–266.



M. V. van der Seijs and D. J. Rixen. 'Efficient Impulse Based Substructuring using Truncated Impulse Response Functions and Mode Superposition'. In: *Proceedings of the International Conference on Noise and Vibration Engineering (ISMA), Leuven, Belgium*. 2012, pp. 3487–3499.



Curriculum vitae








Maarten van der Seijs was born in Heiloo, the Netherlands, on the 10th of June 1986.








After completing his secondary education at *Stedelijk Gymnasium Haarlem*, he started studying Mechanical Engineering at Delft University of Technology in September 2004. He obtained the BSc. degree in 2008 and enrolled in the MSc. track Engineering Dynamics at the department of Precision and Microsystems Engineering (PME). As part of his Master's studies, he participated in a joint study to hybrid autonomous underwater vehicles in collaboration with the *NATO Undersea Research Centre* (NURC) in La Spezia, Italy. After finishing his Master's thesis, titled "Improvements on Time-Frequency Analysis using Time-Warping and Timbre Techniques", he graduated cum laude in June 2011.









In September 2011 he started a PhD project within the Engineering Dynamics group of PME at TU Delft under the supervision of prof. dr. Daniel Rixen and dr. Dennis de Klerk. The project, initially focusing on real-time and impulse-based substructuring, took a turn in the fall 2012 when collaboration was found with the BMW Group in Munich, Germany. During the 3½ years to follow, Maarten has conducted research both at TU Delft and at the *Forschungs- und Innovationszentrum* (FIZ) in Munich, presented at international conferences and supervised several students. The results of this joint research project are compiled in this thesis.











As of 2016, Maarten has co-founded *VIBES.technology*, a Dutch company based at the *YES!Delft* start-up incubator, that specialises in sound & vibration engineering by application of experimental dynamic substructuring and transfer path analysis techniques.











References





- [1] T. J. S. Abrahamsson and D. C. Kammer. ‘Finite element model calibration using frequency responses with damping equalization’. In: *Mechanical Systems & Signal Processing* 62 (2015), pp. 218–234. 
- [2] T. Abrahamsson. *Linear System Theory in Vibration Engineering*. Lecture notes at Chalmers University of Technology. Publication U72. May 1998.
- [3] S. Adhikari. ‘Damping Models for Structural Vibration’. PhD thesis. University of Cambridge, 2000.
- [4] R. J. Allemang and D. L. Brown. ‘A complete review of the complex mode indicator function (CMIF) with applications’. In: *Proceedings of the International Conference on Noise and Vibration Engineering (ISMA), Leuven, Belgium*. 2006, pp. 36–44.
- [5] R. Allemang. ‘The Modal Assurance Criterion: Twenty Years of Use and Abuse’. In: *Sound and Vibration Magazine* (Aug. 2003), pp. 14–21. ISSN: 1541-0161.
- [6] M. S. Allen, D. C. Kammer, and R. L. Mayes. ‘Uncertainty in experimental/analytical substructuring predictions: a review with illustrative examples’. In: *Proceedings of the International Conference on Noise and Vibration Engineering (ISMA), Leuven, Belgium*. 2010, pp. 1833–1850.
- [7] M. Allen, R. Mayes, and E. Bergman. ‘Experimental modal substructuring to couple and uncouple substructures with flexible fixtures and multi-point connections’. In: *Journal of Sound & Vibration* 329.23 (2010), pp. 4891–4906. ISSN: 0022-460X. 
- [8] P. Alpar, R. Alt, F. Bensberg, H. L. Grob, P. Weimann, and R. Winter. *Anwendungsorientierte Wirtschaftsinformatik – Strategische Planung, Entwicklung und Nutzung von Informationssystemen*. Springer Fachmedien Wiesbaden, 2014. ISBN: 978-3-658-00520-7. 
- [9] H. van der Auweraer, P. Mas, S. Dom, A. Vecchio, K. Janssens, and P. van de Ponsele. *Transfer path analysis in the critical path of vehicle refinement: the role of fast, hybrid and operational path analysis*. Tech. rep. 2007-01-2352. SAE Technical Paper, 2007. 
- [10] P. Avitabile. ‘Experimental modal analysis (a simple non-mathematical presentation)’. In: *Sound and vibration* 35.1 (2001), pp. 20–31.
- [11] E. Balmès, J. Bianchi, and J. Leclère. *Structural Dynamics Toolbox*. User’s Guide. SDTools, Dec. 2014.
- [12] E. Barten, M. V. van der Seijs, and D. de Klerk. ‘A Complex Power Approach to Characterise Joints in Experimental Dynamic Substructuring’. In: *Dynamics of Coupled Structures*. Vol. 6. Proceedings of the 32nd IMAC, A Conference and Exposition on Structural Dynamics. Springer New York, 2014. Chap. 27, pp. 281–296. 
- [13] M. Bello, A. Sestieri, W. D’Ambrogio, and F. La Gala. ‘Development of a rotation transducer based on bimorph PZTs’. In: *Mechanical Systems & Signal Processing* 17.5 (2003), pp. 1069–1081. 
- [14] J. S. Bendat. ‘Solutions for the multiple input/output problem’. In: *Journal of Sound & Vibration* 44.3 (1976), pp. 311–325. ISSN: 0022-460X. 










- [15] J. S. Bendat. 'System Identification from Multiple Input / Output Data'. In: *Journal of Sound & Vibration* 49.3 (1976), pp. 293–308. 
- [16] J. S. Bendat and A. G. Piersol. *Random Data: Analysis and Measurement Procedures*. New York: John Wiley and Sons, Inc., 1971.
- [17] J. S. Bendat and A. G. Piersol. *Engineering Applications of Correlation and Spectral Analysis*. New York, London, Sydney: John Wiley & Sons, Inc., 1980.
- [18] D. Berckmans, P. Kindt, P. Sas, and W. Desmet. 'Evaluation of substitution monopole models for tire noise sound synthesis'. In: *Mechanical Systems & Signal Processing* 24.1 (2010), pp. 240–255. 
- [19] D. Berckmans, B. Pluymers, P. Sas, and W. Desmet. 'Numerical comparison of different equivalent source models and source quantification techniques for use in sound synthesis systems'. In: *Acta Acustica united with Acustica* 97.1 (2011), pp. 138–147. 
- [20] B. Besselink, U. Tabak, A. Lutowska, N. van de Wouw, H. Nijmeijer, D. J. Rixen, M. E. Hochstenbach, and W. H. A. Schilders. 'A comparison of model reduction techniques from structural dynamics, numerical mathematics and systems and control'. In: *Journal of Sound & Vibration* 332.19 (2013), pp. 4403–4422. 
- [21] R. L. Bisplinghoff, H. Ashley, and R. L. Halfman. *Aeroelasticity*. Cambridge, MA: Addison-Wesley Publishing Company, 1955.
- [22] A. Blakeborough, M. S. Williams, A. Darby, and D. M. Williams. 'The development of real-time substructure testing'. In: *Philosophical Transactions of the Royal Society A - Mathematical, Physical and Engineering Sciences* 359 (Sept. 2001), p. 1869.
- [23] Y. I. Bobrovnikskii and G. Pavic. 'Modelling and characterization of airborne noise sources'. In: *Journal of Sound & Vibration* 261.3 (2003), pp. 527–555. 
- [24] S. de Boer and J. Cruijff. *Johan Cruijff uitspraken – een biografie in citaten*. Schuyt Nederland, 2011, p. 256. ISBN: 978-9081797412.
- [25] H. A. Bonhoff. 'The influence and significance of cross-order terms in interface mobilities for structure-borne sound source characterization'. PhD thesis. Technische Universität Berlin, 2010, p. 270. ISBN: 978-3-7983-2226-4.
- [26] D. D. van den Bosch, M. V. van der Seijs, and D. de Klerk. 'Validation of Blocked-Force Transfer Path Analysis with Compensation for Test Bench Dynamics'. In: *Dynamics of Coupled Structures*. Vol. 6. Proceedings of the 32nd IMAC, A Conference and Exposition on Structural Dynamics. Springer New York, 2014. Chap. 4, pp. 37–49. 
- [27] H.-E. de Bree. 'An overview of microflown technologies'. In: *Acta acustica united with Acustica* 89.1 (2003), pp. 163–172.
- [28] H.-E. de Bree, P. Leussink, T. Korthorst, H. Jansen, T. S. Lammerink, and M. Elwenspoek. 'The μ -flown: a novel device for measuring acoustic flows'. In: *Sensors and Actuators A: Physical* 54.1 (1996), pp. 552–557. 
- [29] L. Bregant and M. Sandersons. 'Rotational degrees of freedom: an historical overview on techniques and methods'. In: *Proceedings of the International Conference on Noise and Vibration Engineering (ISMA), Leuven, Belgium*. 2000, pp. 973–980.
- [30] G. Cerrato. 'Automotive Sound Quality – Powertrain, Road and Wind Noise'. In: *Sound & vibration* 43.4 (2009), pp. 16–24.











- [31] H. G. Choi, A. N. Thite, and D. J. Thompson. ‘Comparison of methods for parameter selection in Tikhonov regularization with application to inverse force determination’. In: *Journal of Sound & Vibration* 304.3 (2007), pp. 894–917. 
- [32] R. W. Clough. ‘The finite element method in plane stress analysis’. In: *Proceedings of the 2nd Conference on Electronic Computation, Reston, VA*. American Society of Civil Engineers, 1960.
- [33] J. W. Cooley and J. W. Tukey. ‘An algorithm for the machine calculation of complex Fourier series’. In: *Mathematics of Computation* 19.90 (1965), pp. 297–301. 
- [34] R. Courant. ‘Variational methods for the solution of problems of equilibrium and vibrations’. In: *Bulletin of the American Mathematical Society* 49.1 (1943), pp. 1–23.
- [35] R. R. J. Craig and M. C. C. Bampton. ‘Coupling of Substructures Using Component Mode Synthesis’. In: *AIAA Journal* 6.7 (1968), pp. 1313–1319. 
- [36] R. R. J. Craig and A. J. Kurdila. *Fundamentals of Structural Dynamics*. 2nd. New York, London, Sydney: John Wiley & Sons, Inc., 2006. ISBN: 978-0-471-43044-5.
- [37] L. Cremer, M. Heckl, and E. E. Ungar. *Structure-borne sound. Structural Vibrations and Sound Radiation at Audio Frequencies*. 1st. Springer Berlin Heidelberg, 1973. ISBN: 978-3-662-10120-9. 
- [38] J. R. Crowley, A. L. Klosterman, G. T. Rocklin, and H. Vold. ‘Direct structural modification using frequency response functions’. In: *Proceedings of the II International Modal Analysis Conference (IMAC), Orlando, FL*. Society for Experimental Mechanics. Bethel, CT, Feb. 1984.
- [39] J. R. Crowley, A. L. Klosterman, G. T. Rocklin, and H. Vold. ‘Direct structural modification using frequency response functions’. In: *Proceedings of the II International Modal Analysis Conference (IMAC), Orlando, FL*. 1984, pp. 58–65.
- [40] W. D’Ambrogio and A. Fregolent. ‘Decoupling of a substructure from modal data of the complete structure’. In: *Proceedings of the International Conference on Noise and Vibration Engineering (ISMA), Leuven, Belgium*. 2004, pp. 2693–2706.
- [41] W. D’Ambrogio and A. Fregolent. ‘Decoupling procedures in the general framework of frequency based substructuring’. In: *Proceedings of the XXVII International Modal Analysis Conference (IMAC), Orlando, FL*. Society for Experimental Mechanics. Bethel, CT, 2009.
- [42] W. D’Ambrogio and A. Fregolent. ‘The role of interface DoFs in decoupling of substructures based on the dual domain decomposition’. In: *Mechanical Systems & Signal Processing* 24.7 (2010), pp. 2035–2048. 
- [43] W. D’Ambrogio and A. Fregolent. ‘Direct decoupling of substructures using primal and dual formulation’. In: *Linking Models and Experiments*. Vol. 2. Proceedings of the 29th IMAC, A Conference on Structural Dynamics. Springer New York, 2011, pp. 47–76. 
- [44] W. D’Ambrogio and A. Fregolent. ‘Inverse dynamic substructuring using the direct hybrid assembly in the frequency domain’. In: *Mechanical Systems & Signal Processing* 45.2 (2014), pp. 360–377. 
- [45] W. D’Ambrogio and A. Fregolent. ‘Ignoring Rotational DoFs in Decoupling Structures Connected Through Flexotorsional Joints’. In: *Dynamics of Coupled Structures*. Vol. 4. Proceedings of the 33rd IMAC, A Conference and Exposition on Structural Dynamics. Springer New York, 2015. Chap. 6, pp. 57–69. 













- [46] B. J. Dobson and E. Rider. 'A review of the indirect calculation of excitation forces from measured structural response data'. In: *Proceedings of the Institution of Mechanical Engineers, Part C: Journal of Mechanical Engineering Science* 204.2 (1990), pp. 69–75. 
- [47] M. L. M. Duarte and D. J. Ewins. 'Rotational degrees of freedom for structural coupling analysis via finite-difference technique with residual compensation'. In: *Mechanical Systems & Signal Processing* 14.2 (2000), pp. 205–227. 
- [48] T. S. Edwards. 'Implementation of Admittance Test Techniques for High-precision Measurement of Frequency Response Functions'. In: *Topics in Experimental Dynamic Substructuring*. Vol. 2. Proceedings of the 31st IMAC, A Conference on Structural Dynamics. Springer New York, 2013. Chap. 18, pp. 217–243. 
- [49] A. S. Elliott and A. T. Moorhouse. 'Characterisation of structure borne sound sources from measurement in-situ'. In: *Journal of the Acoustical Society of America* 123.5 (2008), pp. 3176–3176. 
- [50] A. S. Elliott, A. T. Moorhouse, T. Huntley, and S. Tate. 'In-situ source path contribution analysis of structure borne road noise'. In: *Journal of Sound & Vibration* 332.24 (2013), pp. 6276–6295. 
- [51] A. S. Elliott, A. T. Moorhouse, and G. Pavić. 'Moment excitation and the measurement of moment mobilities'. In: *Journal of Sound & Vibration* 331.11 (2012), pp. 2499–2519. 
- [52] A. S. Elliott. 'Characterisation of structure borne sound source in-situ'. PhD thesis. University of Salford, 2009.
- [53] D. J. Ewins. *Modal Testing: Theory, Practice and Application*. 2nd. New York, London, Sydney: John Wiley & Sons, Inc., 2000. ISBN: 978-0-86380-218-8.
- [54] D. J. Ewins. 'Exciting Vibrations: A philosophical approach to resolving structural dynamics problems'. In: *Structural dynamics @ 2000: current status and future directions*. Ed. by D. J. Ewins and D. J. Inman. Baldock, Hertfordshire, England: Research Studies Press, 2001, pp. 17–28. ISBN: 0863802516.
- [55] D. J. Ewins. 'Around the World in 80 Courses'. In: *Special Topics in Structural Dynamics*. Vol. 6. Proceedings of the 31st IMAC, A Conference on Structural Dynamics. Springer New York, 2013. Chap. 27, pp. 265–269. 
- [56] D. J. Ewins and D. J. Inman. *Structural dynamics @ 2000: current status and future directions*. Baldock, Hertfordshire, England: Research Studies Press, 2001. ISBN: 0863802516.
- [57] F. J. Fahy. 'The vibro-acoustic reciprocity principle and applications to noise control'. In: *Acta Acustica united with Acustica* 81.6 (1995), pp. 544–558.
- [58] F. J. Fahy. 'Some applications of the reciprocity principle in experimental vibroacoustics'. In: *Acoustical Physics* 49.2 (2003), pp. 217–229. 
- [59] C. Farhat and F.-X. Roux. 'A method of finite element tearing and interconnecting and its parallel solution algorithm'. In: *International Journal for Numerical Methods in Engineering* 32.6 (1991), pp. 1205–1227. 
- [60] D. Fernandez Comesaña, K. Holland, J. Wind, and H. E. de Bree. 'Comparison of inverse methods and particle velocity based techniques for transfer path analysis'. In: *Acoustics 2012*. 2012.
- [61] F. A. Firestone. 'A new analogy between mechanical and electrical systems'. In: *Journal of the Acoustical Society of America* 4.3 (1933), pp. 249–267. 








- [62] F. A. Firestone. 'Thixt Earth and Sky with Rod and Tube; the Mobility and Classical Impedance Analogies'. In: *Journal of the Acoustical Society of America* 28.6 (1956), pp. 1117–1153. 
- [63] M. Fontul, A. M. R. Ribeiro, J. M. M. Silva, and N. M. M. Maia. 'Transmissibility matrix in harmonic and random processes'. In: *Shock and Vibration* 11.5–6 (2004), pp. 563–571. 
- [64] P. Gajdatsy, K. Janssens, W. Desmet, and H. Van Der Auweraer. 'Application of the transmissibility concept in transfer path analysis'. In: *Mechanical Systems & Signal Processing* 24.7 (2010), pp. 1963–1976. 
- [65] P. Gajdatsy, K. Janssens, L. Gielen, P. Mas, and H. Van Der Auweraer. 'Critical assessment of Operational Path Analysis: effect of coupling between path inputs'. In: *Journal of the Acoustical Society of America* 123.5 (2008), p. 3876. 
- [66] P. Gajdatsy, K. Janssens, L. Gielen, P. Mas, and H. Van der Auweraer. 'Critical assessment of Operational Path Analysis: effect of neglected paths'. In: *Proceedings of the XV International Congress on Sound and Vibration (ICSV), Daejeon, Korea. 2008*, pp. 1090–1097.
- [67] P. Gardonio and M. Brennan. *Mobility and impedance methods in structural dynamics: an historical review*. Technical Report. Institute of Sound and Vibration Research (ISVR), University of Southampton, 2000.
- [68] P. Gardonio and M. Brennan. 'On the origins and development of mobility and impedance methods in structural dynamics'. In: *Journal of Sound & Vibration* 249.3 (2002), pp. 557–573. ISSN: 0022-460X. 
- [69] A. Gaudin and J. F. Beniguel. 'Low frequency road noise decomposition at wheel center on a roller bench'. In: *Acoustics 2012*. Société Française d'Acoustique. Nantes, France, 2012.
- [70] M. Géradin and D. J. Rixen. *Mechanical vibrations: theory and application to structural dynamics*. 3rd. John Wiley & Sons, 2015, p. 616. ISBN: 978-1-118-90020-8.
- [71] M. Gibanica. 'Experimental-Analytical Dynamic Substructuring'. Master's thesis. Göteborg, Sweden: Chalmers University of Technology, 2013.
- [72] B. M. Gibbs, N. Qi, and A. T. Moorhouse. 'A practical characterisation for vibro-acoustic sources in buildings'. In: *Acta Acustica united with Acustica* 93.1 (2007), pp. 84–93.
- [73] C. Gontier and M. Bensaïbi. 'Time domain identification of a substructure from in situ analysis of the whole structure'. In: *Mechanical Systems & Signal Processing* 9.4 (1995), pp. 379–396. 
- [74] O. Guasch. 'Direct transfer functions and path blocking in a discrete mechanical system'. In: *Journal of Sound & Vibration* 321.3 (2009), pp. 854–874. 
- [75] O. Guasch, C. García, J. Jové, and P. Artís. 'Experimental validation of the direct transmissibility approach to classical transfer path analysis on a mechanical setup'. In: *Mechanical Systems & Signal Processing* 37.1 (2013), pp. 353–369. 
- [76] O. Guasch and F. X. Magrans. 'The Global Transfer Direct Transfer method applied to a finite simply supported elastic beam'. In: *Journal of Sound & Vibration* 276.1 (2004), pp. 335–359. 
- [77] M. Harrison, A. O. Sykes, and M. Martin. 'Wave effects in isolation mounts'. In: *Journal of the Acoustical Society of America* 24.1 (1952), pp. 62–71. 











- [78] J. Harvie and P. Avitabile. ‘Effects of Precise FRF Measurements for Frequency Based Substructuring’. In: *Topics in Experimental Dynamic Substructuring*. Vol. 2. Proceedings of the 31st IMAC, A Conference on Structural Dynamics. Springer New York, 2013. Chap. 22, pp. 277–285. 
- [79] O. Heaviside. *Electrical Papers*. Vol. 1–2. London: Macmillan, 1882–1884.
- [80] S. Helderweirt, H. Van der Auweraer, P. Mas, L. Bregant, and D. Casagrande. ‘Application of accelerometer-based rotational degree of freedom measurements for engine subframe modelling’. In: *Proceedings of the XIX International Modal Analysis Conference (IMAC)*, St. Louis, MO. Vol. 2. Society for Experimental Mechanics. Bethel, CT, 2001, pp. 1298–1304.
- [81] H. L. F. von Helmholtz. ‘II. Über einige Gesetze der Verteilung elektrischer Ströme in körperlichen Leitern mit Anwendung auf die thierisch-elektrischen Versuche [Some laws concerning the distribution of electrical currents in conductors with applications to experiments on animal electricity]’. In: *Annalen der Physik und Chemie* 89.6 (1853), pp. 211–233.
- [82] E. L. Hixson. ‘Mechanical Impedance and Mobility’. In: *Shock and Vibration Handbook*. Ed. by C. M. Harris and C. E. Crede. 1st. McGraw-Hill, 1961. Chap. 10, pp. 1–59.
- [83] C. Höller and B. M. Gibbs. ‘Indirect determination of the mobility of structure-borne sound sources’. In: *Journal of Sound & Vibration* 344 (2015), pp. 38–58. 
- [84] A. Hrennikoff. ‘Solution of problems of elasticity by the framework method’. In: *Journal of Applied Mechanics* 8.4 (1941), pp. 169–175.
- [85] W. C. Hurty. ‘Vibrations of Structural Systems by Component Mode Synthesis’. In: *Journal of the Engineering Mechanics Division* 86.4 (1960), pp. 51–70.
- [86] P. Ind and D. Ewins. ‘Impedance based decoupling and its application to indirect modal testing and component measurement’. In: *Proceedings of the XXI International Modal Analysis Conference (IMAC)*, Orlando, FL. 252. Society for Experimental Mechanics. Bethel, CT, 2003.
- [87] ISO Technical Committee 43 / Subcommittee 1 / Workgroup 22 (ISO/TC43/SC1/WG22). *Acoustics – Estimation of airborne noise emitted by machinery using vibration measurement*. ISO 7849. International Standards Organisation, 1987.
- [88] ISO Technical Committee 43 / Subcommittee 1 / Workgroup 22 (ISO/TC43/SC1/WG22). *Acoustics – Characterization of sources of structure-borne sound with respect to sound radiation from connected structures – Measurement of velocity at the contact points of machinery when resiliently mounted*. ISO 9611. International Standards Organisation, 1996.
- [89] ISO Technical Committee 43 / Subcommittee 1 / Workgroup 22 (ISO/TC43/SC1/WG22). *Measurement of noise emitted by accelerating road vehicles – Engineering method – Part 1: M and N categories*. ISO 362-1. International Standards Organisation, 2015.
- [90] K. Janssens, P. Mas, P. Gajdatsy, L. Gielen, and H. Van der Auweraer. ‘A novel path contribution analysis method for test-based NVH troubleshooting’. In: *Proceedings of the International Conference on Noise and Vibration Engineering (ISMA)*, Leuven, Belgium. 2008, pp. 3673–3683.
- [91] K. Janssens, P. Gajdatsy, L. Gielen, P. Mas, L. Britte, W. Desmet, and H. van der Auweraer. ‘OPAX: A new transfer path analysis method based on parametric load models’. In: *Mechanical Systems & Signal Processing* 25 (2011), pp. 1321–1338. 
- [92] M. H. A. Janssens and J. W. Verheij. ‘A pseudo-forces methodology to be used in characterization of structure-borne sound sources’. In: *Applied Acoustics* 61.3 (2000), pp. 285–308. 








- [93] M. H. A. Janssens, J. W. Verheij, and T. Loyau. 'Experimental example of the pseudo-forces method used in characterisation of a structure-borne sound source'. In: *Applied Acoustics* 63.1 (2002), pp. 9–34. 
- [94] M. H. A. Janssens, J. W. Verheij, and D. J. Thompson. 'The use of an equivalent forces method for the experimental quantification of structural sound transmission in ships'. In: *Journal of Sound & Vibration* 226.2 (1999), pp. 305–328. 
- [95] B. Jetmundsen, R. Bielawa, and W. G. Flannelly. 'Generalized Frequency Domain Substructure Synthesis'. In: *Journal of the American Helicopter Society* 33.1 (1988), pp. 55–64. 
- [96] D. H. Johnson. 'Origins of the equivalent circuit concept: the current-source equivalent'. In: *Proceedings of the IEEE* 91.5 (2003), pp. 817–821. 
- [97] D. H. Johnson. 'Origins of the equivalent circuit concept: the voltage-source equivalent'. In: *Proceedings of the IEEE* 91.4 (2003), pp. 636–640. 
- [98] T. Jungblut, S. Wolter, M. Matthias, and H. Hanselka. 'Using Numerical Models to Complement Experimental Setups by Means of Active Control of Mobility'. In: *Applied Mechanics and Materials* 70 (2011), pp. 357–362.
- [99] D. C. Kammer. 'Input force reconstruction using a time domain technique'. In: *Journal of Vibration and Acoustics* 120.4 (1998), pp. 868–874. 
- [100] G. R. Kirchhoff. 'Electricität und magnetismus'. In: *Vorlesungen über mathematische Physik*. Ed. by M. Plank. Vol. 3. 1891.
- [101] D. de Klerk. 'Dynamic Response Characterization of Complex Systems through Operational Identification and Dynamic Substructuring'. PhD thesis. Delft University of Technology, The Netherlands, 2009. ISBN: 978-90-90240-95-4.
- [102] D. de Klerk and A. Ossipov. 'Operational transfer path analysis: Theory, guidelines and tire noise application'. In: *Mechanical Systems & Signal Processing* 24.7 (2010). Special Issue: ISMA 2010, pp. 1950–1962. ISSN: 0888-3270. 
- [103] D. de Klerk and D. J. Rixen. 'Component transfer path analysis method with compensation for test bench dynamics'. In: *Mechanical Systems & Signal Processing* 24.6 (2010), pp. 1693–1710. ISSN: 0888-3270. 
- [104] D. de Klerk, D. J. Rixen, and S. N. Voormeeren. 'General Framework for Dynamic Substructuring: History, Review and Classification of Techniques'. In: *AIAA Journal* 46.8 (2008), pp. 1169–1181. 
- [105] D. de Klerk, D. Rixen, and J. de Jong. 'The Frequency Based Substructuring Method reformulated according to the Dual Domain Decomposition Method'. In: *Proceedings of the XXIV International Modal Analysis Conference (IMAC), St. Louis, MO*. Society for Experimental Mechanics. Bethel, CT, 2006.
- [106] D. de Klerk, D. Rixen, S. Voormeeren, and F. Pasteuning. 'Solving the RDoF Problem in Experimental Dynamic Substructuring'. In: *Proceedings of the XXVI International Modal Analysis Conference (IMAC), Orlando, FL*. Society for Experimental Mechanics. Bethel, CT, 2008.
- [107] D. de Klerk and S. Voormeeren. 'Uncertainty Propagation in Experimental Dynamic Substructuring'. In: *Proceedings of the XXVI International Modal Analysis Conference (IMAC), Orlando, FL*. Society for Experimental Mechanics. Bethel, CT, 2008.
- [108] D. de Klerk, M. Lohrmann, M. Quickert, and W. Foken. 'Application of operational transfer path analysis on a classic car'. In: *DAGA*. Rotterdam, 2009.











- [109] P. Le Corbeiller and Y.-W. Yeung. ‘Duality in mechanics’. In: *Journal of the Acoustical Society of America* 24.6 (1952), pp. 643–648. 
- [110] Q. Leclère, N. B. Roozen, and C. Sandier. ‘Experimental estimation of transmissibility matrices’. In: *Proceedings of the International Conference on Noise and Vibration Engineering (ISMA), Leuven, Belgium*. 2012.
- [111] D. Lennström and A. Nykänen. *Interior Sound of Today’s Electric Cars: Tonal Content, Levels and Frequency Distribution*. Tech. rep. 2015-01-2367. SAE Technical Paper, 2015. 
- [112] D. Lennström, M. Olsson, F. Wullens, and A. Nykänen. ‘Validation of the blocked force method for various boundary conditions for automotive source characterization’. In: *Applied Acoustics* 102 (2016), pp. 108–119. 
- [113] A. Liljerehn and T. Abrahamsson. ‘Dynamic sub-structuring with passive state-space components’. In: *Proceedings of the International Conference on Noise and Vibration Engineering (ISMA), Leuven, Belgium*. 2014, pp. 3879–3890. ISBN: 978-907380291-9.
- [114] J. Liu, W. Zhu, Q. Lu, and G. Ren. ‘An efficient iterative algorithm for accurately calculating impulse response functions in modal testing’. In: *Journal of Vibration and Acoustics* 133.6 (2011), p. 064505. 
- [115] J. Liu, M. Li, L. Qin, and J. Liu. ‘Principle Research on a Single Mass Piezoelectric Six-Degrees-of-Freedom Accelerometer’. In: *Sensors* 13.8 (2013), pp. 10844–10855. 
- [116] L. Liu and T. C. Lim. *Application of FRF-based inverse substructuring analysis to vehicle NVH problems*. Tech. rep. 2003-01-1607. SAE Technical Paper, 2003. 
- [117] W. Liu and D. Ewins. ‘The importance assessment of RDOF in FRF coupling analysis’. In: *Proceedings of the XVII International Modal Analysis Conference (IMAC), Kissimmee, FL*. Society for Experimental Mechanics. Bethel, CT, 1999, pp. 1481–1487.
- [118] W. Liu and D. J. Ewins. ‘Transmissibility properties of MDOF systems’. In: *Proceedings of the XVI International Modal Analysis Conference (IMAC), Santa Barbara, CA*. Society for Experimental Mechanics. Bethel, CT, 1998, pp. 847–854.
- [119] LMS International. *Transfer Path Analysis: The Qualification and Quantification of Vibroacoustic Transfer Paths*. Leuven, Belgium, 1995.
- [120] M. Lohrmann. ‘Operational transfer path analysis: Comparison with conventional methods’. In: *Journal of the Acoustical Society of America* 123 (2008), pp. 3534–3534. 
- [121] I. Lopez Arteaga, R. Scholte, and H. Nijmeijer. ‘Improved source reconstruction in Fourier-based Near-field Acoustic Holography applied to small apertures’. In: *Mechanical Systems & Signal Processing* 32 (2012), pp. 359–373. 
- [122] M. B. Madsen. ‘Electrical Power Assisted Steering – Dynamic Source Strength Characteristic and Vehicle NVH Prediction’. MA thesis. University of Southern Denmark, 2014.
- [123] F. X. Magrans. ‘Method of Measuring Transmission Paths’. In: *Journal of Sound & Vibration* 74.3 (1981), pp. 321–330. 
- [124] F. X. Magrans, P. V. Rodriguez, and G. C. Cousin. ‘Low and mid-high frequency advanced transmission path analysis’. In: *Proceedings of the XII International Congress on Sound and Vibration (ICSV), Lisbon, Portugal*. 2005.
- [125] N. M. M. Maia, J. M. M. Silva, and A. M. R. Ribeiro. ‘The Transmissibility Concept in Multi-Degree Systems’. In: *Mechanical Systems & Signal Processing* 15.1 (2001), pp. 129–137. ISSN: 0888-3270. 









- [126] P. Mas and P. Sas. ‘Indirect force identification based upon impedance matrix inversion: a study on statistical and deterministical accuracy’. In: *Proceedings of the International Conference on Noise and Vibration Engineering (ISMA), Leuven, Belgium*. 1994.
- [127] R. L. Mayes and M. R. Ross. ‘Advancements in hybrid dynamic models combining experimental and finite element substructures’. In: *Mechanical Systems & Signal Processing* 31 (2012), pp. 56–66. 
- [128] R. Mayes. ‘Tutorial on Experimental Dynamic Substructuring using the Transmission Simulator Method’. In: *Topics in Experimental Dynamics Substructuring and Wind Turbine Dynamics*. Vol. 2. Proceedings of the 30th IMAC, A Conference on Structural Dynamics, 2012. Springer, 2012. Chap. 1, pp. 1–9. 
- [129] J. D. Maynard, E. G. Williams, and Y. Lee. ‘Nearfield acoustic holography: I. Theory of generalized holography and the development of NAH’. In: *Journal of the Acoustical Society of America* 78.4 (1985), pp. 1395–1413. 
- [130] J. M. Mondot and B. A. T. Petersson. ‘Characterization of structure-borne sound sources: The source descriptor and the coupling function’. In: *Journal of Sound & Vibration* 114.3 (1987), pp. 507–518. ISSN: 0022-460X. 
- [131] D. Montalvao, A. Ribeiro, N. Maia, and J. Silva. ‘Estimation of the rotational terms of the dynamic response matrix’. In: *Shock and Vibration* 11.3–4 (2004), pp. 333–350. 
- [132] A. T. Moorhouse. ‘On the characteristic power of structure-borne sound sources’. In: *Journal of Sound & Vibration* 248.3 (2001), pp. 441–459. 
- [133] A. T. Moorhouse. ‘Virtual acoustic prototypes: Listening to machines that don’t exist’. In: *Acoustics Australia* 33.3 (2005), pp. 97–105.
- [134] A. T. Moorhouse, A. S. Elliott, and T. A. Evans. ‘In situ measurement of the blocked force of structure-borne sound sources’. In: *Journal of Sound & Vibration* 325.4–5 (2009), pp. 679–685. ISSN: 0022-460X. 
- [135] A. T. Moorhouse and G. Seiffert. ‘Characterisation of an airborne sound source for use in a virtual acoustic prototype’. In: *Journal of Sound & Vibration* 296.1–2 (2006), pp. 334–352. 
- [136] A. Moorhouse and A. Elliott. ‘The “round trip” theory for reconstruction of Green’s functions at passive locations’. In: *The Journal of the Acoustical Society of America* 134.5 (2013), pp. 3605–3612. 
- [137] P. A. Nelson and S.-H. Yoon. ‘Estimation of acoustic source strength by inverse methods: Part I, conditioning of the inverse problem’. In: *Journal of Sound & Vibration* 233.4 (2000), pp. 639–664. 
- [138] D. Nicgorski. ‘Investigation on experimental issues related to frequency response function measurements for frequency based substructuring’. MA thesis. University of Massachusetts Lowell, 2008, p. 156.
- [139] D. Nicgorski and P. Avitabile. ‘Conditioning of FRF measurements for use with frequency based substructuring’. In: *Mechanical Systems & Signal Processing* 24.2 (2010), pp. 340–351. 
- [140] D. Nicgorski and P. Avitabile. ‘Experimental issues related to frequency response function measurements for frequency-based substructuring’. In: *Mechanical Systems & Signal Processing* 24.5 (2010), pp. 1324–1337. 
- [141] E. L. Norton. *Design of finite networks for uniform frequency characteristic*. Tech. rep. Technical Report TM26–0–1860, Bell Laboratories, 1926.














- [142] K. Noumura and J. Yoshida. 'A method of transfer path analysis for vehicle interior sound with no excitation experiment.' In: *Proceedings of FISITA 2006 World Automotive Congress*. F2006D183. JSAE, 2006.
- [143] J. C. O'Callahan, P. Avitabile, and R. Riemer. 'System Equivalent Reduction Expansion Process (SEREP)'. In: *Proceedings of the VII International Modal Analysis Conference (IMAC), Boston, MA*. Vol. 1. Society for Experimental Mechanics. Bethel, CT, 1989, pp. 29–37.
- [144] G. J. O'Hara. 'Mechanical Impedance and Mobility concepts'. In: *Journal of the Acoustical Society of America* 41.5 (1967), pp. 1180–1184. 
- [145] F. J. On. *Mechanical Impedance Analysis for Lumped Parameter Multi-Degree of Freedom/Multi-Dimensional Systems*. Tech. rep. NASA Technical Note D-3865, May 1967.
- [146] E. A. Pasma. 'Towards A Robust Component Transfer Path Analysis Method: Application and Validation in Automotive Research'. MA thesis. Delft University of Technology, The Netherlands, 2014.
- [147] F. Pasteuning. 'Experimental Dynamic Substructuring and its Application in Automotive Research'. MA thesis. Delft University of Technology, The Netherlands, 2007.
- [148] G. Pavić and N. Totaro. 'Noise source characterisation using patch impedance technique'. In: *Journal of the Acoustical Society of America* 123.5 (2008), pp. 3310–3310. 
- [149] F. Penne. 'Shaping the sound of the next-generation BMW'. In: *Proceedings of the International Conference on Noise and Vibration Engineering (ISMA), Leuven, Belgium*. 2004, pp. 25–39.
- [150] B. Petersson. 'On the use of giant magnetostrictive devices for moment excitation'. In: *Journal of Sound & Vibration* 116.1 (1987), pp. 191–194. 
- [151] B. A. T. Petersson and B. M. Gibbs. 'Use of the source descriptor concept in studies of multi-point and multi-directional vibrational sources'. In: *Journal of Sound & Vibration* 168.1 (1993), pp. 157–176. 
- [152] B. A. T. Petersson and B. M. Gibbs. 'Towards a structure-borne sound source characterization'. In: *Applied Acoustics* 61.3 (2000), pp. 325–343.
- [153] R. Plunkett. 'Interaction between a vibratory machine and its foundation'. In: *Noise Control* 4.1 (1958), pp. 18–22.
- [154] J. Plunt. *Examples of using transfer path analysis (TPA) together with CAE-models to diagnose and find solutions for NVH problems late in the vehicle development process*. Tech. rep. 2005-01-2508. SAE Technical Paper, 2005. 
- [155] J. Plunt. 'Finding and fixing vehicle NVH problems with transfer path analysis'. In: *Sound & vibration* 39.11 (2005), pp. 12–16.
- [156] J. Plunt, E. Kamph, and D. Fothergill. *Dynamic analysis and acoustic optimization of the Volvo multi-link rear suspension*. Technical Paper 891142. SAE International, 1989. 
- [157] R. E. Powell and W. Seering. 'Multichannel structural inverse filtering'. In: *Journal of Vibration and Acoustics* 106.1 (1984), pp. 22–28. 
- [158] J. Putner, H. Fastl, M. Lohrmann, A. Kaltenhauser, and F. Ullrich. 'Operational transfer path analysis predicting contributions to the vehicle interior noise for different excitations from the same sound source'. In: *InterNoise12, New York City, NY*. INTER-NOISE and NOISE-CON Congress and Conference Proceedings 3. 2012, pp. 2336–2347.







- [159] J. Putner, M. Lohrmann, and H. Fastl. ‘Contribution analysis of vehicle exterior noise with operational transfer path analysis’. In: *Journal of the Acoustical Society of America* 133.5 (2013), pp. 3323–3323. 
- [160] J. W. Strutt (3rd Baron Rayleigh). *The Theory of Sound*. Vol. 1. Macmillan, 1877.
- [161] Y. Ren and C. Beards. ‘On substructure synthesis with FRF data’. In: *Journal of Sound & Vibration* 185.5 (1995), pp. 845–866. 
- [162] P. Reuss, B. Zeumer, J. Herrmann, and L. Gaul. ‘Consideration of interface damping in dynamic substructuring’. In: *Topics in Experimental Dynamics Substructuring and Wind Turbine Dynamics*. Vol. 2. Proceedings of the 30th IMAC, A Conference on Structural Dynamics. Springer New York, 2012. Chap. 10, pp. 81–88. 
- [163] A. M. R. Ribeiro, N. M. M. Maia, and J. M. M. Silva. ‘Experimental evaluation of the transmissibility matrix’. In: *Proceedings of the XVII International Modal Analysis Conference (IMAC), Kissimmee, FL*. 1999.
- [164] A. M. R. Ribeiro, J. M. M. Silva, and N. M. M. Maia. ‘On the generalisation of the transmissibility concept’. In: *Mechanical Systems & Signal Processing* 14.1 (2000), pp. 29–35. 
- [165] D. J. Rixen. ‘A dual Craig–Bampton method for dynamic substructuring’. In: *Journal of Computational and applied mathematics* 168.1 (2004), pp. 383–391. 
- [166] D. J. Rixen. ‘Substructuring using Impulse Response Functions for Impact Analysis’. In: *Proceedings of the XXVIII International Modal Analysis Conference (IMAC), Jacksonville, FL*. Society for Experimental Mechanics. Bethel, CT, 2010.
- [167] D. J. Rixen, A. Boogaard, M. V. van der Seijs, G. van Schothorst, and T. van der Poel. ‘Vibration source description in substructuring: A theoretical depiction’. In: *Mechanical Systems & Signal Processing* 60–61 (2015), pp. 498–511. 
- [168] D. J. Rixen and P. L. C. van der Valk. ‘An impulse based substructuring approach for impact analysis and load case simulations’. In: *Journal of Sound & Vibration* 332.26 (2013), pp. 7174–7190. 
- [169] D. Rixen. ‘How Measurement Inaccuracies Induce Spurious Peaks in Frequency Based Substructuring’. In: *Proceedings of the XXVI International Modal Analysis Conference (IMAC), Orlando, FL*. Society for Experimental Mechanics. Bethel, CT, 2008.
- [170] D. Rixen. ‘A Substructuring Technique Based on Measured and Computed Impulse Response Functions of Components’. In: *Proceedings of the International Conference on Noise and Vibration Engineering (ISMA 2010), Leuven, Belgium, 20–22 September 2010*. 2010.
- [171] N. B. Roozen and Q. Leclère. ‘On the use of artificial excitation in operational transfer path analysis’. In: *Applied Acoustics* 74.10 (2013), pp. 1167–1174. 
- [172] S. Rubin. ‘Improved component-mode representation for structural dynamic analysis’. In: *AIAA Journal* 13.8 (1975), pp. 995–1006. 
- [173] S. Rubin. ‘Transmission matrices for vibration and their relation to admittance and impedance’. In: *Journal of Manufacturing Science and Engineering* 86.1 (1964), pp. 9–21. 
- [174] S. Rubin. ‘Mechanical Immittance- and Transmission-Matrix Concepts’. In: *Journal of the Acoustical Society of America* 41.5 (1967), pp. 1171–1179. 
- [175] D. Sachse, T. Geluk, and T. van Wayenberge. ‘Accuracy of inverse load identification techniques for transfer path analysis’. In: *Automotive Acoustics Conference 2013, 2nd International ATZ Conference*. ATZlive. 2013.

- [176] M. A. Sanderson and C. R. Fredö. ‘Direct measurement of moment mobility: Part I: A theoretical study’. In: *Journal of Sound & Vibration* 179.4 (1995), pp. 669–684. 
- [177] F. L. M. dos Santos, B. Peeters, J. Lau, W. Desmet, and L. C. S. Góes. ‘An Overview of Experimental Strain-Based Modal Analysis Methods’. In: *Proceedings of the International Conference on Noise and Vibration Engineering (ISMA), Leuven, Belgium*. 2014.
- [178] V. Saouma and M. Sivaselvan, eds. *Hybrid Simulation: Theory, Implementation and Applications*. Taylor & Francis, 2008.
- [179] J. Scheuren and M. Lohrmann. ‘Transfer Path Analysis – Experiences, Expectations and Perspectives’. In: *International Noise and Vibration Colloquium*. SAE Brazil. 2014.
- [180] R. M. Schmidt, G. Schitter, A. Rankers, and J. van Eijk. *The design of high performance mechatronics – High-Tech Functionality by Multidisciplinary System Integration*. 2nd Revised Edition. IOS Press, 2014, p. 928. ISBN: 978-1-61499-367-4. 
- [181] M. Schneider, M. Wilhelm, and N. Alt. *Development of vehicle sound quality-targets and methods*. Tech. rep. 951283. SAE Technical Paper, 1995.
- [182] G. van Schothorst, M. A. Boogaard, G. W. van der Poel, and D. J. Rixen. ‘Analysis of ground vibration transmission in high precision equipment by Frequency Based Substructuring’. In: *Proceedings of the International Conference on Noise and Vibration Engineering (ISMA), Leuven, Belgium*. 2012, pp. 3501–3514.
- [183] H. Schwarz. ‘Gesammelte Mathematische Abhandlungen’. In: vol. 2. First published in Vierteljahrsschrift der Naturforschenden Gesellschaft in Zürich, volume 15, 1870, 272–286. Berlin: Springer Verlag, 1890, pp. 133–143.
- [184] M. V. van der Seijs, D. D. van den Bosch, D. J. Rixen, and D. de Klerk. ‘An improved methodology for the virtual point transformation of measured frequency response functions in dynamic substructuring’. In: *4th ECCOMAS Thematic Conference on Computational Methods in Structural Dynamics and Earthquake Engineering (COMPdyn)*. Ed. by M. Papadrakakis, V. Papadopoulos, and V. Plevris. Kos Island, Greece, 2013, pp. 4334–4347. 
- [185] M. V. van der Seijs, D. de Klerk, and D. J. Rixen. ‘General Framework for Transfer Path Analysis: History, Theory and Classification of Techniques’. In: *Mechanical Systems & Signal Processing* 68–69 (2016), pp. 217–244. 
- [186] M. V. van der Seijs, D. de Klerk, D. J. Rixen, and S. Rahimi. ‘Validation of current state Frequency Based Substructuring Technology for the characterisation of Steering Gear – Vehicle Interaction’. In: *Topics in Experimental Dynamic Substructuring*. Vol. 2. Proceedings of the 31st IMAC, A Conference on Structural Dynamics. Springer New York, 2013. Chap. 20, pp. 253–266. 
- [187] M. V. van der Seijs, E. A. Pasma, D. de Klerk, and D. J. Rixen. ‘A robust Transfer Path Analysis method for steering gear vibrations on a test bench’. In: *Proceedings of the International Conference on Noise and Vibration Engineering (ISMA), Leuven, Belgium*. 2014. 
- [188] M. V. van der Seijs, E. A. Pasma, D. de Klerk, and D. J. Rixen. ‘A Comparison of Two Component TPA Approaches for Steering Gear Noise Prediction’. In: *Dynamics of Coupled Structures*. Vol. 4. Proceedings of the 33rd IMAC, A Conference and Exposition on Structural Dynamics. Springer New York, 2015. Chap. 7, pp. 71–79. 
- [189] M. V. van der Seijs and D. J. Rixen. ‘Efficient Impulse Based Substructuring using Truncated Impulse Response Functions and Mode Superposition’. In: *Proceedings of the International Conference on Noise and Vibration Engineering (ISMA), Leuven, Belgium*. 2012, pp. 3487–3499. 

- [190] M. V. van der Seijs, P. L. C. van der Valk, T. van der Horst, and D. J. Rixen. 'Towards Dynamic Substructuring Using Measured Impulse Response Functions'. In: *Dynamics of Coupled Structures*. Vol. 1. Proceedings of the 32nd IMAC, A Conference and Exhibition on Structural Dynamics. Springer New York, 2014. Chap. 6, pp. 73–82. 
- [191] P. Sjövall and T. Abrahamsson. 'State-space model identification for component synthesis'. In: *Proceedings of the XXV International Modal Analysis Conference (IMAC), Orlando, FL*. Society for Experimental Mechanics. Bethel, CT, 2007.
- [192] P. Sjövall and T. Abrahamsson. 'Component system identification and state-space model synthesis'. In: *Mechanical Systems & Signal Processing* 21.7 (2007), pp. 2697–2714. 
- [193] P. Sjövall and T. Abrahamsson. 'Substructure system identification from coupled system test data'. In: *Mechanical Systems & Signal Processing* 22.1 (2008), pp. 15–33. 
- [194] P. Sjövall, T. McKelvey, and T. Abrahamsson. 'Constrained state-space system identification with application to structural dynamics'. In: *Automatica* 42.9 (2006), pp. 1539–1546. 
- [195] J. Snowdon. 'Mechanical four-pole parameters and their application'. In: *Journal of Sound & Vibration* 15.3 (1971), pp. 307–323. ISSN: 0022-460X. 
- [196] J. C. Snowdon. 'Vibration isolation: use and characterization'. In: *Journal of the Acoustical Society of America* 66.5 (1979), pp. 1245–1274. 
- [197] Society of Experimental Mechanics. *Proceedings of the International Modal Analysis Conference (IMAC)*. Bethel, CT, since 1982.
- [198] J. Soliman and M. Hallam. 'Vibration isolation between non-rigid machines and non-rigid foundations'. In: *Journal of Sound & Vibration* 8.2 (1968), pp. 329–351. ISSN: 0022-460X. 
- [199] M. Sturm, A. T. Moorhouse, T. Alber, and F. F. Li. 'Force reconstruction using an adaptive algorithm in time domain'. In: *Proceedings of the International Conference on Noise and Vibration Engineering (ISMA), Leuven, Belgium*. 2012, pp. 17–19.
- [200] M. Sturm, A. T. Moorhouse, W. Kropp, and T. Alber. 'Robust calculation of simultaneous multi-channel blocked force signatures from measurements made in-situ using an adaptive algorithm in time domain'. In: *Proceedings of the XX International Congress on Sound and Vibration (ICSV), Bangkok, Thailand*. Vol. 2. 2013, pp. 1610–1617.
- [201] T.-J. Su and J.-N. Juang. 'Substructure system identification and synthesis'. In: *Journal of Guidance, Control, and Dynamics* 17.5 (1994), pp. 1087–1095. 
- [202] A. O. Sykes. 'Application of Admittance and Impedance Concepts in the Synthesis of Vibrating Systems'. In: *Synthesis of vibrating systems: (Colloquium) Winter Annual Meeting of the ASME, Washington, D.C.* Ed. by V. Neubert and J. Raney. Shock and Vibration Committee of the Applied Mechanics Division, American Society of Mechanical Engineers. 1971, pp. 22–33.
- [203] M. L. Thévenin. 'Sur un nouveau théoreme d'électricité dynamique [On a new theorem of dynamic electricity]'. In: *Comptes Rendus hebdomadaires des des Séances de l'Académie des Sciences* 97 (1883), pp. 159–161.
- [204] A. N. Thite and D. J. Thompson. 'The quantification of structure-borne transmission paths by inverse methods. Part 1: Improved singular value rejection methods'. In: *Journal of Sound & Vibration* 264.2 (2003), pp. 411–431. 
- [205] A. N. Thite and D. J. Thompson. 'The quantification of structure-borne transmission paths by inverse methods. Part 2: Use of regularization techniques'. In: *Journal of Sound & Vibration* 264.2 (2003), pp. 433–451. 

- [206] A. N. Thite and D. J. Thompson. 'Selection of response measurement locations to improve inverse force determination'. In: *Applied Acoustics* 67.8 (2006), pp. 797–818. 
- [207] D. J. Thompson, W. J. van Vliet, and J. W. Verheij. 'Developments of the indirect method for measuring the high frequency dynamic stiffness of resilient elements'. In: *Journal of Sound & Vibration* 213.1 (1998), pp. 169–188. 
- [208] E. Ungar and C. Dietrich. 'High-frequency vibration isolation'. In: *Journal of Sound & Vibration* 4.2 (1966), pp. 224–241. 
- [209] A. P. V. Urgueira. 'Dynamic analysis of coupled structures using experimental data'. PhD thesis. Imperial College of Science, Technology and Medicine, University of London, 1989.
- [210] P. L. C. van der Valk and D. J. Rixen. 'Substituting Internal Forces for Blocked Forces or Free Interface Displacements in Substructured Simulations'. In: *Topics in Experimental Dynamic Substructuring*. Vol. 2. Proceedings of the 31st IMAC, A Conference on Structural Dynamics. Springer New York, 2014. Chap. 8, pp. 77–96. 
- [211] P. L. C. van der Valk and D. J. Rixen. 'An Impulse Based Substructuring method for coupling impulse response functions and finite element models'. In: *Computer Methods in Applied Mechanics and Engineering* 275 (2014), pp. 113–137. 
- [212] D. D. Van den Bosch. 'Impulse Based Substructuring Unravelling; Simulation and Coupling of Structural Dynamics in the Time Domain'. MA thesis. Delft University of Technology, The Netherlands, 2014.
- [213] T. Van der Horst. 'Experimental dynamic substructuring using direct time-domain deconvolved impulse response functions'. MA thesis. Delft University of Technology, The Netherlands, 2014.
- [214] P. L. C. Van der Valk and D. J. Rixen. 'Impulse based substructuring for coupling offshore structures and wind turbines in aero-elastic simulations'. In: *Proceedings of 53rd AIAA/ASME/ASCE/AHS/ASC structures, structural dynamics and materials conference, Honolulu, Hawaii*. American Institute of Aeronautics and Astronautics. 2012, pp. 23–26. 
- [215] P. L. C. Van der Valk. 'Coupled Simulations of Wind Turbines and Offshore Support Structures: Strategies based on the Dynamic Substructuring Paradigm'. PhD thesis. Delft University of Technology, The Netherlands, 2014. ISBN: 9789462036819. 
- [216] P. S. Varoto and K. G. McConnell. 'Single point vs. multi point acceleration transmissibility concepts in vibration testing'. In: *Proceedings of the XVI International Modal Analysis Conference (IMAC), Santa Barbara, CA*. Vol. 1. Society for Experimental Mechanics. Bethel, CT, 1998, pp. 83–90.
- [217] J. W. Verheij. 'Measuring sound transfer through resilient mountings for separate excitation with orthogonal translations and rotations'. In: *InterNoise80, Miami, FL*. INTERNOISE and NOISE-CON Congress and Conference Proceedings 2. Institute of Noise Control Engineering. Institute of Noise Control Engineering, 1980, pp. 723–726.
- [218] J. W. Verheij. 'Multi-path sound transfer from resiliently mounted shipboard machinery: Experimental methods for analyzing and improving noise control'. PhD thesis. Delft University of Technology, The Netherlands, 1982.
- [219] S. N. Voormeeren, P. L. C. van der Valk, and D. J. Rixen. 'Generalized methodology for assembly and reduction of component models for dynamic substructuring'. In: *AIAA Journal* 49.5 (2011), pp. 1010–1020. 

- [220] S. Voormeeren and D. Rixen. 'A family of substructure decoupling techniques based on a dual assembly approach'. In: *Mechanical Systems & Signal Processing* 27.18 (2012), p. 379. 
- [221] S. N. Voormeeren. 'Dynamic Substructuring Methodologies for Integrated Dynamic Analysis of Wind Turbines'. PhD thesis. Delft University of Technology, The Netherlands, 2012. 
- [222] M. Vorländer. *Auralization: Fundamentals of Acoustics, Modelling, Simulation, Algorithms and Acoustic Virtual Reality*. 1st. Springer-Verlag Berlin Heidelberg, 2007. ISBN: 3540488294, 9783540488293. 
- [223] M. Vorländer and P. Dietrich. 'Transfer Path Analysis and Synthesis for Auralization'. In: *39th Congreso Espanol de Acústica 2008, Coimbra, Portugal*. 2008.
- [224] J. Wang, Z.-w. Wang, and L.-x. Lu. 'Step-by-step decoupling method for inverse substructuring analysis of a three-component coupled packaging system'. In: *Journal of Vibration and Control* 21.4 (2013), pp. 676–683. 
- [225] Z.-W. Wang, J. Wang, Y.-B. Zhang, C.-Y. Hu, and Y. Zhu. 'Application of the inverse substructure method in the investigation of dynamic characteristics of product transport system'. In: *Packaging Technology and Science* 25.6 (2012), pp. 351–362. 
- [226] A. G. Webster. 'Acoustical impedance and the theory of horns and of the phonograph'. In: *Proceedings of the National Academy of Sciences of the United States of America* 5.7 (1919 (submitted in 1914)), p. 275.
- [227] W. Weijtjens, G. De Sitter, C. Devriendt, and P. Guillaume. 'Operational modal parameter estimation of MIMO systems using transmissibility functions'. In: *Automatica* 50.2 (2014), pp. 559–564. 
- [228] T. Weisser, L. O. Gonidou, E. Foltête, and N. Bouhaddi. 'Optimization of substructure dynamic interface forces by an energetic approach'. In: *Structural Dynamics*. Vol. 3. Proceedings of the 28th IMAC, A Conference on Structural Dynamics, 2010. Springer New York, 2011, pp. 801–809. 
- [229] T. Weisser, E. Foltête, N. Bouhaddi, and L.-O. Gonidou. 'A power flow mode approach dedicated to structural interface dynamic characterization'. In: *Journal of Sound & Vibration* 334 (2015), pp. 202–218. 
- [230] E. G. Williams. 'Regularization methods for near-field acoustical holography'. In: *Journal of the Acoustical Society of America* 110.4 (2001), pp. 1976–1988. 
- [231] T. ten Wolde. 'Reciprocity experiments on the transmission of sound in ships'. PhD thesis. Delft University of Technology, The Netherlands, 1973.
- [232] T. ten Wolde. 'Reciprocity measurements in acoustical and mechano-acoustical systems. Review of theory and applications'. In: *Acta Acustica united with Acustica* 96.1 (2010), pp. 1–13. 
- [233] T. ten Wolde and G. R. Gedefelt. 'Development of Standard Measurement Methods for Structureborne Sound Emission'. In: *Noise Control Engineering Journal* 28.1 (1987), pp. 5–14. 
- [234] T. ten Wolde, J. W. Verheij, and H. F. Steenhoek. 'Reciprocity method for the measurement of mechano-acoustical transfer functions'. In: *Journal of Sound & Vibration* 42.1 (1975), pp. 49–55. 
- [235] K. Wyckaert, F. Augusztinovicz, and P. Sas. 'Vibro-acoustical modal analysis: Reciprocity, model symmetry, and model validity'. In: *Journal of the Acoustical Society of America* 100.5 (1996), pp. 3172–3181. 

- [236] Y.-P. Xiong, J. Xing, and W. Price. 'A power flow mode theory based on a system's damping distribution and power flow design approaches'. In: *Proceedings of the Royal Society A: Mathematical, Physical and Engineering Science* 461.2063 (2005), pp. 3381–3411. 
- [237] S.-H. Yoon and P. A. Nelson. 'Estimation of acoustic source strength by inverse methods: Part II, experimental investigation of methods for choosing regularization parameters'. In: *Journal of Sound & Vibration* 233.4 (2000), pp. 665–701. 
- [238] J. Yoshida and H. Ishihara. 'Method for the Separation of Vehicle Interior Noise Contributions Using Only Response Signals'. In: *Journal of System Design and Dynamics* 7.4 (2013), pp. 416–427. 
- [239] P. Zeller. *Handbuch Fahrzeugakustik. Grundlagen, Auslegung, Berechnung, Versuch*. Springer, 2009. ISBN: 978-3-8348-1443-2. 
- [240] J. Zhen, T. C. Lim, and G. Lu. 'Determination of system vibratory response characteristics applying a spectral-based inverse sub-structuring approach. Part I: analytical formulation'. In: *International Journal of Vehicle Noise and Vibration* 1.1-2 (2004), pp. 1–30. 
- [241] J. Zhen, T. C. Lim, and G. Lu. 'Determination of system vibratory response characteristics applying a spectral-based inverse sub-structuring approach. Part II: motor vehicle structures'. In: *International Journal of Vehicle Noise and Vibration* 1.1-2 (2004), pp. 31–67. 
- [242] O. C. Zienkiewicz. *The finite element method*. Vol. 3. McGraw-hill London, 1977.



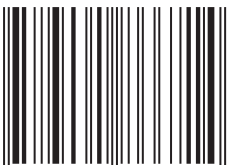
Experimental Dynamic Substructuring

Analysis and Design Strategies for Vehicle Development

Maarten van der Seijs

 **TU Delft** Delft
University of
Technology

ISBN 978-94-6186-671-4



9 789461 866714